Synthesis and Characterization of New Carbon Nitrogen Structures, Thin Films and Nanotubes

Susana Trasobares

To cite this version:

Susana Trasobares. Synthesis and Characterization of New Carbon Nitrogen Structures, Thin Films and Nanotubes. Physique [physics]. Université Paris Sud - Paris XI, 2001. Français. NNT : . tel-00002751

HAL Id: tel-00002751
https://theses.hal.science/tel-00002751

Submitted on 18 Apr 2003

ORSAY

N° ordre 6592

UNIVERSITE PARIS-SUD

CENTRE D’ORSAY

THESE
Presentée
pour obtenir

Le GRADE de DOCTEUR en SCIENCES
De l’Université PARIS XI ORSAY

par

Susana TRASOBARES LLORENTE

SYNTHESIS AND CHARACTERISATION OF NEW CARBON NITROGEN STRUCTURES: THIN FILMS AND NANOTUBES

Soutenue le 27 septembre 2001 devant la Commission d’examen

P. Berthet	Président
S. Csillag	Rapporteur
A. Loiseau	Rapporteur
C. Colliex	
B. Jouffrey	
O.Stéphan	
D.R.M. Walton	Invité

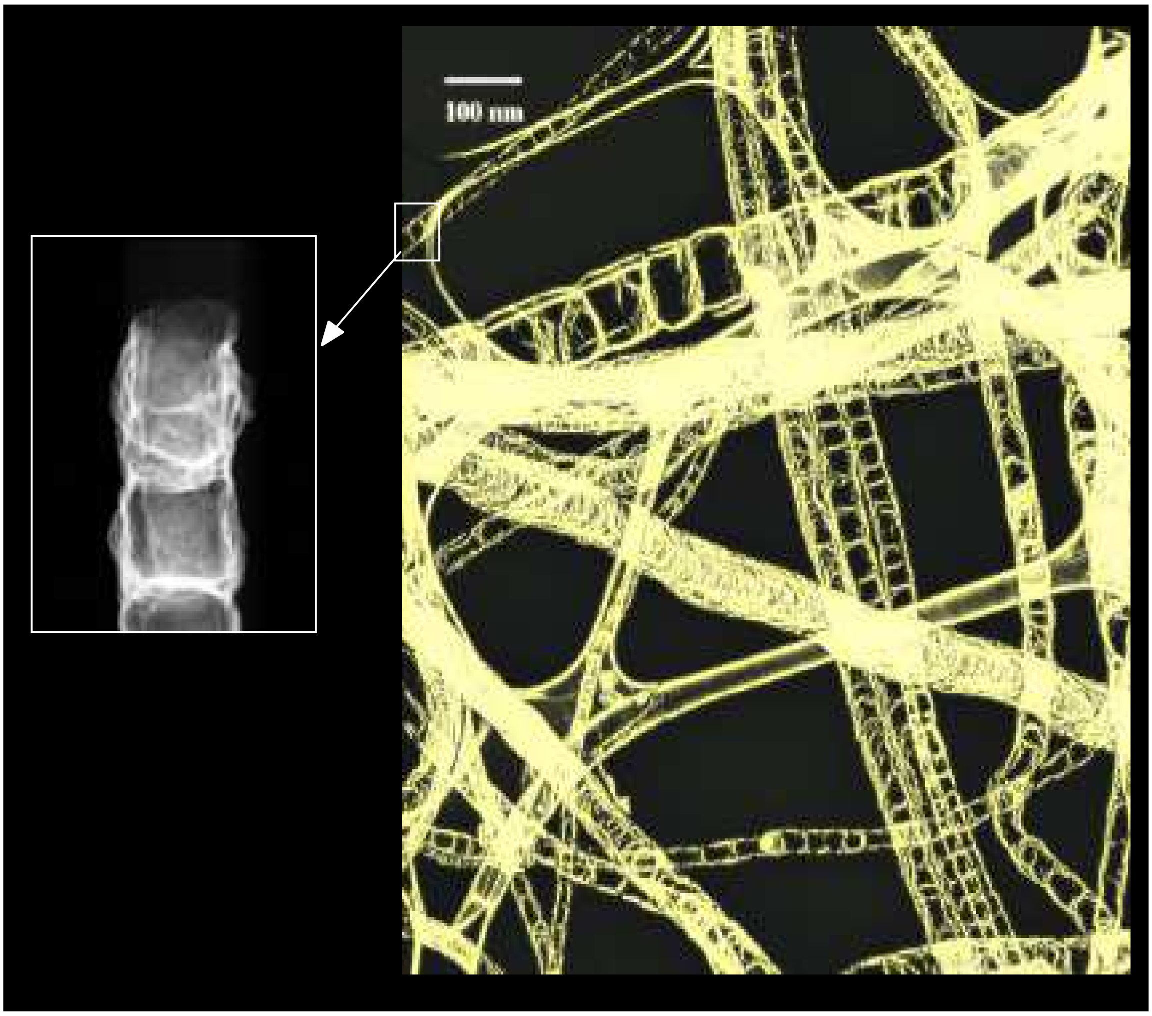

Le Monde 15 Août 2001

« Transmission Electron Microscopy image of carbon nanotubes which contain a small amount of nitrogen. The observed nanotubes have different size and morphology…. »

A mis padres y hermana

« Aunque estemos separados por miles de kilometros

nuestros corazones estaran siempre cerca »

THANK YOU - MERCI – GRACIAS

It is extremely difficult to thank in only few lines all the people that have been involved in this thesis. Before starting the acknowledgements, I would like to apologise if I forget any name but I will try to do my best and do not leave any of "you" outsidefrom this list. Also trying to make personalised acknowledgements and after a so European thesis, some changes of language are unavoidable

First, I would like to thank Prof. Christian Colliex for permitting me to be part of the group STEM at Laboratoire de Physiques des Solides (LPS) where the scientific environment is exceptional. The high number of collaborations that this group lead by C. Colliex has, has permitted me to work with people from different countries, to attend a huge number of conference and to meet different cultures which I did not have the chance to know. Also I would like to thank him for the fruitful discussions and for giving me the opportunity of learning something completely new for me: the Transmission Electron Microscopy technique and more particularity the Electron Energy Loss Spectroscopy.

I thank G. Hug for welcoming me to ONERA, Chatillon. I started to work on CNx films and CNx molecules with him. His theoretical knowledge about EELS spectra simulation has constituted a great support in order to interpret our experimental results.

O. Stéphan, apart from being an exceptional person in the professional and friendship aspect., has been one of the mainstays of this thesis. The success of this thesis could be difficulty achieved without her help. She has been patient enough to explain me, one after other, any conceptual aspect, which I did not have before arriving to this microscopy field due to my completely different background. Also many thanks for her availability, the fruitful discussions and her good advice.

I would like to thank Prof. P. Berthet for accepting to be the president of the jury, A. Loiseau for accepting to be one of the examiners and for all her useful comments, which have been essential for improving the manuscript thesis. I would like to thank S. Csillag for accepting to be examiner of my thesis and for spending part of the summer going through the manuscript. I also acknowledge Prof B. Jouffrey for being part of the thesis jury.

This work could not be done without all our collaborators;

A highly fruitful collaboration has been carried out with the group of Prof Harold Kroto and David Walton at Sussex University, Brighton (England). This collaboration started one year before my thesis (1997-1998) when I was awarded with a British Council-CSIC fellowship. Prof H.W. Kroto and Dr. D.M.R. Walton are thanked for accepting me in their group and for giving me such fruitful time in Sussex. Special thanks are given to Dr. David Walton who has accepted to be member of the thesis jury and has travelled to Paris to attend my thesis. Thanks are given to Dr Kuang W. Hsu for his help with the experiments, the fruitful discussions and his friendship. From Sussex, I also would like to thanks Dr. Malcolm I. Heggie for his continuous support during all these years (muchas gracias Malc de tu siempre amiga). Also many thanks are giving to a person who I met in Sussex and has been really special since the first day, Kostas: thanks for your friendship and our long telephone conversations which helped me a lot in many moments.

I would like to thank A. Kolitsch and S. Malhouitre from Institute Rossendorf, Dresden, G. Safran and G. Radnosky from Hungarian Academy of Science for providing the CN_x *films samples and for the successful discussions. Thanks are given to Prof. L. Pettersson and C. Kolczewski from FISIKUM at Stockholm University for their important contribution with their theoretical calculations. Prof. J. Zhu and S. P. Gao from the University of Tsingua, Beijing for their successful collaboration in the* CN_x *nanocrystals.*

It has been an honour for me to be part of the TMR Network "Synthesis, structure and properties of new carbon based hard materials" co-ordinated by S. Csillag. This network provides an indispensable financial support. Further more it provides a good working and social environment. Working in this network has provided fruitful collaborations and given me the opportunity of knowing excellent people from different places (Stockholm, Linköping, Dresden, Toulouse, Bordeaux, Paris, Newcastle, and Budapest). Thus I would like to thank everybody belonging to this TMR Network. Special thanks to Riitta Raty, who spent one year as a post-doc at LPS. Apart from teaching me the basis about the characterisation techniques, she has made easier my stay in Paris. Thanks Riita for the nice time we have passed together working, sharing the office, discovering France, learning the French culture (French). Also I would like to thank Niclas Borglund (this time it is not in a train station), for his friendship and all nice time we have shared during this three years in the TMR meetings, in Barcelona, in the bars.

Last but not less, special thanks to all of the members of the STEM group at LPS which provides a great environment either scientific or personal. Paul and Alex are *highly thanked for their help with the French manuscript, without them such manuscript would be far for being finished. I would like to thank Marcel for his help on the computer and instrumental side. Thank you for being around every time I had a problem either with the microscope or computer and thanks also for your important advice during acquisition experiments. I would like to thank Mathieu for his continuous support and help on the Akashi experiments. Also thanks for the nice time spent together either in the lab or in any of our travels for conference. I would like to thank Dom who has been my office-mate during the last two years of this thesis and had to stand all my questions, music and so on. I also would like to thank Dario for the Italian coffee breaks during the hard working days. Claudie, Daniele, Lolwa, Nathalie, Abdel (and Therese) and Marc are thanked for their friendship and support.*

A pesar de estar lejos de Zaragoza (a unos 1200Km) todos vosotros habeis estado muy cerca de mi y sobre todo me habeis ayudado mucho con vuestro incondicional apoyo. En esta ultima parte de los agradecimientos (pero no la menos importante) me gustaria agradecer a mi familia y amigos.

1 INTRODUCTION

PRESENTATION OF THE SUBJECT

Without materials, there would be no social progress. Materials are daily transformed and used for benefit of mankind. The importance of the materials in our life can be deduced by just looking at how many different materials pass through our hands along one day, polymers, semiconductors, composites in the form of clothes, computers, automobiles etc…

Hard materials are valuable in industry for use in cutting tools, abrasives and wear-resistant protective coatings. Diamond has long been considered as the hardest material in the nature. However a provocative and potentially useful prediction of a new material, carbon nitride, which would rival or exceed the hardness of diamond, came out in 1989. Using a pseudoempirical calculation Liu and Cohen suggested that a compound made of carbon and nitrogen covalently bonded, β-C_3N_4 which presents similar structure to that of β-Si_3N_4, could behave as an ultra-hard material presenting high thermal conductivity and useful electrical and optical properties [1,2]. If this material exists it could serve as an inexpensive substitute for diamond, or it could be used to carve diamonds into intricate shapes for uses as semiconductors in electronic devices. Moreover super-hard materials could be used to cut steel and thin layers of metal, which can not be done with diamond. Mechanical components such as gear and bearing coating made of super-hard compounds, would last much longer than normal pieces, and could be used in machines where liquid lubricants are unsuitable.

This prediction about the stability of β-C_3N_4 or other carbon nitride crystalline structures has motivated researchers to develop different synthesis methods for producing such stimulating compounds.

Only a few experimental studies on CN films show crystallites embedded in amorphous CN films [3-7]. Moreover, the N content observed in the samples is usually lower than that expected for C_3N_4. Experimentally it has been shown that films with low N content like $CN_{0.2}$ films with fullerene-like microstructure (three-dimensional network of covalent C-N bonds) possess a hardness and an elastic modulus (60, 900 GPa) close to those of diamond (100, 1050 GPa) [8]. The experimental evidence of hard CN_x materials has motivated further theoretical studies on new CN structures. Miyamoto et al have proposed the existence of CN tubules, which should be metallic independently on their diameter and chirality [9]. Recently, different chemical and physical synthesis routes (as for example chemical vapour deposition (CVD), magnetron sputtering, and electron cyclotron resonance) have achieved the production of CN_x nanotubes. The highest N/C ratio (~0.7) has been found in "amorphous nanotubes" prepared by electron cyclotron resonance [10].

Despite many efforts to produce such exciting materials, characterisation of the sample by diverse techniques has shown that a crystalline material is rarely obtained and when it is present it appears in the form of small crystals embedded in an amorphous matrix. Because of the small size of the crystals and the presence of amorphous matrix, the structure of the produced crystalline carbon nitride is still not completely defined, a mixing of β, α (derived from α-Si_3N_4), and other phases has been reported [5,6] and other new structures have been theoretically predicted. Therefore, in order to fully characterise the material, information about the bonding configuration is essential. Using X-ray photoelectron spectroscopy XPS analysis, the first experimental evidence of C-N covalent materials was reported by Niu et al [11]. This technique has also been used to identify the presence of at least two kinds of C-N bonds in CN_x nanotubes and films (N in sp^2 and sp^3 hybridisation) [10,12]. However, the results are still controversial due to the uncertainty in the absolute position of the peaks and the choice of number of peaks used to fit the spectrum. The small size of the crystal structures, the presence of amorphous material and the inhomogeneity of the material make the characterisation of the CN_x materials highly difficult. A technique at the nanometer scale, which will also provide information about the chemical and bonding configuration of the elements, is needed. As it will be further described (chapter 4), Electron Energy Loss Spectroscopy (EELS) in a transmission microscope permits to correlate a spectroscopic information to morphological and structural features of the specimen, allowing an accurate characterisation of materials at the nanometer scale [13,14]. Moreover, the last developments performed in the dedicated Scanning Transmission Electron Microscope (STEM) available in Orsay, have reduced the required acquisition times for achieving a satisfactory signal-to noise ratio on any spectrum up to the order of 1-5 milliseconds for the plasmon region and of 50 milliseconds to 1 second for the core loss region. This short time permits us to investigate the transformation of the materials under the beam (Time Resolved EELS) and increases the area of analysis by performing 1D and 2D scans on the sample (Spatially Resolved EELS).

Nowadays, the observed N/C ratio and the crystallinity in CN_x materials are still far from that of the predicted C_3N_4. Further work on production and characterisation of CN_x material is needed in order to understand the N incorporation process in the C network. In this context, the Training Mobility Research (TMR) network "Synthesis, structure and properties of new carbon based hard materials" was created in 1997. Groups belonging to different countries in Europe (France, Sweden, England, and Germany) have collaborated to produce and characterise materials both hard and flexible. As part of this network, this thesis deals with the synthesis and characterisation of CN_x materials. Particularly, Transmission Electron Microscopy (TEM) and Spatial and Time Resolved EELS have been used in order to extract information about the atomic structure and bonding configuration of CN_x films and nanotubes as well as to monitor the CN transformation under the beam.

The CN_x films were prepared by our collaborators at Institute Rossendorf and sent to our laboratory for characterisation. The CN_x nanotubes samples were synthesised in collaboration with Dr W. K. Hsu during my stay at Sussex University, Brighton (1998, and short period of time in 1999).

PLAN OF THE THESIS

In the following chapter, chapter 2, an introduction to carbon based materials and the effect of incorporating nitrogen on the properties of such materials (structural, electronic, optical…) is reported. In chapter 3, the synthesis methods utilised for the preparation of CN_x materials are described. Particularly, the pyrolysis system as well as the effect of the different synthesis parameters in the production of CN_x nanotubes are written up.

In chapter 4, the characterisation techniques (TEM and EELS) are described. Spatially and Time Resolved EELS (acquired methods) and the different processes used for extracting the information from the acquired data (Multivariate statistical analysis, MSA, and Non Negative Least Square fitting (NNLS)) are explained.

Finally, in chapter 5, a summary of the papers presented in this dissertation is given. The first paper *"Modulated CN_x films prepared by Ion Beam Assisted Deposition"* deals with the synthesis and characterisation of

CN_x films prepared at Rossendorf Institute, the TEM analysis was carried out by the group in Budapest and the EELS analysis was performed at the Laboratoire de Physiques des Solides in Orsay. In Paper II, *"Compartmentalised CN_x nanotubes; Chemistry, Morphology and Growth process"*, the effect of the different synthesis parameters in the incorporation of N into carbon nanotubes produced by catalytic pyrolysis is reported. As a result, a growth mechanism for such structures is proposed and a comparison of the results with those previously reported is also carried out. Paper III shows the identification of the CN_x nanocrysrtals embedded in an amorphous CN_x matrix. Papers IV, *"A route to study the Carbon-Nitrogen bond: Chrono-spectroscopy in melamine"*, and V *"Electron Beam Puncturing of Carbon Nanotube Containers for Release of Stored N_2 Gas"*, are the results of in-situ EELS experiments. The former describes the decomposition process of melamine under beam radiation as well as the identification of the different decomposition stages by EELS. In the latter a new nanotube morphology, nanotubes containing nanocapsules, is reported. Moreover, using time-resolved analysis, the transformations produced in the carbon nanotubes when a high-energy electron beam is focused on it, are monitored and simultaneously analysed. Finally, paper VI is a review concerning EELS on carbonaceous materials of the different studies performed at the Laboratoire de Physiques des Solides, thus part of the results obtained in CN_x materials are included.

2 CARBON BASED MATERIALS

2.1 CARBON CRYSTALS

Carbon is present in the nature in various crystalline and amorphous phases. The two best-known allotropic forms of carbon are diamond and graphite. However, a new crystalline form, which is based on a molecule with 60 C atoms called buckminsterfullerene (C_{60}, fullerene), was discovered in 1985 by H.W. Kroto et al. [15]. This fascinating result did open up the research field on new carbon nano-structures, leading in 1991 by S. Iijima, to the discovery of another crystalline nano-structure [16], called nanotubes.

2.1.1 DIAMOND

The ideal structure of diamond has the characteristic that every C atom is surrounded by four other C atoms at the corners of a regular tetrahedron with a cube edge length of a_o= 3.567Å. This carbon is bonded to these neighbours by strong covalent bonds (bond length 1.544 Å), Figure2-1A. The close-knit bonded crystal structure yields diamond special properties, which are different from those of graphite or other C forms. Apart from being one of the most expensive gemstones, it has a higher sound velocity than any solid, it is also the best conductor of heat and the hardest naturally occurring substance known. All these special properties provide it with huge number of applications. It is used to produce hard coatings for industrial equipment such as grinding wheels, machine tools and mining drills. Diamond films, grown on various materials by subjecting carbon containing gas to extreme heat, can also be used in windows for optical devices, or substrates for semiconductors. In addition, industrial diamond, which presents many imperfections and is directly extracted from a mine or synthesised, is used as abrasive.

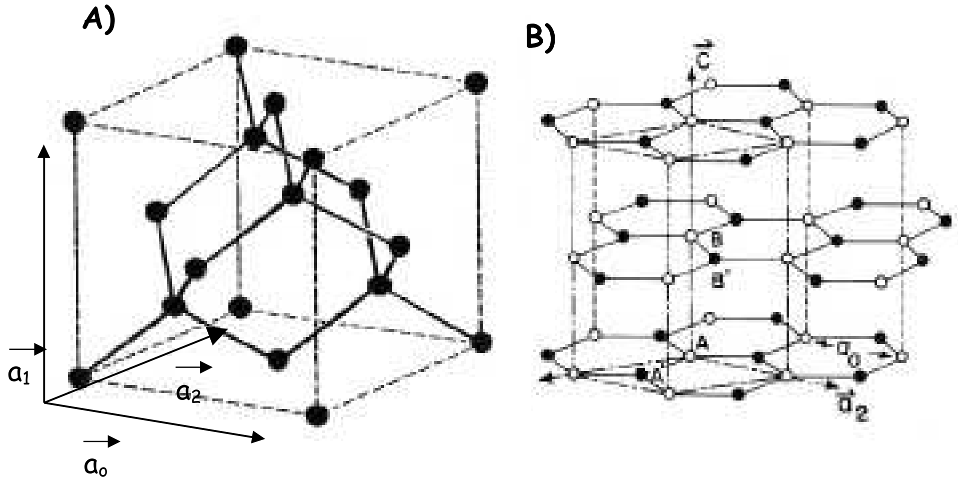

Figure 2-1.- Structure of diamond A) and graphite B).

2.1.2 GRAPHITE

Graphite, also called plumbago or black lead, has a layered structure that consists of rings of six carbon atoms arranged in widely spaced horizontal sheets. The carbon atoms are arranged in an open honeycomb network, so that the A and B atoms of consecutive layers are on top of one another, but the A' atoms in one plane are over the unoccupied centres of the adjacent layers, Figure 2-1B. This gives rise to an ABAB planar stacking arranged with an in-plane nearest neighbour distance C-C of 1.421 Å, an in-plane lattice constant a_o of 2.462Å and an interplanar distance $c_o/2$ of 3.359 Å. Contrary to diamond (isotropic, cubic and insulating crystal), graphite is highly anisotropic, exhibiting metallic behaviour in the basal plane and poor electrical conductivity along the c axis. In terms of mechanical properties it is a soft slippery solid and along with diamond it exhibits the highest thermal conductivity. It is used in lubricants, pencils, foundry facing and because it conducts electricity but does not melt, graphite is also used for electrodes in electric furnace and dry cells as well as for making crucibles in which metals are melted.

2.1.3 FULLERENE CRYSTALS

It is the third form of crystalline carbon known to exist, after the solid network solid of graphite and diamond. By definition, a fullerene molecule is any of a class of closed, hollow, aromatic carbon compounds that are made up of 12 pentagonal and different hexagonal faces. [17]. It consists of an even number of carbon atoms, in a range of from 32 to 600 atoms. The first discovered fullerene was the buckminsterfullerene (C_{60}), which is made of 60 C atoms located at the vertices of a truncated icosahedron where all carbons sites are equivalent, Figure 2-2A. The C_{60} molecules, also called bucky-balls due to their spherical molecular shape, are quite strong and almost incompressible. In the solid state, the C_{60} crystallise into a face centred cubic (fcc) lattice structure, with a one nanometer spacing between the centres of two adjacent balls, which are weakly bonded by Van der Waals interactions. The physical and chemical properties of fullerene crystals are still investigated, however it is known that a C_{60} solid can resist very high temperatures and pressures without losing its structure. The outer surface of the molecule is highly reactive and the cavity can be used to encapsulate different atoms. Recently, the identification of Gd atoms inside fullerenes (Gd@C_{60}) enclosed in a single nanotube, Figure 2-2B, has been reported [13]. The unique structure and properties of buckminsterfullerenes suggest potential utilities for fullerenes as superconductors, lubricants, industrial catalysis and drug-delivery systems (e.g. target cancer therapy).

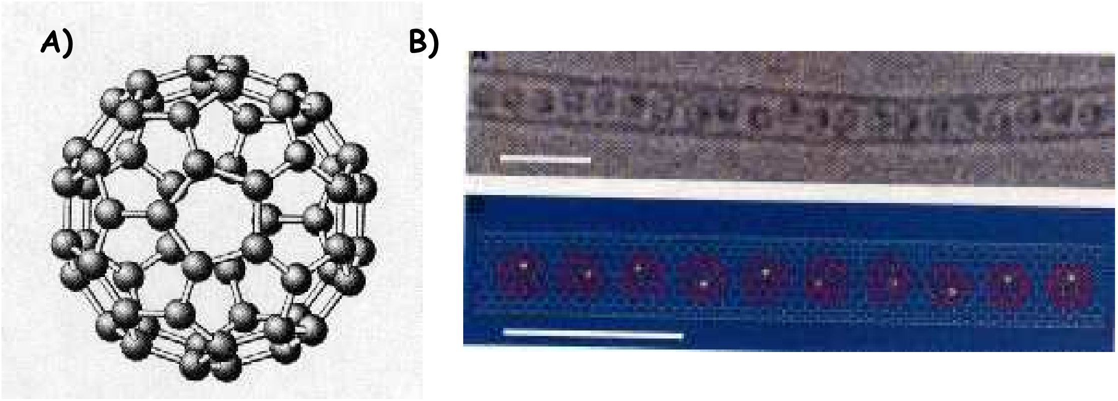

Figure 2-2.- A) Fullerene structure B) HRTEM of a single nanotube containing fullerenes which have Gd atoms encapsulated as indicated in the scheme, the scale bar corresponds to 3nm, (courtesy of K.Suenaga)[13].

2.1.4 NANOTUBES

The structure of carbon nanotubes has been efficiently studied by Transmission Electron Microscopy (TEM) [16] yielding a direct confirmation that nanotubes are cylindrical structures based on the hexagonal lattice of carbon atoms that forms crystalline graphite, Figure 2-3A. Depending on the number of walls present in the nanotube, they can be classified as single wall nanotube (SWNT, only one wall, Figure 2-3B) or multiwall nanotubes, Figure 2-3C, when the nanotube is made of coaxial cylindrical layers. A single wall nanotube can be understood by a simple construction of rolling a perfect graphite sheet. Thus, three kinds of nanotubes are possible depending on how the graphite sheet is rolled up: "Armchair", if the nanotube axis is perpendicular to one C-C bond, "zigzag" when the nanotube axis is parallel to one C-C bond and "chiral" nanotube in any other intermediate structure. The electronic properties of nanotubes depend on their chirallity and diameter. Consequently controlling their structure

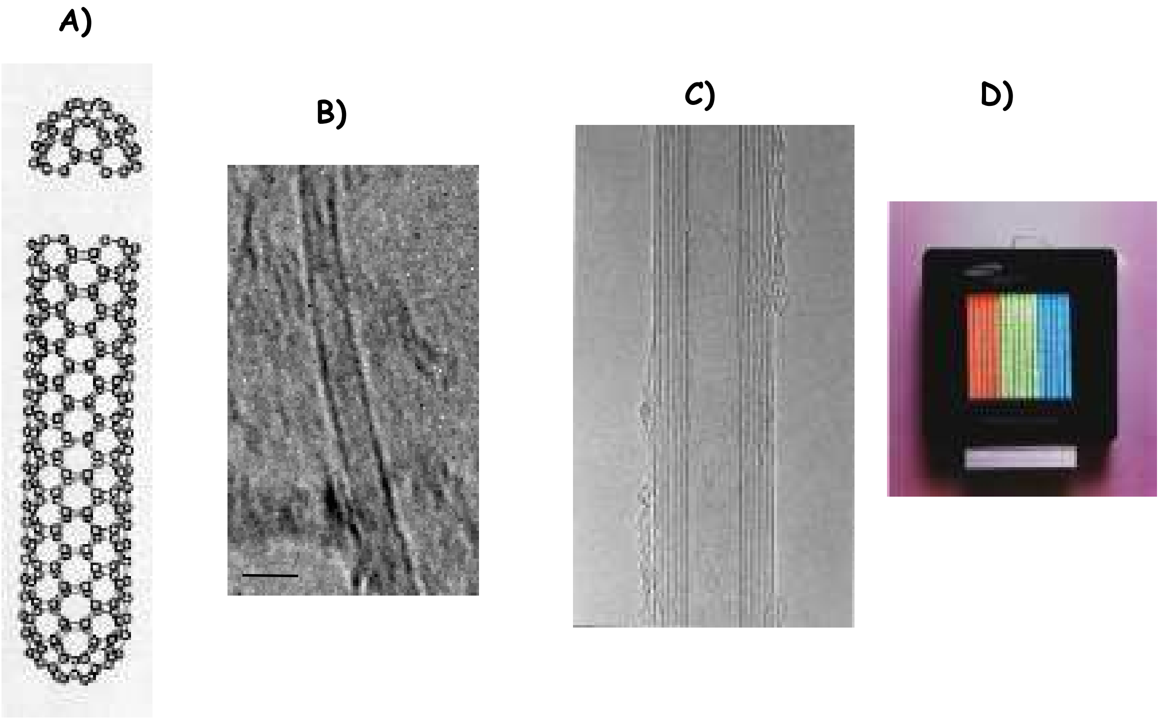

Figure 2-3.- A) Nanotube scheme, HRTEM images of a SWNT B) and C) MWNT. D) Full colour flat display made of carbon nanotubes.

means also handling their properties. Nanometre-scale devices could therefore be based on coaxial nanotubes or junctions between nanotubes; for example a metallic inner tube surrounded by a large semiconductor (or insulating nanotube) would form a shielded cable at the nanometre-scale

[18]. Because of their very small diameter (from 1 to a few nanometers) and relatively long length (up to several microns), carbon nanotubes are perfect test nanostructures for studying one-dimensional physics, both theoretically and experimentally. For example the Luttinger like liquid behaviour of the electron gas was evidenced by tunneling transport experiments [19,20]. The investigations on transport properties have lead to the discovery of proximity induced superconductivity in SWNT's [21] and intrinsic superconductivity [22]. Moreover, Treacy et al have reported that thanks to their high crystallinity and high aspect ratio nanotubes have an exceptionally high elastic Young's modulus (five times the value for steel) [23] and they could be used in lightweight-bullet proof vest and earthquake resistant buildings. However further progress is still needed in order to optimise the properties of the nanotubes, to create materials by incorporating the nanotubes in a matrix. As first applications, tips for scanning probe microscopes and full colour flat displays made of carbon nanotubes are already available on the market [24].

2.2 BONDING AND ELECTRONIC CONFIGURATION IN THE CARBON CRYSTALS

We have already seen that although the above crystalline phases are made up with the same atomic element, carbon, they present different structures and properties. Carbon is a good metal in the form of graphite, a wide gap semiconductor as diamond or fullerene and superconductor when intercalated with appropriate guest species. Furthermore, carbon-based electronic materials provide examples of materials showing the entire range of dimensionalities from fullerenes which are 0D quantum dots to carbon nanotubes which are 1D quantum wires, to graphite a 2D layered anisotropic material, and finally to diamond a 3D isotropic solid. The diversity in the properties of the C based materials finds its origin in the differences in bonding configuration.

The valence-shell electron configuration of an isolated carbon atom is $2s^2\ 2p_x^1\ 2p_y^1$ which suggests that it can form only two bonds, in which case carbon would have a valence of 2. However the normal valence of carbon in its high variety of compounds is 4. When considering bonding with neighbouring atoms, apart from s and p orbitals, hybridised wave functions are formed as a result of a linear combination of the well-oriented orbitals. Thus three kinds of hybridisation are possible in C atoms;

- When one 2s and three 2p orbitals of a carbon atom are hybridised, they give rise to four lobe-like sp^3 hybrid orbitals, that are equivalent to one another apart from their orientations, which are towards the four corners of a regular tetrahedron, Figure 2-4A. Each hybrid orbital contains an unpaired electron and can form four σ bonds, bonds in which the electron density has a circular symmetry when viewed along the bond axis.
- The sp^2 hybrid orbitals, Figure 2-4B, have lobe-like boundary surfaces that point to the corners of an equilateral triangle. They are the result of a coupling between one 2s and two $2p_{x-y}$ orbitals which leave an unhybridised $2p_z$ orbital now side-by-side which can overlap to form a π bond (presence of delocalised π electrons and double bonds).
- sp hybridisation, Figure 2-4C, is present when one 2s and one 2p orbitals are mixed leaving two 2p unhybridised orbitals ready for forming π bonds (triple bonds). This hybridisation is mainly observed in molecules as acetylene.

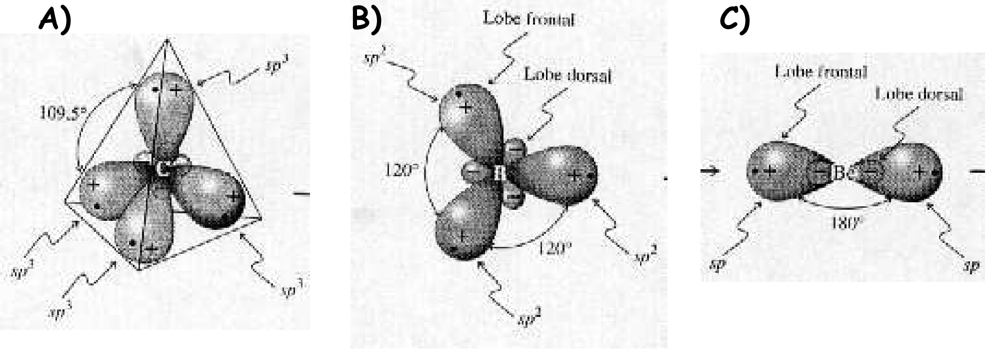

Figure 2-4.- A) sp^3 B) sp^2 and C) sp hybrid orbitals.

The cohesion in compounds or crystals is insured by the formation of bonds between atoms. Thus diamond is made of pure sp^3 carbon atoms which are strongly covalently bonded, the absence of π electrons makes diamond an insulating solid. In graphite the carbon atoms are truly sp^2 bonded with a planar configuration in contrast to the case of fullerenes where the sp^2 bonding between adjacent carbons occurs on a curved surface. This curvature of the trigonal bonds in C_{60} leads to some admixture of sp^3 bonding, characteristic of tetrahedrally bonded diamond but absent in graphite. In sp^2 bonded networks like graphite and nanotubes, the π electrons are delocalized, and a resonance structure is formed. There is not single or double bonds, instead each carbon-carbon bond can be treated as having a bond with a length in between that of double and single bond. The presence of delocalized electrons makes graphite and nanotubes (for given diameter and chiralities) a good electrical conductor.

2.3 DOPING C CRYSTALS

The electronic properties of the materials can be drastically changed by the presence of impurities. When an impurity is added to a system, a slight modification is observed in the energy bands. From the electronic point of view, two types of impurities can be present, donor and acceptor impurity. In the former one, also called n-type doping, the impurity provides an extra electron, which can only be accommodated in the conduction band (for example N in carbon materials). In the latter, denominated p-type doping, the impurity provides one less electron to the system and therefore leaves one state unoccupied in the valence band (B in C systems). From the chemistry point of view, the impurity, atomic or molecular species, can be incorporated in the crystal structure by substituting a C atom (doped C, typically observed in diamond) or by being intercalated between the C layers (intercalated C in graphite). In the case of diamond, which presents strong sp^3 bonding and high isotropic character, the intercalation is not possible. On the other hand, in the case of cages or tubes, because they are closed, the guest-species can also be encapsulated in their cavity.

Since a carbon atom is very small and the average nearest neighbour C-C distance in only 1.41 Å in graphite, it is believed that the only likely substitution dopant in graphite is boron. However few works have already been reported about N-doped graphite, as it will be shown below. Because diamond has a larger neighbour distance C-C=1.54 Å, both boron and nitrogen can enter in the diamond lattice substitutionally. In the case of fullerenes the C-C distance is slightly larger than that in graphite and the interaction forces are somewhat weaker due to the curvature of C_{60}

surface. Consequently it may also be possible to dope the C_{60} shell with N atoms.

2.3.1 N-DOPED DIAMOND

In the case of diamond, impurities play a very important role because they induce changes in the electrical and optical properties. The best nature diamond contains impurities with concentration in the range of 1 part in 105. However only few species can enter in the diamond structure (B, N) and when doping is possible, the concentration is very low. It has been observed that the strong infrared absorption of Ia diamond (specific kind of diamond [25]) is due to the fairly amount of N (up to 0.1%) inhomogeneously distributed in the crystal and mainly concentrated in small agglomerates. Besides, because of their negative electron affinity, diamond surfaces terminated with hydrogen are expected to emit electrons spontaneously and therefore they could be used in microelectronics and flat-panel displays. However in order to use diamond in battery-driven cold cathodes a low-threshold emission is needed. Okano et al [26] have measured the electron emission of diamond surface doped with nitrogen Figure 2-5. Comparing the results with those obtained in samples doped with boron and phospohorous, they observed that the difference in the emission properties are fundamentally due to the different impurities induced in diamond and the lowest threshold field is present in the N-doped diamond. Nevertheless it is still not clear which is the real effect of N in the diamond system. Recently, Show et al [27], studying the electron emission from nitrogen doped diamond films (N/C from 0 to 10), reported that the N atoms are located at a substitutional site, providing paramagnetic defects in the diamond film and increasing the current density of the electron emission.

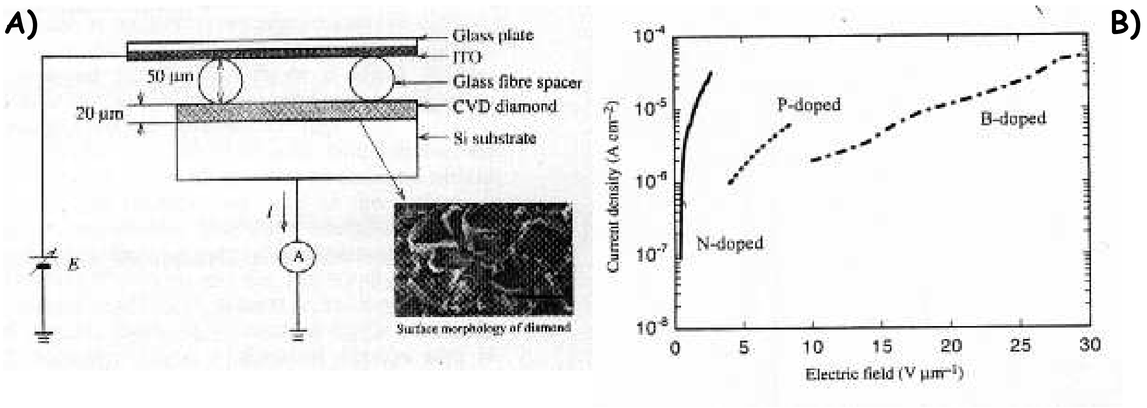

Figure 2-5- A) Schematic structure of the electron emission measurement circuit, inset morphology of the diamond surface doped with nitrogen. B) Comparison of emission properties of N, B and P doped crystalline diamond films (courtesy of K. Okano) [26].

2.3.2 N-DOPED GRAPHITE

Because of the weak van der Waals forces between the graphite planes, two kind of modifications of graphite can occur. Apart from reactions occurring at defect sites or domain boundaries, graphite can be intercalated both by donor and acceptor species. Up to now there is not much done on N-doped graphite. Few attempts to incorporate nitrogen in graphite by thermal decomposition of hetereoaromatic compounds [28] have shown that disorder graphite domains with a N enrichment in their periphery are formed. Moreover N is easily eliminated when the sample is exposed at temperature. Using a non-equilibrium doping exposure of the graphitic domains to hot N atoms, N-doped graphite has been produced and its structural and electronic properties have been determined [29]. When graphite is doped with N (N incorporated =2.3%), the graphitic lattice is expanded, the gap is narrowed and the conductivity increases. Dos Santos et al, using semiempirical pseudopotential techniques, have found a transition from planar to corrugated structures upon nitrogen incorporation for concentrations above 20%. Buckling of the structure leads to localisation of electrons in the lone-pair orbitals [30].

2.3.3 AZAFULLERENES

Each carbon atom in a C_{60} is in an identical environment. Since all the intramolecular bonding requirements of the carbon atoms are satisfied, it is expected that C_{60} is a van der Waals insulator (semiconductor) with an energy gap between the occupied and unoccupied states in agreement with optical measurements [31]. To make C_{60} conducting, doping is necessary to provide the charge transfer and to move the Fermi Level into the conduction bands. Because of their structure, fullerenes can be doped in several different ways. Endohedral doping, where the dopant is located in the hollow core of the fullerene, exohedral doping where the dopant is outside or between fullerenes and finally substitutional doping (also called "on-ball") where the dopant substitutes one or more of the carbon. The chemistry of heterofullerenes only opened in 1995 when $C_{59}N$ and its dimer $(C_{59}N)_2$ were isolated for the first time [32]. However earlier studies had shown the strong interaction between nitrogen and C_{60} in C_nN_m molecules [33]. The isoelectronic structure of an ionic form of N-doped hetereofullerene is almost identical to the parent neutral material, which could be of essential importance in separation of liquid fractions of hetereofullerenes [34]. From quantum chemical calculations, optical absorption spectroscopy and electron energy loss spectroscopy it was found that $(C_{59}N)_2$ is non-metallic and has an optical gap of 1.4ev, 0.4 eV smaller than that of solid C_{60} [35]. Recently Stäfström et al, using ab initio quantum chemistry type of calculations, have studied the stability of a series of azafullerenes $C_{60-2n}N_{2n}$. [36].

2.4 CN_x COVALENT SOLIDS

Apart from modifying the electronic properties, the presence of hetero-atoms in C based compounds, could influence the mechanical properties. Hardness is a quality related to the extent to which solids resist both elastic and plastic deformations. On the microscopic level (for ideal systems) hardness is determined by the bulk modulus (B), which can be defined in tetrahedral solids using the Philip van Vechtem scheme [1] as following:

$$\mathrm{B} = \frac{19.71 - 2.20\lambda}{d^{3.5}} \quad (1)$$

where B is the Bulk modulus in megabars, d is the bond length in angstrom and λ is an empirical term which takes into account the ionic contribution to the bond. Using the above model, Liu and Cohen predicted the stability of the β-C_3N_4. Moreover, Sjöström et al have experimentally observed that $CN_{0.2}$ films with fullerene-like microstructure (three-dimensional network of covalent C-N bonds), have hardness and elastic modulus (60, 900 GPa) close to those of diamond (100, 1050 GPa) [8]. Therefore it is expected that incorporation of N in C based materials provides a new class of materials with exciting electrical and mechanical properties.

2.4.1 C_3N_4 COVALENT SOLIDS

The crystalline β-C_3N_4, which structure is based on the known β-Si_3N_4 where C substitutes to Si, has been predicted to be an ultra-hard material. The structure is shown to consist of buckled layers. The unit cell is hexagonal and contains two formula units (14 atoms) per unit cell with local order such that C atoms occupy slightly distorted tetrahedral sites, while N atoms sit in nearly planar triply co-ordinated sites. This atomic coordination suggests sp^3 hybrids on the C atoms and sp^2 hybrids on the N atoms. The average C-N distance is 1.47Å intermediate between the C tetrahedrally bonded (sp^3) with the sp^2 N and C-N sp^3 tetrahedral bonded. In 1993 Niu et al claimed the production of a covalent C-N solid by pulsed laser ablation of graphite targets within an intense atomic nitrogen source [37]. Photoelectron spectroscopy showed that the cohesion of the produced solid results from an unpolarised covalent bonding and qualitative tests also indicated that the material is thermally robust and hard. Later on, using different techniques (rf diode sputtering and arc-plasma) Yu *et* al and Yen *et* al have reported the production of small crystalline grains (<1μm) [7,38]. From Transmission Electron Diffraction (TED) and Raman characterisation, they claimed that the small grains could correspond to the predicted β-C_3N_4. , However the obtained N content in the above reported results (37-45 N%) is far from the predicted one in C_3N_4 (57%).

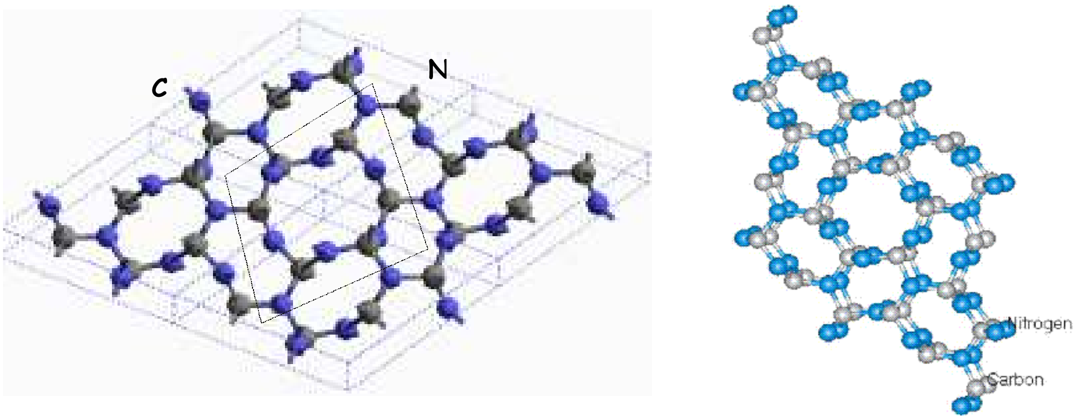

Figure 2-6.- Structure of β-C_3N_4 –blue C and grey N) (Courtesy of M. Matessini [39]).

Because only microscopic amounts of β-C_3N_4 are claimed to be obtained, the study of the mechanical properties can not be performed experimentally. Theoretical calculations have predicted a direct and indirect band gap (6.4 and 6.75 eV respectively) larger than the minimum gap in diamond. Therefore it is suggested that β-C_3N_4 may find many uses as a transparent hard material [2]. In addition the velocity of sound in β-C_3N_4 is estimated to be over 20% larger than that of β-Si_3N_4. This high sound velocity could lead to useful thermal properties in β-C_3N_4, such as high thermal conductivity [40]. Experimentally further work is needed for confirming the existence of the predicted ultra-hard carbon nitride covalent solid.

In 1995, research activity on CN_x materials explode after Sjöström et *al* synthesised super-hard and elastic $CN_{0.2}$ films [8] by reactive dc magnetron sputtering. From their theoretical and experimental results based on XPS and TEM studies of the $CN_{0.2}$ sample, they proposed a new carbon nitride phase, a **fullerene-like microstructure**. The structure can be described as graphite-like with interplanar distance of 0.347, 0.209 and 0.120 nm, where the basal planes are curved into a three-dimensional structure due to the presence of pentagons in the hexagonal network. The incorporation of N atoms induces buckling of the basal planes and thereby facilitates cross-linking between the planes by sp3-hybridised carbon, Figure 2-7.

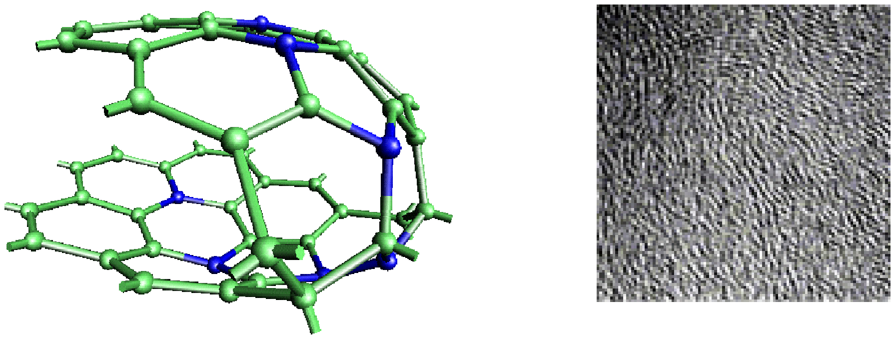

Figure 2-7.- A) Model of fullerene-like microstructure and B) HRTEM image of a super-hard $CN_{0.2}$ sample produced by magnetron sputtering, (Courtesy N. Hellgren)[67].

The above modelling and experimental results have opened up the research in new CN materials with low ionicity and short bond length. In 1996 Teter et al proposed the α-**C_3N_4** and **graphitic C_3N_4** structures as new carbon nitride phases, which are energetically preferred over β-**C_3N_4** [41]. The α-C_3N_4 has hexagonal symmetry and contains 28 atoms per unit cell. It can be described as an ABAB… stacking sequence of layers of β-C_3N_4 (A) and its mirror image (B), Figure 2-8B. The graphitic form (g-C_3N_4) is represented by a planar structure with ABAB… stacking mode, (stacking AAA mode has also been proposed [42] Figure 2-8A. Two different graphitic structures (hexagonal and orthorhombic) have been proposed. In both of them, each carbon atom is three-fold co-ordinated as is one of the four N atoms per cell while the other N are two-fold. A difference in the vacancy ordering is observed between the structures, the N atom between the rings participates in to the π delocalization in the C_3N_3 heterocycle [43] and offers the possibility of providing a delocalized electron along the graphitic layer. Mattesini et al have shown that these two graphitic structures have approximately similar energy, however a higher metallic behaviour is expected in the orthorhombic g-C_3N_4 [39]. Recently, the production of graphitic C_3N_4 by thermal decomposition of melamine in the presence of a nitriding solvent (NH_2NH_2) has been reported [44]. Cubic and pseudocubic structures were also proposed by Teter [45]. The **pseudocubic-C_3N_4**, Figure 2-8D, can be classified as a defect-zincblended structure type [46]. Each C atom has four N neighbours and each N atom has three neighbours as in the β-C_3N_4 structure. However the C-N-C angle is close to the sp^3 angle (109.47°) rather than to the sp^2 value of 120°C. The **cubic** structure, Figure 2-8C, is based on the high-pressure willemite II structure of Zn_2SiO4 where C substitutes Zn and Si, and N substitutes oxygen. The same year, Wang et al claimed the preparation of a solid, which consists of irregular-oriented prismatic crystals, made of a mixed phase of α, β and tetragonal C_3N_4, proposing a new tetragonal structure [47].

Despite many efforts to synthesise the C_3N_4 crystalline structures, only the production of small crystals in amorphous matrix has been obtained. Moreover the nitrogen content found in the samples is lower than the expected one in the predicted C_3N_4. Therefore the inhomogeneity of the sample, the small size of the crystals and the lower N content make impossible the characterisation of the mechanical properties. Consequently, theoreticians have been motivated to search new CN_x ($x< 1$) structures, which will have closer composition to that founded by the experimentalists, and to prognosticate the mechanical and electrical properties of such new CN_x structures.

2.4.2 CN_x COVALENT SOLIDS ($x \leq 1$)

The experimental observation of hard and elastic carbon nitride materials with lower N content than the expected one for C_3N_4 [8] and the observation of a transition between graphitic and fullerene like structure [48] has motivated theoreticians to explore crystalline structures with low nitrogen content like $C_{11}N_4$ and CN. A graphitic $C_{11}N_4$ structure with arranged layers in the stacking sequence AA... has been proposed by Snis et al [49]. In such structure, the nitrogen atoms are two and three-fold coordinated and C atoms are linked to different N. Recently, the stability of this structure has been compared with that found in a three-dimensional structure (α-$C_{11}N_4$) and C_3N_4, Figure 2-9, showing that $C_{11}N_4$ is more stable than C_3N_4. Moreover, the theoretical thermodynamic stability investigations suggest that the proposed $C_{11}N_4$ phases can be experimentally produced but they should be probably mixed due to the small energy separation between both structures (0.03eV) [50].

Guo et al have claimed the production of crystalline CN films composed of three mixed phases, two known-phases (α and β) and one unknown phase, which they described as a monoclinic phase[51]. Recently this phase has been theoretically identified as the tetragonal rocksalt phase and a new series of carbon nitride phases having **CN** stoichiometry, have been predicted by Kim et al [52].

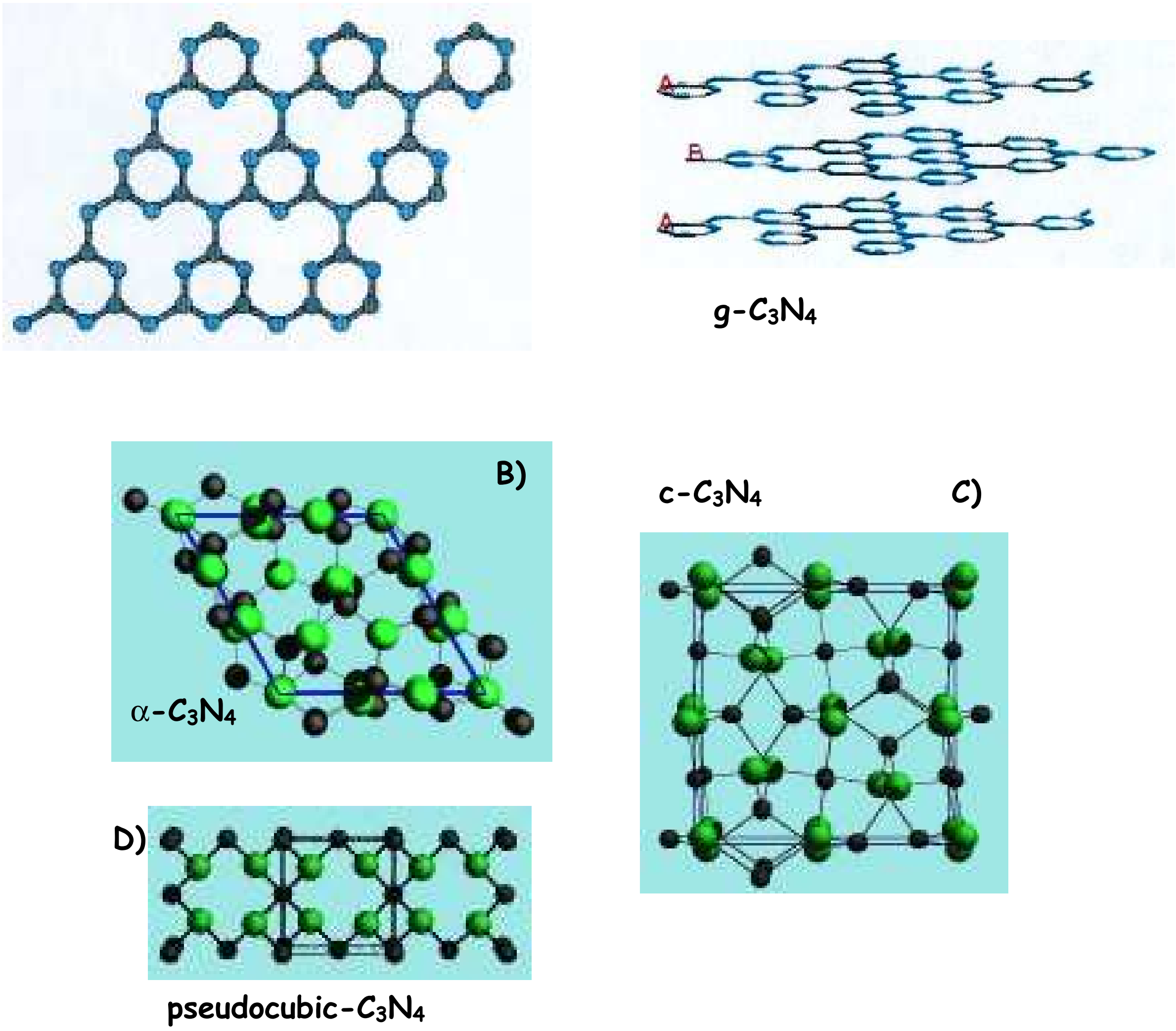

Figure 2-8.- A) Hexagonal structure and stacking order of graphitic C_3N_4 (gr-C_3N_4) B) Structure of α-C_3N_4, cubic (C) and pseudocubic C_3N_4 D).

Using ab initio calculations, the stability of C_3N phases has been reported. It has been shown that different structures, dimerised, polymerised and N substituted graphite, present similar stabilisation energies. Consequently, entropy effects may become important and a wide variety of local structures could be encountered. Furthermore, the calculation of energy barriers between them leads to relatively small values. Consequently at room temperature, C_3N compounds may transform dynamically from one structure to another over a limited period of time ($\lesssim$ 1 s) [53].

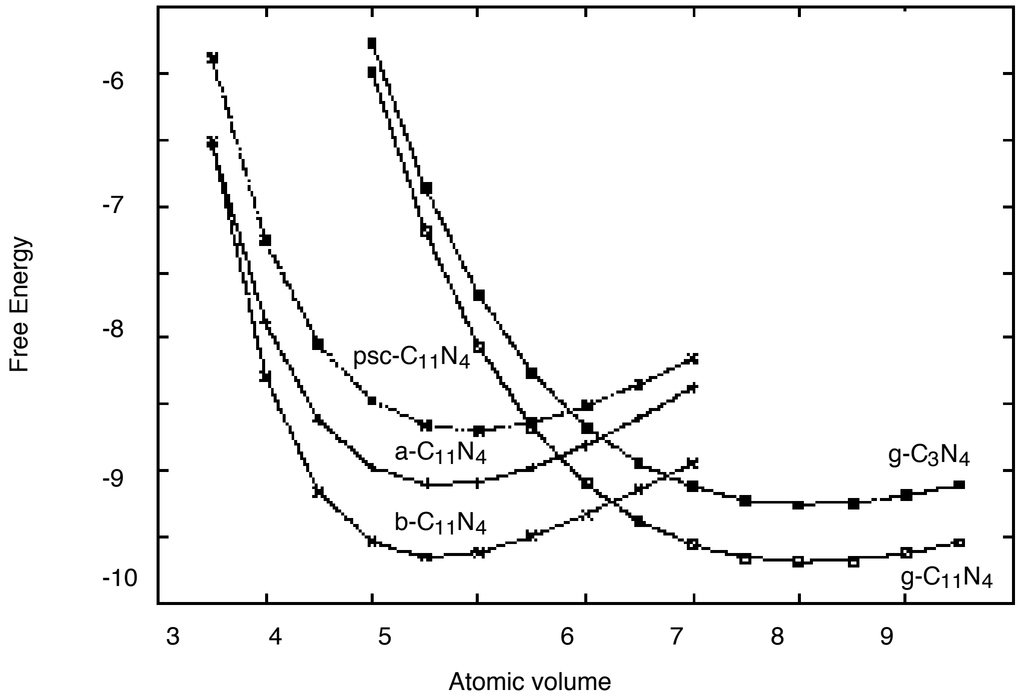

Figure 2-9.- Free-energy (eV/atom) versus atomic volume (Å^3/atom) for various C_3N_4 and $C_{11}N_4$ (Courtesy of M. Matessini [50])

2.4.3 CN_x NANOTUBES

The exciting properties of nanotubes, the prediction of ultra-hard materials made of carbon and nitrogen and the experimental evidence of B-doping of nanotubes [54] have motivated Miyamoto et al to study the stability of CN_x nanotubes [9]. Using pseudopotential total-energy calculations, they proposed that C_3N_4 and CN tubules should be metallic independently on the tubule diameter and chirality. Following these theoretical calculations, experimentalists have investigated and successfully achieved different synthesis routes for producing CN_x nanotubes. Sen et al [55] prepared CN_x nanotubes (x=0.03-0.09) by pyrolysis of pyridine using Co as a catalyst. From the current Intensity versus applied Voltage (I-V) curves obtained by scanning tunnelling microscopy (STM) they have observed that the conductance of the C-N MWNT's (1.2 nA/V) is generally higher than that of multi-wall C nanotubes (0.5nA/V). The production of aligned CN_x nanotubes ($x \leq 0.02$) by pyrolysis of triazine over laser-patterned catalytic has been reported by Terrones et al. [56]. The same research group [57] has shown that higher N content ($x \leq 0.07$) is observed in the nanotubes when a nitrogen rich organic precursor is pyrolysed. CN_x nanotubulites with a homogeneous N content (x=0.3-0.4) have been produced by magnetron sputtering [58]. However, chemical vapour deposition of Ni-phthalocyanine [59] has provided CN_x nanotubes with inhomogeneous N content ($x \leq 0.05$ in the graphitic region and approximately 0.15 in the amorphous region). Up to now the higher N content has been observed in the amorphous carbon nitride nanotubes produced by electron cyclotron resonance ($N/C \approx 0.72$) [60]. However such N content is far away from the C_3N_4 composition and crystallinity predicted in the expected ultra-hard materials. All these experiments have also shown the difficulty of incorporating a high amount of N in the nanotube.

2.4.4 C-N BONDS

Despite many different structures have been proposed for CN_x material, a well-defined structure is highly difficult to be experimentally obtained. A review about the different chemical structures of N in CN_x seems unavoidable to well-understand such kind of materials.

In the case of well-known CN_x aromatic systems as pyrrole and pyridine, the N atoms present sp^2 hibridisation but they contribute differently to the molecular orbital structure. The fifth valence electron of the N atom can form a lone pair either with the remaining unhybridized $2p_z$ orbital, or with one of the sp^2 orbitals. The first case leads to a localized $2p_z$ lone pair and the three sp^2 hybrid orbitals bond to other atoms. This case is observed in the pyrrole molecule, fig 2-10A. If the fifth electron instead forms a lone pair with one of the sp^2 hybrid orbitals, the atom is left with two sp^2 hybrid orbitals and one unfilled $2p_z$, and can therefore form one π and two σ bonds as observed in the pyridine molecule, fig 2-10B.

In the case of CN_x alloys, the situation is more complex. Using theoretical models and ab initio Hartree-Fock wave function Casanovas et al [61] investigated the N 1s core level binding energies of N containing carbonaceous materials. They reported the existence of three different C-N bonds, which are associated at different energy binding values.

> * Pyridine-like (398eV) refers to N atoms, which contribute to the π system with one p-electron, as in the case of pyridine, fig. 2-10A.

* Pyrrolic (399eV) corresponds to N atoms with two p-electrons on the π system, although not necessary in a five-member ring as in pyrrole, fig 2-10B.

* Graphitic like (401-403eV) where N substitutes C in the graphene layers

Shimoyama et al [62], using x-ray absorption fine structure, have confirmed the experimental existence of three different C-N bonds. The existence of pyridine like and graphite like are clearly observed; however the existence of pyrrolic like is not considered, instead the existence of triple C-N bonds is proposed.

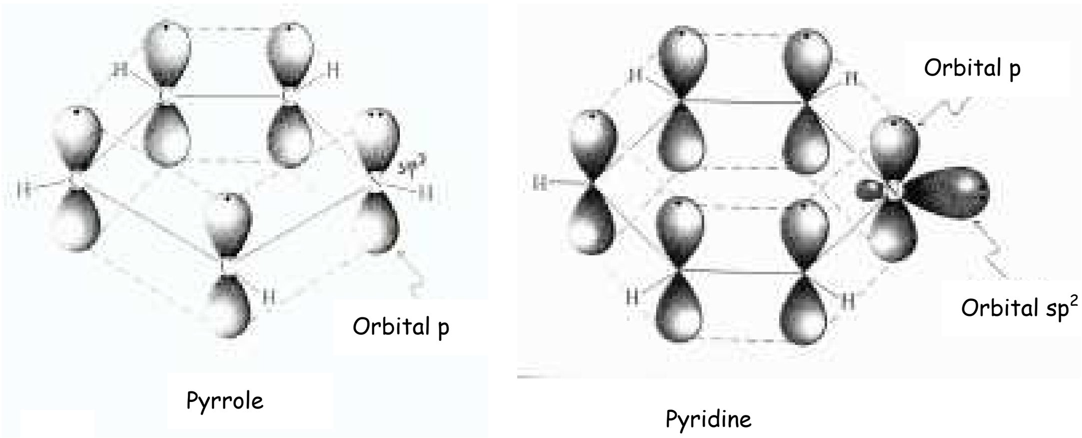

Figure 2-10.- Molecular orbitals scheme of two well-known aromatic systems as pyrrole A) and pyridine B).

2.5 PERSPECTIVES AND PRESENT WORK

As it has been above reported, nitrogen plays an important role in the formation of exciting materials like CN_x. Its incorporation into graphite increases the conductivity of the solid carbon, the optical and emitting properties of diamond is improved by adding the optimum amount of nitrogen in the system and CN_x nanotubes have been found to have higher conductance than that found in C MWNT's. Moreover super-hard elastic $CN_{0.2}$ films have been experimentally manufactured by magnetron sputtering. However there is still much work to do in order to understand the N incorporation process as well as the different possible structures. Different synthesis methods can be used to prepare CN_x materials (film and nanotubes), as it is reported in the next chapter. We will see that most of them lead to the production of amorphous materials.

3 SYNTHESIS METHODS

The first synthesis of CN materials dates from the 70's when Cuono et al prepared paracyanogen-like films by sputtering a carbon target in N_2 [63]. Later on in 1982 Jones and Stewart incorporated nitrogen into α-C:H films by plasma decomposition of methane and N_2 [64] . However the research on CN did not take off before 1989, when Cohen et al proposed that CN covalent solids could behave as ultra hard materials. Such prediction on C_3N_4 joined to the feasibility of modifying the properties of C based materials (graphite, diamond, nanotubes) by doping them with N, has increased the number of synthesis routes to attempt the production of such exciting materials. More than ten different synthesis methods have been tested during the last ten years as it is fully reported by S. Muhl and J.M. Mendéz [65]. In this chapter, a summary review of the different synthesis processes used in the production of CN_x as well as a detailed presentation of the synthesis methods used during this thesis (Ion beam assisted deposition and pyrolysis of organic precursors), will be described.

3.1 PHYSICAL METHODS

3.1.1 MAGNETRON SPUTTERING

This technique has been successfully used for the preparation of CN_x and carbon films due to its capabilities of evaporating high melting point materials like carbon, with relatively high flux. A magnetron (Figure 3-1A) consists of a plate of the material of which the film is to be made (carbon target), with magnets arranged behind it to create a magnetic trap for charged particles, such as N ions, in front of the target. When the special magnetron driven power supplier is turned on, the target is subjected to a voltage, which attracts the ionised gas particles to the target surface at high speed. When the ionised gas particles hit the surface two important effects are produced. i) Atoms are knocked out of the target surface by ions (sputtering). These sputtered atoms are not charged either positively or negatively, so they go straight out of the magnetic trap and they are posteriorily deposited on the substrate to form the coating. ii) The surface also releases electrons, which are negatively. These are hold in the magnetic trap, and their energy is used to produce more ionised gas particles. Therefore the ions which are attracted to the surface are replenished all the time, so that the magnetron can operate continuously. Using this technique, different CN_x morphologies have been reported as CN_x films, CN_x nanotubulites and CN_x nanocrystals in an amorphous matrix [48,58,66].

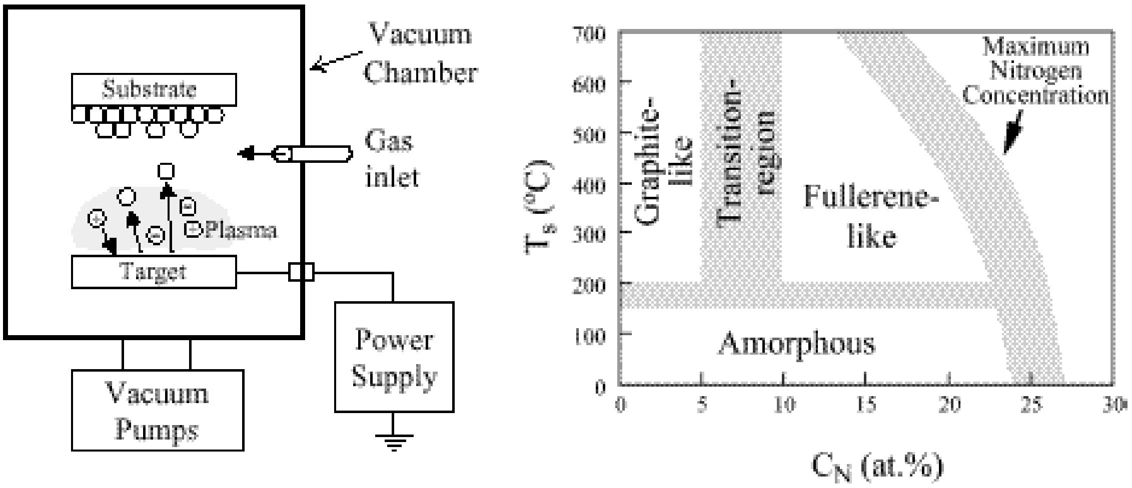

Figure 3-1.- A) Magnetron sputtering system B) Diagram phase of the different CN_x morphologies observed by magnetron sputtering [67].

The first experimental evidence of $CN_{0.2}$ super-hard elastic films with fullerene like microstructure was obtained using reactive direct current (dc) magnetron sputtering of a graphite target in pure nitrogen discharges [68]. Moreover a detailed study of the different parameters (ion flux, temperature substrate and nitrogen content) provided a well-defined diagram where the different possible morphologies are related to their concentration of nitrogen and a phase transition between graphitic and fullerene like structures is observed at approximately (5-10% N content), Figure 3-1B. The same group has also prepared carbon nitride nanotubulites (10-50nm in diameter and 20-50 nm in length), which grow perpendicular to the CN_x film and are homogeneously made of carbon and nitrogen [58].

CN_x crystals in an amorphous matrix have been grown on single-crystal Si(100) substrate by reactive sputtering in a radio frequency (rf) magnetron sputtering system. The Si substrate was first etched in 5% HF solution to eliminate the native oxide layer and then cleaned ultrasonically before introduction in the vacuum chamber. The target composed of a C disc, 50mm in diameter, was set 35 mm from the substrate holder. Before deposition, the vacuum chamber was evacuated to 3×10^{-5} Pa and N_2 introduced at a constant pressure of 10 Pa. The sputtering powder and the substrate temperature were 175W and 1073K respectively. This sample was prepared in Beijing [66] and sent to our lab where we have performed the characterisation analysis, which will be described later on in this work (paper III).

3.1.2 ION BEAM ASSISTED DEPOSITION (IBAD)

Ion Beam Assisted Deposition (IBAD) is a deposition technique, which combines physical vapour deposition (PVD) with an energetic ion irradiation from an ion source. The use of an ion source (nitrogen) and of a vapour source (evaporated C on silicon wafers), allows a well controllable, reproducible and flexible IBAD process. Ion flux, atom flux, ion energy, ion incidence angle, arrival ratio of the ions to atoms and the substrate temperature vary independently from each other over a wide range. The deposition can be made by a carbon ion beam in a nitrogen atmosphere (single beam) or by fast-switched carbon and nitrogen sources (dual beam). Most of the as-deposited films are found to be amorphous [69], however Wang et al have recently reported the formation of cubic-nanoparticles (10-60nm) embedded in the amorphous CN_x matrix in a CN_x/TiN_x multilayered sample [6] using IBAD.

The CN_x films studied during this thesis were prepared by our collaborators in Rossendorf Institute (Dresden) as following, Figure 3-2A. The Si substrates were mounted on a heater placed at an angle of 45° to the carbon source and normal to the ion beam provided by a 3 inch diameter Kaufman ion source. The substrate temperature could be adjusted between room temperature and 700°C by resistive heating. The base pressure of the chamber was 0.3 Pa and the working pressure was 20 Pa. Prior to deposition, the Si substrates were cleaned in situ by exposing them to an Ar^+ ion beam of 1000 eV and a current density of 100 $\mu A/cm^2$ for 2 min. Carbon was evaporated from a graphite ingot by means of an electron gun (AP&T, HVP4). The evaporation rate of carbon (1-3 Å/s) was measured by a quartz thickness monitor and regulated by an automatic deposition controller. The carbon deposition onto the Si substrate was assisted by a simultaneous nitrogen ion beam. The energy of the N_2^+ ions could be varied from 200 eV to 1200 eV. The current density, measured with a Faraday cup positioned on the shutter in front of the substrate holder, could reach 200 $\mu A/cm^2$. Modulated CN_x samples were produced with the following deposition parameters: ion current density of 40 μA/cm^2 and ion energy of 200 eV and the carbon evaporation rate was adjusted to first 0.1nm/s (region A) then 0.2nm/s (region B) and finally again 0.1nm/s (region C). After production the samples were prepared for plane view and cross-section microscopy analysis as it is indicated in section 4.2 (sample preparation for microscopy analysis) chapter 4.

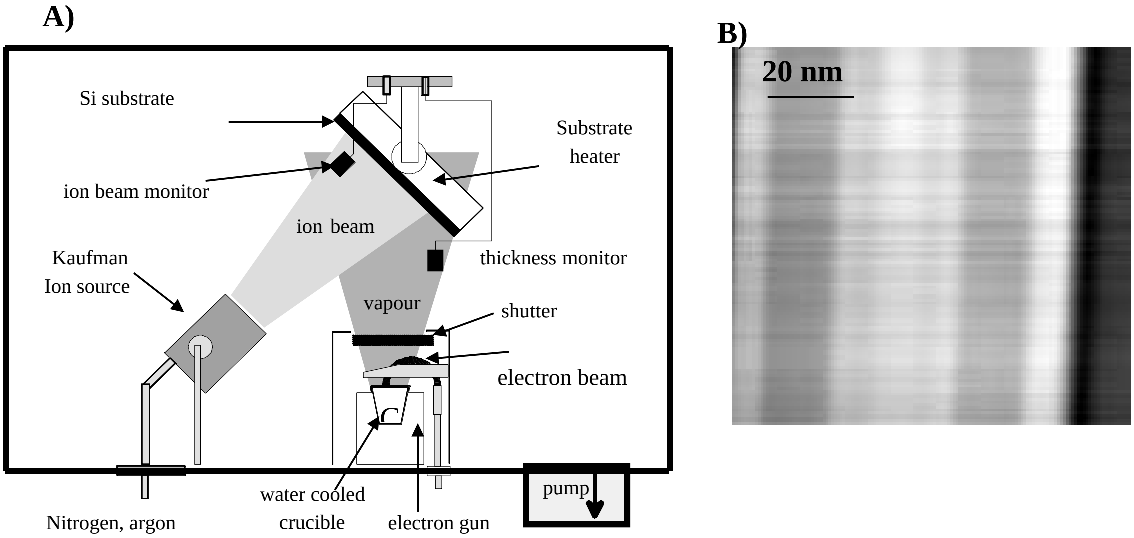

Figure 3-2.- A) Ion Beam assisted deposition system available in Rossendorf institute for the production of CN_x films. B) Bright Field (BF) image of a modulated CN_x cross section sample prepared by IBAD.

3.2 CHEMICAL METHODS

Synthesis of carbon nitride compounds has been attempted by a variety of chemical reactions. A graphite-like hexagonal polymer $[(C_3N_3)_2(NH)_3]_n$ has been prepared and found to be stable up to 500°C [70]. Interesting ferromagnetic crystalline material, $C_3N_4O_{1.2}H_{4.1}$ have been obtained from the reaction of $C_3N_3Cl_3$ and Li_3N in N_2 at 220°C [71]. Shock wave compression, a method used in the production of hard materials like diamond and wurtzite boron nitride, has been attempted to produce carbon nitride. Notwithstanding that different carbon nitride organic precursors have been tried, no one has produced hard carbon nitride, however an extraordinarily well-ordered shock synthesis diamond was produced [72]. Nitrogen rich carbon nitride networks (C_3N_4 and C_3N_5) have recently been produced by retarding the decomposition of the energetic molecular azide $(C_3N_3)(N_3)_3$. These compounds are robust and sublime to a significant extent above 600°C. On the basis of experimental evidence, they can be described as disordered planar system somewhere between cross-linked polymers and graphitic sheets [73].

Other additional chemical processes for CN_x production are vapour growth processes such as chemical vapour deposition and pyrolysis of organic precursors. The former has successfully been used in the preparation of CN_x nanotubes and some groups have also claimed the production of crystalline C_3N_4 using such process. The latter did produce amorphous CN_x films, however it has been efficiently used for the production of carbon nitride nanotubes.

3.2.1 CHEMICAL VAPOUR DEPOSITION (CVD).

CVD provides the formation of a film on a surface from a volatile precursor (vapour or gas), as a consequence of one or more chemical reactions, which change the state of the precursor. Many different films can be deposited with crystalline, polycrystalline, and amorphous structure. Most films can be deposited from several different precursor systems. Plasma discharges can be used to help things along, or the substrate and/or the gas can be heated or cooled.

This technique includes different process direct-current (DC) arc, hot-filament chemical vapour deposition (HFCVD) and plasma enhanced chemical vapour deposition (PECVD). Nevertheless, in every case, CVD processes must: i) provide a volatile precursor containing the constituents of the film, ii) transport that precursor to the deposition surface, iii) encourage or avoid reactions in the gas phase, iv) encourage surface reactions that form the film, v) and do it rapidly, reproducibly, and uniformly for industrial applications.

CVD is one of the most successful techniques for growing CN_x films containing C_3N_4 crystals. Small grains (~0.1μm) ad nanocrystallites have been grown and claimed to be β-C_3N_4 embedded in CN_x films [7]. Later on Veprek et al [74] showed that compact uniform films with the composition C_3N_4 can be produced by plasma CVD in an intense nitrogen discharge, but the film was absent of any crystal structure. Wang et al reported the production of pure crystalline C-N films on silicon and nickel substrates by HFCVD. The films were claimed to be constituted of α, β and other unknown phases [5,75].

Recently this technique has also been used for the production of CN_x nanotubes [59]. The nanotubes are coiled with inhomogeneous diameter along the axis and they grow perpendicular to the quartz substrate. EELS on such nanotubes reveal an inhomogeneous distribution of N in the nanotubes. They are nitrogen rich in a few external layers, amorphous in the core of the tube while a slight incorporation of nitrogen is found in the graphite layer. In this dissertation the results obtained by CVD are compared with our results from pyrolysis of organic precursors.

3.2.2 PYROLISIS OF ORGANIC PRECURSORS; Synthesis of CN_x Nanotubes

The pyrolysis of different organic precursors, melamine, triazole, tetracyanoethylene to name a few examples, has shown that the presence of hydrogen in the organic precursor reduces the amount of residual solid due to the thermodynamically stability of NH_3, HCN, CH_4, which are released as soon as they are formed. The produced solids are amorphous with a short-range layered structure containing both trigonal carbon and nitrogen [76]. The production of C_3N_4 thin films by pyrolysis have been reported by Koubetakis et al [77], the sample results amorphous and the presence of sp^2 bonds for carbon and nitrogen is obtained from Infra Red (IR), EELS and Nuclear Magnetic Resonance (^{13}CNMR). Therefore, up to now the pyrolysis method has not successfully been used for the preparation of CN_x crystalline films. However when a catalyst is present, fruitful production of carbon nanotubes containing nitrogen is achieved.

Since the discovering of carbon nanotubes, different synthesis routes have been developed for their production; Arc-discharge and laser evaporation have been found to be well-suited techniques for the formation of large quantities of single and multiwalled nanotubes. However a system which could work in continuously is needed to scale up nanotube production. Catalytic pyrolysis of organic precursors (vapour growth process) has been found to be a versatile synthesis method because of the possibility of having a continuous process and a better control in the synthesis process than with arc discharge or laser ablation. Moreover, a variety of nanotubes can be produced by only changing the organic precursor and the physical form of the catalyst. The first experimental write up about CN_x nanotubes appeared in 1997 when Terrones et al [56] reported the preparation of aligned nanotubes by catalytic pyrolysis of triazine. The produced nanotubes are highly graphitic and some traces of N (<2-5%) are also detected. One year later, Sen et al [55] produced BCN, CN and BN nanotubes by pyrolysis of precursor molecules over Co catalyst. The quantification of the sample using XPS and EELS indicates a N content of approximately 4%. Although large efforts have been done to produce CN_x nanotubes, only a minor amount of N has been incorporated in the system. Moreover information about how N is incorporated in the system is still lacking. During this thesis, in order to study the dependence of the different pyrolysis parameters on the N incorporation into C nanotubes, series of nanotubes samples, varying the synthesis conditions, were produced.

3.2.2.1 PYROLYSIS SET-UP

In the present work, CN_x nanotubes and C nanotubes containing nitrogen were produced by catalytic pyrolysis of an organic precursor. The pyrolysis was carried out in a two-stage furnace system fitted with an independent temperature controller Figure 3-3. The organic precursor 0.10-0.15 g was placed in one end quartz tube (0.6 cm ID, length 60 cm), and the catalyst in a quartz boat at the other end. The tube was located inside the furnace and subject to a gas flow (20-60 cm^3/min). The furnace containing the metal catalyst was heated to temperature of reaction (T) and maintained at this temperature throughout the experiment. Subsequently, the furnace 2, containing the organic precursor, was raised to 950 °C, when it reached the sublimation temperature of the organic precursor, a white smoke appeared inside the reaction tube until the carbon source had disappeared. The furnace 2 was switched off and the furnace 1 was held at the reaction temperature for an additional 15 minutes. After the experiment the obtained black powder was dispersed in acetone for posterior microscopy analysis.

In order to study the dependence of the synthesis parameter (organic precursor, catalyst, temperature and gas flow) on the N incorporation into the carbon nanotubes, a series of experiment, Table 3-1, were performed. First, an organic precursor rich in nitrogen was catalytically pyrolised in an inert atmosphere at different temperatures to control the high yield on CN_x nanotubes. The experiments were repeated using different catalysts to study their effect on the production of CN_x nanotubes. Secondly, N rich gases (N_2 and NH_3) were introduced in the system to study the possible increase of N in the carbon nanotubes by increasing the nitrogen source. Finally an organic precursor free of nitrogen (camphor) was pyrolysed in the presence of N rich gases. The results of the above experiments will be described in chapter 5 and papers II and V.

3.2.2.2 ORGANIC PRECURSORS

Using hydrocarbons (benzene, acetylene), carbon nanotubes, graphitic cones and helix-shape graphite nanotubes have been produced [78-80], BCN precursors (CH_3CN. BCl_3) have provided $[BC2N_z]_n$ (z=0.3-0.6) nanotubes with inhomogeneous composition and more recently, CN precursors (as pyridine and triazine) have been used to produce CN nanotubes with N content lower than 3%. During this thesis, melamine (a rich organic precursor) and camphor (a free nitrogen precursor) have been used to produce CN nanotubes and C nanotubes containing encapsulated-nitrogen gas.

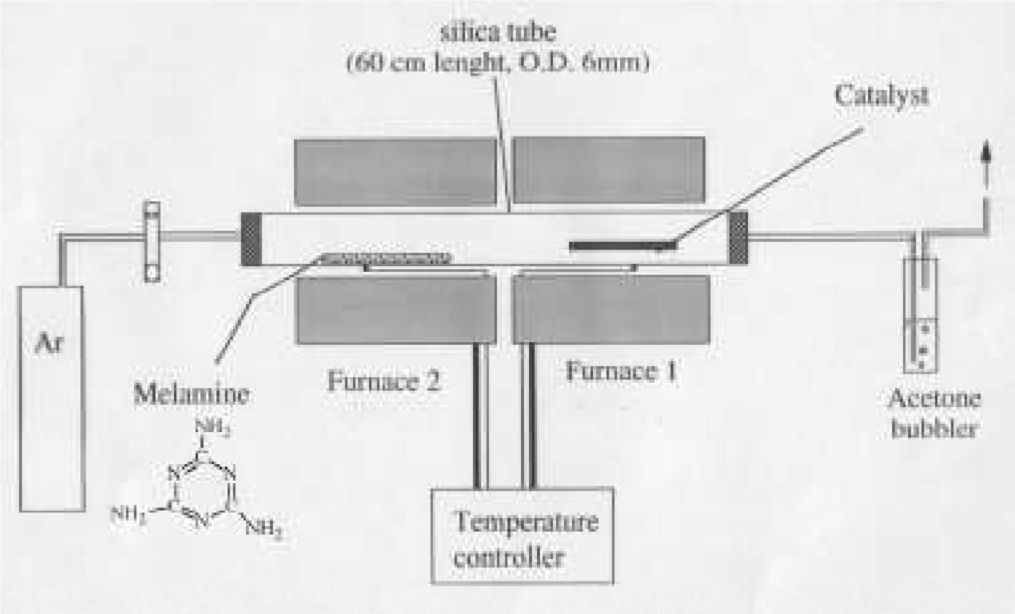

Figure 3-3.- Pyrolysis set-up used during the present thesis for producing C and CN nanotubes.

Table 3-1.- Series of experiments performed for the dependence study of the N incorporation into the C nanotubes.

Organic precursor	Catalyst	Gas flow	Temperature
N Rich (melamine)	Laser etched films	Ar	950°C
	As powder (Ni or Fe)	Ar	950, 850, 750, 550°C
		N_2	950°C
		NH_3	950°C
Free of N (camphor)	Fe powder	N_2	950°C
		NH_3	950°C
		N_2/NH_3	950°C

3.2.2.2.1 Melamine (1,3,5 triamino-triazine)

Melamine ($C_3H_9N_6$), Figure 3-6A, also called cyanuramide, or triaminotriazine, is a crystalline substance belonging to the family of heterocyclic organic compounds. Melamine is manufactured by heating dicyandiamide under pressure. Its most important reaction is that with formaldehyde, it produces resinous compounds of high molecular weight. These resins form under the influence of heat but, once formed, are insoluble and infusible. Usually impregnated with fillers and pigments, they are molded into dishes, containers, utensils and handles or used as laminating agents or coating materials for wood, paper, and textiles. Formica and Melmac are well-known trade names for products based on melamine resins. Melamine has been also used in the production of flame retards [81]. The presence of mobile hydrogen atoms from the amino group, which can be shifted to the N atoms of the aromatic ring, enhances the decomposition process. Melamine, serving as spumific compound, has everincreasing importance in plastics industry as flame and heat retardant. Upon decomposition of the spumific compounds, large quantities of non-flammable gases (e.g. N_2) are produced. The sublimation temperature of this compound is approximately 340°C. In the present thesis, melamine (Aldrich 99.9% purity) has been used as C and N source in the formation of CN_x nanotubes.

3.2.2.2.2 Camphor

Camphor, ($C_{10}H_{16}O$), which belongs to a group of organic compounds defined as terpenoid ketones, has been used for many centuries as a component of incense and as a medicinal. Modern uses of camphor have been as a plasticier for cellulose nitrate and as an insect repellent, particularly for moths. The pure compound is a white, waxy solid that melts at about 178°–179°C.

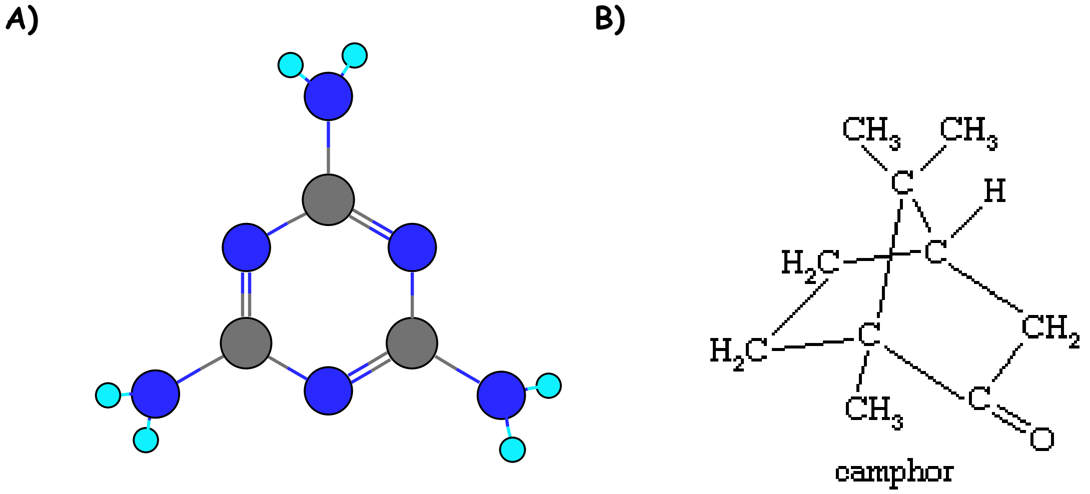

Figure 3-4.- Structure of the different organic precursor catalytic pyrolised for the production of nanotubes A) melamine (N atoms in blue and C atoms in grey) and B) camphor.

Camphor is derived from Cinnamomum camphora, the camphor tree, of China, Taiwan, and Japan. It is obtained by steam distillation of wood chips. The wood of the camphor tree may contain up to 5 percent of the crude oil, and a single tree can yield up to three tons of the oil, which settles from the distillate and crystallises. Since the early 1930s camphor has been made by several processes from the compound α–pinene. The structure and the peculiar reactions were important problems of 19th-century organic chemistry. At least 30 structures were proposed before the definition of the correct one Figure 3-6B.

During the present thesis, camphor (Technical grade camphor, purity c.a. 98%, Camphor & Allied Products Ltd., India) has been pyrolysed in the presence of nitrogen rich gases and nanotubes containing nanocapsules have been produced, as it will be described in the following sections.

3.2.2.3 CATALYST

The catalyst plays an important role in the production of nanotubes as responsible for their growth. MWNT's could be produced without any catalyst by arc discharge but their presence is indispensable for the formation of SWNT and when they (MWNT and SWNT) are synthesised by vapour growth techniques like pyrolysis. Despite the importance of catalyst in the growth mechanism, its role or the way that it influences on the nanotubes production is still not clear. Two main growth mechanisms have been proposed; the first one consists of surface diffusion of the carbon species over the catalytic particles ([82], Fig.3-5A). In the second one, the carbon dissolves in the metal and precipitates at the other side of the metal particles ([83], Figure. 3-5, B and C). The mechanisms can further be classified as “tip growth” and “based growth” mechanism Figure 3-5. However, experimental observations on nanotubes indicate that the above mechanisms are not the only possible process. Because of the variety of synthesis methods and the variety of carbon nanotubes morphology, different growth mechanisms could act together in their production.

In order to control the nanotube production by pyrolysis, different physical forms of catalyst have been used during the last years. The pyrolysis of metallocene molecules (metal–containing molecules as $Fe(CO)_5$) produces metal filled nanotubes, however if an additional carbon source is included in the system, hollow carbon nanotubes are produced [84]. Aligned nanotubes have been produced using either catalyst-etched films [56], or a dispersion of Co metal nanoparticles (4nm diameter) pre-treated with H_2S [85] or using ferromagnetic molecules as a ferrocene-acetylene mixture to name a few examples. In this section, first we present the pyrolysis of melamine on laser etched films, confirming the production of aligned carbon nitride nanotubes and secondly we report on the use of the catalyst as a powder to study the different parameters which influence on the N incorporation into the carbon system.

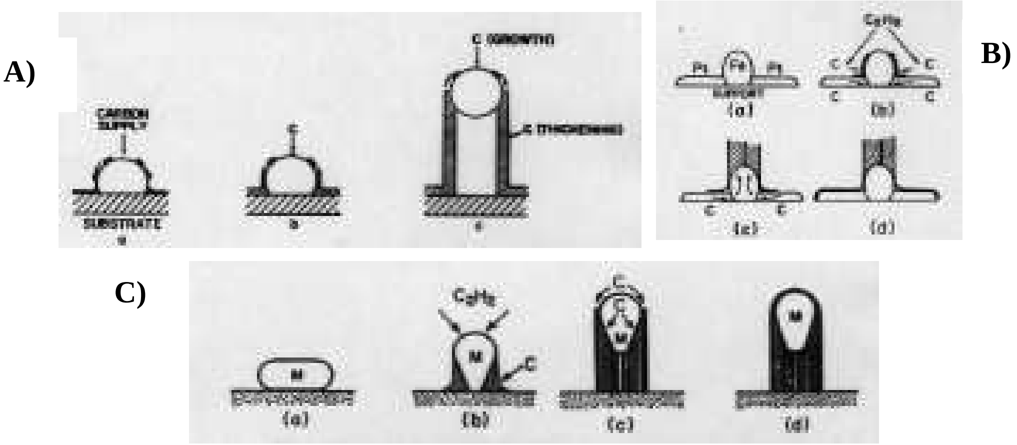

Figure 3-5.- Different growth mechanisms proposed for the formation of carbon nanotubes. A) Diffusion of the carbon source on the catalytic surface. B) and C) Diffusion of the carbon source through the catalytic particle.

3.2.2.3.1 Laser etched films

The pyrolysis of triazine using laser-etched films has produced aligned nanotubes with nitrogen traces. The same system was used to pyrolyse melamine and to produce CN aligned nanotubes [57]. The catalyst (Fe, Co or Ni) was deposited by electron beam (operating at 4-5 kV and 15 A in order to evaporate the metal Fe, Ni, Co) onto a silica substrate. The silica substrate was placed 15 cm above the subliming metal source and was heated at 200-300°C under vacuum (10^{-6}-10^{-7} Torr). After deposition, the film was subsequently etched in air with single laser pulses (Nd:YAG, 266nm and 355nm, 2-10mJ) using a cylindrical lens to create linear tracks (1-120μm, lengths ≤ 5mm) across the substrates. Figure 3-6 shows a scheme of the etching technique and an atomic force microscopy (AFM) micrograph of an etched nanotrack. The AFM observations reveals that the Si film has been damaged during the process and areas free of catalyst as well as clusters (≤ 50 nm) of catalytic particles (≤ 50 nm) are observed.

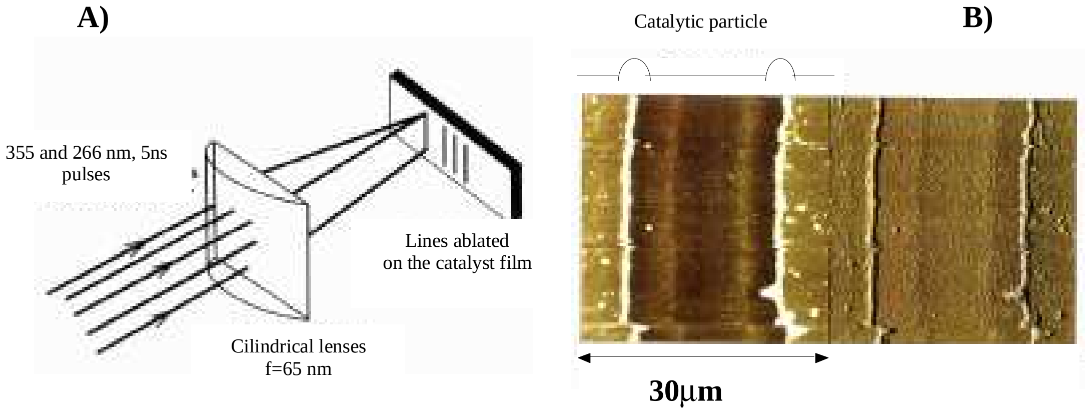

Figure 3-6.- A) Nd:YAG Laser system used for the preparation of catalyst etched films. B) AFM micrograph (lighter areas are raised, darker areas are deeper) of a catalyst etched films before pyrolysing in the presence of an organic precursor. The white spots observed in B) left image, correspond to the catalytic particles.

Once the catalyst film is ready, it is located in the pyrolysis system and the process is carried out with melamine as an organic precursor. After the pyrolysis, the etched-catalyst film is covered with a black layer and a high amount of material is observed, where the tracks were present (white lines fig A). From Scanning Electron Microscopy (SEM) observations, it is obvious that the preparation conditions of the film play an important role in the alignment of the nanotubes.Thus, depending on the etching energies, high or low content of nanotubes as well as either aligned or non-aligned nanotubes could be obtained. Figure 3-7 reveals different situations depending on the utilised etched energy; A) Shows a low magnification of a pyrolysed film, the white lines correspond to the area where the nanotubes are grown. B) low content of nanotubes in a Fe-laser etched film, C) partially aligned nanotubes in a Ni-laser-etched film.

When the catalyst films are prepared in the optimum conditions, aligned nanotubes in a Fe-laser-etched film are produced, Figure 3-7E,F. The nanotubes grow as a carpet, with a mean length of 'pile' of 30μm. Apart from the etched energy, another important parameter to take into account for the alignment and morphology of the nanotubes is the age of the metal film. Melamine pyrolysis over aged Ni or Co films (exposed to air for several weeks) generates helically coiled fibres (length≤50 μm) grown within the tracks as well as on the surface of the metal film close to the track. As a conclusion aligned nanotubes are produced when the catalytic etched films are prepared in the optimal conditions at medium etched energy (around 5 mJ/shot). This energy depends also on the utilised catalyst. The nanotubes are made of C and N with N content ≤7% as it is observed by X-ray photoemission and electron energy loss spectroscopies.

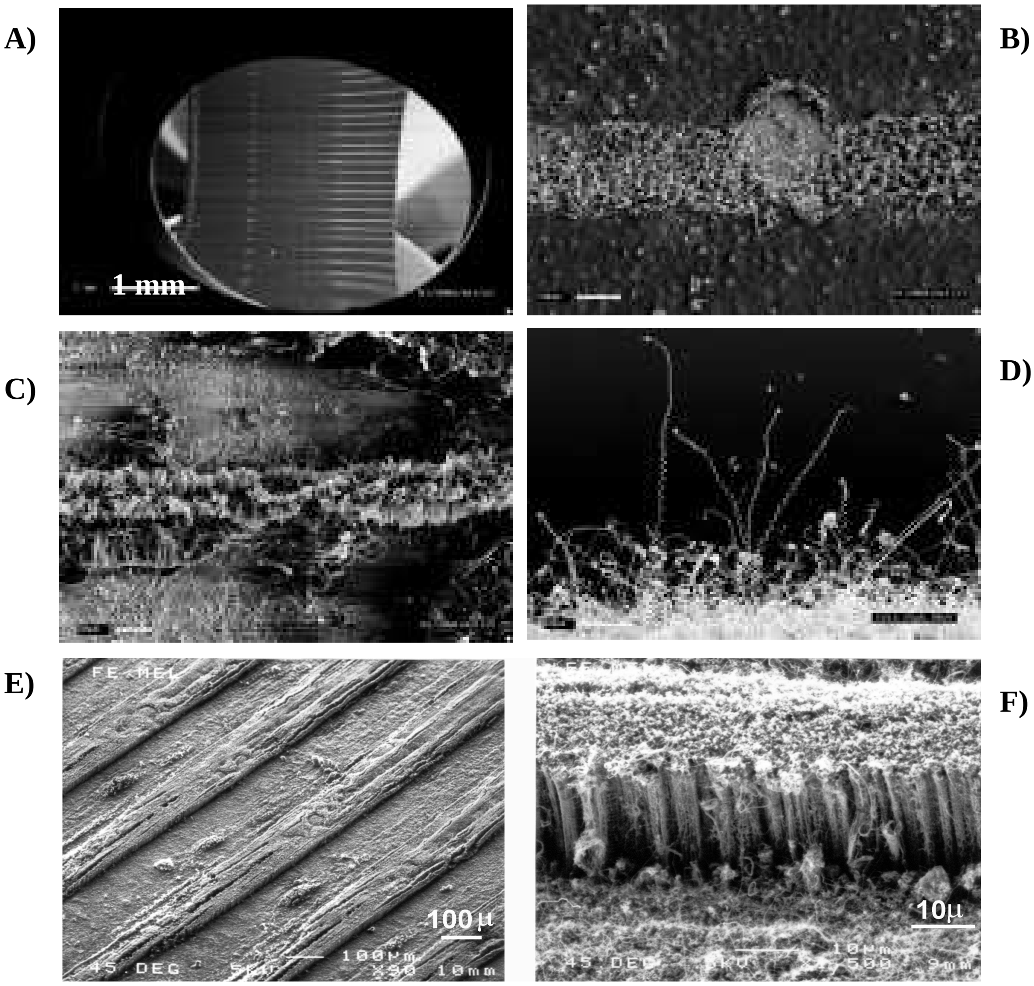

Figure 3-7.- SEM images of etched-catalyst films after being pyrolised in the presence of melamine. A) Low magnification of a film partially covered of aligned nanotubes (white area). B) Fe film (etched at low energy 1-3mJ/shot) presenting low content of nanotubes. C) Ni film presenting nanotubes partially aligned. D) Co film, which was exposed to air during a few days before the pyrolysis experiment was performed, presenting helically coiled fibres. E and F) Aligned nanotubes on etched-Fe films.

3.2.2.3.2 Catalyst as powder

As it has been observed above, many parameters influence the alignment of the nanotubes: energy etching, age of the substrate, nature of the catalyst. Therefore, once the production of carbon nitride aligned nanotubes has been confirmed by using etched catalytic films, the catalyst was used as a powder to study the dependence of the different synthesis parameters on the N incorporation into the nanotubes.

First, melamine was pyrolysed in the presence of Ni catalyst in an inert atmosphere at different temperatures to control the production of nanotubes. CN nanotubes (<60nm) are the main product observed in the samples grown at 1000°C . However, large particles (700nm) and a low yield of C and CN nanotubes (15-20nm diameter) are observed when the pyrolysis is carried out at lower temperature Figure 3-8. TEM images show that the diameters of the obtained nanotubes at higher temperature (1000°C) are significantly larger that those of the nanotubes grown at lower temperature (750°C), as previously observed by Lee et al in their study of nanotubes grown by pyrolysis of Fe-phtalocyannine[86]. Similar results are observed with Fe as a catalyst, however the number of metal particles encapsulated in the nanotube is higher with Fe than with Ni. Detailed results about the influence of the catalysts on the CN_x nanotube production are presented in chapter 5 and paper II.

The highest yield of CN nanotubes is produced at 950-1000°C. Therefore the next series of experiments (in order to check the effect of a reactive gas) are performed at such temperature.

3.2.2.4 GAS FLOW

In order to study the effect of an additional nitrogen source in the system, the pyrolysis experiments were carried out in the presence of N-rich gases. As it will be further described in chapter 5 and papers II and V, there is no incorporation of N when the experiment is performed in a N_2 atmosphere. Unfortunately NH_3 reacts with melamine at low temperature making impossible the pyrolysis experiment. However when the organic precursor free of nitrogen (camphor, $C_{10}H_{19}0$) was pyrolysed in presence of NH_3 or N_2/NH_3 a new morphology has been observed. Different ellipsoid sections, nanocapsules, are distributed all along the tubes which thus display a rather compartmentalised morphology. As it is

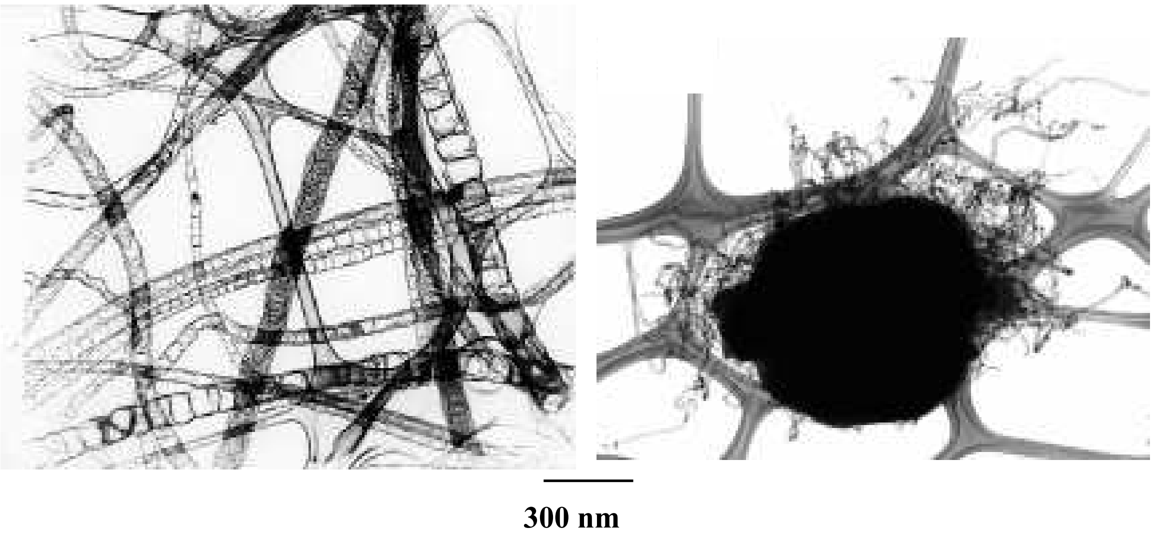

Figure 3-8.- CN nanotubes produced by catalytic pyrolysis of melamine at 1000°C and 750°C.

further described in chapter 5 and paper V, EELS analysis shows that N_2 gas is originally contained in these nanocapsules, Figure 3-9.

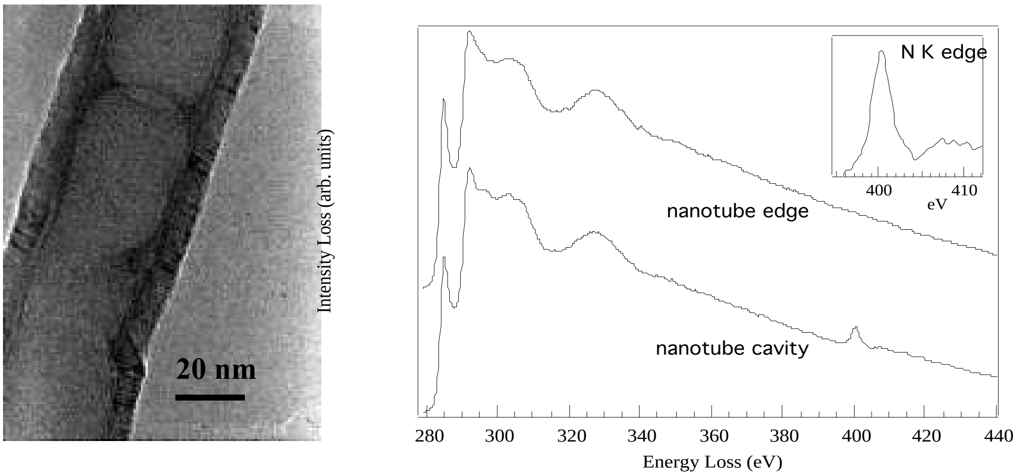

Figure 3-9.- A) TEM image of a nanotube containing nanocpasules. B) EELS spectra, C K edge and N K edge which correspond to graphite and N_2 respectively.

3.3 SUMMARY AND INTRODUCTION TO NEXT CHAPTER

This chapter has given a survey of the different synthesis methods used in the production of CN_x materials during the last years. Moreover IBAD and pyrolysis have been more extensively described because they are the methods utilised during the present dissertation to prepare CN_x films and nanotubes respectively. The prepared samples were characterised by TEM and EELS as it is described in the next chapter, together with the principles of the theory and the techniques used for processing the acquired data (MSA and NNLS methods).

4 CHARACTERISATION TECHNIQUES

During this dissertation the samples have been structurally characterised by using a Topcon EM-002B electron microscope with a LaB_6 filament, in the High Resolution imaging mode. The chemical information has been obtained by performing Electron Energy Loss Spectroscopy in a dedicated VG 501 STEM. Both microscopes have been operated at 100kV to reduce the radiation damage in the samples.

4.1 (SCANNING)-TRANSMISSION ELECTRON MICROSCOPE, (S)TEM.

As a general definition a microscope is an instrument that produces enlarged images of small objects, allowing them to be viewed at a convenient scale for examination and analysis. Large variety of microscopes are available on the market, however we will focus our attention on Transmission Electron Microscopes, where fast electrons are transmitted through a thin sample and several information about the sample are collected as a result of the interaction between the primary beam and the material. One should distinguish between a Conventional-TEM (CTEM) and a Scanning-TEM (STEM). Figure 4-1. The main difference between these two systems arrives from the image formation principle. In the former, a determined area of the sample is irradiated with a fixed parallel electron beam and the scattered electrons are collected over a narrow solid angle and focused by the objective lenses onto the image plane. The elastically scattered beam (electrons that have changed the direction but not lost any energy during interaction with the specimen) interfere with the unscattered beam to produce a phase contrast image. The inelastically scattered beam (electrons that have changed both direction and energy on interaction with the matter) generates a diffuse background image, which it is in some electron microscopes eliminated by an energy filter. On the other hand, in a STEM, an electron beam (emitted by a Cold Field emission Gun) is focused, at the surface of a specimen by the effect of various magnetic lenses to form a high-brightness subnanometer incident probe (0.5-1 nm) and all the scattered electrons can then be collected by a variety of detectors placed behind the sample. An image is generated by scanning the focused beam over the specimen. The detectors sequentially collect an information, which corresponds to an individual pixel of the image, consequently punctual information is directly recorded. On the other hand, in the CTEM, the global information arrives to the detector where it is transformed into punctual information (after pixelation). The most important advantage of a STEM is the possibility of collecting simultaneously different characteristic signals generated from the nano-volume defined by the diameter of the probe and the local thickness of the sample. This multidetection is possible thanks to the absence of important electronic optics after the sample. This specific design makes STEM a well-suited technique to characterise, morphologically and chemically, materials at the nanometer scale.

Which kind of information can be obtained with a TEM? When the electrons enter the matter, they can pass through it without being scattered or they can interact with the constituent atoms via electrostatic (Coulomb) forces. As a result of these forces some electrons are scattered; the direction of their momentum is changed and in many cases they transfer an appreciable amount of energy to the specimen. When the electron does not transfer any amount of energy to the specimen, the diffusion process correspond to an elastic scattering while inelastic scattering, occurs when some energy is transferred. Therefore, the interaction of the fast electron with the matter provides a series of different signals which can be further explored in order to characterise the sample. Among the elastic signals (see figure 4-2), diffraction provides

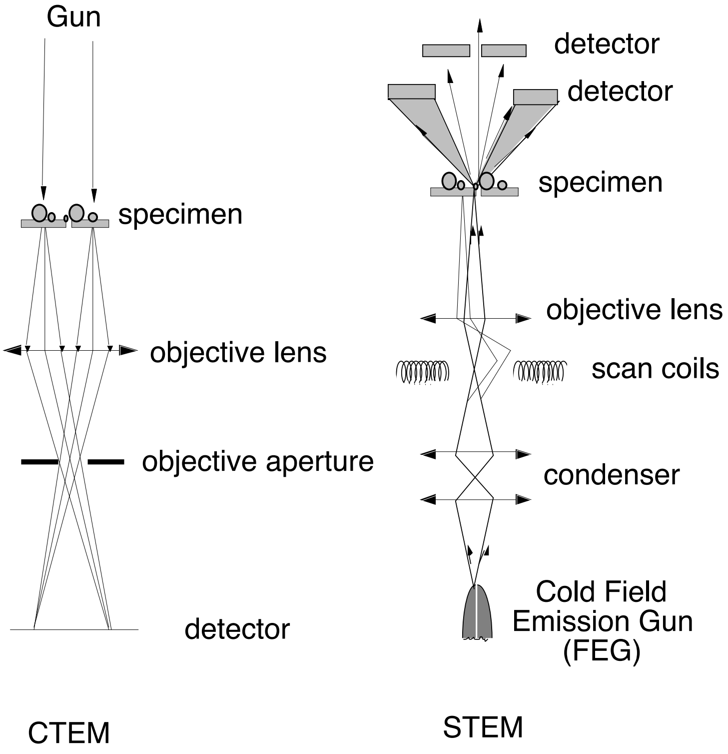

Figure 4-1.- CTEM and STEM schematic diagram of image forming.

information about the crystallinity of the material and High Annular Dark Field (HADF) signal is sensitive to the morphology (more precisely to the thickness) and to the local chemistry (Z-contrast) of the sample. The inelastic signals are used in most microanalysis methods. Electron Energy Loss spectroscopy sorts out the scattered electrons of the primary beam according to the energy loss suffered. On the other hand, several techniques make use of the various secondary radiation which can be emitted when the specimen returns to its fundamental state by losing the energy gained during the interaction; these signals may be X-rays, Auger electrons or light (cathodoluminescent). All these signals can be independently recorded in a TEM while they can be simultaneously collected in a STEM. During the present dissertation, EELS and HADF are simultaneously recorded with a dedicated STEM.

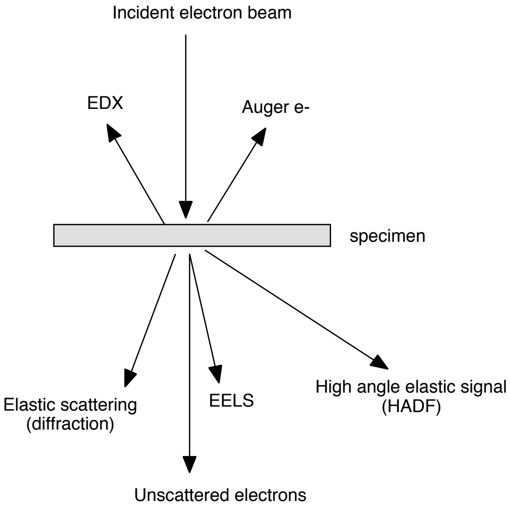

Figure 4-2.- Different signals produced when an incident electron beam interacts with the matter.

4.2 SAMPLE PREPARATION

In order to get the above mentioned information, the sample has to be thin enough (electron transparent) to transmit electrons with relatively moderate changes in direction and transfer of energy, before recording on the detectors. Therefore, thick samples need special preparation before being introduced in the microscope. Different systems can be used for thinning the specimen. However, we have to keep in mind that some of these processes can affect the sample, changing both its structure and its chemistry. During this dissertation CN_x nanotubes have been dispersed in acetone and deposited directly in a carbon holey grid, no thinning process has been required, this is the easiest situation for specimen preparation. However, the IBAD prepared CN$_x$ films (200-400μm) needs a thinning process. Two different methods have been used in order to prepare plane-view and cross-section samples.

4.2.1 PLANE-VIEW SAMPLE

The CN$_x$ films deposited on a Si substrate have been prepared for plane view analysis using a chemical etching process. It consists of removing part of the sample to leave an area, which is electron transparent. First the CN$_x$ film is protected with a resin. Then the Si layer is attacked with an acid solution (HF:CH$_3$COOH:HNO$_3$) up to the film is thin enough, Figure 4-3A. The thinning process has been followed with an optical microscope, the process is slowed when the Si layer colour becomes red and stopped as soon as a small window starts to appear, Figure 4-3B.

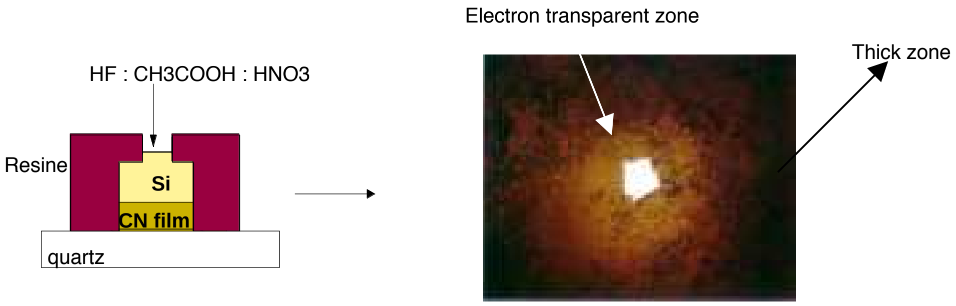

Figure 4-3.- A) Schematic diagram of a plane-view sample preparation. B) Optical microscope micrograph of the plane view sample.

4.2.2 CROSS-SECTION SAMPLE

Cross section samples are specific for studying interfaces. In this configuration, the area of study (interface) is parallel-oriented to the electron beam. In order to prepare the cross section sample, the sample is cut into slices (50μm) using a chemical wire and glued together to produce several layers, like a sandwich, Figure 4-4A. At this stage, the gluing of the sections is critical, the thickness of the glue layer has to be thick enough for good adhesion, but not too thick so that it is completely thinned away during final ion milling. Then the sandwich-layer is sectioned into slices (500μm) normal to the interfaces, grinded and polished with SiC up to thickness less than 50μm and pasted to the Cu grid. The final step of the sample preparation is the thinning, process performed by ion milling. The sample is bombarded with energetic neutral atoms (Ar, 2.5-5keV) and material is sputtered from the sample until it is thin enough to be studied in a (S)TEM. In order to avoid preferential thinning, the sample is continuously rotated and the incident beam is inclined (5-6°). During the electron microscopy analysis we have to keep in mind that the ion milling thinning process could modify the chemistry and morphology of the sample.

4.3 HRTEM (TEM) AND ADF (STEM) IMAGING

During the present thesis, different imaging methods (HRTEM, HAADF and BF) have been used to characterise the morphology of the different CN_x analysed samples (films, nanocrystals and nanotubes). We describe hereafter the different contrast formation principles and the information that can be extracted from the analysis of such contrasts.

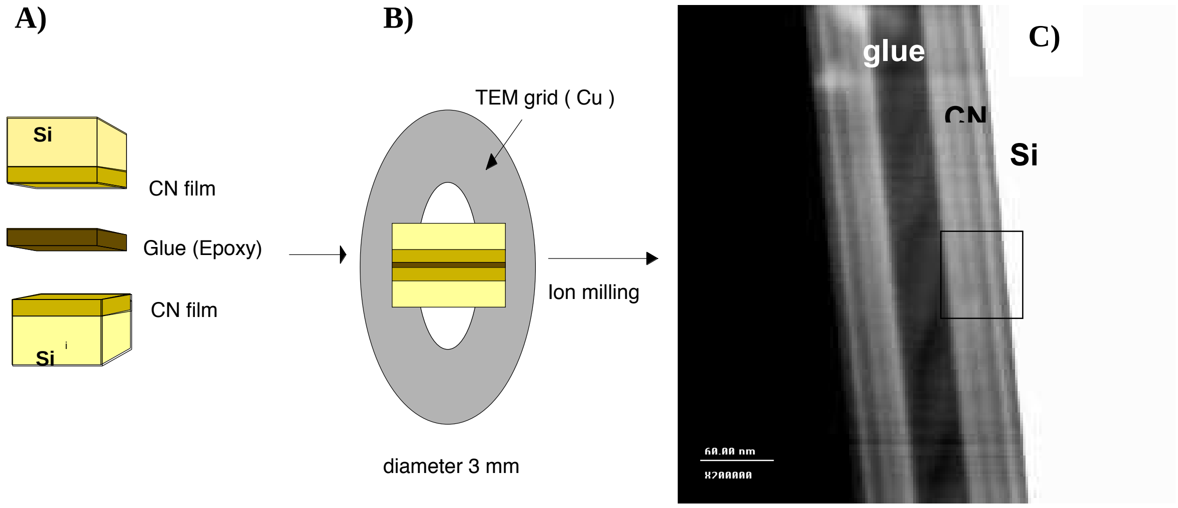

Figure 4-4.- Schematic diagram of cross-section sample preparation. A) and B) present the different steps of the process. C) TEM image of the cross section sample.

4.3.1 HRTEM IMAGES

In order to get information about the atomic structure of a material, HRTEM is an indispensable technique. It provides lattice images, which are interference patterns between the direct beam and diffracted beams, viewed in direct space. In these images the spacing of a set of fringes is proportional to the lattice spacing when the corresponding lattice planes meet the Bragg condition. The spatial resolution of a microscope is given by the smallest inter-fringes distance observable. In the utilised TEM the spatial resolution determined by the spherical aberration of the objective lenses is 2Å (point to point resolution). Thus the spacing distance typically present in a multi-walled carbon nanotube (3.4Å) is in the observed range, however the fringes distance corresponding to Fe metal can not be observed because they are under the spatial resolution range.

In the case of amorphous materials, there is not periodicity and no preferential orientation. Then no fringes are visible, instead a weak noodle-like contrast is observed. This contrast is typical of amorphous materials but no direct information about the atomic arrangement can be extracted. However, this kind of image gives direct information about the microscope characteristics and constitutes a useful tool for correcting the astigmatism of the objective lenses [87].

Generally speaking, the observed fringes in a HRTEM image result from constructive interference after reflection of the incident beam on the reticular planes oriented in the Brag condition. In a TEM microscope for an incident energy (Eo) of 100 keV, a wavelength (λ) of 0.037Å, and a d distance between the reflected planes, the Bragg angle [87];

$$\theta \approx \sin\theta \approx \frac{n\lambda}{2d} \approx \text{a few } 10^{-3}\,\text{radians} \quad (1)$$

As a result, the observed fringes are associated with reticular planes that are oriented parallely to the beam. In many cases, the interpretation of these images is not trivial and needs the support of simulations. In this thesis, HRTEM has been used to study the possible graphitization of the C and CN_x nanotubes. In that case, the observed contrast can be easily directly interpreted. If the nanotube is graphitic a series of black fringes, which are directly correlated to the position of the atoms located in the corresponding graphitic sheets are observed. A HRTEM image of a crystalline nanotube is shown in Figure 4-5A. The coaxial multi-shell structure is revealed by intense parallel fringes separated by 3.4Å. At Scherzer focus, to each black fringe (called 002) corresponds a single graphitic sheet. Only a small number of atoms located in the area of the cylindrical shell locally parallel to the beam, (see Figure 4-5B) contributes to the observed contrast.

In favourable cases, a shorter distance (Figure 4-5D) associated with the hexagonal network of the graphitic sheets can be observed. This distance is 2.1 Å and corresponds to the periodicity between successive zig-zag atomic chains as indicated in Figure 4-5C. Moreover, the fact that the 0.21 nm fringes are perpendicular to the tube axis suggest that the majority of tubes are of zig zag type. Such contrast can be only observed when a significant amount of graphitic shells posses the same helicity resulting in a stacking of atoms on top of each other.

4.3.2 IMAGING WITH A STEM

As it has been indicated in section 4.1 the basic principle of image formation in the STEM is different from a CTEM. The beam is scanned on the specimen by means of the scan coils and the image of the specimen is sequentially produced by monitoring the scattered intensity measured through a combination of scintillator and photomultiplier. One advantage of forming images in this way is that, because of the absence of magnify lenses, the intensity of the image is not varying with the magnification. Moreover the absence of optics after the specimen makes possible the multidetection.

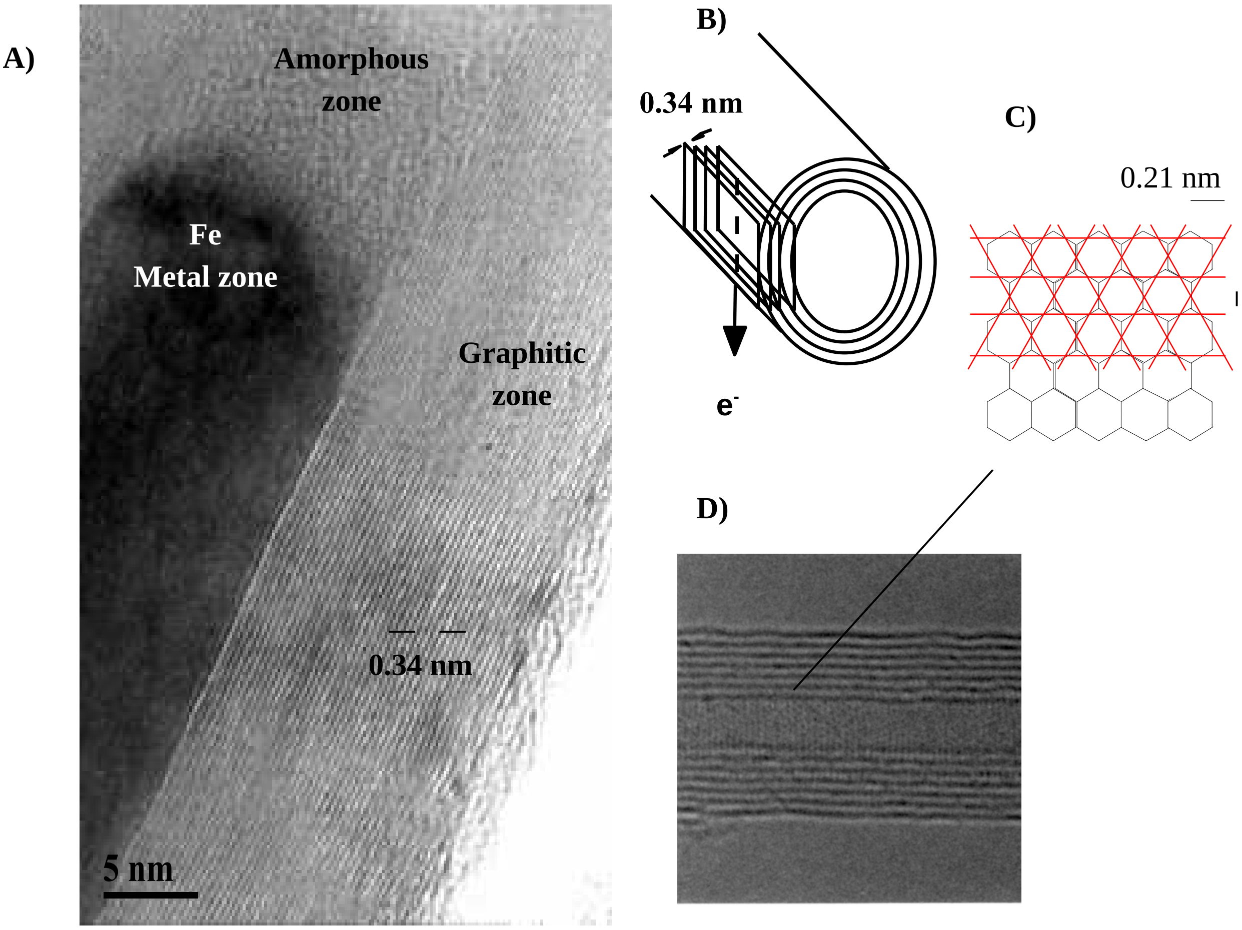

Figure 4-5.- A) HRTEM image of a multi-walled nanotube (40 walls), partially filled with Fe. The spacing between the observed fringes corresponds to the interplanar distance in the nanotube as shown in the inset-scheme (B). The presence of Fe metal and amorphous C in the cavity of the nanotube is also shown. C) Hexagonal network of a graphite layer. D) HRTEM image of a C nanotube where the 0.21nm distance are observed (weak fringes perpendicular to the tube axis mostly visible close to the core of the tube).

Second, two kinds of images, Bright Field (BF) and Annular Dark Field (ADF, High angle –HAADF- or small angle –SAADF-) images, can be recorded with a STEM depending on the collected signal. The former consists in collecting part of the transmitted beam and the latter is the result of collecting the electrons elastically scattered at large angle. Roughly speaking HAADF image is an incoherent image where the spatial resolution is limited by the probe size, while formation of the BF images results from coherent and incoherent processes. In both cases, the spatial resolution is limited by the objective lenses aberrations. Finally, SAADF images display a contrast resulting from both incoherent and coherent processes, thus difficult to interpret. In the dedicated STEM available in Orsay (Figure 4-6), the High Angle Annular Dark Field (HAADF) detector is centred on the optical axis and has a hole in the middle within which the SAADF and the bright detectors sit. The resultant HAADF image is complementary to the BF image. In the HAADF signal, only the high angle elastically scattered electrons contribute. The direct beam is not detected and holes in the sample appear black, as displayed in Figure 4-7A. This figure presents BF and HAADF images of a CN_x nanotube with a compartmentalised structure and Fe metal particles encapsulated in the cavity on the tube. The metal particle is displayed in black in the BF meanwhile it is white in the HAADF. The corresponding images of a cross-section of a CN_x film, Figure 4-7B), show clearly the layered structure. The displayed BF images correspond to coherent and incoherent signals, consequently it is not a trivial process to explain.

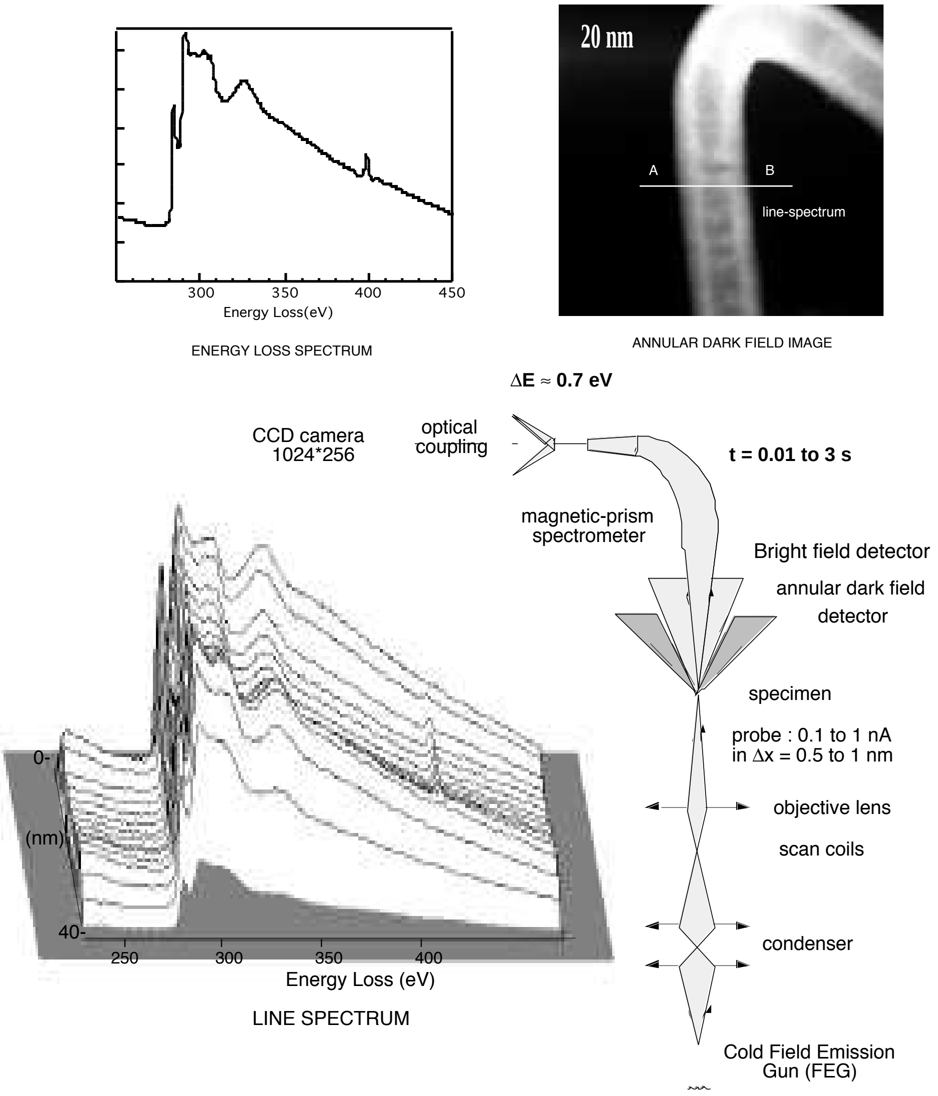

Figure 4-6.- Principle of the dedicated STEM available in Orsay. Microscope scheme, HADF image of a C nanotube containing N_2 gas in the cavity, EELS spectrum exhibiting the characteristic signals of carbon and nitrogen and a 2D plot of a sequence of 100 spectra acquired at 1 nm intervals while the probe is scanned across the tube.

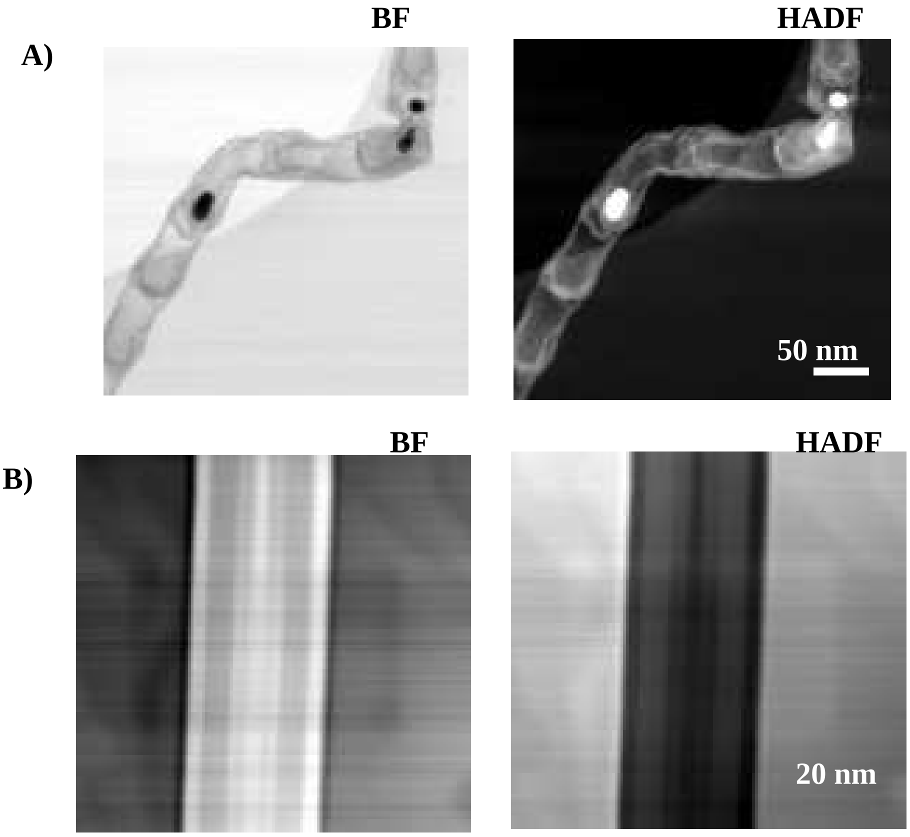

Figure 4-7.- A) BF and HADF images of CN_x nanotubes with encapsulated Fe particles. B) BF and HADF images of a cross sectioned CN_x film.

Apart from displaying a simple contrast to get qualitative information about the morphology of the sample, HAADF images contain quantitative information. The HAADF detected intensity I_{el} is sensitive to the composition (through the cross-section), the thickness and the density of the material as follows [88];

$$I_{el} = I_o \overline{NT} \sigma_{el} \qquad (2)$$

where I_o is the primary beam intensity, NT the average number of atoms per unit area in the analysed volume and σ_{el} the elastic cross-section (which dimension is homogeneous to a surface). When assuming that most ellasticaly scattered electrons are picked by the HAADF detector, the elastic cross-section depends on Z as following [89];

$$\sigma_{\mathbf{el}} = (\mathbf{1.87x10^{-24}m^2})\mathbf{Z}^{4/3}(\mathbf{v/c})^{-2} \qquad (3)$$

where v is the velocity of the incident electron, c is the speed of light in vacuum and Z is the atomic number. When different atoms are present in the analysed area, as it is the case of CN_x materials, Z has to be replaced by Z_{eff} [88]

$$\mathbf{Z_{eff}} = \frac{\sum_{\mathbf{i}} \mathbf{f_i Z_i^{1.3}}}{\sum_{\mathbf{i}} \mathbf{f_i Z_i^{0.3}}} \qquad (4)$$

where fi is the atomic ration and Z the atomic number [88], for example for a film $CN_{0.2}$;

$$Z_{eff} = \frac{0.8*12^{1.3}+0.2*14^{1.3}}{0.8*12^{0.3}+0.2*14^{0.3}} = 12.41 \qquad (5)$$

HAADF signal combined with EELS spectroscopy has been used to fully characterise the modulated CN_x films as it is demonstrated in paper II.

4.4 ELECTRON ENERGY LOSS SPECTROSCOPY

Electron Energy Loss Spectroscopy (EELS) directly studies the primary processes for exciting the electrons of a solid, each of which results in a fast electron losing a characteristic amount of energy. In the EELS spectrometer the transmitted electrons are separated by a magnetic field according to their kinetic energy and an energy loss spectrum is detected on a charge-coupled device (CCD) camera, showing the scattered intensity as a function of the decrease in kinetic energy of the fast electrons.

We can distinguish two kinds of interactions, inner-shell and outer-shell, which are correlated to two types of electronic transitions in the solid and to two energy ranges in the EELS spectrum. The inner-shell electrons (whose ground-state energy lies typically hundreds or thousands of eV below the Fermi level) can make an upwards transition to the unoccupied states, which are above the Fermi Level, if they receive an amount of energy greater than their binding energy. As the total energy is conserved, the fast electron loses an amount of energy equal to that communicated by the inner shell electron and it is scattered at an angle of approximately 1 mrad for a primary energy 100 KeV and an energy loss of 100 eV . These transitions are reflected in the EELS spectrum by the formation of **core edges**, which rise at the corresponding binding energy. Typically the involved binding energies are larger than 50eV.

Single excitations involving outer-shell electrons can also occur. Then the fast electron is scattered through an angle 10 times smaller. Many electrons can also be involved in this kind of transition and a collective excitation of the valence electrons (**plasmon**) takes place. The associated energy loss lie in the range of (0-50eV), this low loss energy region also involves the electrons, which have not interacted with the sample (or whose energy-loss is too small to be detected), i.e. the **zero-loss peak**.

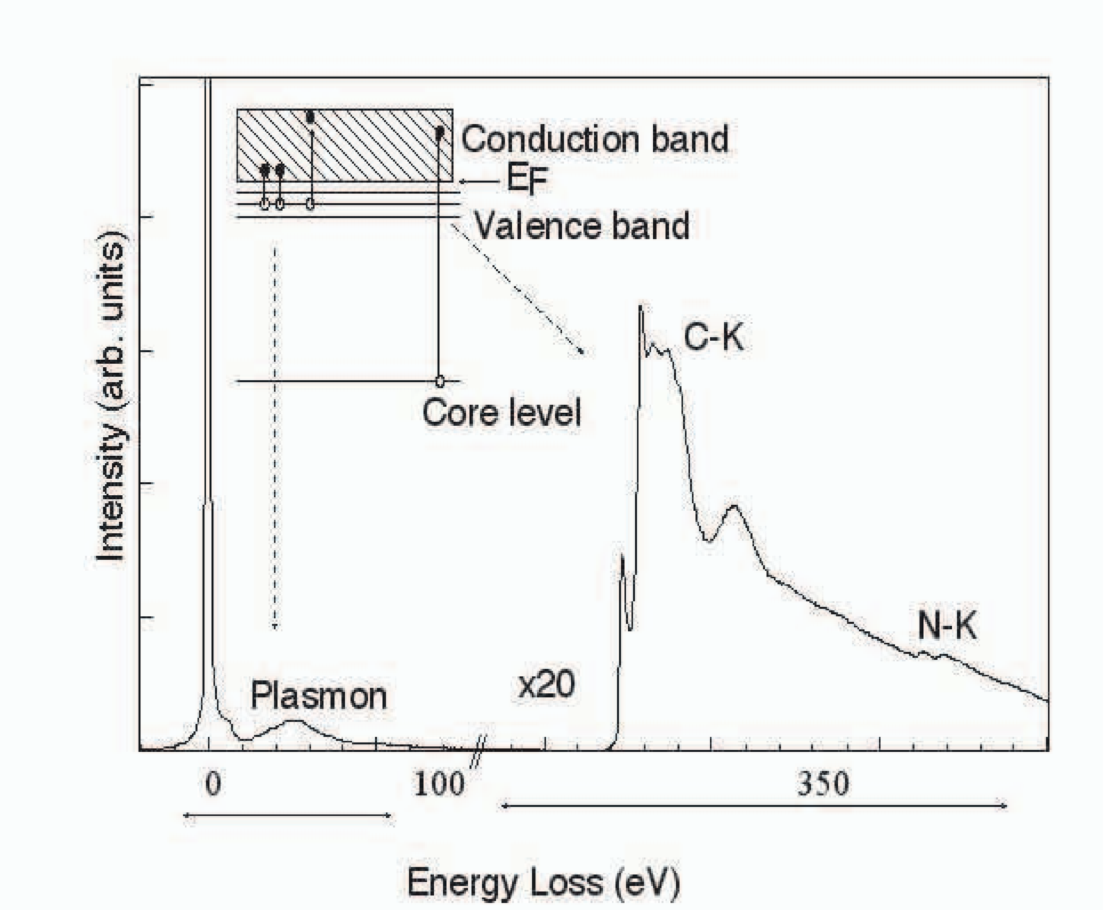

Figure 4-8.- EELS spectrum of a CN material. The different parts of the spectrum as well as the corresponding transitions are displayed.

Figure 4-8, displays a typical EELS spectrum from a CN_x material. Between 0 and 50eV, one observes two plasmon peaks, approximately at the energy found for graphite at 6eV and 25eV. Superimposed on a continuous decreasing background (tail of the plasmon peaks), two element-specific edges (C and N K edges) at higher energy-losses (285.5 eV and 400eV) are present. The observed edges do not display similar shapes. Their general shape is roughly described by an ionisation cross section calculated for an isolated atom. This general shape is further more modulated by the fine structures, which are the signature of solid state effects on the final states. In this example the C and N K edges features show the splitting of the conduction states into two families of energy bands π* and σ*.

4.4.1 ACQUISITION OF A SPECTRUM

EELS can be performed in any transmission electron microscope equipped with a spectrometer. In the STEM, the transmitted electrons from a given area of the specimen are collected and analysed by an EELS spectrometer, which is fixed after the column and consists of a magnetic sector coupled to a detector. The electrons are separated according to their kinetic energy and focused to the detector by the applied magnetic field and the signal is simultaneously recorded using a position sensitive detector of electrons. These detectors are available in the form of a photodiode array (PDA) or CCD. The former was used during the first year of this thesis. However, a series of improvements have been performed in the detector system, and currently a 2D detector (CCD camera, 1024*256) is inserted in the system and coupled to the magnetic sector *via* a pure optical system. Thanks to these improvements the sensitivity of the detector system has increased from 25-30 electrons/count (for the PDA) to 6 counts per one electron (for the CCD camera)[13,90]. This increase in sensitivity has decreased the required acquisition times for achieving a satisfactory signal-to noise ratio on any spectrum and has permitted to perform the first in-situ EELS studies on nanotubes, as it is reflected in papers IV and V. In best conditions, this set-up offers to record spectra with 0.3-0.4 eV energy resolution on the zero-loss peak, 0.7 eV on core edges, from a 0.5 nm diameter probe, within an acquisition time of 10-50 milliseconds for the plasmon region and of 50 milliseconds to 1 second for the core loss region. During EELS acquisition, two different modes of acquiring sequences of spectra have been used: spatially-(spectrum imaging) and time-resolved EELS (chrono-spectroscopy).

4.4.1.1 SPATIALLY RESOLVED EELS

The spectrum-imaging approach (Spatially resolved EELS), first developed in Orsay [91,92], consists in acquiring a series of spectra while the probe is scanned over the sample following a well digitally controlled 1D or 2D pattern. This technique provides an accurate correlation between a spectroscopic information and a specific (sub)nanometer area of the sample defined by the probe size. In the line spectrum mode (1D pattern), the probe is scanned along a predefined line on the specimen. This technique has successfully been used for the characterisation of C nanotubes containing gas (paper V), to mention one spectacular example. Figure 4-9 displays a 2D plot of a sequence of 15 spectra acquired with a 2.5 nm spatial increment while the 0.5 nm probe is scanned across the tube from A to B, as indicated in the inset figure. The characteristic signals of carbon (at 285.5 eV) and nitrogen (at 401.1eV) are observed, demonstrating their presence in the analysed nanotube. The C signal is observed all across the tube while the N signal is only detected in the central part of the tube: the correlation between the EELS spectrum and the ADF image (simultaneously recorded), shows the hollow structure of the nanotube.

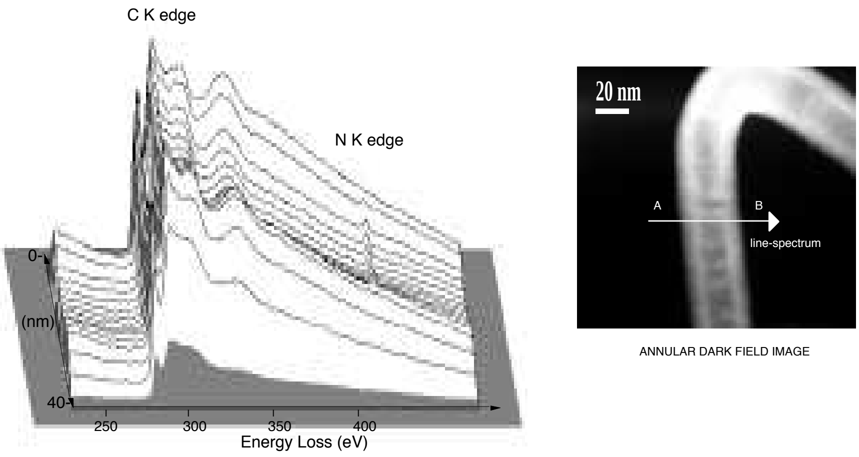

LINE SPECTRUM

ANNULAR DARK FIELD IMAGE

Figure 4-9 .- Sequence of 15 EELS spectra recorded with the spectrum imaging mode, while the electron probe is scanned across the C nanotube from A to B.

Using such a short acquisition time for each spectrum, a high number of spectra can be obtained in a reasonable total amount of time, so that 2D scans from the selected area of the sample can be performed. Using this technique, a 2D scan (32x32 pixels) from a selected area (80nm*80nm) of a SiN nanowire of 20 nm in diameter is presented on Figure 4-10. For each pixel a complete spectrum covering the energy loss domain of interest is acquired. The stored data are further processed to subtract the non characteristic background, following the Egerton method [88], which will be further described in this section. Figures 4-10 show a series of 32x32 chemical images images calculated using the Si L , C K , O K and N K edges. The nanowire is made of a SiN core wrapped with a SiO_2 layer and covered by an amorphous carbon layer.

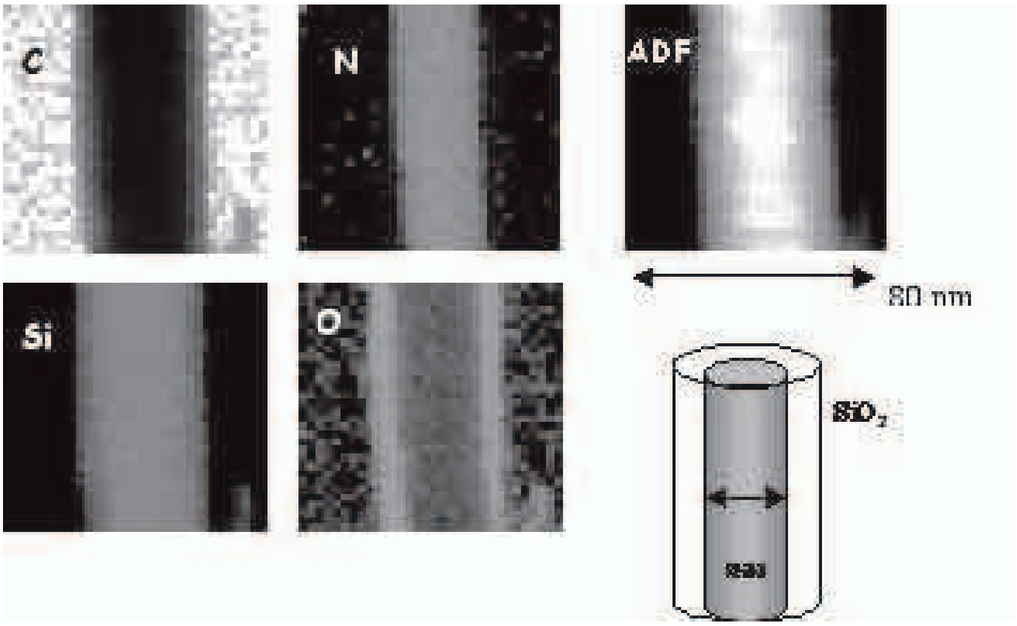

Figure 4-10.- Elemental map (Si, C, N, and O)extracted from a 32*32 spectrum image on a nanowire of 20 nm in diameter.

4.4.1.2 TIME RESOLVED EELS

The chronospectroscopy mode (or Time Resolved EELS) is realised in the spectrum-imaging mode, by maintaining the current in the scanning coils at stable value. Therefore, the electron probe is fixed in a specific position and a series of spectra are acquired as a function of time. This technique had permitted us to monitor the changes occurring in the sample during electron beam irradiation and to perform an in-situ EELS study of material transformation (paper IV and V). Melamine, a CN_x molecule, has been observed to be highly sensitive to electron irradiation as it can be deduced from the time sequence spectra, a bunch of 30 spectra recorded with 90 millisecond intervals, Figure 4-11. The characteristic signals of C and N are present and a strong decrease of the C signal is observed as a function of time. For the N K signal an increase in intensity is detected in the initial part of the sequence, followed by a posterior decrease in intensity and a change of structure, as this will be further explained in paper IV.

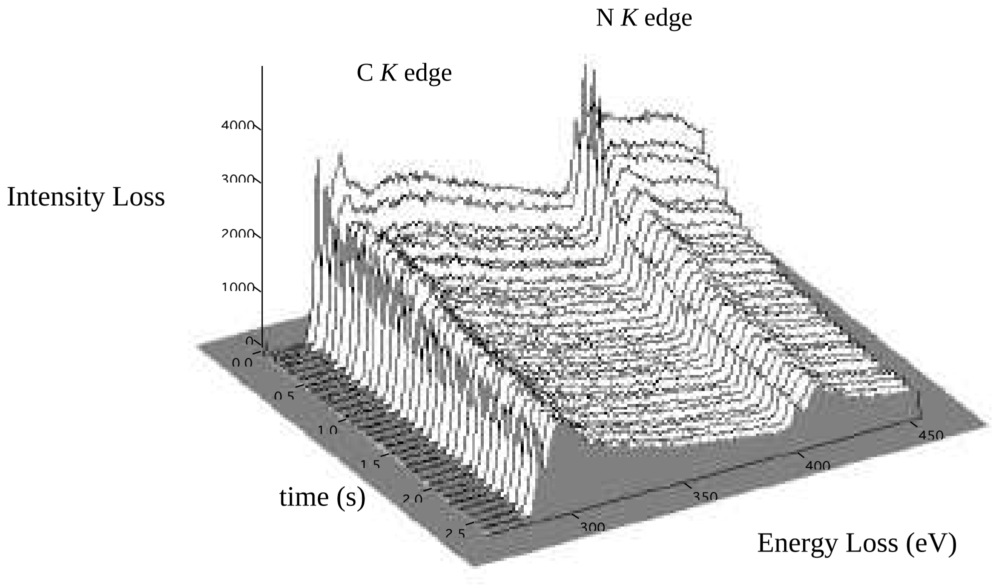

Figure 4-11.- A) Time sequence of 30 spectra in the C K and N K region recorded with 90 milliseconds intervals. The electron probe was fixed on a localised area of the melamine.

4.4.2 INFORMATION TO BE EXTRACTED FROM AN EELS SPECTRUM

The information contained in an EELS spectrum is manyfold and can be extracted after more or less refined spectrum analysis. From the Low loss region, the electronic density of the material can be determined. Moreover, the energy position of a characteristic edge corresponds to the binding energy of a core electron. Therefore, an identification of the elements present in the analysed volume is possible together with the quantification of the edge by measuring an area under the core edge. Finally, considering the fine structures of a core edge, one can also get information about the electronic structure of the analysed sample, such as the unoccupied density of states.

4.4.2.1 LOW ENERGY LOSS REGION

In a condensed material, the assembly of loosely bound electrons behaves as a plasma in which collective oscillations can be induced by a fast external charge, similarly to the case of a metal particle. The oscillations are rapidly damped, having a life time of about 10^{-15} s and are consequently quite well defined in energy . The plasmon-peak is the second most dominating signal in an EELS spectrum, (Figure 4-8), after the zero loss-peak. The energy Ep lost by the electron beam when it generates a plasmon of frequency ω_p is given by;

$$Ep = \hbar\omega_p = \hbar\left(\frac{n_{el}\ e^2}{\varepsilon_o m^*}\right)^{1/2} \qquad (6)$$

where $\hbar$ is Plank's constant , e and m* are the electron charge and effective mass of the electron respectively, ε_o is the permittivity of free space and n_{el} is the free-electron density. As shown in C. Colliex et al **[93]**, reasonable agreement with the experiment is obtained when setting m^* to m_o (the rest mass of the electron) for low atomic mass elements. Therefore, eq 6 can be used to determine the electron density of a determined material, if the plasmon energy is accurately measured. Using this method, the variation in density of the CN_x modulated film has been investigated, paper I. A map of the plasmon energy values Figure 4-12A has been performed by plotting for each pixel the energy of the maximum of the plasmon peak. In such an image, a brighter contrast corresponds to a higher value in the plasmon energy. Since the intensity of the plasmon is not considered, such an image does not suffer from thickness effect. A maximum shift of about 1eV (Figure 4-12B) to lower energy is observed when nitrogen is incorporated in the system. Following the Drude model and relying on the previous assumption ($m^*=m_o$), the 1 eV shift corresponds to a relative decrease of 8% in the density between carbon rich and the CN_x materials (for any CN_x layer of the sample).

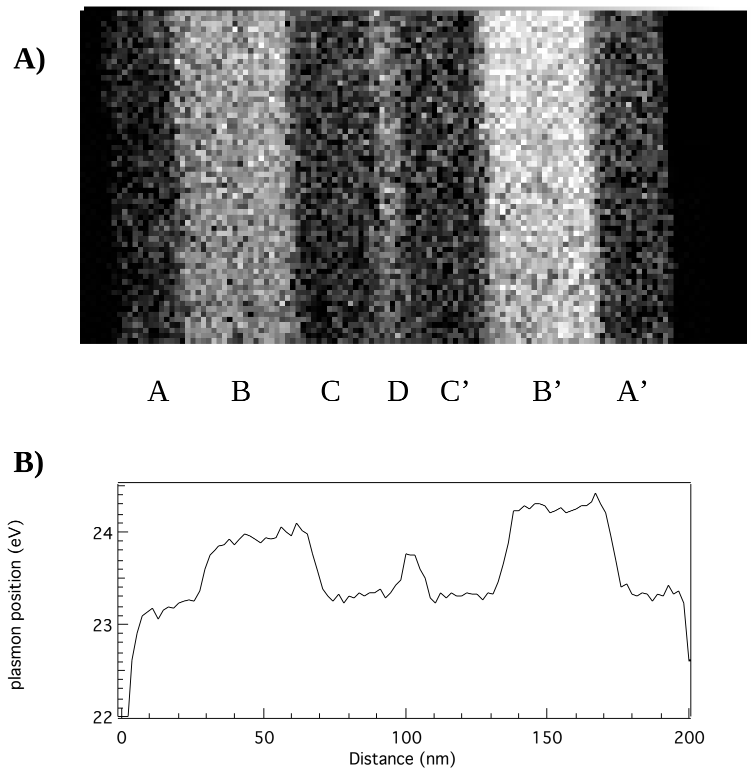

Figure 4-12.- A) Map of the energy position of the plasmon across a modulated CN_x sample. The white value corresponds to the highest peak position. B) Energy position profile of the plasmon peak.

4.4.2.2 CORE LOSS REGION

4.4.2.2.1 Identification and Quantification

The inner shell ionisation edges correspond to the binding energy of the core electrons (c.a. 285 eV for C and 399 eV for N), which permit an identification of the elements present in the sample. These edges are superimposed upon a monotonically decreasing background, which is due to the excitation of core levels of lower binding energy. In order to quantify the edge, the non-characteristic signal (background) has first to be removed.

During the present work, a power law function $F(E) = AE^{-r}$ has been used to match the pre-edge background in a fitting window of c.a. 30eV on the low energy side of the ionisation edge and the function has been posteriorily extrapolated to higher energy.

Once the background is withdrawn, the quantification of the edge is obtained by integrating the core loss intensity over a defined energy window (ΔE). The characteristic signal (S), for a given collection angle (β), is defined as following:

$$S(\beta, \Delta E) = I_0(\beta, \Delta E) N\sigma(\beta, \Delta E) \qquad (7)$$

where Io is the incident beam current and Io (β, ΔE) is the signal encompassing the zero-loss peak, measured over a ΔE window and collected within a β semi-angle acceptance. N is the number of atoms per unit area, σ is the ionisation cross section in the relevant (β, ΔE) conditions [94]. The partial cross section is a measurement of the ionisation probability whereby the fast electron loses energy within an integration energy window (fitting window ΔE) above threshold energy and with scattered angles less than β (collection angle) [95].

$$\sigma_x = \int_0^{\beta} 2\pi d\theta \int_{E_x}^{E_x+\Delta} \left[\frac{\partial^2 \sigma_x(\theta, E)}{\partial\theta \partial E} \right] d\mathrm{E} \qquad (8)$$

where θ is the scattering angle, E is the energy-loss and β is the collection angle. A number of approaches have been used for estimating the partial cross sections. However, all of the used methods concern isolated atoms and they do not predict the near edge fine structure that arise from the distribution of bound states in the solid. Nevertheless, the results provide the best computed estimates for partial and total ionisation cross sections. During the present work, tabulated cross-sections [96] have been used for quantification purpose and the integrated energy window has been carefully chosen so that the fine structures are properly averaged over this energy window.

When more than one element is present in the sample, for example C and N, one is usually interested in measuring relative concentrations of different elements (Figure4-13), thus the N/C ratio is defined by:

$$\frac{\mathrm{N_N}}{\mathrm{N_C}} = \frac{\mathrm{S_N}(\beta, \Delta\mathrm{E})}{\mathrm{S_C}(\beta, \Delta\mathrm{E})} \frac{\sigma_\mathrm{C}(\beta, \Delta\mathrm{E})}{\sigma_\mathrm{N}(\beta, \Delta\mathrm{E})} \qquad (9)$$

Up to now, we have described how to obtain information from an individual spectrum. However the recent developments performed in Orsay have increased the number of acquired spectra (for example an image 50*50 will provide 2500 spectra) and processing adapted routines are necessary to treat the spectra. Some routines are simple extension of the techniques previously developed for processing individual spectra and can be straightforwardly used for providing elemental maps as already shown for an image 30*30 (Figure 4-10).

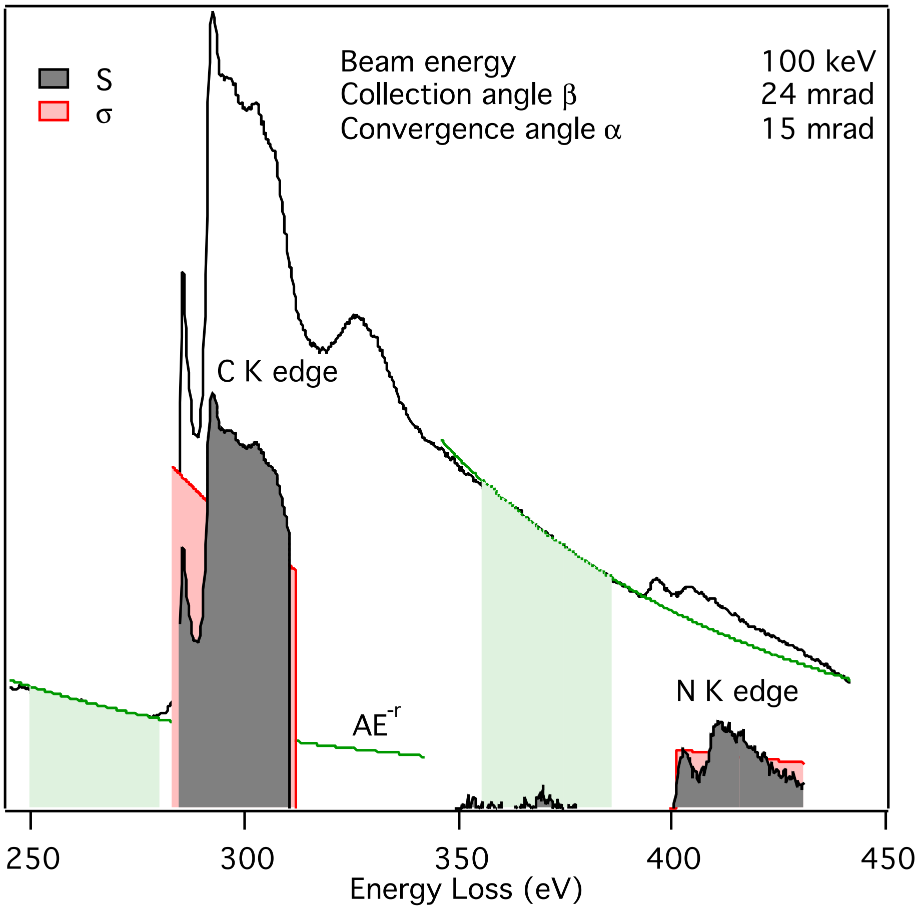

Figure 4-13.-Spectrum from a CN_x nanotube sample recorded at Eo=100 keV. The spectrum has been recorded with a collection angle of 24 mrad and an acquisition time of 3 s. Quantitative analysis of the spectrum provides a N/C ratio of 0.067 ± 0.01.

4.4.2.2.2 Near Edge Fine Structures

As it has been shown in previous sections, the identification and quantification of the elements in the sample and the study of the average electron density of the material can be obtained from an EELS spectrum. Moreover, information about the local electronic structure can also be extracted from the spectrum. The characteristic edges arise from the excitation of inner shell electrons. The basic edges shapes are determined by atomic physics and so are independent of the environment or bonding of the atom. Superimposed on the basic shape, one sees oscillations, often called fine structures, which are strongly dependent on bonding, coordination or nearest neighbour distances. Two areas are defined in the fine structure, strong oscillations up to 20 to 30 eV above threshold called Electron Loss Near Edge Structures (ELNES) and weaker oscillations beyond about 30eV, called the extended fine structures (EXELFS). In this work we will focus our attention onto the ELNES part of the spectrum.

The Near Edge Structure provides information about the bonding configuration in the system. However the interpretation of the ELNES is not trivial. In the simplest case, the useful signal is directly observed in the EELS spectrum and it is identified by comparing the recorded ELNES with fingerprints (reference ones previously acquired from standards) available in the existing libraries [97,98]. For example, this technique has been successfully used in paper V for revealing the presence of N_2 gas in the cavity of the C nanotubes. A comparison between the experimental spectra with those from graphite and N_2 gas, is displayed in Figure4-14.

Following the Fermi golden rule, in the band structure approach, the ELNES intensity can be expressed as [99]:

$$\frac{\partial^2\sigma}{\partial E\partial\Omega} = \frac{8\pi}{a_o^2 q^4}\left|\int \phi_c(r)\exp(i\vec{q}\bullet\vec{r})\phi_v(r)\partial^3 r\right|^2 \rho_c(E) \tag{10}$$

where $\partial^2\sigma$ is the differential cross section, E is the energy-loss, Ω is the solid angle of detection, a_o is the Bohr radius, $\phi_c(r)$ is the conduction band (final state) wave function, ϕ_v (r) is the **core state** (initial state) wave function, $\rho_c(E)$ is the density of **unoccupied states** in the conduction band

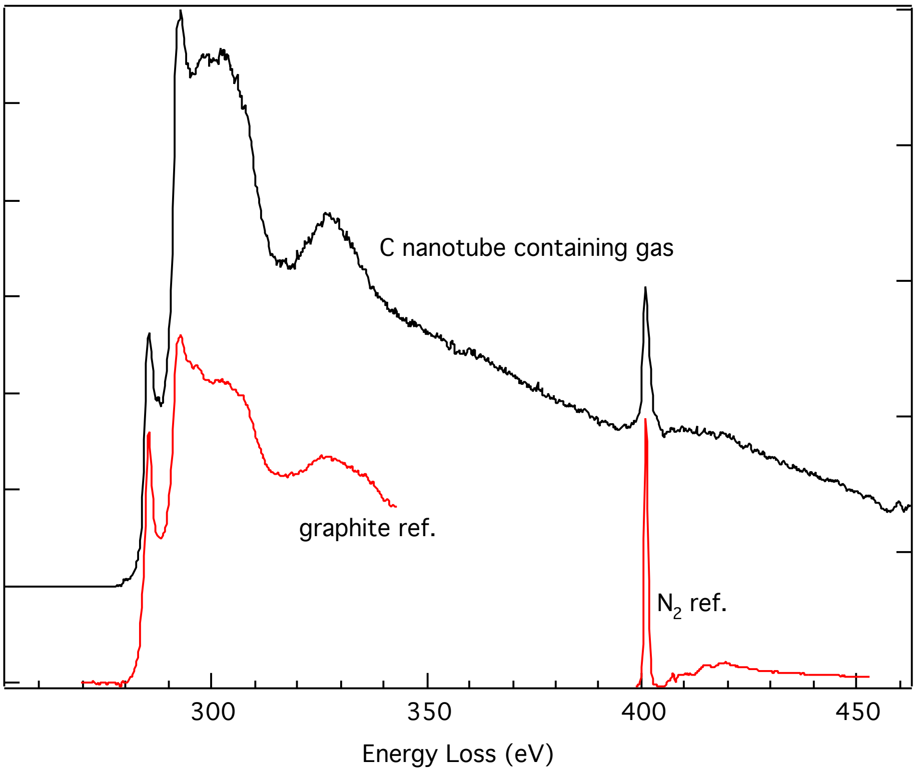

Figure 4-14 EELS spectrum from a carbon nanotube containing N_2 gas, compared to the fingerprints of graphite and N_2 gas found in the libraries of spectra [100,101].

and **q** is the momentum transfer. The initial state is the atomic level and the final state is the appropriate wave function for an empty conduction band state as given by a band structure calculation. Practically in EELS, a cut-off in q values is introduced by the use of an aperture limiting the electron collection at the entrance of the spectrometer. For small $\vec{\mathrm{q}}$, the operator in expression (11) can be developed as:

$$\exp(i\vec{q}.\vec{r}) = 1 + i\vec{q}.\vec{r} - (\vec{q}.\vec{r})^2 + ... \qquad (11)$$

Typically for a 10 mrad collection angle and with 100 keV incident electrons, the maximal $|\mathrm{q}|$ value is 2 Å^{-1} while the distribution of inelastically scattered characteristic electron is ten times smaller with a r value of a fraction of Å, the product remains much below unity. Since the square of the matrix element in (11) is divided by q^4, the contribution of the higher order non-dipole terms ($(\vec{q}.\vec{r})^2 + ...$) is considerably suppressed and the dipole approximation is quite acceptable for apertures up to 20-30 mrad. Therefore for usual experimental conditions, the dipolar approximation is commonly assessed [102]. In other words, the transitions that are involved are vertical transitions ($\mathrm{q} \to 0$) in the band structure. As a matter of fact, core-signals recorded by EELS in a transmission electron microscope are directly comparable to soft X-ray absorption signals.

As the initial state wave functions are confined on the atomic site of the excitation, for a simple understanding of the inelastic cross-section, it is convenient to use wave functions, which are products of radial wave functions and spherical harmonics. The angular integration over the spherical harmonics gives the dipole selection rules for angular momentum quantum number $\ell' = \ell \pm 1$. Then, under common scattering conditions, the intensity in the near-edge region can be re-expressed as:

$$\frac{d^2\sigma}{dEd\Omega} = |M_{\ell-1}(E)|^2 D_{\ell-1}(E) + |M_{\ell+1}(E)|^2 D_{\ell+1}(E) \qquad (12)$$

where $M_{\ell'}(E)$ is a simplified matrix element for transitions to final states with angular momentum ℓ'. $D_{\ell'}(E)$ is the projected density of states (DOS) on a given atomic site and on the final states of ℓ' symmetry. Therefore, in Fermi's golden rule, the matrix elements select the appropriate combination of projected DOS compatible with the dipole approximation. Moreover, $D_{\ell'}(E)$ is a local density of states (LDOS) obtained when the overlap between the localised core state wave function and the final state Bloch wave function is significant (projection on a given atomic site). Therefore, because EELS is a site-selective spectroscopy, there can be noticeable differences in fine structures between edges associated with different elements in the same compound. For example, in figure 4-13 are shown C K and N K edges acquired on a CN_x nanotube. Both C and N edges display a π^* peak at the onset (respectively at 285.5 eV and 400 eV) and a broader σ^* band at higher energy (above 293eV and 405 eV respectively) which attests for the sp^2 bonding between the atoms. However, the intensity of the π^* peak which is related to the number of unoccupied electrons of p_z symmetry on each site is higher on the C edge than on the N edge.

The matrix elements $M_{\ell'}(E)$ in equation (12), can be shown to vary slowly with energy [99]. Their study is interesting in the case of anisotropic materials where valence orbitals are directional. Large changes in their values are to be expected when the direction of the momentum transfer $\vec{q}$ is varied with respect to the direction of the valence orbitals.

Therefore, a core edge can be studied from two points of view:

- Its energy dependence, which gives access to the unoccupied density of states projected on final states of symmetry allowed by the dipole selection rules and on a given atomic site $D_{\ell'}(E)$.

- Its angular dependence (the variations as the momentum transfer $\vec{q}$ is changed in orientation with respect to the crystal) which is governed by the value of the atomic-like matrix elements $M_{\ell'}(E)$.

During this work, we have mostly concentrated on the study of the energy dependence of the ELNES. However, as this will be illustrated briefly in paper III, we have also performed some angular dependence studies on both C K and N K edges recorded on CN_x nanocrystals in order to confirm the anisotropic character of the structure identified by HRTEM and electron diffraction.

In materials where no definite structural hypotheses can be made, as for example amorphous CN materials, the interpretation of the ELNES by relying on band-structure calculation is an extremely difficult and tedious task. An alternative interpretation of the ELNES can be obtained by modelisation of the electronic structure or by using molecular orbitals (MO) theory. The local band structure is approximated as a linear combination of atomic orbitals of the excited atom and its immediate neighbours. This last method has been used to identify the different stages in the decomposition process of the melamine. A series of theoretical spectra has been calculated using the deMon-KS program [103], which is a realisation of the Linear Combination of Gaussian type orbitals (MO solution of the Khon-Sham DFT equations).

4.4.2.2.3 Multivariate Statistical Analysis and Non Negative Linear Square Fiitting (NNLS) analysis

In some cases the experimental ELNES signal is not trivially obtained and sophisticated adapted methods are needed to extract the characteristic signal. Non Negative Linear Square (NNLS) fitting method and Multivariate Statistical analysis (MSA) are some of the available methods.

NNLS is a Multiple Least Square (MLS) fitting method, which consists in simulating the experimental ELNES as a linear combination of weighted elemental reference components. The ELNES references can be calculated or may also come from experimental spectra recorded on standards [104]. It is extremely important to well select the reference signals : identical instrumental recording conditions and same thickness are required. During the present experiment, the reference signals have been recorded within the spectrum image of interest, which insures the identical instrumental conditions. A MLS approach which constraints of positiviness (i. e. in the final result the weight of an element can not be negative) has been used for the fitting process.

During the present work this method has been used to localise the signal of a new ELNES profile detected in a C nanotube. A spectrum image of 50*10 pixels (EELS and HAADF signals are acquired for every pixel with a spatial interval of 0.8nm) has been recorded from an area of a nanotube where defects are present (Figure 4-15A, B). The references corresponding to graphite, amorphous C and a new ELNES, Figure 4-15, have been used for the NNLS analysis. This new ELNES could be associated to the signature of defects in the graphitic structure. The presence of a pentagon is a highly probable hypothesis. In Figure 4-15D the NNLS images corresponding to the location of the different signals, pentagon graphite and amorphous C, are displayed. As it can be observed from the images, only one spectrum corresponds to the signal of a “pentagon”. We mention that with a finer sampling, the signature of the pentagon would occur on different adjacent spectra.

The NNLS method is quite efficient but its main limitation is due to the lack of freedom in the choice of the reference spectra. On the contrary, MSA treats the data as a whole and does not make any a priori hypothesis on the choice of the reference signals. The goal of this method is to identify several basis sources of information as contributing (through linear combination) to the overall experimental data [105]. MSA is a statistical method, which aims to analyse the variance and covariance of a multidimentional data set.

The first part of this method consists in performing an eigenvalue decomposition of the experimental matrix $X_{nj.}$ In such a matrix, the lines are the spectra number i=1,... n and the columns are the energy channels. The eigenvectors constitute a new representation space of the data set and the number of significant eigenvalues (K<N) corresponds to the number of sources of information or degrees of freedom. Once the eigenvectors and eigenvalues are obtained they have to be carefully analysed in order to know how many independent sources of information are present and therefore how many components (eigenvalues K) have to be consider for further information. Different tools are available for this purpose. One way to get an idea on the number of really useful components is to display the reconstituted spectra obtained with a varying number of components, and to compare the reconstituted spectra to the experimental one. A variant consists of visualising the difference between original and reconstituted spectra.

The first step of MSA assumes that any experimental spectrum can be considered as a linear combination of a few basic spectra which are orthogonal to each other, therefore it prevents from any possibility to identify an unknown spectrum. Thus a second step is needed. It consists in moving from a space by spanned orthogonal eigenspectra to a space spanned by non-orthogonal reference spectra. This step is called oblique analysis and consists in defining a rotation matrix, which can be easily obtained via least square procedure. In order to perform correctly this part of the analysis, some additional knowledge about the analysed sample are required.

Using this technique the fine structures relative to the different stages in the local transformation of carbon nanotubes containing N_2 under the beam have been extracted. This is illustrated in Figure 4-16. The global acquired data as a function of time are shown in Figure 4-16A, each line of the image corresponds to an EELS spectrum. Figure 4-16B shows the different ELNES obtained from the MSA analysis, their distribution as a function of time is also plotted, Figure 4-16C.

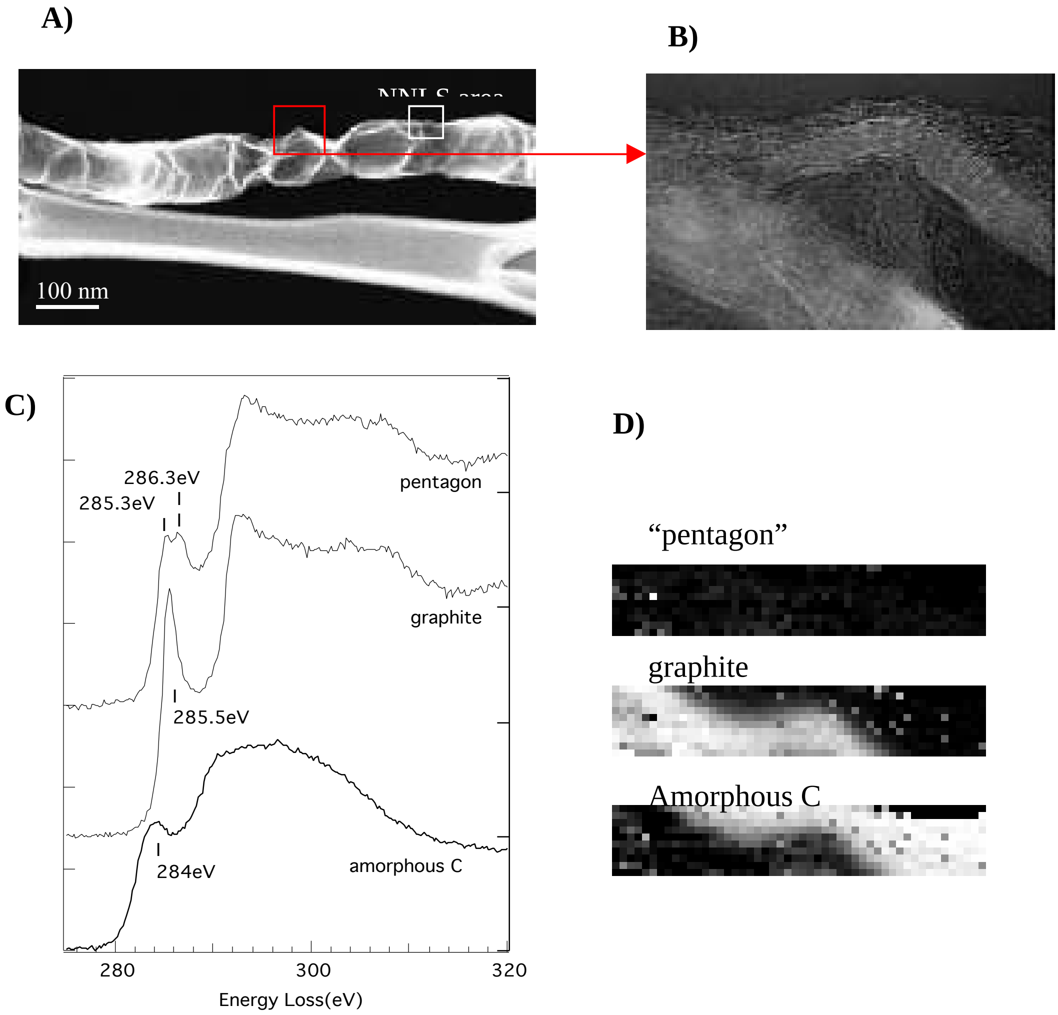

Figure 4-15 A) HAADF and HRTEM B) images of a C nanotube, which present a high number of defects. C) ELNES references used for the NNLS analysis. D) "pentagon", graphite and amorphous C map.

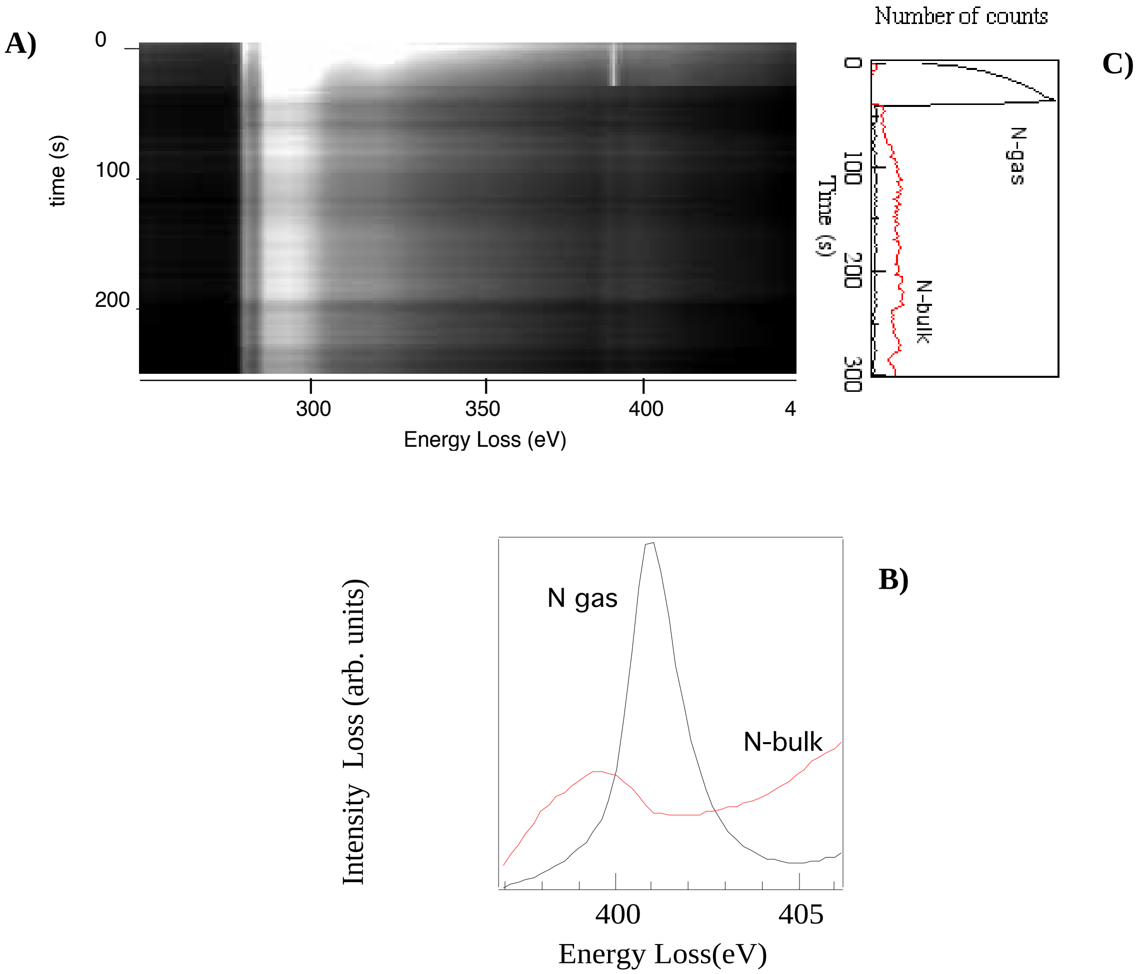

Figure 4-16.- A) EELS signal as a function of time obtained from a C nanotubecontaining gas in the cavity. B) The two components (ELNES) obtained from the MSA analysis. C) Time dependence profile of N K ELNES obtained from the MSA treatment.

5 RESULTS-SUMMARY OF THE PAPERS

The results obtained during this thesis work have been reported in six publications, which are summarised in the present chapter. In all of them my personal contribution has been dominant and I have detailed it when necessary. The first two papers deal with the synthesis process and characterisation of different of CN_x materials, films and nanotubes. Paper III, reports the identification of CN_x nanocrystals embedded in an amorphous matrix. Finally, paper IV and V are the result of in-situ EELS analysis. The former describes the decomposition process of melamine under electron beam irradiation as well as the identification of the different decomposition stages by exploring the NES. In the latter, a new nanotube morphology, nanotubes containing nanocapsules, is reported. Moreover, using time-resolved analysis, the transformations produced in the carbon nanotubes when a high-energy electron beam is focused on it, is monitored and simultaneously analysed. Paper VI is a review of the different EELS studies on carbonaceous materials performed in the Laboratoire de Physiques des Solides by the different members of the group, and the part of the results obtained in CN_x materials, which I am responsible for, has been included.

5.1 PAPER I "Modulated CN_x Films Prepared By Ion Beam Assisted Deposition"

This paper is the result of the strong collaboration between the different groups of the TMR network "Synthesis, structure and properties of new carbon based hard materials". The CN_x samples were produced at the Institute of Rossendorf, using IBAD and the characterisation task was performed using the different techniques available in the network, TEM, Energy Dispersion X-ray

(EDX), Elastic Recoil Detection Analysis (ERDA), Auger depth profiling and EELS. My contribution to this paper has consisted in performing and analysing the characterisation of the film using EELS spectroscopy (section 3.2.4 and 4.2 of paper I). I have also participated in the writing of the manuscript.

Modulated CN_x samples have been produced by IBAD, the different characterisation techniques have confirmed their modulated structure. A direct evidence is a modulation in the TEM image contrast. However many parameters can participate to this contrast variation. The feasibility of performing simultaneously measurements of the HAADF signal and Spatially Resolved EELS (in the low and core loss region) has provided an essential information to confirm such a modulation and to correlate it to the control of the deposition parameters.

Spatially Resolved EELS in the core loss region of the spectra, figure 4-paper I, has been used to determine the composition and bonding configuration in the sample. The darker layers observed in the bright field image correspond to amorphous-like C, while the brighter layers present a N/C ratio which varies from 0.26 in layers A, C and C' to 0.17 in layer A'. The C K edge from the C layers contains a π^* peak at 284 eV and a σ^* band. Similar features are observed for the σ^* band in the CN_x layers, however the π^* peak exhibits a contribution of and extra peak at 285.5eV, which could be assigned to C-N bonds. The N K NES are similar to those observed in CN_x films [59].

From the low-loss region of the spectra, Figure 5-paperI, the variation in density is estimated using the Drude model. The shift of 1 eV observed in the plasmon energy position between the carbon and CN_x layers, corresponds to a relative decrease in the density of 8% between pure C and CN_x material (for any CN_x layer of the sample).

To conclude, the variation observed in the HAADF image contrast, can be explained considering the density changes between layers B and C. However the abrupt thickness variation between C and CN_x layers after the beam erosion has to be taken into account in order to explain the strong contrast variation observed between A and B layers.

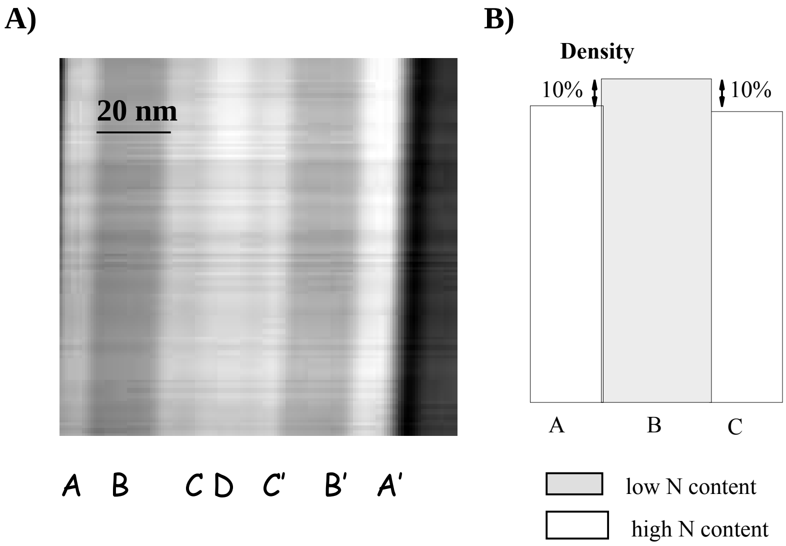

Figure 5-1 A) Bright field image of the modulated CNx sample, showing the contrast variations. B) Schematic diagram explaining the contrast variation in terms of density and thickness contributions.

5.2 PAPER II, "Compartmentalised CN_x Nanotubes; Chemistry, Morphology And Growth Process"

As it has been previously described in chapter 2, different synthesis methods can be used to produce CN_x nanotubes. However, it is difficult to incorporate a high amount of N in the nanotube structure and a systematic study of the incorporation process is still lacking. In this paper, the effect of the different synthesis parameters on the incorporation of N into carbon nanotubes produced by catalytic pyrolysis is reported. As a result, a growth mechanism for such structures is proposed and a comparison of the results with those previously reported is also carried out.

The highly compartmentalised morphology with a remarkable periodicity structure all along the nanotube present in the CN_x nanotubes produced by catalytic pyrolysis of melamine, is first demonstrated. The spectrum imaging mode indicates that the nanotubes are made of carbon and nitrogen inhomogeneously distributed with an enrichment of carbon in the external surface. The evolution of the C K ELNES across the nanotube reveals the existence of a transition from a graphitic stacking on the outside to a disorganised mixed type in the core of the nanotube. For the N K edge, the situation is more complex. The fine structure of the N-K edge is different depending on the used catalyst, which indicates differences in the bonding configuration. When Ni is used as a catalyst, the N K edge exhibits a broadened π^* peak (401-404eV) and an asymmetric σ^* band (408eV) with a triangular shape independently on the N content. However, when the catalyst is Fe, a sharp π^* peak at lower energy (398 eV) and a highly asymetric σ^* band (above 404eV) are observed. Comparing our results with the theoretical and experimental reported values, we suggest that in the produced nanotubes, N is substituting C in the graphitic structure when Ni is used as a catalyst, while C-N pyridinic like bonds are formed when the catalyst is Fe.

The compartmentalised periodic morphology is the result of a systematic movement of the catalytic particle from the root of the nanotube to the up-top tip. This displacement is defined by the nature of the catalyst (Fe or Ni), diffusion and supersaturation (C/N) in the liquid particle and the precipitation process. The differences in the N incorporation process can be explained by the differences in the diffusion process. Carbon or/and Nitrogen both diffuse through the Fe catalytic particle while only C diffuses through the Ni particle.

5.3 PAPER III, "Isolating and Identifying the ELNES Signal of CN Nanocrystals"

This paper describes the identification of CN nanocrystals (*c.a.* 10 nm in size) embedded in an amorphous matrix, using EELS spectroscopy, HRTEM and electron diffraction. In such complex samples where different phases are simultaneously present, we show that spatial resolved EELS combined with sophisticated data processing methods are necessary to isolate the characteristic signature of the nanocrystal. The observed structure does not correspond to any previous reported C_3N_4 or CN structures. Therefore, a new type of CN crystalline structure is suggested.

5.4 PAPER IV, "A Route To Study The Carbon-Nitrogen Bond: Chrono-Spectroscopy In Melamine"

The above-described papers are the result of using Spatially Resolved EELS. This paper is the first of a series of two, which use Time Resolved EELS as an in-situ analysis technique.

Melamine is extremely sensitive to radiation damage under high-energy electron beam irradiation and the observed changes in the ELNES permit to monitor their decomposition process. However, the obtained ELNES needs theoretical simulations for their identification. Thus, a collaboration with the quantum chemistry group at the University of Stockholm was initiated and this paper is the result of the good interchange of information between the theoreticians and experimentalists. My contribution to this paper has consisted in performing the Time Resolved EELS. I have also written most of the paper.

Using chronospectroscopy, the total and partial (C and N) rates of mass losses have been measured and the different ELNES exhibited during the decomposition process have been acquired. Then, using "deMonde" code, the calculated ELNES of different molecules have been compared to the experimental ones. This comparison suggests the following decomposition pathway. At the first stage of the decomposition process, N atoms from the amino groups connected to the ring are eliminated as N_2 gas and an intermediate product is formed. Then a reduction of the carbon-nitrogen double bonds takes place either through addition of hydrogen or through bond cleavage.

5.5 PAPER V, "Electron Beam Puncturing Of Carbon Nanotube Containers For Release of Stored N_2 Gas"

The most important results have been obtained by using a combination of the spatially and time resolved EELS. These results constitute the first evidence of trapping a gas in the cavity of a nanotube during the synthesis process. They further demonstrate how the electron beam can be simultaneously used to modify the carbonaceous specimen and to monitor the associated chemical and electronic changes. The samples were prepared by W.K. Hsu at the University of Sussex.

The pyrolysis of an organic precursor free of nitrogen, camphor, in the presence of a N-rich (N_2/NH_3) gas, provides carbon nanotubes containing nitrogen gas encapsulated in nanocontainers regularly distributed along the tube axis, as revealed by spatially resolved EELS. Time resolved EELS (chronospectroscopy mode) has been used in order to assess the stability of the nanotube structure under the electron beam. We have found that the beam is able to puncture the tube walls, thus partly releasing N_2 gas, while the tube wall structure is gradually changing. Moreover if the radiation is sufficiently long, N can be reincorporated into the walls to form regularly distributed C-N nanodomains in the nanotube structure.

5.6 PAPER VI, "Spatially Resolved EELS on Carbon-Based Nanostructures"

This paper is a review of the different researches on EELS in carbonaceous materials, carried out at the Laboratoire de Physique des Solides by the different members of the group. This review was written by C. Colliex and was the subject of a 3-hour course at the NATO school "Nanostructured carbon for advanced applications", in Erice, July 2000. In section 4 of the paper, part of the work, which I have realised during my thesis preparation, has been reported.

6 CONCLUSIONS AND PERSPECTIVES

Theoretical studies have proposed that the crystalline β-C_3N_4 compound could exist and behave as an ultra-hard material presenting high thermal conductivity and useful electrical and optical properties [1, 2]. Different synthesis routes have been attempted to produce such an exciting compound. However, only a few experimental studies on CN films show crystallites embedded in amorphous CN films. Moreover the observed N/C ratio is still far from that of the predicted C_3N_4. Further work on production and characterisation of CN_x material is needed in order to understand the N incorporation process in the C network.

Therefore, our work intended to explore alternative routes for synthesising different morphologies, like thin films or nanotubes, of carbonaceous materials with a high concentration of nitrogen. The major emphasis of the present dissertation has been to use and adapt the most recent developments in spatially and timely resolved Electron Energy Loss Spectroscopy (EELS), in the context of a Scanning Transmission Electron Microscope (STEM), to characterise the topography, structure, chemistry and electronic properties of the grown specimens. In particular the chemical composition of complex objects has been worked out at a subnanometer level, indicating various processes for insertion of nitrogen into carbon-based materials (as substitution in disorganised arrays, as gas in compartmentalised nanotubes, as CN nanocrystals embedded within an amorphous matrix).

CN_x films

The combination of EELS measurements, either in the low loss or core loss region, with the High Annular Dark Field signals (HADF) detection has permitted us to confirm the modulated-layered (C/CN_x) structure observed in the films prepared by Ion Beam Assisted Deposition. Above all, we have pointed out the density changes between the C and CN_x layers; the CN_x layer presenting the highest porosity (at least 8% increase in density is observed). Consequently the studied CN_x films have a loose structure which is far from the compact structure expected for ultra-hard materials. This specific property has been confirmed by other groups of the TMR network. By performing nano-indentation measurements in the CN_x modulated films a high elasticity has been found. This unexpected mechanical property and the fact that the samples present a modulated layered structure make this material a good candidate as shock absorbent. In the future we could imagine modifying the mechanical properties of these amorphous materials by including CNx nanocrystals in the matrix. Some attempts of preparing this material have already been shown in the present dissertation, CN_x nanocrystals were embedded in an inhomogeneous amorphous matrix. Further work is needed to control the structure and composition of the matrix and to well-determine the mechanical properties of the prepared material.

CN_x nanotubes

CN_x nanotubes can be synthesised using different synthesis methods, chemical vapour deposition, electron cyclotron, and pyrolysis to name some examples. During this dissertation a systematic study of the production of CN_x nanotubes by catalytic pyrolysis has been performed. The fundamental aspect of this synthesis process is the thermal decomposition of the organic precursor. Therefore a detailed study of the decomposition process of the organic precursor could be a preliminary stage to understand the growth mechanism of such nanostructures. In this context, we have attempted to identify the different stages in the decomposition process of melamine (organic precursor already used for the production of nanotubes). As a result, we suggest that the amino groups are first eliminated as a release of N_2 gas. Then the degradation of the molecule occurs through a reduction of the carbon-nitrogen double bonds either by addition of hydrogen or by bond cleavage. If the irradiation is maintained over longer periods, the formation of different CN fragments and of extended triazine rings could then be possible. This study did not provide a significant outcome for the growth mechanism of the nanotubes due to the absence of the catalyst but it provided the important result about CN_x materials: N tends to be easily eliminated from a CN_x structure as a release of N_2 gas.

Three parameters are critical in the incorporation process of N into the nanotube structure (the nature of the catalyst, the organic precursor and the gas porter -nature and flux-). From a systematic study of the influence of different pyrolysis parameters on the N incorporation into the C system, we have found the following results;

- We have confirmed the difficulty of incorporating N in the C nanotube. This difficulty was previously observed in the CN_x films.
- We have shown that CN_x nanotubes are produced when a N rich organic precursor is pyrolysed in Ar atmosphere while nanotubes containing N_2 gas are the product of the catalytic pyrolysis of a N free organic precursor in a N rich atmosphere (N_2/NH_3). Moreover it has been shown that performing the experiment in a N_2 atmosphere does not improve the N content in the nanotubes, instead pure C nanotubes are produced whatever the organic precursor is (melamine or camphor). These results suggest that the growth process preserves at least some of the pre-existing C-N bonds when the precursor contains nitrogen atoms. Moreover it

is not possible to create C-N bonds from ab-initio separated carbon and nitrogen atoms in the studied experimental conditions.

- We have pointed out that the incorporation process is different as a function of the used catalyst. Most specifically, two types of C-N bonds have been identified for Ni and Fe, which correspond to two different growth mechanisms.

Finally, an important outcome from this dissertation is the synthesis of new nanotube morphologies;

- Compartmentalised nanotubes with a remarkable periodicity are produced by catalytic pyrolysis of melamine in an inert atmosphere. The origin of this compartment is not yet identified, however we can suggest that this morphology is the result of a systematic catalytic particle movement from the root of the nanotube to the up-top tip.
- Nanotubes containing nanocapsules, where N_2 gas is trapped, are produced by catalytic pyrolysis of camphor in a nitrogen rich atmosphere.

Nowadays different points about the growth mechanism are still far from be clarified. A new series of experiments needs to be carried out in order to test the reproducibility of the synthesis of a compartmentalised structure. It is important to check if this structure is formed whatever the organic precursor and gas. These experiments, apart from helping to understand the origin of such structure will tend to clarify the origin of the incorporation or non miscibility of N in the C system.

As for the applications, this thesis has reported the first experimental evidence of trapping gas in the C nanotubes during the synthesis process, without posterior treatment. Therefore, this synthesis opens a new field in the application of C nanotubes, the utilisation of C nanotubes for storage of gas or liquids. Moreover, it has been reported that CN_x nanotubes are more conducting than C nanotubes, thus these CN_x nanotubes could shown higher performance as field emitters.

Towards an active microscope

This dissertation has shown the efficiency of different characterisation techniques for exploring with a subnanometric probe the structural, chemical and electronic properties of the materials. In this way, the production of CN_x samples produced by new synthesis techniques can be controlled.

The recent developments in parallel detection have opened new possibilities for monitoring in real time at the 10^{-2} s level, the dynamics of the electron radiation effects on molecular precursors and on selected nanostructures. Using a combination of chronospectroscopy and ab initio calculations, we have identified the different stages in the decomposition process of melamine. Moreover we have shown that the electron beam can be used for drilling the nanocapsules present in the C nanotubes, for releasing the N_2 gas and for creating CN_x nanodomains by incorporation N in the amorphous matrix.

These two examples demonstrated the possibility of performing local nano-transformations in different materials. Moreover the transformations were controlled and monitored by simultaneously recording of EELS measurements. Consequently, these results pave the way for transforming the electron microscope from a passive into an active machine. In other terms, the general conception of the instrument is quite well suited to the selection, observation and characterisation of unique isolated nano-objects, during in-situ experiments: irradiation with the primary electron beam or with an external photon beam, heating over different temperature ranges, controlled strain during in-situ deformation. All these considerations should convince us that all conditions are now gathered for the future STEM microscopes to be run as nano-laboratories.

7 REFERENCES

1. Liu, A. Y. and Cohen, M. L. *Science*, **245**, 841 (1989).
2. Cohen, M. L. *Materials Science &Engineering A*, **209**, 1 (1996).
3. Li, D., Lin, X., Dravid, V. P., Chung, Y.-W., Chen, M. Y., Wong, M.-S. and Sproul, W. D. *Diamond Films and Technology*, **4**, 99 (1994).
4. Haller, E. E., Cohen, M. L., Hansen, W. L. and Creek, W. (The Regents of the University of California, Berkeley, Calif, U.S. Patent, 1992).
5. Wang, E. G., Chen, Y. and Guo, L. *Phys. Scr. T*, **69**, 108 (1997).
6. Wang, T. S., Yu, D. L., Tian, Y. J., Xiao, F. R., He, J. L., Li, D. C., Wang, W. K. and Li, L. *Chemical Physics Letters*, **334**, 7 (2001).
7. Yen, T.-Y. and Chou, C.-P. *Applied Physics Letters*, **67**, 2801 (1995).
8. Sjöström, H., Stafström, S., Boman, M. and Sundgren, J.-E. *Phys. Rev. Lett.*, **75**, 1336 (1995).
9. Miyamoto, Y., Cohen, M. L. and Louie, S. G. *Solid State Communications*, **102**, 605 (1997).
10. Sung, S. L., Tsai, S. H., Liu, X. W. and Shih, H. C. *Journal of Materials Research*, **15**, 502 (2000).
11. Niu, C., Lu, Y. Z. and Lieber, C. M. *Science*, **261**, 334 (1993).
12. Marton, D., Boyd, K. J., Al, B. A. H., Todorov, S. S. and Rabalais, J. W. *Phys. Rev. Lett.*, **73**, 118 (1994).
13. Suenaga, K., Tence, T., Mory, C., Colliex, C., Kato, H., Okazaki, T., Shinohara, H., Hirahara, K., Bandow, S. and Iijima, S. *Science*, **290**, 2280 (2000).

14. Suenaga, K., Stephan, O., Colliex, C., Willaime, F., Pascard, H., Demoney, N. and Loiseau, A. *Electron Microscopy and Analysis Institute of Physics Conferences Series*, **153**, 375 (1997).

15. Kroto, H. W., Heath, J. R., O'Brien, S. C., Curl, R. F. and Smalley, R. F. *Nature*, **318**, 162 (1985).

16. Iijima, S. *Nature*, **354**, 56 (1991).

17. www.britannica.com.

18. Suenaga, K., Colliex, C., Demoncy, N., Loiseau, A., Pascard, H. and Willaime, F. *Science*, **278**, 653 (1997).

19. Bockrath, M., Cobden, D. H., Lu, J., Rinzler, A. G., Smalley, R. E., Balents, T. and McEuen, P. L. *Nature*, **397**, 598 (1999).

20. Yao, Z., Postma, H. W. C., Balents, L. and Dekker, C. *Nature*, **402**, 273 (1999).

21. Kociak, M., Kasumov, A. Y., Guéron, S., Reulet, B., Khodos, I. I., Gorbatov, Y. B., Volkov, V. T., Vaccarini, L. and Bouchiat, H. *Physical Review Letters*, **86**, 2416 (2001).

22. Kasumov, A. Y., Deblock, R., Kociak, M., Reulet, B., Bouchiat, H., Khodos, I. I., Gorbatov, Y. B., Volkov, V. T., Journet, C. and Burghard, M. *Science*, **284**, 1508 (1999).

23. Treacy, M. M. J., Ebbesen, T. W. and Gibson, J. M. *Nature*, **381**, 678 (1996).

24. Dai, H. J., Hafner, J. H., Rinzler, A. G., Colbert, D. T. and Smalley, R. E. *Nature*, **384**, 147 (1996).

25. Dresselhaus, M. S., Dresselhauss, G. and Eklund, P. C. *Science of Fullerrenes and Carbon nanotubes* (Academic Press Limited, London, 1995).

26. Okano, K., Koizumi, S., Silva, S. R. P. and Amaratunga, G. A. J. *Nature*, **381**, 140 (1996).

27. Show, Y., Matsukawa, T., Ito, H., Iwase, M. and Izumi, T. *Diamond and Related Materials*, **9**, 337 (2000).

28. Kim, D. P., Lin, C. L., Mihalisin, T., Heiney, P. and Labes, M. M. *Chemistry of Materials*, **3**, 686 (1991).

29. Glenis, S., Nelson, A. J. and Labes, M. M. *Journal of Applied Physics*, **80**, 5404 (1996).

30. dos Santos, M. C. and Alvarez, F. *Physical Review B*, **58**, 13918 (1998).

31. Faiman, D., Goren, S., Katz, E. A., Koltun, M., Melnik, N., Shames, A. and Shtutina, S. *Thin Solid Films*, **295**, 283 (1997).

32. Hummelen, J. C., Knight, B., Pavlovich, J., Gonzalez, R. and Wudi, F. *Science*, **269**, 1554 (1995).

33. Praddep, T., Vijayakrishnan, V., Santra, A. K. and Rao, C. N. R. *Journal of Physical Chemistry*, **95**, 10564 (1991).

34. Huczko, A. *Fullerene Science and Technology*, **5**, 1091 (1997).

35. Haffner, S., Pichler, T., Umlauf, B., Friedlein, R., Golden, M. S., Fink, J., Keshavarz-K, M., Bellavia-Lund, C., Sastre, A., Hummelen, J. C. and Wudl, F. *European Physical Journal B*, **1**, 11 (1998).

36. Stafström, S., Hultman, L. and Hellgren, N. *Chem Phys. Lett*, **340**, 227 (2001).

37. Niu, C., Lu, Y. Z. and Lieber, C. M. *Science*, **261**, 334 (1993).

38. Yu, K. M., Cohen, M. L., Haller, E. E., Hansen, W. L., Liu, A. Y. and Wu, I. C. *Physical Review B*, **49**, 5034 (1994).

39. Mattesini, M., Matar, S. F. and Etourneau, J. *Chemistry of Materials*, **10**, 709 (1999).

40. Liu, A. Y. and Cohen, M. L. *Phys. Rev. B (Condens. Matter)* , **41**, 10727 (1990).

41. Teter, D. M. and Hemley, R. J. *Science*, **271**, 53 (1996).

42. Ortega, J. and Sankey, O. F. *Phys. Rev. B (Condens. Matter)* , **51**, 2624 (1995).

43. Alves, I., Demazeau, G., Tanguy, B. and Weill, F. *Solid State Communications*, **102**, 605 (1999).

44. Montigaud, H., Tanguy, B., Demazeau, G., Alves, I., Birot, M. and Dunogues, J. *Diamond and Related Materials*, **8**, 1707 (1999).

45. Teter, D. M. and Russel, J. H. *Science*, **271**, 53 (1996).

46. Liu, A. Y. and Wentzcovitch, R. M. *Phys. Rev. B*, **50**, 10362 (1994).

47. Wang, E. G., Chen, Y. and Guo, L. in *17th Nordic Semiconductor Meeting* (ed. Chinese Acad. Sci., B., China) (Trondheim, Norway, 1996).

48. Hellgren, N., Johansson, M. P., Broitman, E., Hultman, L. and Sundgren, J.-E. *Phys. Rev. B*, **59** (1999).

49. Snis, A. and Matar, S. F. *Phys. Rev. B.*, **60**, 10855 (1999).

50. Mattesini, M. and Matar, S. F. *Phys. Rev. B* , **in press** (2001).

51. Guo, L. P., Chen, Y., Wang, E. G., Li, L. and Zhao, Z. X. *Chemical Physics Letters*, **268**, 26 (1997).

52. Kim, E., Chen, C., Köhler, T., Elstner, M. and Frauenheim, T. *Phys. Rev. Lett.*, **86**, 652 (2001).

53. Sandré, E., Pickard, C. J. and Colliex, C. *Chemical Physics Letters*, **325**, 53 (2000).

54. Stephan, O., Ajayan, P. M., Colliex, C., Redlich, P., Lambert, J. M., Bernier, P. and Lefin, P. *Science*, **266**, 1683 (1994).

55. Sen, R., Satishkumar, B. C., Govindaraj, A., Harikumar, K. R., Raina, G., Zhang, J. P., Cheetham, A. K. and Rao, C. N. R. *Chemical Physics Letters*, **287**, 671 (1998).

56. Terrones, M., Grobert, N., Olivares, J., Zhang, J. P., Terrones, H., Kordatos, K., Hsu, W. K., Hare, J. P., Townsend, P. D., Prassides, K., Cheetham, A. K., Kroto, H. W. and Walton, D. R. M. *Nature*, **388**, 52 (1997).

57. Grobert, N., Terrones, M., Trasobares, S., Kordatos, K., Terrones, H., Olivares, J., Zhang, J. P., Redlich, P., Hsu, W. K., Reeves, C. L., Wallis, D. J., Zhu, Y. Q., Hare, J. P., Pidduck, A. J., Kroto, H. W. and Walton, D. R. M. *Appl. Phys. A*, **70**, 175 (2000).

58. Suenaga, K., Johansson, M. P., Hellgren, N., Broitman, E., Wallenberg, L. R., Colliex, C., Sundgren, J. E. and Hultman, L. *Chemical Physics Letters*, **300**, 695 (1999).

59. Suenaga, K., Yudasaka, M., Colliex, C. and Iijima, S. *Chem. Phys. Lett*, **316**, 365 (2000).

60. Sung, S. L., Tsai, S. H., Tseng, C. H., Chiang, F. K., Liu, X. W. and Shih, H. C. *Applied Physics Letters*, **74**, 197 (1999).

61. Casanovas, J., Ricart, J. M., Rubio, J., Illas, F. and Jimenez-Mateos, J. M. *Jounal American Chemical Society*, **118**, 8071 (1996).

62. Shimoyama, I., Wu, G. H., Sekiguchi, T. and Baba, Y. *Physical Review B*, **62**, R6053 (2000).

63. Cuomo, J. J., Leary, P. A., Yu, D. L., Reuter, W. and Frisch, M. *J. Vac. Sci. Technol*, **16**, 299 (1979).

64. Jones, D. I. and Stewart, A. D. *Phil. Mag. B*, **46**, 423 (1982).

65. Muhl, S. M., J.M. *Diamon Related Materials*, **8**, 1809 (1999).

66. Zhang, Q., Qin, Z. C. and Zhu, J. *Phil. Mag. Lett.*, **80**, 585 (2000).

67. Hellgren, N. *Sputtered Carbon Nitride Thin Films*, Ph.D. Dissertation, Thin Films Physics Division, Linköping University, (1999)

68. Sjöström, H., Ivanov, I., Hultman, L., Sundgren, J.-E., Hainsworth, S. V., Page, T. F. and Wallenberg, L. R. *Thin Solid Films*, **246**, 103 (1994).

69. Férnandez, A., Prieto, P., Quiros, C., Sanz, J. M., Magula, V., Martin, J. M. and Vancher, B. *Appl. Phys. A.*, **69**, 764 (1996).

70. Kawaguchi, M. and Nozaki, K. *Chem. Mater.*, **7**, 257 (1995).

71. Kawaguchi, M., Tokimatsu, Y., Nozaki, K., Kaburagi, Y. and Hishiyama, Y. *Chem. Lett.*, **110**, 1003 (1997).

72. Wixom, M. R. *Journal of the American Ceramic Society*, **73**, 1973 (1990).

73. Gillan, E. G. *Chemistry of Materials*, **12**, 3906 (2000).

74. Veprek, S., Weidmann, J. and Glatz, F. *Journal of Vacuum Science & Technology A (Vacuum, Surfaces, and Films)*, **13**, 2914 (1995).

75. Chen, Y., Guo, L., Chen, F. and Wang, E. G. *J. Phys. Condens. Matter*, **8**, L685 (1996).

76. Maya, L., Cole, D. R. and Hagaman, E. W. *Journal of the American Ceramic Society*, **74**, 1686 (1991).

77. Kouvetakis, J., Bandari, A., Todd, M., Wilkens, B. and Cave, N. *Chem. Mater.*, **6**, 811 (1994).

78. Amelinckx, S., Zhang, B., Benaerts, D., Zhang, X. F., Ivanov, V. and Nagy, J. B. *Science*, **236**, 635 (1994).

79. Krishnan, A., Dujardin, E., Treacy, M. M. J., Hugdahl, J., Lynum, S. and Ebbesen, T. W. *Nature*, **388**, 451 (1997).

80. Terrones, M., Benito, A. M., MantecaDiego, C., Hsu, W. K., Osman, O. I., Hare, J. P., Reid, D. G., Terrones, H., Cheetham, A. K., Prassides, K., Kroto, H. W. and Walton, D. R. M. *Chemical Physics Letters*, **257**, 576 (1996).

81. Vandershall, H. L. J. *Fire Flam*, **2**, 97 (1971).

82. Oberlin, A. and Endo, M. *J. Crystal Growth*, **32**, 335 (1976).

83. Baker, R. T. K. *Carbon*, **27**, 315 (1988).

84. Sen, R., Govindaraj, A. and Rao, C. N. R. *Chemical Physics Letters*, **267**, 276 (1997).

85. Ago, H., Komatsu, T., Ohsima, S., Kuriki, Y. and Yumura, M. *Applied Physics Letters*, **77**, 79 (2000).

86. Li, D. C., Dai, L., Huang, S., Mau, A. W. H. and Wang, Z. L. *Chem Phys. Let*, **316**, 349 (2000).

87. Williams, D. B. and Carter, C. B. *Transmission Electron Microscopy; A text book for Material Science* (Plenum Press, New York, 1996).

88. Egerton, R. F. *Electron Energy-Loss Spectroscopy in the Electron Microscope* (Plenum Press, New York, 1996) pp305.

89. Egerton, R. F. in *Electron Energy-Loss Spectroscopy in the Electron Microscope*, 134-135 (Plenum Press, New York, 1996).

90. Ballongue, P. and Tencé, M. (paper presented to JEELS 99-Autrans, 1999).

91. Colliex, C., Tence, M., Lefevre, E., Mory, C., Gu, H., Bouchet, D. and Jeanguillaume, C. *Mikrochimica Acta*, **114**, 71 (1994).

92. Jeanguillaume, C. and Colliex, C. *Ultramicroscopy*, **28**, 252 (1989).

93. Colliex, C. in *In Advances in Optical and Electron Microscopy*, (eds. Cosslet, V. E. & Barer, A.) 65-177 (Academic Press, London, 1984).

94. Egerton, R. F. *Ultramicroscopy*, **3**, 243 (1978).

95. Leapman, R. D. in *Transmission Electron Energy Loss Spectrometry in Material Science*, (ed. Disko, M. M., Ahn, C. C., Fultz, B.) (The Mineral, Metals & Materials Society, 1992).

96. Leapman, R. D., Rez, P. and Mayers, D. F. *Journal of Chemical Physics*, **72**, 1232 (1980).

97. Hitchcock, A. P. and Mancini, D. C., The Atomic and Molecular Core Edge Excitation Database, **xray1.physics.sunsyb.edu/corex.html**,,(1993).

98. Serin, V. and Sikora, T., Inner shell & Outer shell Excitation Spectrum Database, **www.cemes.fr/eelsdb/**,,(2000).

99. Pickard, C. *Ab Initio Electron Energy Loss Spectroscopy*, PhD dissertation, University of Cambridge, (1997)

100. McLaren, R., Clark, S. A. C., Ishii, I. and Hitchcock, A. P. *Physical Review A*, **36**, 1683 (1987).

101. Stéphan, O., Ajayan, P. M., Colliex, C., Cyrot Lackmann, F. and Sandré, E. *Physical Review B*, **53**, 13824 (1996).

102. Rez, P., Weng, X. D. and Hong, M. *Microscopy, Microanalysis, Microstructures*, **2**, 143 (1991).

103. deMon-KS StoBe version 1.0 ed. (deMon Software, 2001).,Casida, M. E., Daul, C., Goursot, A., Hermann, K., Koester, A., Pettersson, L. G. M., Proynov, E., St-Amant, A. and Sala-hub, D. R.(main authors),Carravetta,V., Duarte, H., Godbout, N.,Guan, J. Jamorski, C., Leboeuf, M., Malkin, V., Malkina, O., Nyberg, M., Pedocchi, L., Sim, F., Triguero, L., Vela, A.,(Contributing authors).

104. Tence, M., Quartuccio, M. and Colliex, C. *Ultramicroscopy*, **58**, 42 (1995).

105. Bonnet, N., Brun, N. and Colliex, C. *Ultramicroscopy*, **77**, 97 (1999).

PAPER I

MODULATED CN$_X$ FILMS PREPARED BY IBAD

G. Sáfrán, A. Kolitsch, S. Malhuitre*,* ***S. Trasobares*******, I. Kovács, O. Geszti, M. Menyhárd, C. Colliex**, G. Radnóczi.***

Research Institute for Technical Physics and Materials Science Hungarian Academy of Sciences, Budapest XII., Konkoly-Thege út 29-33, Hungary

**Forschungszentrum Rossendorf, Institute of Ion Beam Physics and Materials Research P.O.Box 51 01 19, D-01314 Dresden, Germany*

***Laboratoiree de Physique des Solides Batiment 510 Universite Paris Sud 91405 Orsay Cedex, France*

ABSTRACT

CN$_x$ thin films have been prepared by IBAD varying the C-atom to N-ion ratio during deposition. The layers were studied by means of TEM and EELS investigation, ERDA, and AES depth profiling.

The obtained films were amorphous. The incorporation probability of N into the films was found to depend on the N/C arrival ratio. Large amount of N incorporation was found above and small amount below a N/C arrival rate of 0.3. Due to intentional change in the N/C arrival rate, modulated structures have been produced. The N concentration in the individual layers of modulated samples was found to exhibit distinct values of about 5 and 20 at%. The erosion rate of the various CN$_x$ layers upon Ar$^+$-ion bombardment depends on their N content. The relative erosion rate of the samples containing of 20 and 5 at% nitrogen was found to be $r_{rel}=r_{20\%}/r_{5\%}=1.6$ (1.2 keV, 83^o angle of incidence) considering the thickness of the individual layers and their necessary removal time during AES depth profiling. It was determined by XTEM and EELS that the origin of the TEM image contrast marking out the individual sublayers is mainly due to density variations in the modulated structure and partly due to thickness differences of the cross sectional TEM samples as a result of variable Ar$^+$ion milling rate of layers of various compositions.

Submitted to Diamond and Related Materials

1 INTRODUCTION

The preparation and investigation of CN_x thin films are of high importance because of the expected outstanding physical properties of C_3N_4 such as hardness comparable to diamond combined with high toughness predicted by Liu and Cohen [1, 2], as well as tribological, chemical and electrical specific features. A variety of methods were applied to prepare carbon nitride films from atmospheric-pressure chemical processes including pyrolysis and explosive shock through ion beam and laser techniques to various hot filament and CVD processes, reviewed together with the obtained results by Muhl and Méndez [3]. Up to now, most of the publications report on CN_x films exhibiting amorphous structure and nitrogen content below 30%, however, papers demonstrating crystalline carbon-nitride of high nitrogen content have also been published [4-7]. Multilayers of carbon film of different chemical bonding and density have also been prepared by laser ablation and arc deposition techniques [8].

In this work we study and discuss the structure, morphology, composition and sputter erosion rate of layered CN_x films prepared by N_2^+ ion beam assisted deposition (IBAD) of carbon, as a dependence of the deposition parameters.

2 EXPERIMENTAL

2.1 FILM PREPARATION

CN_x thin films were deposited in a high vacuum system by IBAD. The schematic diagram of the system is shown in Fig. 1.

The Si substrates were mounted on a heater placed at an angle of 45° to the carbon source and normal to the ion beam provided by a 5 cm diameter Kaufman ion source. The substrate temperature could be adjusted between room temperature and 700°C by resistive heating. The base pressure of the chamber was $3x10^{-4}$ Pa and the working pressure was $2x10^{-2}$ Pa.

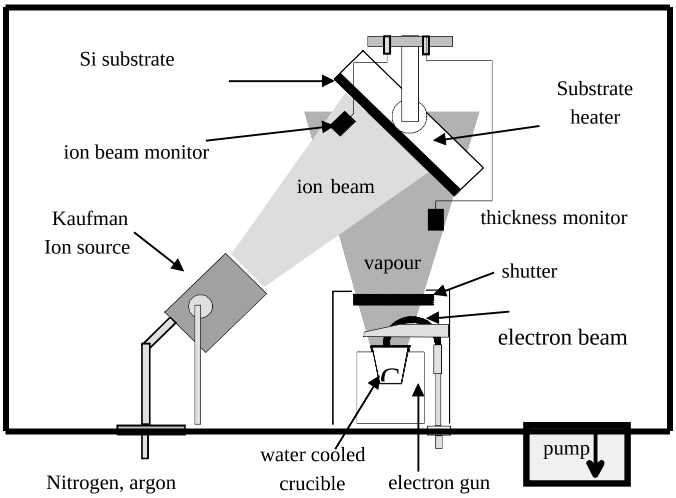

Figure 1.- Schematic diagram of the IBAD chamber used for the deposition of thin CN_x

Prior to deposition, the Si substrates were cleaned in situ by exposing them to an Ar^+ ion beam of 1 keV and a current density of 100 _A/cm ^{2} for 2 min. Carbon was evaporated from a graphite ingot by means of an electron gun (AP&T, HVP4). The evaporation rate of carbon (1-3 Å/s) was measured by a quartz thickness monitor and regulated by an automatic deposition controller. The carbon deposition onto the Si substrate was assisted by a simultaneous nitrogen ion beam. The energy of the N_2^+ ions could be varied from 200 eV to 1200 eV. The current density, measured with a Faraday cup positioned on the shutter in front of the substrate holder, could reach 200 _A/cm ^{2}.

The CN_x sample shown in cross section in fig. 2 is a characteristic example of modulated structures prepared. It was produced at ion current density of 40 _A/cm ^{2}, ion energy of 200 eV and the carbon evaporation rate was adjusted to first 0.1nm/s (region A) then 0.2nm/s (region B) and finally again 0.1 nm/s (region C)

2.2 TEM SAMPLE PREPARATION

Samples for plan view TEM investigation were prepared using different procedures. The layers were detached from their substrate in 10%-50% HF or a solution of HF-HNO_3, and in some cases we etched away the Si substrate through a window of a mask from the backside by a solution of acetic acid and HNO_3 mixture.

Samples for cross-sectional TEM (XTEM) were prepared by mechanical polishing and subsequent Ar^+ ion beam thinning procedure developed by Á. Barna [10]. This technique consists of embedding two pieces of the sample face to face into a 3mm diameter Ti disk, mechanical grinding and polishing till 50 _ m residual thickness, followed by 10kV Ar^+ ion bombardment at a glancing incidence angle below 5°. During ion milling the sample is rotated and later on rocked till transparency occured. As a final treatment the bombarding energy is lowered to 3kV in order to reduce ion beam induced damage.

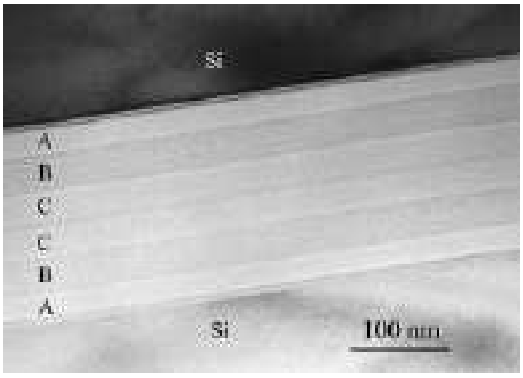

Figure 2. Cross sectional TEM micrograph of a CN_x sample exhibiting layered structure.

2.3 APPLIED TECHNIQUES

The composition of the layers was determined by elastic recoil analysis (ERDA) and Auger electron spectroscopy (AES) depth profiling, energy dispersive X-ray spectroscopy (EDS) and electron energy loss spectroscopy (EELS). The lateral- and the cross-sectional TEM samples were investigated by a Philips CM20 electron microscope attached with a germanium detector NORAN EDS and by a VG 501 Scanning Transmission Electron Microscope (STEM) operating at 100 keV, equipped with a Gatan parallel EELS detector. The energy resolution of the whole EELS system was about 0.6 eV.

3 RESULTS

3.1 RESULTS OF THE XTEM MEASUREMENTS

Fig. 2. represents a TEM micrograph of the cross section of a modulated CN_x sample, having sufficiently broad sublayers for individual investigations. According to the applied XTEM preparation technique, two pieces of the same sample are shown glued face to face together, therefore each film feature appears twice in the micrographs in mirror position. Three broad sublayers appear according to the expectation, each of about 30 nm thick, giving a bright "A", a dark "B" and again a bright "C" contrast region in the TEM. The reasonably homogeneous TEM contrast within each layer indicates that the parameters were well controlled during the deposition of this sample. The boundaries between the layers are sharp and planar, no transition layer could be detected.

3.2 ANALYTICAL RESULTS

3.2.1 ERDA measurements

The Elastic Recoil Detection Analysis (ERDA) measurement of the specimen, fig. 2, gave an average composition of 20 at% N in sublayers "A" and "C", and practically no nitrogen in sublayer "B" (fig. 3a). It is clearly recognised in fig. 3a, however, that the depth resolution of the ERDA is lower than that of the AES in this case. The three subsequent layers are distinguishable both in the N and C profile, but the fine details of the depth profile revealed by AES are not resolved in this case.

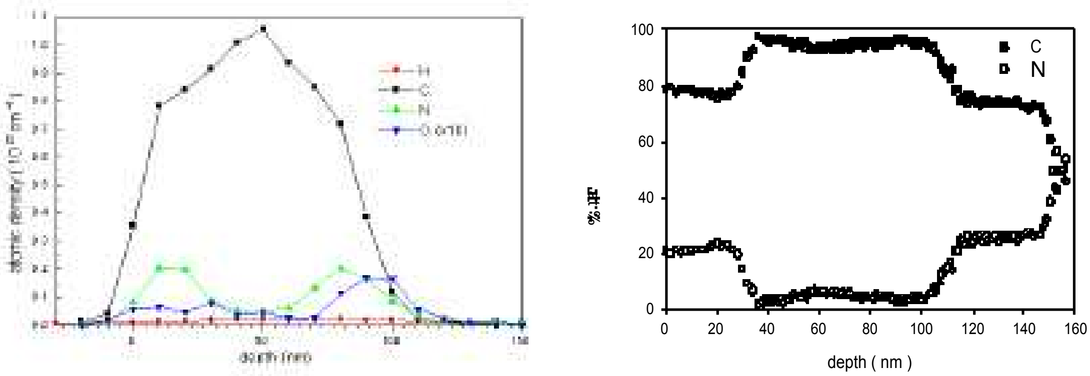

Figure 3.- a.) ERDA measurements of the sample (as in Fig2). A composition of 20 at%N was measured in sublayers "A" and "C", and practically no nitrogen in sublayer "B" b) AES depth profile of the two main componets, C and N, measured on the sample of shown by XTEM in Fig. 2. The curves show three sublayers ("A" "B" and "C") where the C- and N concentrations change adversely. The first sublayer "A" (bright contrast in TEM) exhibits low C and high N content. In "B", dark contrast in the TEM, the carbon concentration jumps to a remarkably higher value and practically no N is measured. The composition of "C", bright in the TEM, reproduces again the composition of sublayer "A".

3.2.2 AES depth profiles

Auger depth profiling of the sample shown in fig.2. was carried out in a dedicated device [11] in which sequential sputtering and AES measurement were performed. The depth profiling of the samples was carried out at glancing incidence angle ion bombardment using rotation of the sample with the aim of optimising the depth resolution. The Ar^+ ion current was stabilized by the measured target current of the specimen. The ion beam diameter was about 0.3 mm. The error of the ion current setting was estimated to be around 10 %. The sputtering parameters were as follows: projectile Ar^+ energy 1200 eV, angle of incidence 83^o (with respect the surface normal) and the specimen was rotated during ion sputtering.

Carbon, nitrogen and silicon peaks were measured by a pre-retarded CMA (Staib DESA 100) in counting mode. The measured curves were numerically derivated and used for concentration calculation. The relative sensitivity factors for these alloys or compounds are not known. From the (not well resolved) ERDA results (see in fig.3a) we could extrapolate the nitrogen concentration of sublayer "B". So, a relative sensitivity factor was derived for AES concentration calculation. The results are presented as the calculated concentration in function of the sputtering time (fig. 3b).

Using the calibration of the ERDA analysis, the N content of the sublayers "A" and "C" are 20-22 at%, while that of "B" contains N up to only 5 at%.

The compositional changes of the two main components in the sample, C and N, against the depth in nm are plotted in fig. 3b. Both the carbon and the nitrogen curve show three regions along the depth, which are well distinguishable. The first region "A" appearing with a bright contrast in XTEM (fig. 2.) exhibits low C and high N content.

In the next region "B", (dark in XTEM) the carbon concentration jumps to a remarkably higher value and the N content drops simultaneously. In this region the N signal shows some variation in the form of a small and wide local maximum in the middle. This weak incrase in N content can be recognised also in the XTEM image as a slightly brighter stripe in the centre of sublayer "B" and "B'" (fig. 2.). The third sublayer "C" reproduces again that of the first ("A"). This region appears also bright in the TEM.

The transitions between the layers are sharp in the depth profile, being of about 4-6 nm wide.

Knowing the thickness of the layers we could calculate the ratio $r_{rel} = r_{(20\%N)}/r_{(5\%N)}=1.6$ of sputter erosion rates of the layers, for the given sputtering conditions (1.2 keV 83° angle of incidence (with respect to the surface normal).

3.2.3 EDS measurements of lateral samples

For this measurement the fims were detached from their Si substrate in an etchant and picked up on a copper grid. The EDS analysis of the plan view sample prepared in this way revealed a N concentration of about 16 at%. Considering, that the sample consists of three equally thick layers of about 20, 5 and 20 at% of N (measured by ERDA and AES), giving an average N content of 15 at%. Consequently the EDS measured value (16 at%) is a satisfactory value, correponding to the AES and ERDA measurements, which were also carried out on as deposited (not ion milled) samples.

3.2.4 EELS Measurements of the cross sectional TEM sample

In order to determine the chemical composition and the possible bonding changes in specimen shown in fig. 2, EELS analysis was carried out on the cross section sample, which was prepared by mechanical and ion beam thinning. The data were recorded using the spectrum imaging approach, which consists of acquiring a collection of spectra as the electron probe is scanned under digital control over 1D or 2D patterns. [12-13]. The High Angle Annular Dark Field (HAADF) image, Fig 4a, and the corresponding intensity profile of the analysed area, Fig 4b, show the layered structure previously observed by XTEM (Fig. 2). The additional layer, D, corresponds to the glue, in between the two pieces of the sample. The carbon and nitrogen intensity profiles extracted from a 1D scan across the sample, Fig. 4c, show the presence of C over the whole sample and a N content below the detection limit in B and B' layers.

Fig 4.d represents the normalised spectra corresponding to the different layers. The characteristic signal of C is observed in all the layers, however, the N signal at 397eV is not observed in sublayer "B" and "B’". The N/C atomic ratio was measured from the EELS data by determining the integrated intensity of the C and N ionisation K edges after background subtraction [14]. The different sublayers are practically C (layers "B" and "B’", where less than 5at% N is detected) and CN_x layers, where x is 0.26±0.04 in the layers "A", "C" and "A’" and 0.17±0.03 for the layer "C’".

The details in the Near Edge Structures (NES) can be studied more closely. The K edges correspond to transitions from 1s state to unoccupied states above the Fermi level. Thus, they reflect any change in the bonding [15]. The C K edge contains a π^* peak at 284 eV and a σ^* band in layer "B" and "B’", which correspond to those observed in amorphous carbon (Fig 4e). Very similar features are observed for the σ^* band in the CN_x layers, however, the π^* peak gets a contribution of an extra peak at 285.5 eV. We suppose that this peak is the representation of C-N bonds. The N K edge is similar to those observed in CN materials (Fig. 4f) [16].

4 DISCUSSION

4.1 COMPOSITION OF THE LAYERS

In earlier experiments, samples were deposited at different ion fluences and energies and investigated by XTEM. Modulated structures were also identified, though the individual layers were too thin to be resolved by the available analytical tools. In the present experiments, however, the deposition parameters were strictly controlled and as a result regular modulated structures were grown. We obtained multilayered CN_x films with designed (Fig. 2) layered structure consisting of sublayers A", "B" and "C" showing an overall N content of about 16 at%. ERDA (Fig. 3a.) and AES (Fig. 3b) depth profiles as well EELS analysis (fig.4) have provided the chemical compositions of the individual layers, as being either below 5 at % (layer "B") or around 20 at % (layers "A" and "C"). The results are summarised in Table 1. Considering the evaporation rates of carbon being respectively 0.1 (layer "A"), 0.2 (layer "B") and finally again 0.1 (layer

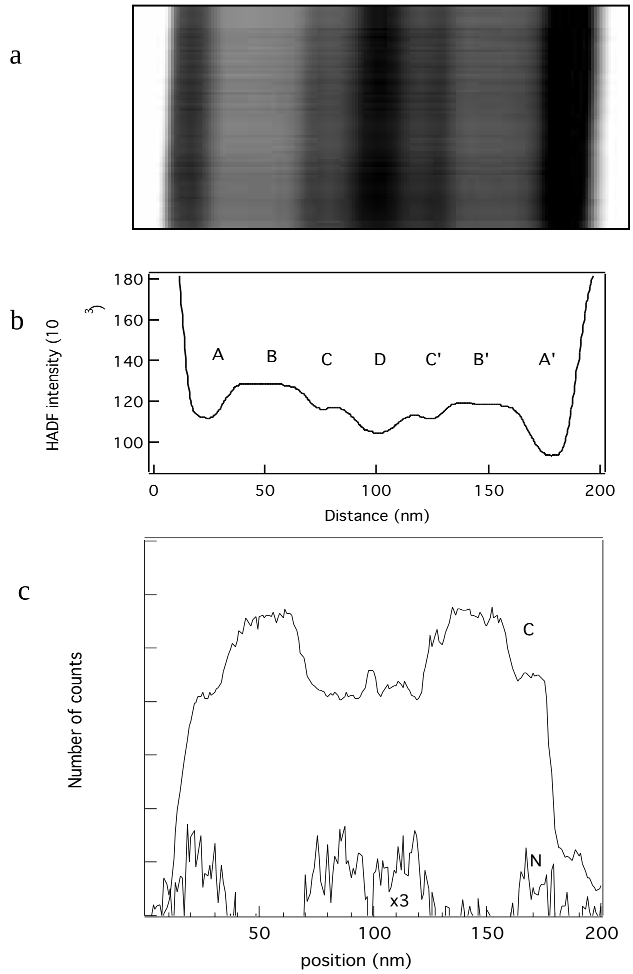

Figure 4. - a) High Angle Annular Dark Field (HAADF) image of the modulated CN$_x$ film. b) HAADF profile of image in a). c) Carbon and nitrogen intensity profile, across the modulated CN$_x$ film, extracted from the individual spectrum.

"C") nm/s, the N/C impinging ratio changed with a factor of 2 during deposition. At the given conditions one would expect a N concentration in layer "B" half as high as in layer "A" and "C". In spite of that, the measured N content in the sample changed from about 20-26 at% to about 2-5%, which gives a N/C ratio below 1/4 in the film. Besides, according to the AES depth profile, the nitrogen concentration in the CN$_x$ films exhibited distinct values (no intermediate values in between as about 2-5 and about 20-24 at %). This means, that the incorporation rate of N into CN$_x$ and the N/C ratio may

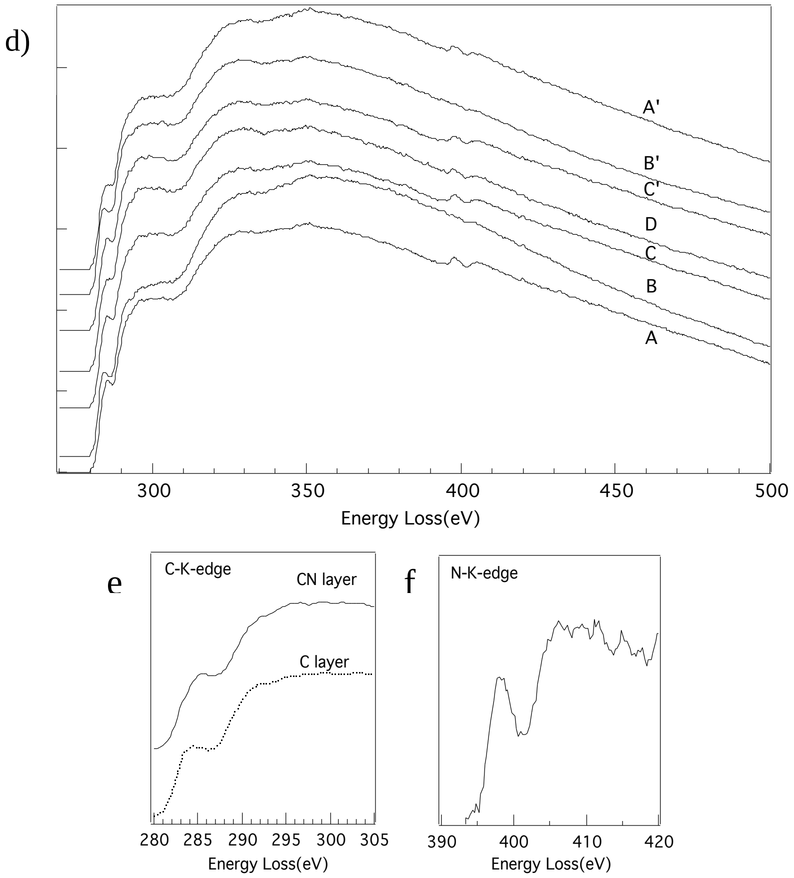

Figure 4.-d) EELS spectra corresponding to the different layers presented in the modulated CN$_x$ film. e) Near Edge Structure for the C K edge of the C and CN$_x$ layer. f) Near Edge Structure for the N K edge.

be not simple corresponding to the arrival ratio of C and N atoms, rather, below a certain N fraction practically no nitrogen incorporates. This behaviour suggests the existence of a treshold or critical level, i.e. a certain N/C arrival ratio is needed for the incorporation of N at all into the growing film. Considering the ion current density (40 _A /cm^2) and the ion to atom ratio (0.12) of the assisting N_2^+ ion beam and the C evaporation rate (0.2 nm/s), we have found that film deposition at a N/C impinging ratio of 0.3 and below results in low N incorporation value (2-5 at%), while above 0.3 high amount of N incorporates (20-24 at%).

Table 1.-Composition of the CNx sample of modulated structure with 3 sub-layers.

Sub layer	Composition, N at %			
	AES	ERDA	EELS	EDS
A	22-25	20	26	16
B	<5	<5	<5	
C	22-25	20	17-26	

4.2 DENSITY OF THE LAYERS

The HAADF image (fig.4a) gives the evidence of a layered (modulated) structure, as the intensity decreases by about 8% when going from the carbon reach layer (B or B’) to CN$_x$ layers C or C’ and about 15% from carbon reach layers (B or B’) to the CN$_x$ layers A and A’. However, there is no straightforward interpretation of the contrast changes. The HAADF signal I_{el} (fig. 4b) is sensitive to three different local parameters: the composition (through the elastic cross-section), the thickness and the density of the material as follows [17]:

$$I_{el} = I_o \overline{NT} \sigma_{el} \tag{1}$$

Where I$_o$ is the primary beam intensity, NT the average number of atoms per unit area, T is sample thickness and _$_{el}$ the elastic cross-section. As for the composition effect, by assuming that the elastic cross section σ_{el} is proportional to (Z$_{eff}$)$^{4/3}$ (where Z$_{eff}$ is the effective atomic number of the material and that the maximum N content in CN$_x$ corresponds to the value of x=0.20), we could expect a relative increase in intensity of 4% in the HAADF, when we go from carbon rich to nitrogen rich layers (from B to C or A). Instead of, a decrease of intensity signal is observed in the sample, fig 4b, therefore the composition changes can not explain the observed decrease of HAADF intensity.

The variation in density was estimated from the plasmon energy. Indeed, using the Drude model it can be shown that the plasmon energy (w$_p$) is proportional to the square root of the electron density n$_{el}$ as:

$$w_p = \left(\frac{n_{el} e^2}{\varepsilon_o m^*} \right)^{1/:} \tag{2}$$

Where *e* is the electron charge and *m** is the effective mass of the electrons. As shown in C. Colliex et al [18], reasonable agreement with the experiment is obtained when setting *m** to m_o (the rest mass of the electron) for low atomic mass elements. We have produced a map of the plasmon energy values as shown on fig. 5a, by plotting for each pixel the energy of the maximum of the plasmon peak. In such an image, a brighter contrast corresponds to a higher value in the plasmon energy. Since the intensity of the plasmon is not considered, such image is free of any thickness effect. The corresponding profile, Fig 5b, shows a maximum shift of about 1eV to lower energy when nitrogen is incorporated in the system. A shift in the energy position of the plasmon to lower values when N is incorporated in the system has also been reported by Barreca et al. [19]. This is also illustrated on the low loss spectra in fig. 5c. Following

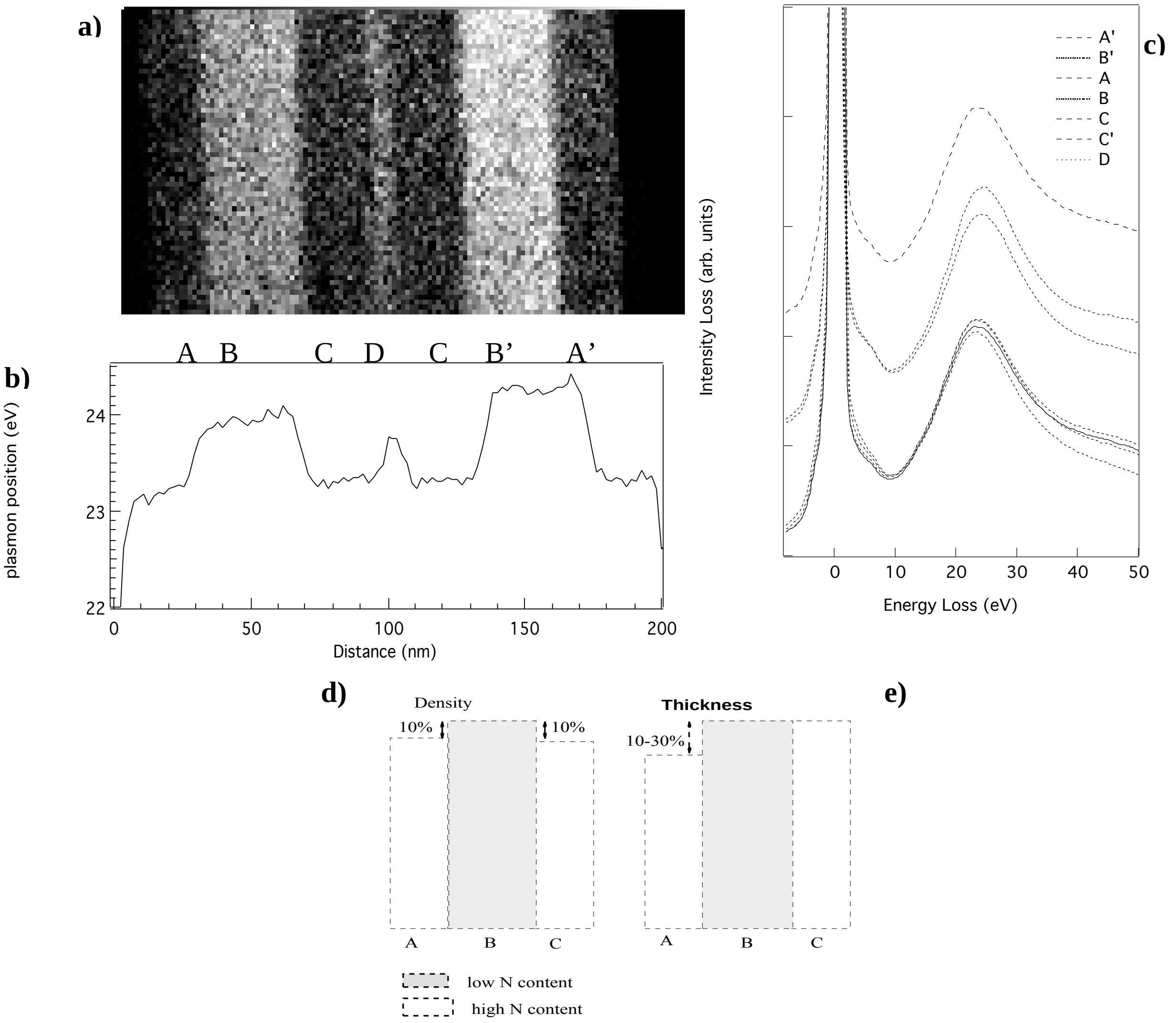

Figure 5.- a) Map image of the energy position of the plasmon. The white value corresponds to the highest peak position. b) Energy position profile of the plasmon across the modulated CN_x sample. c) Energy Low Loss spectra for the different layers. d) Scheme corresponding to the density variation and e) to the thickness variation odf the sample

the Drude model and relying on the previous assumption ($m^*=m_o$), the 1 eV shift corresponds to a relative decrease of 8% in the density between carbon reach, (fig.2.) and CN_x material (for any CN_x layer of the sample).

Therefore the variation in the HAADF image contrast (eq.1) of the sample (fig.4b) can be explained considering the density changes between B and C, C' layers. This situation is different for the A and A' layers of the CN_x material where the HAADF signal variation is twice higher. Such variation can be explained when taking into account an abrupt variation in the thickness between CN_x and C layers, which might be induced by the thinning process, and can be concluded also from the AES measurement.

4.3 SPUTTER EROSION RATES OF CN_x

A difference in the removal rates of the layers of different compositions of the CN_x samples due to Ar^+ ion bombardment was found during AES depth profiling. The sputtering rate of the individual layers was determined from layer thickness, known from XTEM and sputtering time, measured during AES depth profiling. According to that, a relative sputter erosion rate of

$$r_{rel}= r_{A,C}/r_B=1.6$$

was determined for the CN_x layers of approximate compositions of $C_{0.8}N_{0.2}$ and $C_{0.96}N_{0.04}$ at the sputtering conditions of: projectile Ar^+ energy 1.2 keV, angle of incidence 83° (with respect the surface normal).

The sputtering yields for the given compositions at the same sputtering conditions were determined also by calculation using TRIM code [20] (which considers only ballistic processes) and the ratio of the sputtering yields was found to be $r_{rel}=1.52$. Though the connection between the sputtering yield and erosion rate is not straightforward, yet the good agreement suggests that in this case the ballistic processes are the important ones.

Based on this good agreement we calculated the ratio of the yield at 3 keV and 88° angle of incidence that is for the conditons of ion milling for XTEM sample preparation and r_{rel} was found to be 1.28. Thus we conclude that the erosion rate for the N rich layers is higher than for the N poor layer in the case of ion milling for XTEM as well. Consequently, despite of the smoothening effect ot the used milling procedure, thickness differences are present in the XTEM sample due to the differences in the erosion rate of different (i.e. CN_x and C-rich) layers. These differences could be observed on samples, in which the layers were cut through by the ion beam, displaying thicker and outstanding parts of the C layer compared to CN_x.

The observed sputter erosion rate differences can be attributed to slow erosion rate of carbon (layer B), being present in this case in the form of a graphite like amorphous carbon layer (Fig. 4d-4f), showing no structural dissimilarity compared to the carbon in the neighbouring CN_x layers (layers A and C).

4.4 THE ORIGIN OF THE TEM CONTRAST

The contrast differences of the individual layers of cross sectionally prepared CN_x samples can be related to composition differences, as revealed by ERDA (Fig. 3a.), AES (Fig. 3b) and EELS (Figs. 4, 5.) measurements, namely, the darker in fig. 2 layers are composed of 2-5% N, while the layers, appearing brighter in contrast in the TEM at large (1000 nm) underfocus, contain nitrogen about/above 20 at %. The composition differences are accompanied with an 8% difference in density of these layers (the CNx layer being less dense) as concluded from EELS. Since the contrast change is rather abrupt when moving from layer to layer, and since HREM and electron diffraction did not reveal further structural differences between the layers, we come to the conclusion, that the density difference can be the basic reason of the contrast observed in TEM.

Additionally, TEM revealed that the Ar^+ ion milling initiated thickness differences between regions belonging to carbon and nitrogen rich layers, the carbon layers being thicker. This can have an additional contrast effect in HREM image.

B. Schultrich at al. [8] prepared C/C multilayers and carried out their XTEM investigation and came to a similar conclusion as of the origin of the TEM contrast: according to their conclusion, the layers are composed of graphitic and diamond like amorphous carbon, and the TEM contrast arises from density differences amounting up to 10 % in their layers. They also admit N incorporation into the graphitic layers. The question of thickness differences within the cross sectional TEM samples due to ion milling is not considered in their work.

As the C-C multilayers in [8] were prepared by laser and arc evaporation, and in the present work by IBAD, the formation mechanisms of the layers can be different, including differences in bonding and composition. In the present investigation, C-C bonds are similar in the sublayers, and carbon is present in graphitic form. The basic difference is the presence of about 20 at % Nitrogen in layers "A" and "C", and consequently C-N bonds in these layers.

5 CONCLUSIONS

ERDA and AES measurements revealed a composition modulation of amorphous structure in CNx films deposited by IBAD varying the N_2^+/C transport ratio.

A wide range of N/C arrival rates resulted in distinct compositions of below 5 at% N and of 20-27 at% N, in the case of CN_x films exhibiting an average of about 16 at% N. Apparently amorphous carbon layers are formed, when the N/C arrival ratio is N/C=0.3 or below and about 20-26 at%N incorporates above this value. Therefore, N/C=0.3 is a threshold or critical value of N incorporation at the given conditions.

A relative sputter erosion rate of CN_x (x being less than 0.05 and 0.2 respectively) for sublayers "B" and "A" or "C" under Ar+ ion bombardment was found to be $r_{rel} = r_{CN0.2}/r_{CN0.05}=1.6$ in case of 1.2 keV Ar^+ ions at 7° glancing incidence. The different sputter erosion rates are due to the different composition accompanied by a difference in film density revealed by EELS and amounting to 8%.

The contrast difference of the ion milled cross sectional samples observed in XTEM is attributed to density and thickness variations arising from compositional and erosion rate differences of the individual layers, respectively.

This work provides possibilities for growth and tailoring of modulated structures of CN_x films and CN_x/C multilayers. The present results enlight the importance of further study of the correlation between deposition parameters and physical properties to understand the mechanism of N incorporation into CN_x films.

6 ACKNOWLEDGEMENTS

This work was carried out within a cooperation in the TMR project FMRX-CT97-0103 and was supported by the EU under the contract no. ICAI-CT-2000-70029. The Hungarian partners were financially supported by the OMFB EU-98-B4/145, OTKA T030424 and T030340 projects.

7 REFERENCES

[1] A.Y. Liu, L. Cohen, Science 245 (1989) 841.

[2] A.Y. Liu, L. Cohen, Phys. Rev B 41 (1990) 10727.

[3] S. Muhl, J.M. Méndez, Diamond and Related Materials 8 (1999) 1809.

[4] Y. Zhang, Z. Zhou, H. Li, Appl. Phys. Lett. 68 (1996) 534.

[5] Y. Peng, T. Ishigaki, S. Horiuchi, Appl. Phys. Lett. 73 (1998) 3671.

[6] S. Xu, H-S. Li, Y-A. Li, S. Lee, C.H.A. Huan, Chem. Phys. Lett. 287 (1998) 731.

[7] A.K.M.S. Chowdhury, D.C. Cameron, M.S.J. Hashmi, J.M. Gregg, J. Materials Research 14 (1999) 2359.

[8] B. Schultrich, H-J Scheibe, H. Mai, Advanced Engineering Materials 2 (2000) 419.

[9] A. Kolitsch, E. Richter, H. Dummer, U. Roland, J. Ullmann, Nucl. Instr. & Methods B 106 (1995) 511.

[10] Á. Barna, G. Radnóczi, B. Pécz, Sample Preparation Techniques for TEM, in Handbook for Microscopy, ed. by S. Amelickx, D. Van Dyck, J. van Tendeloo, VCH Verlaggesellschaft mbH, Weinheim, Germany (1997) vol. 3. Chapter 3. pp. 751-801.

[11] Á. Barna, M.Menyhard, Phys. Stat. Sol. (a) 145 (1994) 263.

[12] C. Jeanguillaume, C. Colliex, Ultramicroscopy 28 (1989) 252.

[13] C. Colliex et al., Mikrohimica Acta 114 (1994) 71.

[14] R.D. Leapman, P. Rez, D.F. Mayers, J. Chem. Phys. 72 (1980) 1232.

[15] J. Stöhr, NEXAFS Spectroscopy. G. Ertl, R. Gomer, D. L. Mills, Eds., Springer Series in Surface Science (Springer-Verlag, Berlin Heidelberg, vol. 25 (1996).

[16] K. Suenaga, M. Yudasaka, C. Colliex, S. Iijima, Chem. Phys. Lett. 316 (2000) 365.

[17] R.F. Egerton, Electron Energy-Loss Spectroscopy in the Electron Microscope, Plenum Press, New York and London, Second Edition, (1996) pp. 302.

[18] C. Colliex, Electron Energy Loss Spectroscopy in the Electron Microscope. In Advances in Optical and Electron Microscopy, ed V.E. Cosslett and R. Barer, Academic Press, London, vol 9 (1984) pp. 65-177.

[19] F. Barrac, A.M. Mezzasalma., G. Mondio, F. Neri, S. Trusso, C. Vasi, Thin Solid Films 377-378 (2000) 631.

[20] J.P. Biersack, Nucl. Instr. Methods B27 (1987) 21.

PAPER II

Compartmentalised CN_x Nanotubes; Chemistry, Morphology and Growth

Susana Trasobares, Odile Stephan, Christian Colliex[1], Wen K. Hsu[2], Harold W. Kroto[2], David R.M. Walton[2]

Laboratoire de Physiques de Solides,UMR-CNRS 8502 Universite Paris Sud, Bâtiment 510, 91405 Orsay, France

1 also at Laboratoire Aimé Cotton, UPR CNRS 3321, Université Paris Sud, Bâtiment 505, 91405 Orsay, France

2 School of Chemistry, Physics and Environmental Science, University of Sussex, Brighton BN1 9QJ, UK

A systematic study of the effect of different synthesis parameters on the N incorporation into C nanotubes is presented. CN_x nanotubes prepared by catalytic pyrolysis of melamine exhibit a highly compartmentalised morphology with a remarkable periodicity structure all along the nanotube axis. Spatially resolved EELS (in the spectrum imaging mode) indicates that the nanotubes are made of carbon and nitrogen, inhomogeneously distributed with an enrichment of carbon on the external surfaces. The evolution of the C-K edge shape across the nanotube reveals a transition from a graphitic stacking on the outside to a disorganized mixed type in the core of the nanotube. For the N-K edge, the situation is more complex. The fine structure of the N-K edge is different depending on the used catalyst, which indicates differences in the bonding configuration. When Ni is used as a catalyst, N is substituting C in the graphitic structure while C-N pyridinic-like bonds are formed when the catalyst is Fe. The compartmentalised periodic morphology is the result of a systematic catalytic particle movement from the root of the nanotube to the tip. This displacement is defined by the nature of the catalytic particle, diffusion and supersaturation (C/N) in the liquid particle and precipitation process.

Submitted to Journal of Chemical Physics

Introduction

The discovery of carbon nanotubes[1] and the theoretical prediction that material conforming to C_3N_4 stoichiometry is likely to be the hardest known[2], have triggered several attempts to incorporate nitrogen into carbon nanotubes. At present, the highest N content in CN_x nanotubes lies in the range x = 0.02-0.09[3,4] which is much lower than in C_3N_4. For example, Sen *et al*[3] have prepared CN_x nanotubes (x = 0.03-0.09) by pyrolyzing pyridine over a Co catalyst, aligned CN_x nanotubes (x ≈ 0.02) have been made by pyrolysing triazine over a laser-patterned Co substrate[4], and CN_x nanofibres (x ≈ 0.07) have been produced by pyrolysis of N-rich organic precursors[5]. Chemical vapour deposition of Ni-phthalocyanine[6] generates CN_x nanotubes with an inhomogeneous N content (*e.g.* x ≈ 0.05 in the graphitic region and *ca.* 0.15 in the amorphous region). The highest N content, N/C, is *ca*. 0.72, found in the amorphous region of CN nanotubes, produced by electron cyclotron resonance[7]. Han *et al*[8] have also compared the results obtained by pyrolysing ferrocene/melamine/Ar, ferrocene/C_{60}/NH_3 and ferrocene/C_{60}/N_2. They concluded that pyrolysis in the presence of NH_3 provides an efficient route to higher N-content nanotubes than can be achieved using gaeous N_2 or N-containing solid precursors such as melamine. The presence of N in nanotubes enhances conductivity[3]. For example, the I-V curves of CN_x nanotubes showed 1.2 nA/V conductance, which is higher than the value for multi-walled carbon nanotubes (0.5 nA/V). In addition to conductivity enhancement, it was found that the morphology and chemical composition of CN_x nanotubes depends on the production methods. In particular, CN_x tube growth is strongly dependent on the method of synthesis. Production of CN_x nanotubes mainly involves magnetron sputtering[9], CVD of Ni-phthalocyanine[6] and electron cyclotron resonance[7]. To date, a comparative study on the influence of different synthesis conditions (catalyst, temperature, gas flow) for incorporating N into C nanotubes (using the same synthesis route) is lacking. In this paper, the products obtained by catalysed pyrolysis of melamine, are investigated using Transmission Electron Microscopy (TEM) imaging and Electron Energy Loss Spectroscopy (EELS) analysis. The results are compared with existing data. In particular, a detailed study of the structures has been undertaken using high-resolution transmission electron microscopy (HRTEM) and EELS chemical mapping. The nature of the chemical bonds in CN_x nanotubes is evaluated, in conjunction with the interpretation of N-K absorption edges.

Experimental Section

CN_x nanotubes were produced by pyrolyzing melamine at various temperatures: 550 °C, 750 °C, 850 °C and 1000 °C, in the presence of Ni or Fe powder under Ar, N_2, NH_3 and N_2/NH_3. Experiments were carried out in a two-stage furnace[5]. Melamine (0.10 - 0.15 g, Aldrich, 99 % pure) was placed at one end of a quartz tube and the catalyst (Ni or Fe, particle size < 1µm, Aldrich, UK) at the other. The tube was then introduced so that the melamine and catalyst were located in the first and second furnaces respectively. At the conclusion of the experiment, the black powder product from the second furnace was dispersed in acetone and mounted on a holey-carbon grid for electron microscopy analysis.

Nanotubes, produced using Fe as catalyst, are highly sensitive to electron beam irradiation. For example, disordered layers formed within the outer layers of the nanotube after a few minutes irradiation in a TEM. Accordingly, HRTEM (LaB_6 filament) was operated at 100 keV accelerating voltage in order to reduce radiation damage as much as possible.

EELS analysis was carried out on the sample using a VG 501 Scanning Transmission Electron Microscope (100 keV), equipped with a Gatan parallel EELS detector and a CCD camera. This equipment provides an energy resolution of *ca*. 0.7 eV. The spectrum imaging technique[10] has been used to acquire the EELS spectra encompassing the C and N K edge. An example is shown on figure 1, 64 spectra were collected across a nanotube at 0.63 nm intervals during an integration time of 600 milliseconds for each spectrum. The characteristic core-edge signals, corresponding to carbon and nitrogen, were measured. High Angle Annular Dark Field (HAADF) image of the analyzed nanotube is displayed in inset figure 1. In such image, electrons that are scattered elastically at large angles, are collected so that the signal intensity is proportional to the sample thicker. Therefore the thickness parts appear as white and the vacuum areas as black.

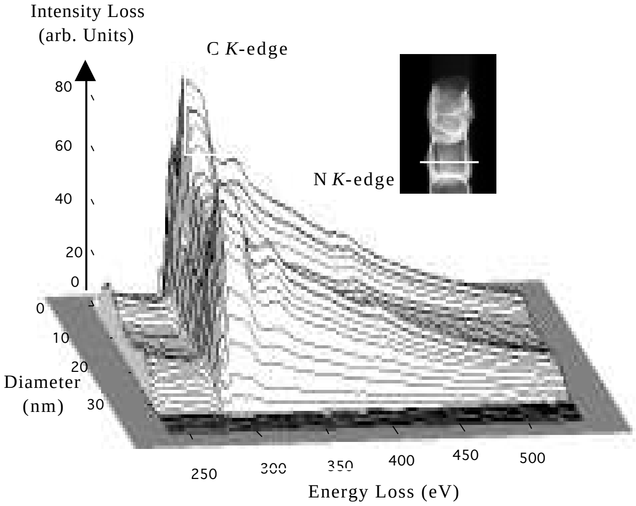

Figure 1.- Spatial sequence of 64 EELS spectra recorded with acquisition time of 600 milliseconds and 0.63 nm intervals. The characteristic signals of C and N are detected. Insert shows HAADF image of the analyzed nanotube. The line indicates the probe scan during the EELS analysis.

Firstly, the extent of N incorporation into the C nanotubes, produced in an Ar atmosphere using Ni (or Fe) as catalysts, was investigated by exploring the morphology and chemical structure of the CN nanotubes. Secondly, N-rich gases were introduced into the pyrolysis system in order to monitor the enhanced N content of the CN nanotubes. Thirdly, a growth mechanism for the production of compartmentalised CN nanotubes is proposed.

Morphology.

CN$_x$ nanotubes (< 60nm diameter) are the main product at 1000°C (Ar flow, Ni catalyst). Large carbon particles (>700nm) and low yields of C and CN nanotubes (15-20nm diameter) are obtained at lower temperatures (Table 1). TEM images show that the nanotube diameters produced at 1000°C are significantly larger than those associated with nanotubes grown at 750°C, as previously observed by Li *et al*[11]. A TEM image of the CN$_x$ nanotubes, produced by pyrolysis of melamine over Ni catalyst at 1000 °C, is shown in Fig. 2a. The nanotubes exhibit a highly-compartmentalised morphology with a remarkably regular dimensional periodicity along the tube axis. Similar structures were observed in CN$_x$ nanotubes prepared using Fe as a catalyst (Fig. 2c). It is noteworthy that only a few compartments contain metal particles in the Ni-catalysed pyrolysis (arrow, Figure 2a), whereas with Fe as catalyst, most compartments contain Fe particles (Fig. 2c).

Chemical Structure.

EELS analysis was employed to quantify the N content and to investigate N spatial distribution across the tubes. Characteristic C and N edges in the EELS spectrum were measured by removing the background intensity and by deconvolution of multiple scattering. The elemental composition of the CN$_x$ nanotubes was determined from the EELS spectra by assessing the integrated intensity of the relevant C- and N-K ionisation edges and using tabulated 1s ionisation cross-sections[13,14]. The N content within the tubes is found to be less than 13 % in Fe- and Ni-CN$_x$ nanotubes; the highest N content is found in Ni-CN$_x$ nanotubes (Table 1). High-resolution EELS line-scans show variation in distribution across the tube with a decrease in N content in the external surfaces (Fig. 3). In Ni-CN$_x$ nanotubes, the fairly high N content (≤ 13 %) is observed within random nano-domains (*ca.* 1-5nm). Such nano-domains do not coincide with the highly curved sections of the nanotube, as previously proposed by Han *et al*[8]. In Fe-CN$_x$ nanotubes, nano-domains with high N content are not found.

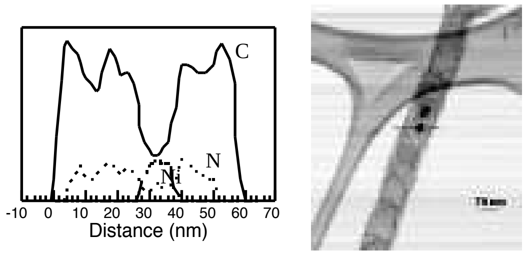

Figure 3. a) Variation of intensity of the C-K N-K and Ni-L edges as the beam is scanned across the nanotube. **b)** Scanning Transmission Electron Microscope (STEM) image of the CN$_x$ nanotube where the analysis was carried out.

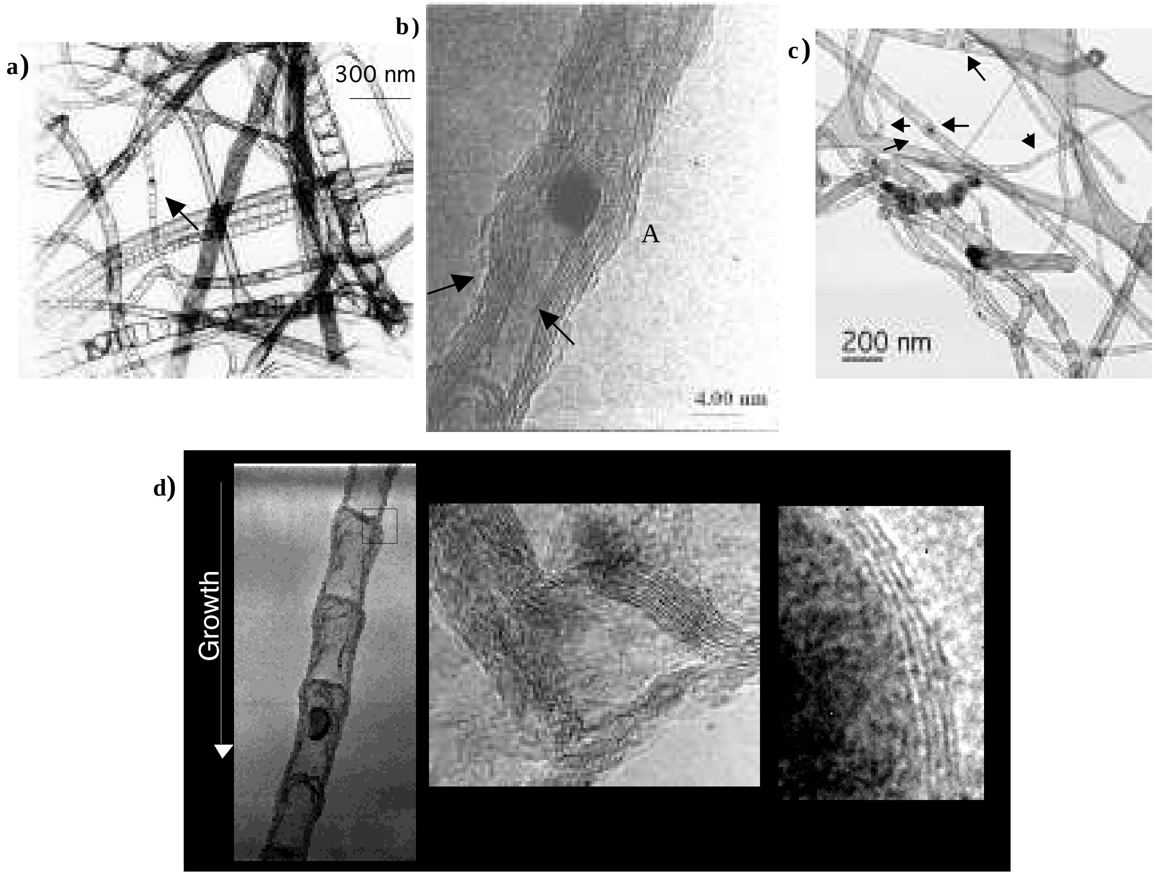

Figure 2.- TEM images of the nanotubes produced by catalytic pyrolysis of melamine a) using Ni as catalyst at 1000°C; **c)** using Fe as a catalyst at 950°C. HRTEM images of CN$_x$ nanotubes produced by pyrolysis of melamine using Ni as a catalyst **b)** or Fe as a catalyst **d)**.

Table 1. Series of experiments performed in order to study the influence of the catalytic particle and temperature in the N incorporation process.

Organic precursor	Catalyst	T °C	Gas	N content in the CN$_x$ nanotubes	Material
Melamine ($C_3N_6H_9$)	Ni	1000	Ar	* External layers free of N. * There are some random nano-domains with higher N content (<13 N at.%)	* CN$_x$ nanotubes ϕ=50-100 nm (main product) * C fibres ϕ=100-150 nm
Melamine ($C_3N_6H_9$)	Ni	850	Ar	* External layers free of N. * There are some random nano-domains with higher N content (<13 N at.%)	* C fibres ϕ=250-300nm (main product) * CN$_x$ nanotubes ϕ=60-70 nm
Melamine ($C_3N_6H_9$)	Ni	750	Ar	* 3-5 N at.% (only few tubes with N)	* Large particles ϕ=700 nm(main product) * C and CN$_x$ nanotubes ϕ=12-20nm
Melamine ($C_3N_6H_9$)	Ni	550	Ar		* Large particles ϕ=1 µm * C and CN$_x$ nanotubes ϕ=12-20nm
Melamine ($C_3N_6H_9$)	Fe	950	Ar	* External layers free of N. * average 4-5 at N % * Nano-domains with higher N are not observed.	* CN$_x$ nanotubes ϕ=20-60nm

Bond configuration information in CN$_x$ nanotubes can be obtained by monitoring the energy loss near-edge fine structures (ELNES) at the core edge. Individual spectra extracted from EELS line-scans are shown in Fig. 4a. The presence of a π* C peak is due to transitions from C1s to empty π* levels above the Fermi level. The position of the π* C peak (285.5 eV) is stable in spite of the varied N content. However, the peak intensity decreases when the N content increases in the tube, as previously observed in CN$_x$ nanotubes produced by magnetron sputtering[9]. Such a decrease in intensity agrees with theoretical predictions by dos Santos *et al*[15] who observed an antibonding π* state filled by the excess of electrons arising from the N. The σ* band (292 eV) of the C-K edge exhibits a similar shape to that of graphite, close to the tube edge, but becomes relatively smoothed as the N content increases. This phenomenon suggests a transition from graphitic stacking on the tube outer layers to disorganised layers in the central core region. We mention that the loss of stacking ordering can also contribute to the π* intensity decrease as observed in amorphous carbon. In Ni-CN$_x$ nanotubes, the C-K σ band becomes less sharp when the N content is *ca*. 10 %. We were unable to explore C-K edge Fe-CN$_x$ nanotube details, due to thickening of the amorphous coated tube surfaces under electron irradiation (contamination).

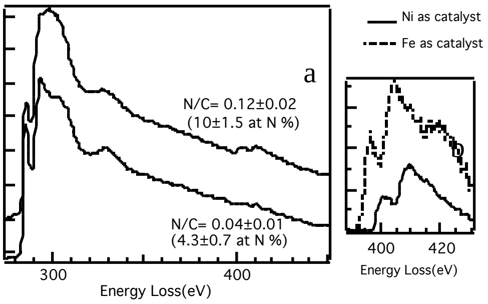

Figure 4. a) Normalised spectra of the CN$_x$ nanotube prepared by catalytic pyrolysis of melamine using Ni as a catalyst. Spectra corresponding to different N compositions. **b)** N-K edge of CN$_x$ nanotubes using Ni or Fe as a catalyst.

Three different types of N-C bond have been theoretically[16] and experimentally[17] reported for CN_x materials. Each type is associated with a peak at the onset of the N-K edge, which exhibits pyridine-like character at 398 eV (*i.e.* each N atom contributes one p-electron to the π system). The peak at 399 eV indicates that N atoms contribute with two p-electrons to the π system. The graphite-like N-C character appears at 401-403 eV. In Ni-CN_x nanotubes, the N-K edge exhibits a broad π^* peak (at 401-404 eV) and an asymmetric σ band (at 408 eV) (Fig.4b). A similar N-K edge is observed when the N content is lower. Comparing our results with the theoretical and experimental data, we suggest that in Ni-CN_x nanotubes, the N displaces C from the graphitic structure. Dos Santos *et al*[15] have proposed that the graphitic structure maintains its planar morphology when the N content is less than 20 %, but adopts a corrugated structure at higher N content. This contention agrees with the HRTEM observation on Ni-CN_x nanotubes, however the situation is different for the Fe-CN_x nanotubes. Here, the N-K edge shows a sharp π^* peak at 398 eV; the σ^* band at 405 eV is clearly asymmetric (Fig. 4b). The presence of a scattering peak at 420 eV is a satellite plasmon peak because of thicker specimen induced by contamination. We conclude that the C-N bond in the Fe-CN_x nanotubes is pyridine-like.

As a summary to the previous observations the outer C layers of all the CN_x nanotubes studied are N-free. Nano-domains with high N content, are produced only in Ni-catalysed experiments. The C-N bond configurations appear therefore to be dependent on the type of catalyst: *i.e.* graphite-like for Ni and pyridine-like for Fe. Both catalysts generate a regular compartmentalised structure, however the number of transverse layers, which form compartments, is greater in the presence of Fe catalysts. The quantity of metal particles encapsulated in the compartments is higher in Fe-CN_x nanotubes.

Influence of Gas and Organic precursors

Han *et al*[8], have proposed that the introduction of NH_3 in pyrolysis experiments provides an efficient route to high N-content CN_x nanotubes. In order to verify this proposition, we pyrolysed melamine in the presence of N_2 or NH_3 (Table 2). We have found that the N_2 flow in pyrolysis experiments does not promote N incorporation into nanotubes. Instead, defective nanotubes with graphitic compartmentalised morphologies are produced. We have also found that the NH_3 reacts rapidly with melamine at low temperatures (250-300 °C), making pyrolysis experiments difficult to perform.

In order to clarify the role of the carrier gas in the N incorporation process, camphor ($C_{10}H_{16}O$) was pyrolysed in the presence of N_2, NH_3 and N_2/NH_3 respectively (Table 2). Incorporation of N into the nanotubes was not observed in N_2 flow experiments, which is consistent with the results described above for melamine pyrolyses. N incorporation into C nanotubes was not observed when NH_3 was used as the carrier gas. For pyrolysis in the presence of NH_3/N_2, C nanotubes containing N_2 gas within regular compartments were produced, as revealed by spatially resolved EELS[18]

Growth mechanisms

Different mechanisms have been proposed to account for the formation of carbon fibres and nanotubes, and to explain the observed morphologies. Oberlin *et al*,[19] introduced a mechanism based upon surface diffusion of carbon over the catalytic particles, for the production of carbon fibres and filaments from benzene. When the filaments form, the metal catalysts are located at the end of growing tubes. The hollow core structure may arise because carbon cannot reach the rear of the metal droplets. The observed compartmentalised morphologies in the CN_x nanotubes, and encapsulated metal particles in the tube compartments, are not consistent with this mechanism.

The growth of compartmentalised CN_x nanotubes consists of four steps. i) The C and CN species encounter the catalyst; in the liquid state ii) a chemical reaction occurs at the vapour-liquid interface; iii) C and/or N diffuse through the metal catalyst; iv) when the carbon is supersaturated in the metal particles, C-precipitation at the rear of the metal droplet occurs and the droplet is located on the top of growing nanotube.[20-22] The metal particles in steps ii-iv are in liquid form. In our study, the metal particles are droplet shaped-like (Fig. 5a and c). We find that all the nanotubes contain Fe-particles at one end (Fig. 5a, 5b) and are free of such particles at the

Table 2. Series of experiments performed in order to study the influence of the gas and precursor organic in the N incorporation process. The experiments were carried out at 950°C and Fe was used as a catalyst.

Organic precursor	Gas	N content in the CN_x nanotubes	Material
Melamine ($C_3N_6H_9$)	Ar	* External layers free of N. * average 4-5 at N % * Nano-domains with high N are not observed.	* CN_x nanotubes ϕ=20-60nm
Melamine	N_2	* No Nitrogen in the nanotubes	
Melamine	NH_3		* Reaction between NH_3 and melamine occurs at low temperature (200-300°C).
Camphor ($C_{10}H_{16}O$)	Ar		* Absence of nanotubes in the sample
Camphor	N_2	* No nitrogen in the nanotubes	* Nanotubes highly graphitic
Camphor	NH_3	* Only three nanotubes containing N in the gas phase	* Fe filled nanotubes. * Only 3 highly curved nanotubes without metal.ϕ=50-60nm
Camphor	N_2/NH_3	* N_2 gas is trapped in the cavity of the nanotube[18].	* Nanaocapsules in C nanotubes. ϕ=50-60nm

other end (Fig. 5e and d). EELS analysis carried out on the tube tip (Fig. 5e) indicates that only C is present; Fe is absent.

We suggest that, after a specific number of layers are formed, the metal particles are forced out of the graphitic sheath and migrate rapidly to the tube tip, due to the accumulated stress which arises from the internal walls.[23] The presence of droplet-like Fe particles implies that they were in a molten state during the catalyzed process and were shaped by the internal carbon walls (Fig. 5c). Compartment formation rapidly inhibits the migration of Fe particles to the tube tip, and the particles become trapped in the compartments (Fig. 5c). Based on Fig. 5, we suggest that nanotube growth occurs in three steps; (i) nanotubes form at the rear of the metal particles. (ii) the tubes, formed at the rear of the particle, rapidly undergo structural stress, which "pushes" the Fe particles upwards; (iii) when this occurs, the Fe particles become droplet-shaped.

At that point, we do not provide a complete explanation for the periodic structure, however some clues can be proposed. First, there is no straightforward relation between the compartment size and the diameter of the nanotube. Second, in cases when the metal particle diminishes while being pushed toward the extremity of the nanotube (some parts of the particle are getting trapped behind), then the periodicity is reduced, fig 5f. These observations give an evidence for strong relation between the size of the particle and the structure periodicity. Figure 5a, displaying a metal particle with the same size and shape as the sequence of formed compartments, supports such statement.

When Fe is used as the catalyst, C and CN species appear to be transported through the Fe particles, *i.e.* C and CN form an alloy with Fe. The C/CN-Fe coalescence is consistent with the phase diagrams for Fe/N and Fe/C.[20-22] When the C is alloyed with Fe (*i.e.* carbide phase), the melting point of Fe drops, which explains why the Fe catalyst is in the molten state. Carbon is also able to form an alloy with Ni[20-22], however N-Ni alloy formation is unlikely[24,25], which may account for the variations in tube structure and C-N bond configurations in the CN_x nanotubes, produced *via* Fe and Ni catalysis. Since both C and N are soluble in Fe, we suggest that C and N diffuse through the Fe particle and when the molten Fe particle is supersaturated by C (or CN), the C (or CN) precipitates at the rear of the particles to form CN_x nanotubes. On the other hand, N cannot diffuse through the Ni catalyst, and the CN fragments may be directly deposited on the surface of the Ni particle. In Fe catalysis, the C and CN may diffuse continuously through the metal particle. Therefore, the structure of Fe-CN_x nanotubes is relatively organised and the CN composition of the tube walls is homogeneous. In Ni catalysis, two processes occur simultaneously; (a) C diffusion through the Ni particle, and (b) direct deposition of CN species on the C tube walls. Accordingly, the structure of Ni-CN_x nanotubes is more disorganised and CN_x nano-domains are randomly distributed throughout the tube walls. It is important to note that the average N content incorporated in the nanotube is much lower than that in the starting organic precursor (melamine, $C_3N_6H_6$). Therefore N incorporation is not a favorable process. Different arguments confirm this statement: pyrolysis of N rich organic precursors has shown the thermodynamically stability of NH_3, HCN, CH_4. These gases are released as soon as they are formed. Consequently, the amount of residual solid and the N incorporated in the system are reduced[26]. The pyrolysis of an organic precursor free of N, in the presence of N rich gases is even worse. In that case, the reaction does not provide at all any N incorporation in the C system.

Comparison of CN_X synthesis processes.

Recently, CN_x nanotubes produced by magnetron sputtering and by CVD at 900-1000 °C, have been studied. It was found that the N incorporation into C tubes is difficult[6], a finding, which is consistent with the present study (Table 3). We have also found that the chemical composition and structural morphologies are dependent upon the synthetis processes and experimental conditions.

The N-K edge, detected in the CN_x nanotubes, has generally a triangular shape. Nevertheless, the splitting of the π^* N peak, previously found in nanotubes produced by CVD and magnetron sputtering, is absent in our CN_x nanotubes. Peak splitting has been previously discussed[6] and it was suggested that the presence of two kinds of C-N bonds in the nanotubes is responsible for peak splitting. In the present study two different C-N bonds are also found, but in different specimen so that their appearance depends on the catalysts used.

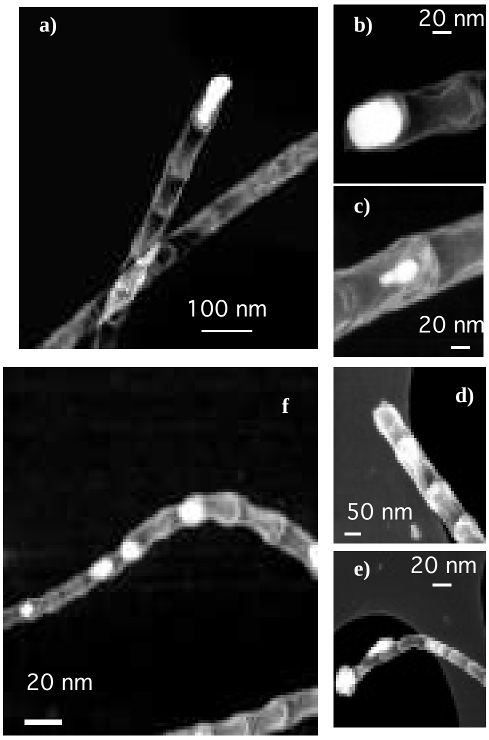

Figure 5.- HAADF images of Fe particles in the Fe-CN_xNT.**a)** Metal particle at the tip with similar shape to the compartment one. **b)** Fe particle at the tip of the nanotube. The particle size is smaller than the compartmenalised one. C) Droplet-shape Fe particle encapsulated in the compartment. d) and e) Nanotube tip free of metal particle, EELS has revealed the only presence of C.f) Fe metal particle encapsulated in successive compartments presented at the tip of the nanotube.

Table 3. Comparison of the properties of CN_x nanotubes grown by different methods

	Magnetron sputtering of C target in N_2 atmosphere[9]	**CVD of Ni-phtalocyanine**[6]	**Pyrolisis of melamine**	
Source of the specimen	Univ. Linköping (Sweden)	NEC, Tsukuba (Japan)	Univ. Sussex (U.K)	
Growth temperature	350°C	700-800°C	950-1000°C	
Catalyst	---------	Ni	Ni,	Fe
Structure	Tubular or leek-like	Tubular	Compartmentalised tubular	
Layers morphology	Heavily buckled	Buckled, herring-bone type	Wavy	Wavy with interlinks
Nitrogen content	Homogeneous	Inhomogeneous	Inhomogeneous	
N/C atomic ratio	Up to 15-30 at %	N enrichment in the peripheral layers (8%) and core of the nanotube (15%) Graphitic internal layers	N free external layer (2 or3)	
			Nanodomains with high N content (13%)	Absence of nanodomains
Growth mechanism		Base growth with diffusion through catalytic particle	Tip growth with diffusion through catalytic particle.	
C-N bonds		$C-NH_2$ in the edge of nanotube N substituted in graphite	N substituted in graphite	pyridine-like

Conclusions

CN_x nanotubes produced by catalytic pyrolysis of melamine in the presence of Ni or Fe, present a highly compartmentalised morphology with a remarkable periodicity all along the axis and inhomogeneous N distribution.

As a result of HRTEM and EELS investigations, a growth mechanism has been proposed. The compartmentalised periodic morphology is the result of a systematic catalytic particle movement from the root of the nanotube to the up-top tip. This displacement is governed by the nature of the catalyst (Fe or Ni), the diffusion and supersaturation (C/N) in the liquid particle, the precipitation process and the size of the metal particle. The difference in the N incorporation process can be explained by the differences in the diffusion process. Carbon or/and nitrogen diffuse through the Fe catalytic particle while only C diffuses through the Ni particle.

This study confirms the difficulty of incorporating N in a graphitic system as well as it shows that the morphology, chemistry and growth mechanism of the nanotube are strongly influenced by the synthesis process. A clear point has been made concerning the influence of the nature of the catalyst on the type of formed C-N bonds (graphitic like in the case of Ni and pyridine-like for Fe). However the role of the gas and organic precursor in the N incorporation need to be further investigated. It is already clear that performing the experiment in a N_2 atmosphere does not provide any N incorporation into the C system whatever the precursor. Also, no N incorporation is obtained when camphor (organic precursor free of nitrogen) is pyrolised in the presence of NH_3 or NH_3/N_2 (in particular pyrolisis of camphor in a NH_3/N_2 atmosphere gives rise to the formation of N_2 containing nanotubes). It suggests that the growth process preserves at least some of the preexisting C-N bonds when the precursor contains nitrogen atoms. On the other hand, it is not efficient at all for creating C-N bonds from ab initio separated carbon and nitrogen atoms. Further experiments involving different N and N-free organic precursors in nitrogen-rich atmospheres are being carried out to improve N incorporation into the C system.

Acknowledgements

We acknowledge provision of financial support by the EU-TMR network CT97-0103 "Synthesis, structure and characterisation of new Carbon Based Materials", the Leverhulme Trust, the EPSRC and the Royal Society of Great Britai

REFERENCES

(1) Iijima, S. *Nature* **1991**, *354*, 56-58.
(2) Liu, A. Y.; Cohen, M. L. *Science* **1989**, *245*, 841 - 842.
(3) Sen, R.; Satishkumar, B. C.; Govindaraj, A.; Harikumar, K. R.; Raina, G.; Zhang, J. P.; Cheetham, A. K.; Rao, C. N. R. *Chem. Phys. Lett.* **1998**, *287,* 671-676.
(4) Terrones, M.; Grobert, N.; Olivares, J.; Zhang, J. P.; Terrones, H.; Kordatos, K.; Hsu, W. K.; Hare, J. P.; Townsend, P. D.; Prassides, K.; Cheetham, A. K.; Kroto, H. W.; Walton, D. R. M. *Nature* **1997**, *388*, 52-55.
(5) Grobert, N.; Terrones, M.; Trasobares, S.; Kordatos, K.; Terrones, H.; Olivares, J.; Zhang, J. P.; Redlich, P.; Hsu, W. K.; Reeves, C. L.; Wallis, D. J.; Zhu, Y. Q.; Hare, J. P.; Pidduck, A. J.; Kroto, H. W.; Walton, D. R. M. *Appl. Phys. A-Mater. Sci. Process.* **2000**, *70*, 175-183.
(6) Suenaga, K.; Yudasaka, M.; Colliex, C.; Iijima, S. *Chem. Phys. Lett* **2000**, *316*, 365-372.
(7) Sung, S. L.; Tsai, S. H.; Tseng, C. H.; Chiang, F. K.; Liu, X. W.; Shih, H. C. *Appl. Phys. Lett.* **1999**, *74*, 197-199.
(8) Han, W. Q.; Kohler-Redlich, P.; Seeger, T.; Ernst, F.; Rühle, M.; Grobert, N.; Hsu, W. K.; Chang, B. H.; Zhu, Y. Q.; Kroto, H. W.; Walton, D. R. M.; Terrones, M.; Terrones, H. *Appl. Phys. Lett.* **2000**, *77*, 1807-1809.
(9) Suenaga, K.; Johansson, M. P.; Hellgren, N.; Broitman, E.; Wallenberg, L. R.; Colliex, C.; Sundgren, J. E.; Hultman, L. *Chem. Phys. Lett.* **1999**, *300*, 695-700.
(10) Jeanguillaume, C.; Colliex, C. *Ultramicroscopy* **1989**, *28*, 252-257.
(11) Li, D. C.; Dai, L.; Huang, S.; Mau, A. W. H.; Wang, Z. L. *Chem Phys. Let* **2000**, *316*, 349-355.
(12) Sjöström, H.; Stafström, S.; Boman, M.; Sundgren, J.-E. *Phys. Rev. Lett.* **1995**, *75*, 1336-1339.
(13) Leapman, R. D.; Rez, P.; Mayers, D. F. *Journal Chemical Physiscs* **1980**, *72*, 1232.
(14) Egerton, R. F. In *Electron Energy-Loss Spectroscopy in the Electron Microscope*; Second Edition ed.; Plenum Press: New York, 1996; pp 245-300.
(15) dos Santos, M. C.; Alvarez, F. *Phys. Rev. B-Condens Matter* **1998**, *58*, 13918-13924.
(16) Casanovas, J.; Ricart, J. M.; Rubio, J.; Illas, F.; Jimenez-Mateos, J. M. *Jounal American Chemical Society* **1996**, *118*, 8071-8076.
(17) Shimoyama, I.; Wu, G. H.; Sekiguchi, T.; Baba, Y. *Phys. Rev. B-Condens Matter* **2000**, *62*, R6053-R6056.
(18) Trasobares, S.; Stéphan, O.; Colliex, C.; Hug, G.; Hsu, W. K.; Kroto, H. W.; Walton, D. R. M. *Eur. Phys. J. B* **2001**, *22*, 117-122.
(19) Oberlin, A.; Endo, M. *J. Crystal Growth* **1976**, *32*, 335-349.
(20) Wagner, R. S.; Ellis, W. C. *Appl. Phys. Lett.* **1964**, *4*, 89-90.
(21) Givargizov, E. I. *J. Crystal Growth* **1973**, *20*, 217-226.
(22) Givargizov, E. I. *J. Crystal Growth* **1975**, *31*, 20-30.
(23) Saito, Y. *Carbon* **1995**, *33*, 979.
(24) Gabriel, A.; Gustafson, P.; Ansara, I. *Calphad-Comput. Coupling Ph. Diagrams Thermochem.* **1987**, *11*, 203-218.
(25) Frisk, K. *Calphad-Comput. Coupling Ph. Diagrams Thermochem.* **1987**, *11*, 127-134.
(26) Maya, L.; Cole, D. R.; Hagaman, E. W. *J. American Chemical Society* **1991**, *74*, 1686-1688.

PAPER III

ISOLATING AND IDENTIFYING THE ELNES SIGNAL OF CN NANOCRYSTALS EMBEDDED IN AN AMORPHOUS MATRIX

S. Trasobares[1], S. P. Gao[2], O. Stéphan[1], A. Gloter[1], C. Colliex[1] and J. Zhu[2]

[1] Laboratoire de Physiques des Solides, UMR 8502, Université Paris Sud, Building 510, 91405 Orsay, France

[2] Electron Microscopy Laboratory, School of Materials Science and Engineering; Tsingua University, Beijiing 100084, PR China.

ABSTRACT

Nanocrystals of a new CN phase of presumable orthorhombic type embedded in an amorphous CN_x ($x<0.2$) matrix produced by magnetron sputtering, have been identified. The evidence for the co-existence of different phases in the sample is first given by spatially-resolved electron energy-loss spectroscopy (EELS). A sophisticated mathematical treatment of collections of EELS spectra applied to the core-edge fine structures (ELNES) was used to isolate the characteristic signature of the different phases. Electron diffraction patterns and high-resolution transmission electron microscopy images (HRTEM) were then carried out from areas displaying the characteristic identified ELNES to confirm the identification of the structure and chemistry of these nanocrystals.

Submitted to Chemical Physics Letters

INTRODUCTION

The initial prediction that ß-C_3N_4 could be ultra hard and would present exciting electronic properties (1), has motivated many experimentalists to develop synthesis methods for achieving the production of this phase and other carbon nitride materials. On the theoretician side, a tremendous effort has been carried out to predict new crystalline phases and to test their stability. The most known phases are α-, ß-, pseudocubic-, cubic- and graphitic-C_3N_4, some of them consisting in a variety of proposed structures. Despite many efforts in synthesis, only a few authors have reported the production of C_3N_4 crystalline structures, which are, in most cases, mixed with another phase. Crystals (<1μm) embedded in a CN_x amorphous matrix have been produced using several synthesis routes, such as radio frequency diode sputtering (2,3), direct current magnetron sputtering (4), ion beam sputtering (5). The preparation of a solid, which consists of irregularly oriented prismatic crystals, made of a mixed phase of α, β C_3N_4 and an unknown C_3N_4 phase, has been described (6). In all these studies, although a reasonable agreement with C_3N_4 structures was found in electron diffraction or Raman scattering measurements, the estimated composition was generally far lower than the C_3N_4 stoichiometry. Furthermore, low N content is a general characteristics of the produced CN_x compounds reported in the literature (7,8). Confronted with this experimental evidence, theoreticians transferred their attention to lower N content compounds, such as tetragonal CN, $C_{11}N_4$, C_3N (9-11).

As microscopic amounts of crystalline CN_x are only obtained in a mixed phase, characterisation techniques at the nanometer scale, providing selective information on the different phases present in the sample, are needed. Electron Energy Loss Spectroscopy (EELS) performed in the context of a Scanning Transmission Electron Microscopy (STEM) delivering a subnanometer probe, is a well-suited technique to investigate the chemistry and the electronic properties of nano-objects (12,13) The development of the spectrum-imaging mode, providing the acquisition of a collection of spectra as a function of the probe position, (14), has increased the nanoanalysis capability of EELS. In this paper, we have also analysed EELS spectra recorded in the spectrum-imaging mode with optimum processing methods. It has permitted first to isolate the characteristic signals of the individual phases present in a CN_X sample. Then High Resolution Transmission Electron Microscopy (HRTEM) and electron diffraction techniques have been used to identify the CN_x crystalline nano-phase. From these measurements, we suggest the existence of a new crystalline CN phase.

EXPERIMENTAL

CN nanocrystals produced by magnetron sputtering (3) have been characterised using Spatially Resolved Energy Electron Loss Spectroscopy (EELS) and Transmission Electron Microscopy in the High Resolution (HRTEM) and diffraction modes.

EELS has been performed with a VG HB501 STEM operated at 100 keV and equipped with a Gatan parallel EELS detector and a CCD camera providing an energy resolution of about 0.7 eV. Spatially Resolved EELS (in the spectrum-imaging approach) (14) has been used to acquire the spectra. This mode consists in recording a collection of individual spectra, as the electron probe is scanned across the sample. Series of 64 spectra recorded with an acquisition time of 0.2 s and a probe size 0.8 nm have been acquired from different areas of the sample, with spatial increments between probe positions varying from 0.6 to 2.5 nm. Well-adapted mathematical methods have been used to isolate the Energy Loss Near Edge Fine Structures (ELNES) characteristic of different phases present in the sample. These processing methods are Non Negative Linear Square Fitting (NNLS) and Multivariate Statistical Analysis (MSA)(15).

Once the ELNES signals have been extracted and isolated, the likely crystalline structures in the analysed area, have been searched for. EELS, HRTEM images and electron diffraction have been performed in the same area of the sample using a LaB_6 Transmission Electron Microscope (TEM) operated at 200 keV and equipped with a Gatan Parallel EELS detector. Consequently, the relation between the ELNES and crystallinity of the sample has been established. The EELS measurements in the TEM have been performed using a probe size of 10 nm and energy resolution of 1.5 eV. The electron diffraction has been performed at a camera length of around 1.2 m and the diffraction constant has been calibrated using a magnetite polycrystalline film.

The composition ([N]/[C] at. ratio) has been measured from the EELS data by determining the integrated intensity in the C and N ionisation K edges after background subtraction. A classical power-law ($A\ E^{-r}$) of the background and a hydrogenic model for the K edge cross sections (16) have been used.

RESULTS

Spatially Resolved EELS on different areas of the CN_x sample reveals the inhomogeneity of the sample. A selection of characteristic ELNES signals for C and N, extracted from the Spatially Resolved EELS series is displayed in figure 1. The variation in the different signals is striking. A quantification of the spectra also shows the variation in composition, which goes from amorphous carbon (100%C) to different N/C ratio varying from 0.3 to 1. Let us describe in more detail the different ELNES in correspondence with the different compositions reported in table 1. As for the C K edge, spec1 is typical of amorphous carbon with a rather broad prepeak at 284 eV corresponding to π^* states and a large featureless resonance above 295 eV associated with σ^* states. When a small amount of nitrogen ($N/C \leq 0.3$, for spec 2) is incorporated, the π^* peak shifts to higher energy (284.8 eV) while no significant change is observed in the σ^* band. This shift increases up to 285 eV in spec 3 where a $N/C \approx 0.35$ value is reached. It is also characterised by the occurrence of a new weak peak at 286.8 eV. This last peaks increases in intensity so that two separated peaks are clearly observed in spec 4. The corresponding N/C is approximately 0.7. As for the N K edge, variations of lower amplitude are observed. The edge is composed of two peaks, which do not shift in

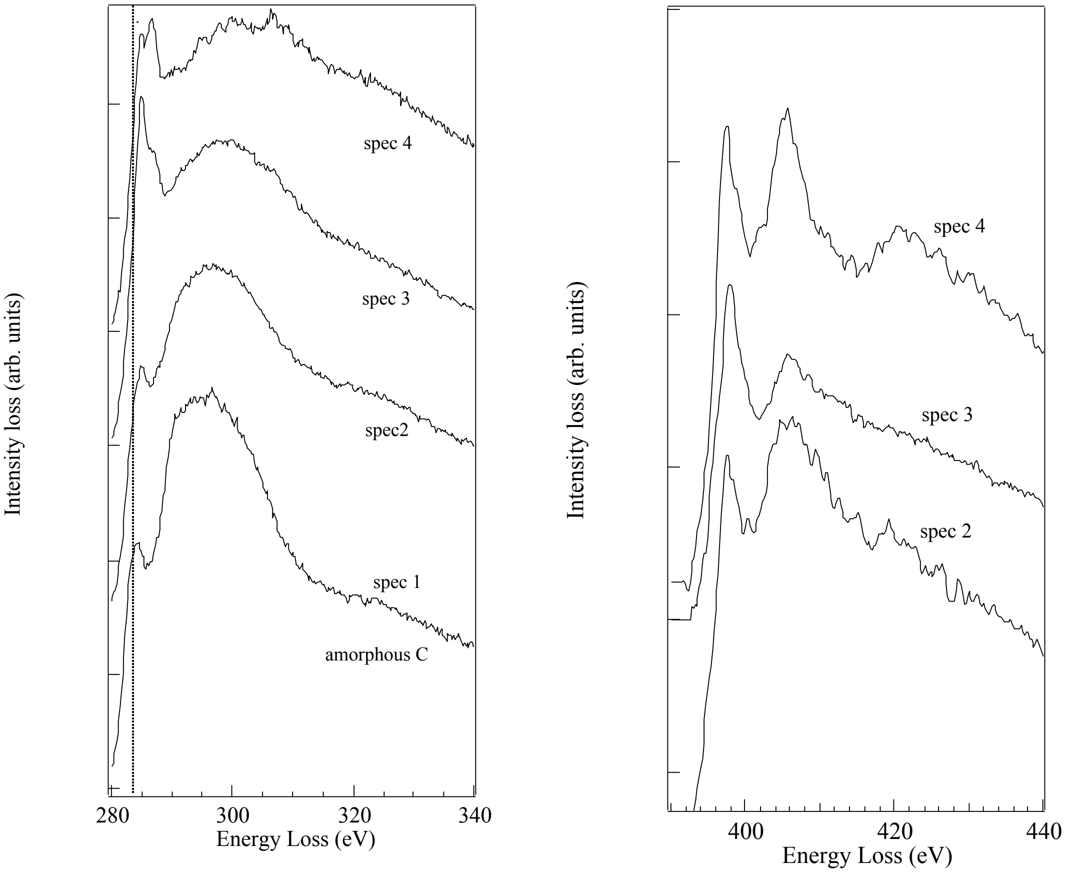

Figure 1.- Individual EELS spectrum obtained from different areas of the sample, corresponding to different compositions and exhibiting varying edge shapes.

energy as the composition is changing. The first peak lies at 397.5 eV and does not change significantly in shape and in position although a change in intensity is observed. However, in spec4, the second peak gets sharper, a shoulder occurs around 413 eV and a broad and more pronounced resonance is visible around 420 eV. The different characteristics extracted from these EELS spectra (composition and peak energy position) are reported in table 1.

Table 1. Composition and π* peak position in the C K edge for the various spectra recorded at different areas of the sample.

	Spec 1	Spec 2	Spec 3	Spec 4	Spec 5
N/C		0.28±0.04	0.35 ± 0.06	O.68±0.11	0.95±0.15
N at.%		22±3 at.%	26 ± 3.6 at. %	40±5.4 at.%	49±6.1at.%
π* peak	284	284.8	285	285	------
(eV)	-----	------	286.8	286.8	286.8

Comparing these results with previous EELS work on CN_x materials, we find that spec2 is very similar to amorphous CN_x films (17). Moreover the shift to higher energy of the π* peak in carbon edge when the amount of incorporated nitrogen increases was also reported (18). Spec3 is in good agreement (shape and peaks energy position) with that reported by Fernandez et al (19) in CN_x films containing 44 atomic % of N prepared by dual ion beam sputtering. Finally, spec 4 resembles to that of reference (3) acquired on the same kind of sample as the one analysed here.

We should however keep in mind that, as we are working in transmission mode on an inhomogeneous sample, the observed spectra might correspond to a mixture of different pure components superposed along the trajectory of the electron microscope beam. Therefore, we have used MSA in order to extract all the pure components contained in the whole set of experimental data acquired in the spectrum imaging approach on several areas of the specimen. Such treatment identifies as a result 4 components: the already mentioned ones, (ref-amorphous carbon (spec1) and ref-CN_x amorphous (spec 2)) and two new spectra, labelled ref-phase1 and ref-phase2 as shown in figure 2. As mentioned before Ref-phase 1 is similar to spectra previously reported for amorphous films (19). In our case the corresponding N/C atomic ratio was found to vary in the range of 0.5-0.7±0.01. Ref-phase 2 exhibits ELNES features very different from the previously displayed experimental spectra. The first peak at 285 eV has disappeared and the second peak at 286.8 eV gets sharper and is quite intense. Moreover, the σ^* band is now split into two broad peaks at 297.6 eV and 307.6 eV. From these results, it is now clear when looking at the carbon edges, that spec 3 and spec 4 are combinations of the last two references. Once this series of basis components has been defined, we have used the NNLS routine for reconstructing every experimental spectrum as a linear combination of these references. Applied to a line scan of 64 spectra over a 20 nm distance, this method delivers the intensity spatial profiles of the different references as shown in figure 2b. In this area, three different phases are detected either isolated or mixed, no contribution from amorphous CN_x is detected. The dominating phase is phase 2. It is found as a pure contribution in the first part and the last part of the scan over 3 regions of 1 nm, 4 nm and 1 nm respectively. In the central part of the scan, the three phases are mixed-up over a 7 nm region.

In order to get some insight about the structure of phases 1 and 2, we have recorded electron diffraction patterns and high-resolution images from areas displaying the characteristic identified ELNES. Phase 1 was found to be amorphous, while phase 2 displayed a polycrystalline character as shown on figure 3. Crystals, identified as phase 2, have sizes ranging from few nanometers to about one hundred nanometers and are usually aggregated to form micrometrical clusters. The selected area diffraction pattern (SAED) of such a polycrystalline cluster is presented in figure 3A. Two intense rings of nearly similar intensity corresponding to distances of 2.73±0.10 and 2.37±0.10 Å and a smaller ring composed of much fewer Bragg spots associated with a distance of 4.64 ±0.10 Å are clearly visible. The six next distances that could be measured on the SAED patterns are also mentioned on the figure.
figure.

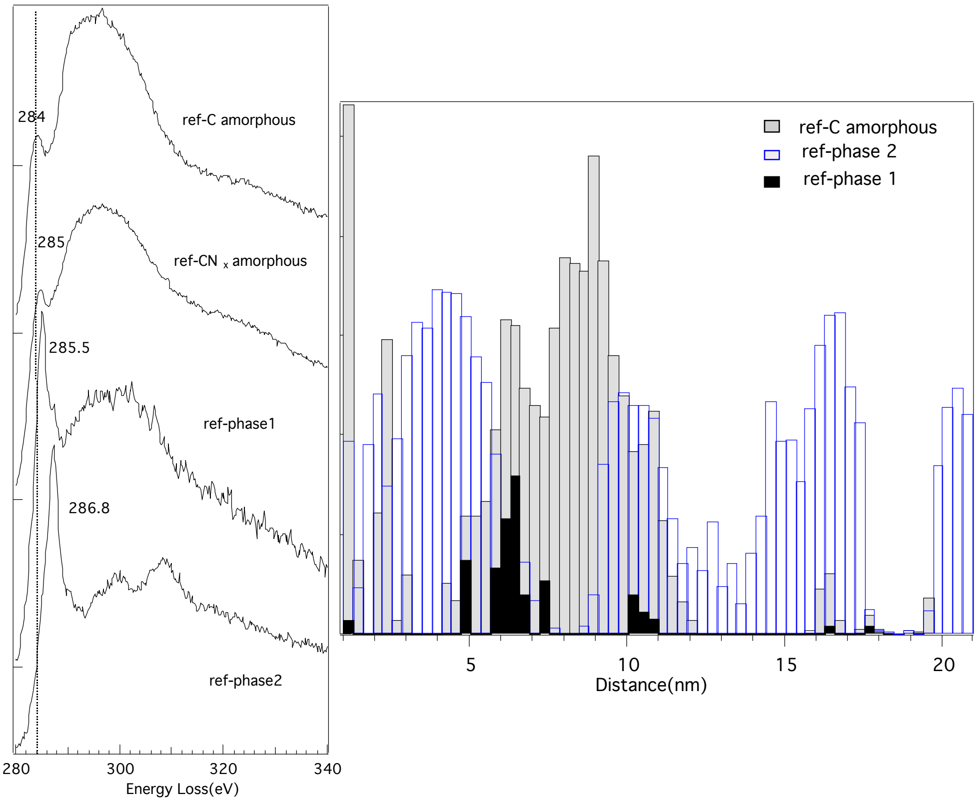

Figure 2.- A) ELNES C K references used for the NNLS analysis. B) Spatial intensity distribution of the ELNES references along a line spectrum.

To our knowledge, these results cannot be correlated to any previous proposed CN_x structure. Indeed, our experimental data do not match with the calculated diffraction intensities and distances obtained by Wang et al. (20) for β-C_3N_4 (either P3 or $P6_3/m$ space groups), α-C_3N_4 (P31c), cubic C_3N_4 (P-43m or I-43d) and graphitic C_3N_4 (R3m or P-6m2) compounds. We have calculated electron powder diffraction patterns for the new models of the graphitic form of C_3N_4 (orthorhombic cell, P2mm space group) recently proposed by Alves et al. (21) which also do not match with our experimental diffraction data. In fact, since we do not observe in figure 3a diffracted intensities corresponding to 3.2-3.4 Å lattice fringes, graphitic-like structures are unlikely. Different structures with lower N amounts such as monoclinic CN phase (8), graphitic $C_{11}N_4$ (22), α-$C_{11}N_4$ and β-$C_{11}N_4$ (10) have been proposed but the calculated diffraction distances and intensities based on these structures are always far from our data. Finally the different C_3N possible structures predicted by *ab-initio* calculations (11) do not fit with the observed structure.

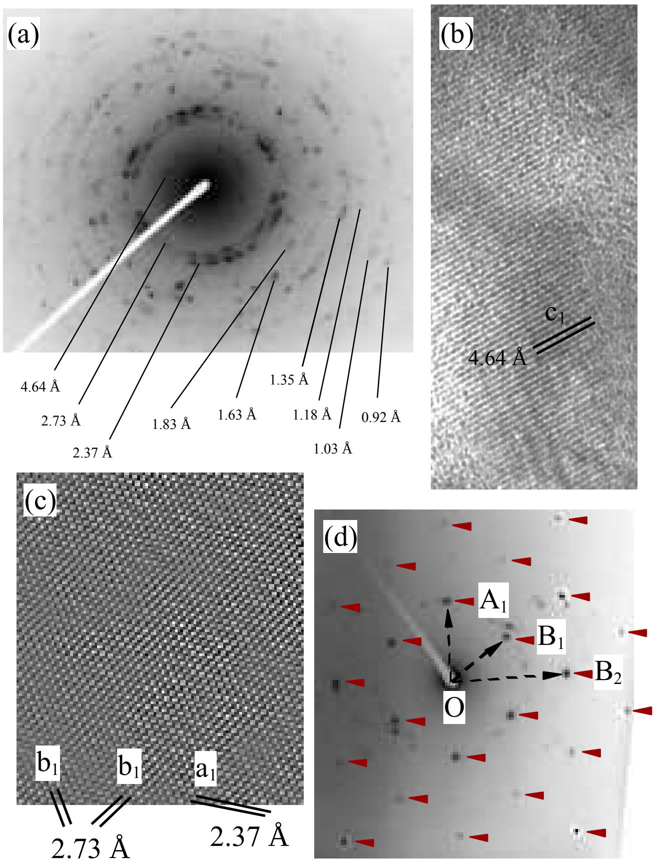

Figure 3.- A) Transmission Electron Diffraction of a CN polycrystal. -B) Raw HREM of a CN crystal showing the largest observed fringes -C) Fourier filtered HRTEM image of a CN_x crystal. D) SAED pattern corresponding to the orientation of the previous HREM image, the contrast of spot located far from the central beam has been enhanced.

Because of the nanocrystalline nature of phase 2 and of the electron diffraction limitations, structural refinement of this new phase is nearly impracticable.

Nevertheless, few structural suggestions might be done on the basis of our HREM and diffraction measurements.

First of all, the large difference in the number of diffracted spots between the first ring (located at 4.68 Å) and the two successive ones, arising from an anisotropy in the distribution of the crystal orientation, might be a signature of an anisotropic character in the structure of the crystal. These 3 first distances are visible on the HRTEM images in figure3b and 3c. We present in figure 3b a lattice fringes image of the 4.68 Å plane and we call c_1 this interplanar distance (keeping in mind that it might be related in a complex manner to a real cell parameter). Nanodiffraction on this area (and similar ones with observable c_1 planes) have demonstrated that the c_1 planes are perpendicular to the planes with interreticular distances of 2.73 Å and 2.37 Å. We present on figure 3c a HREM image collected on the area of the polycrystalline cluster showing the stronger diffraction contrast. Lattice fringes of 2.73 Å (named b_1) and of 2.37 Å (named a_1) distances are observed confirming the two intense rings measured in the powder diffraction pattern. One may also note that the cristallinity of that new CN_x product is good. In fact, no defects have been detected in the HREM images (except an electron beam induced amorphisation at the thinnest part of the crystal). In figure 3d, the SAED pattern corresponding to the same orientation as in the previous HREM image has been collected for one crystal of about 80 nm in size located at the boarder of a cluster. Despite these quite good conditions, several other crystals with different orientations have been involved during the analysis and we have tagged by an arrow the diffraction spot of interest. Bragg spots named A_1 and B_1 correspond respectively to the 2.37 Å and the 2.73 Å distance and the symmetry of the diffraction pattern is 2mm (with mirrors set parallel to OA_1 and OB_2 directions). Since these two sets of planes are perpendicular to the c_1 planes, this SAED pattern correspond to a [001] axis zone where we have assumed that c_1 may be considered as a cell parameter. In this case, the SAED pattern may be described within a non primitive orthorhombic cell with OA_1 and OB_2 as unitary vectors (and presumable extinction at half distance of OA_1 and OB_2 vectors). To summarise, the crystal structure of this new phase is still questionable, but it may belongs to the orthorhombic system with presumable lattice parameters of around a =

4.75 Å (corresponding to half extinction distance of OA_1), b = 3.26 Å (corresponding to half extinction distance of OB_2) and c = 4.64 Å.

A detailed analysis of the EELS data gives complementary information about the structure, the stoechiometry and the bonding configuration of the crystalline phase.

First, a rough quantification of spectra from the crystalline phase (see figure 4) leads to a large distribution of N/C atomic ratios from 0.80±0.15 to 0.95±0.15. This dispersion in composition is due to uncertainties in the quantification method related to changes in the ELNES, which are not reproduced by the tabulated ionisation cross-sections.

Secondly, the observed ELNES display a first narrow peak with very high intensity both on CK and NK edges. These peaks are unusually sharp as compared to other condensed phase CN_x materials which suggests a molecular character of the involved electron states (presumably of π^* symmetry) as observed in pyridine and pyrrole molecules**.** However the peaks energy positions of the present CN_x phase do not fit with those reported for pyridine and pyrrole solids (23) (24). As shown in figure 4, similarities in the ELNES between CK and NK are also observed at high energy (20eV above the onset). On the contrary the intermediate energy region, in between 5eV and 20eV after the onset shows clear discrepancies. Although no interpretation is proposed here, one notes however the unusual observation that the number of unoccupied states in the lower energy level of s symmetry is much higher in nitrogen than carbon.

The anisotropic character of the structure is also revealed by the angular dependence analysis of the ELNES signals . In angular dependence experiments, one varies the direction of the momentum transfer with respect to the crystallographic axis of the material (and therefore to the orbitals orientation). As the probe is scanned over several grains with different orientation, changes in the relative intensity of the different peaks are observed both in the CK and NK edges (figure 4). This variation occurs so that the first and third peaks of CK edge (286.8 eV and 308 eV respectively) are correlated with second peak of nitrogen (405 eV). Such anisotropic effects were confirmed by angular-resolved experiments on isolated nanocrystals (not shown here). Therefore, it appears that the first molecular-like π^* peaks display an anticorrelated angular dependence behaviour in N and C. This corroborates the assumption of non layered phase (CN graphitic like) in which a correlated angular dependence of the π* peaks in C and N would be expected.

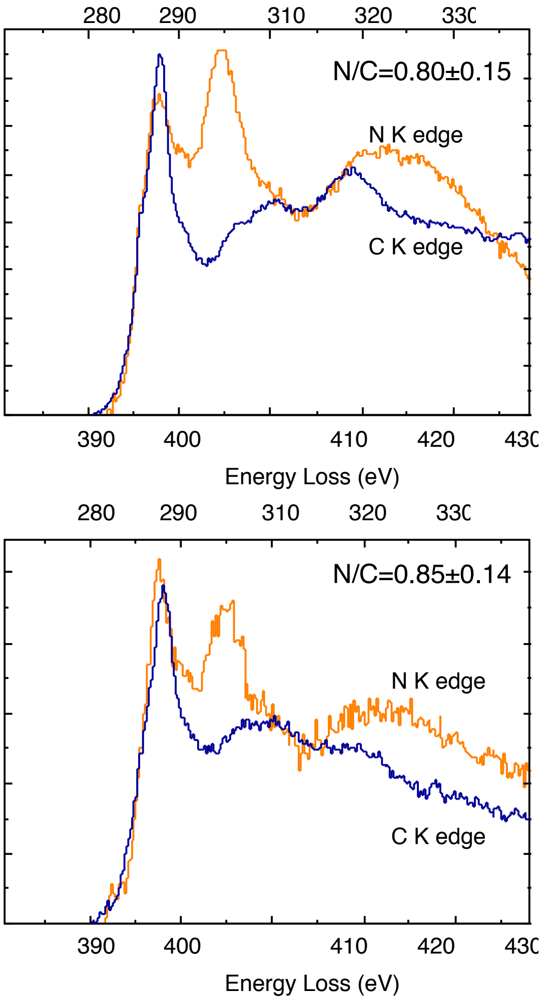

Figure 4.- C and N ELNES of the crystalline phase. The spectra have been extracted from a line-scan series.

CONCLUSION

The combination of spatially resolved EELS with appropriated mathematical analysed methods and electron diffraction and imaging techniques has been proved to be an accurate approach for characterising inhomogeneous materials as CN_x nanocrystals embedded in an amorphous matrix. As a result, the signal from a new CN_x phase has been isolated and characterised. A new crystalline structure of orthorhombic type with a stochiometry close to CN is proposed. The weak anisotropic character is revealed by both electron diffraction and ELNES analysis. Sharp resonances in both CK and NK edges indicate the presence of highly localised electron states in such system.

ACKNOWLEDGMENT

We acknowledge Prof. Z.C. Qin for providing the sample. The financial support from the EU-TMR network CT97-0103 "Synthesis, structure and characterisation of new Carbon Based Materials" and from AFCRST on a French-Chinese project PRAMX99-01 is also acknowledge.

Table 1. Composition and π* peak position in the C K edge for the various spectra recorded at different areas of the sample.

	Spec 1	**Spec 2**	**Spec 3**	**Spec 4**	**Spec 5**
N/C **N at.%**		0.28±0.04 22±3 at.%	0.35 ± 0.06 26 ± 3.6 at. %	O.68±0.11 40±5.4 at.%	0.95±0.15 49±6.1at.%
π* peak **(eV)**	284 -----	284.8 ------	285 286.8	285 286.8	------ 286.8

REFERENCES

(1) AY Liu, ML Cohen: Prediction of new low compressibility solids. Science 245 (1989) 841 - 42.

(2) KM Yu, ML Cohen, EE Haller, WL Hansen, AY Liu, IC Wu: Observation of crystalline C_3N_4. Phys. Rev. B 49 (1994) 5034-37.

(3) Q Zhang, ZC Qin, J Zhu: Atomic and electronic structure of a carbon nitride compound prepared by magnetron sputtering. Phil. Mag. Lett. 80 (2000) 585-90.

(4) J Wei, P Hing: Formation of beta-C3N4 grains by sputtering. Surface Engineering 16 (2000) 221-24.

(5) TS Wang, DL Yu, YJ Tian, FR Xiao, JL He, DC Li, WK Wang, L Li: Cubic-C3N4 nanoparticles synthesized in CNx/TiNx multilayer films. Chem. Phys. Lett. 334 (2001) 7-11.

(6) EG Wang, Y Chen, L Guo: Synthesis and characterisation of pure crystalline C-N film. B. Chinese Acad. Sci., China. 17th Nordic Semiconductor Meeting Trondheim, Norway (1996).

(7) H Sjöström, S Stafström, M Boman, J-E Sundgren: Superhard and elastic carbon nitride thin films having fullerene-like microstructure. Phys. Rev. Lett. 75 (1995) 1336-39.

(8) LP Guo, Y Chen, EG Wang, ZX Zhao: Identification of a new tetragonal C-N phase. J. Cryst. Growth 178 (1997) 639-44.

(9) E Kim, C Chen, T Köhler, M Elstner, T Frauenheim: Tetragonal Crystalline Carbon Nitrides: Theoretical Predictions. Phys. Rev. Lett. 86 (2001) 652-55.

(10) M Mattesini, SF Matar: DFT Investigation of Hardness, Stability and Electron Energy Loss Spectra of Carbon Nitrides in the C11N4 stoichiometry. Phys. Rev. B in press (2001).

(11) E Sandre, CJ Pickard, C Colliex: What are the possible structures for CNx compounds? The example of C3N. Chem. Phys. Lett. 325 (2000) 53-60.

(12) O Stephan, PM Ajayan, C Colliex, P Redlich, JM Lambert, P Bernier, P Lefin: Doping Graphitic and Carbon Nanotube Structures With Boron and Nitrogen. Science 266 (1994) 1683-85.

(13) K Suenaga, T Tence, C Mory, C Colliex, H Kato, T Okazaki, H Shinohara, K Hirahara, S Bandow, S Iijima: Element-selective single atom imaging. Science 290 (2000) 2280-282.

(14) C Jeanguillaume, C Colliex: Spectrum-Image - the Next Step in EELS Digital Acquisition and Processing. Ultramicroscopy 28 (1989) 252-57.

(15) The former combines linearly the different reference signals to best reproduce the experimental ELNES. It is a quite efficient method but its main limitation is due to the lack of freedom in the choice of the reference spectra and the necessity of having access to a series of known references. On the contrary, MSA treats the data as a whole and does not make any a priori hypothesis on the choice of the reference signals. The goal of this method is to identify several basic sources of information as contributing (through linear combination) to the overall experimental data. An integration window of 30 eV and 20 eV, from the onset of the edge towards higher energy, has been used for the NNLS and MSA analysis respectively.

(16) RD Leapman, P Rez, DF Mayers: J. Chem. Phys. 72 (1980) 1232.

(17) KWR Gilkes, J Yuan, GAJ Amaratunga: Electron energy loss spectroscopy of amorphous carbon nitride. Diamond and Related Materials 5 (1996) 560-63.

(18) K Suenaga, M Yudasaka, C Colliex, S Iijima: Radially modulated nitrogen distribution in CN_x nanotubular structures prepared by CVD using Ni phtalocyanine. Chem Phys. Lett 316 (2000) 365.

(19) A Fernandez, JC Sanchez-Lopez, G Lassaletta: Characterisation of carbon nitride thin films prepared by reactive magnetron sputtering. Carbon 36 (1998) 761-64.

(20) J Wang, J Lei, R Wang: Diffraction-pattern calculation and phase identification of hypothetical crystalline C_3N_4. Physical Review B (1998) 11890-895.

(21) I Alves, G Demazeau, B Tanguy, F Weill: On a new model of the graphitic form of C3N4. Solid State Commun. 102 (1999) 605.

(22) A Snis, SF Matar: Electronic density of states, 1s core-level shift, and core ionization energies of graphite, diamond, C_3N_4 phases and graphitic $C_{11}N_4$. Phys. Rev. B. 60 (1999) 10855-63.

(23) JA Horsley, J Stohr, AP Hitchcock, DC Newbury, AL Johnson, F Sette: Resonances in the K-Shell Excitation-Spectra of Benzene and Pyridine - Gas-Phase, Solid, and Chemisorbed States. Journal of Chemical Physics 83 (1985) 6099-107.

(24) DC Newbury, I Ishii, AP Hitchcock: Inner Shell Electron-Energy Loss Spectroscopy of Some Heterocyclic Molecules. Canadian Journal of Chemistry-Revue Canadienne De Chimie 64 (1986) 1145-55.

(25) O Stephan, PM Ajayan, C Colliex, F CyrotLackmann, E Sandre: Curvature-induced bonding changes in carbon nanotubes investigated by electron energy-loss spectrometry. Phys. Rev. B 53 (1996) 13824-29.

(26) A Gloter, J Ingrin, D Bouchet, C Colliex: Composition and orientation dependence of the O K and Fe $L_{2,3}$ EELS fine structures in reference and substituted brownmillerites. Phys. Rev. B 61 (2000) 2587-94.

(27) NK Menon, J Yuan: Quantitative analysis of the effect of probe convergence on electron energy loss spectra of anisotropic materials. Ultramicroscopy 74 (1998) 83-94.

PAPER IV

A ROUTE TO STUDY THE CARBON-NITROGEN BOND: CHRONO-SPECTROSCOPY IN MELAMINE.

S. Trasobares[1], R. Räty[1], N. Borglund[4], A. Bassan[4], C. Kolczewski[4], L.G.M. Pettersson[4], G. Hug[2], C. Colliex[1,3,] S. Csillag[4].

1 Laboratoire de Physique des Solides, UMR8502, Université Paris Sud, Building 510, 91405 Orsay, France

2 ONERA – LEM, BP 72 - 29, Av. de la Division Leclerc, F-92322 CHATILLON CEDEX, France

3 Laboratoire Aimé Cotton, UPR3321, Université Paris Sud, Building 510, 91405 Orsay, France.

4 Department of Physics, Stockholm University, Stockholm Center for Physics, Astronomy and Biotechnique - SCFAB, 10691 Stockholm, Sweden

ABSTRACT

The decomposition process of melamine exposed to a high-energy electron beam has been investigated by monitoring the changes in the Energy Loss Near Edge Structures (ELNES) using Time Resolved Electron Energy-Loss Spectroscopy (EELS). Calculations on different CN containing molecules were performed in order to simulate the experimental ELNES observed at the different decomposition stages and to identify the different intermediate compounds produced during this degradation process. As a result, we suggest that the amino groups are first eliminated as a release of N_2 gas. Then the degradation of the molecule occurs through a reduction of the carbon-nitrogen double bonds either by addition of hydrogen or by bond cleavage. If the irradiation is maintained over longer periods, the formation of different CN fragments and of extended triazine rings could then be possible.

To be submitted to J. Physical Chemisytry

1. INTRODUCTION

Using a semi-empirical assumption based on a range of exciting hard materials, Liu and Cohen [1] predicted from ab initio calculations, that the crystalline β-C_3N_4 compound should be stable and might have mechanical properties stronger than, or similar to, diamond. This has stimulated a lot of experimental efforts to synthesise and characterise carbon nitride materials. The production by different processing routes of CN_x films [2-5] and CN_x nanotubes [6-9], as well as their characterisation using several different techniques, has been reported. All investigations generally show that only a limited amount of nitrogen might be inserted in the carbon network. Among the techniques applied so far, X-ray photoelectron spectroscopy (XPS) and Electron Energy Loss Spectroscopy (EELS) are interesting methods in that they, in the most favourable cases, allow obtaining chemical compositions as well as information on the atomic structure and bonding of the materials. However, a correct identification of the nature of the bonding is difficult in amorphous materials where structural hypotheses are complicated, as for example in amorphous CN materials. The interpretation of the sometimes complicated Near Edge Structure (NES) of the absorption edges is not trivial and a close connection with theory becomes essential. Only transitions from 1s to π^* antibonding orbitals can be easily observed as a sharp peak several eV under the ionisation edge. The position of such a peak is expected to be connected to different atomic configurations as for example in the case of sp or sp^2 bonded carbon and nitrogen atoms. Thus, a precise characterisation of these materials can be greatly facilitated by comparison with reference spectra of known materials or by comparison with reliably predicted NES from possible model structures. These spectra are used as fingerprints of the electronic structure of the material or molecule in order to establish which type of bonding is present. This will be used in the present work to identify the degradation products of melamine exposed to a high-energy electron beam.

Melamine ($C_3H_6N_6$), figure 1a, has been used in the production of melamine-formaldehyde, resins for surface coating, laminates and adhesives and in the production of flame retards [10]. Recently it has been used as organic precursor in the production of CN_x nanotubes by pyrolysis [10] and detonative decomposition [11]. In both cases, a decomposition process of the melamine molecule is observed.

The melamine was found to be extremely sensitive to radiation damage by high-energy electrons during observation in a transmission electron microscopy, which offers the possibility to study its degradation decomposition process. In this study we present the use of the NES spectra at different stages of the decomposition of the melamine molecule to monitor changes in the bonding characteristics in order to clarify the resulting bonding of carbon and nitrogen in the carbon nitride materials.

2. EXPERIMENTAL

Melamine powder (s-triaminotriazine, Aldrich, 99%+), fig. 1a, was ground with a mortar and suspended in acetone for TEM observation. The sample was analysed in a VG 501 Scanning Transmission Electron Microscope (STEM) operating at 100 keV, and equipped with a Gatan parallel EELS detector. The energy resolution of the whole system was about 0.7 eV. Recently, a specific CCD camera was fitted in the spectrometer to improve the sensitivity of the detection [12]. With the new equipment, the required acquisition times for achieving a satisfactory signal-to noise ratio in any spectrum are of the order of 1-5 milliseconds for the plasmon region and 5 milliseconds to 1 second for the core loss region. This short acquisition time permits us to investigate the transformation of the materials under the beam. The modifications in the NES during irradiation were studied by time resolved EELS (chrono-spectroscopy): a probe of 0.5 nm in diameter is fixed at a specific location of the specimen and a series of spectra with the time as variable is recorded. The sample was found to be extremely radiation sensitive. Immediate visual changes could be seen in the image when the beam was focused on the sample. In order to detect the stages in the decomposition process, a bunch of 2000 spectra were recorded at intervals of 9 milliseconds. Figure 1b shows a series of 30 such spectra. The characteristic signals corresponding to the C and N *K* edges are observed. It is noticed at the first stages of the process that the intensity of the sharp peak at the N *K* edge increases during a few milliseconds after which it starts to decrease.

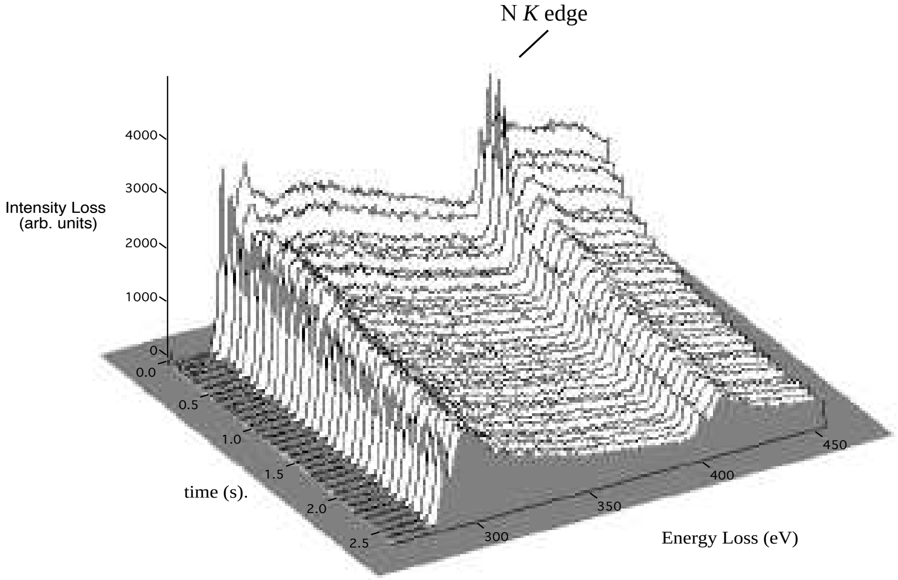

Figure 1.-a) Melamine molecule structure. b) A collection of 30 spectra recorded at 90 millisecond intervals. This represents the first stages in the decomposition process of the melamine.

In order to study the NES, 20 consecutive spectra with identical NES were summed and normalised in the 280-430 eV area. Characteristic spectra of the different transformation stages of the carbon and nitrogen *K* edges can be seen in figure 2.

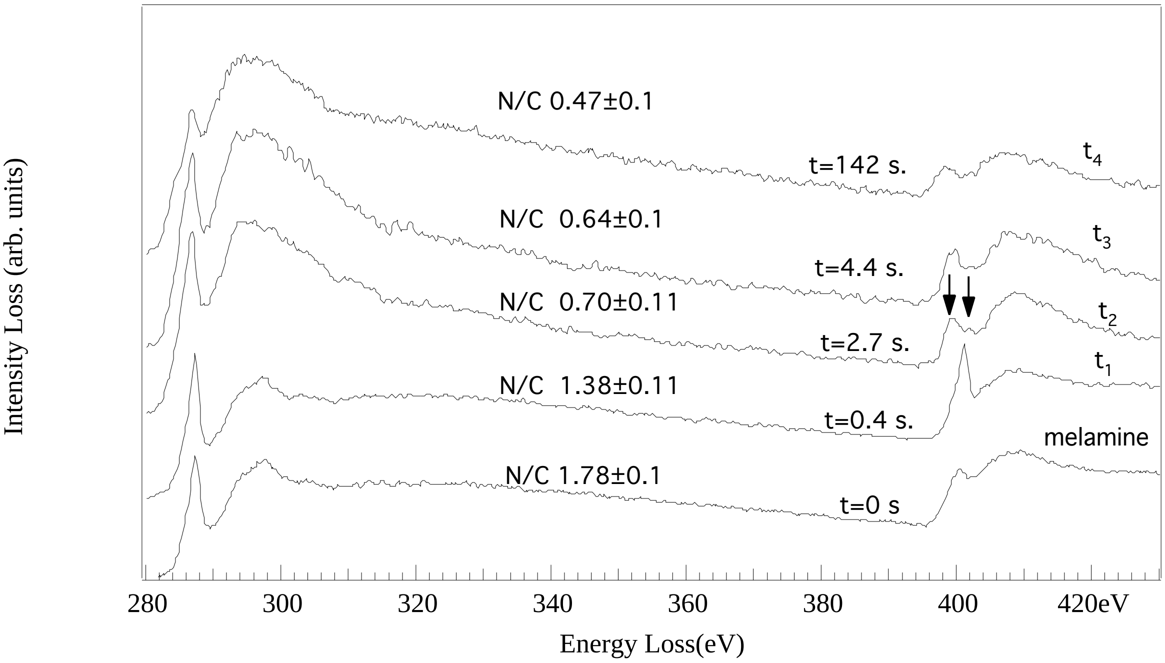

Figure 2.- Normalised spectra corresponding to different stages in the melamine decomposition process. 20 spectra with identical NES were summed and normalised in the 280-430 eV area.

3. COMPUTATIONAL

The density functional theory (DFT) calculations for the NES spectra were performed at the gradient-corrected DFT level using the deMon program [13]. The theoretical X-ray absorption spectra were generated by the transition potential (TP) method [14,15] in combination with a double basis set technique [16]. A detailed description of the method and implementation within the DFT framework can be found in ref.[17]. Briefly, the orbitals for the molecule are determined using a good quality molecular basis set with a half-occupied core-orbital at the ionisation site. The orbitals for the excited electrons are then obtained by diagonalising the Kohn-Sham matrix built from the density from the TP calculation; the basis set is in this second step extended with a large set of diffuse basis functions (~150 functions) centred on the excited atom. The obtained orbital energies and computed transition moments provide a representation of the excitation energies and associated intensities in the theoretical spectrum.

The TP calculation gives most of the relaxation effect upon core-ionisation and provides a single set of orthogonal orbitals for the spectrum calculation. In order to determine the absolute energy position of the spectrum, we performed ΔKohn-Sham (ΔKS) calculations of the ionisation energy (IP), using the fully ionised core hole state. Relativistic effects on the IP of 0.3 eV for the N edge and 0.2 eV for the C edge [18] were added to give the overall shift of the spectrum. In the ΔKS-calculations the non core-excited C (N) atoms were described by effective core potentials (ECP). This simplifies the definition of the core hole state, since the use of an ECP description eliminates the 1s level of the atom to which it is applied. The ECPs introduce insignificant effects on the computed spectrum, see reference [19].

The DFT TP calculation of the spectrum assumes a frozen molecular ion density and thus neglects the relaxation effects on the molecular ion core upon adding the excited electron. This effect is largest for the valence-like π^* excitations and these states were therefore computed with fully relaxed ΔKS calculations. For triazine, pyrrole and pyridine a sequence of most prominent excitations, being transitions into antibonding orbitals of σ symmetry and Rydberg orbitals, were furthermore calculated in fully relaxed ΔKS excited state calculations. It was found that the first transitions show relaxation effects around 2.0 to 2.5 eV, whereas higher transitions with a lesser amount of valence orbital mixing usually show relaxation shifts in the order of the shift of the ionisation potential. For details see reference[20]. For these three molecules the corresponding peaks in the energy-shifted TP spectrum have been shifted to include the additional relaxation effects obtained from the specific ΔKS excited state calculations, whereas for the remaining molecules only the first π* transition was shifted according to the calculated relaxation. The other prominent transitions were shifted, depending on their orbital character, by the same amount as the first π* resonance (valence-like) or according to the ionisation potential (Rydberg character).

As a first step for each molecule a geometry optimisation was performed using a triple-zeta valence plus polarisation (TZVP) basis[21] in a [4s, 3p] contraction with one added d-function for nitrogen and carbon and a primitive (5s) basis set augmented with one p-function and contracted to [3s, 1p] for hydrogen[22]. In order to obtain an improved representation of relaxation effects in the inner orbitals, the ionised centre was described by the IGLO-II basis of Kutzelnigg et al.[22]. In the spectrum calculations a large [19s, 19p, 19d] diffuse even-tempered basis set centred on the ionisation site was added; it was employed only in the last step of the calculation. The spectrum was generated by a gaussian convolution of the discrete spectrum with a broadening in the pre-edge region that was selected to resemble the experimental resolution. For the synchrotron reference spectra we thus used 0.7 eV full-width-at-half-maximum (FWHM) for the features before the edge, while for the EELS data gaussians with FWHM 1.5 eV were used. The continuum states were convoluted using gaussians with a FWHM that was linearly increased over an interval of around 10 eV from the edge up to a FWHM of 3.5 eV. At higher energies the FWHM was kept constant at this value. All DFT calculations were performed using the gradient-corrected Perdew[23] exchange and correlation functionals.

4. INTERPRETATION AND DISCUSSION

The composition ([N]/[C] at. ratio) was measured from the EELS data by determining the integrated intensity of the C and N ionisation *K* edges after background subtraction. A classical power-law (A exp(-rE)) of the background and a hydrogenic model for the *K* edge cross sections[23] have been used. A clear nitrogen loss is observable during the irradiation process as indicated in figure 3. Since the H-K edge at 12 eV was obscured by the strong background due to valence electron losses, it was impossible to have a good quantification for hydrogen from the EELS analysis, however a tendency can be observed. Figure 3 shows the integrated intensity of the background before the C *K* edge, which is associated to be proportional to the total number of atoms, compared to the intensity profile for carbon and nitrogen. The loss of carbon is linearly decreasing with time. The nitrogen loss, first, follows an exponential law before becoming linearly decreasing after 1.2 seconds. This suggests that there is a rapid loss of nitrogen at the beginning of the process. In order to study the rate of decrease of N and H, a logarithmic analysis of the total intensity, I_t, and of the nitrogen intensity, I_N, is presented in figure 3b. The same behaviour as for nitrogen is observed for the total intensity profile, but in this case the negative slope is even larger. Therefore, we can assume a simultaneous loss of hydrogen and nitrogen at the beginning of the process. This correlated loss can be explained as follows: when the molecule is exposed to the electron beam, core electrons are excited to antibonding or continuum states. This is followed by Auger decay, which creates a dipositive ion that may involve loss of electrons from bonding as well as from non-bonding orbitals. This dipositive state is highly repulsive and dissociates. The amino groups are connected to the ring by single bonds, whereas the ring atoms have two bonds (as well as the π-system) that must be broken before they can leave the molecule. Thus, it is much more probable that an amino group will leave as a result of the deexcitation processes, which explains the observed correlated loss of hydrogen and nitrogen.

The decomposition of melamine has been previously reported and different mechanisms have been proposed. The formation of melam (molecular weight (MW)=235, $C_6H_9N_{11}$) and melem (MW=218, $C_6H_6N_{10}$), both extended rings, and elimination of NH_3 as a gas, have been observed by thermal decomposition of melamine[24,25]. Ju *et al* [26] have studied the fragmentation of the melamine ring via electron impact ionisation, laser desorption ionisation and collision-induced dissociation. They observed that bombardment with 70 eV electrons, apart from melamine ions, yielded mainly $CH_3N_2^+$ and $CH_4N_5^+$. In addition, other molecular fragments, as well as NH_4^+, can be observed in the mass spectroscopy data. It has been found that the higher the electron energy, the higher is the fraction of small fragments. As the electrons in the microscope have a kinetic energy about a thousand times higher than in the experiments of Ju *et al*[26], it can be presumed that molecules will indeed be fragmented.

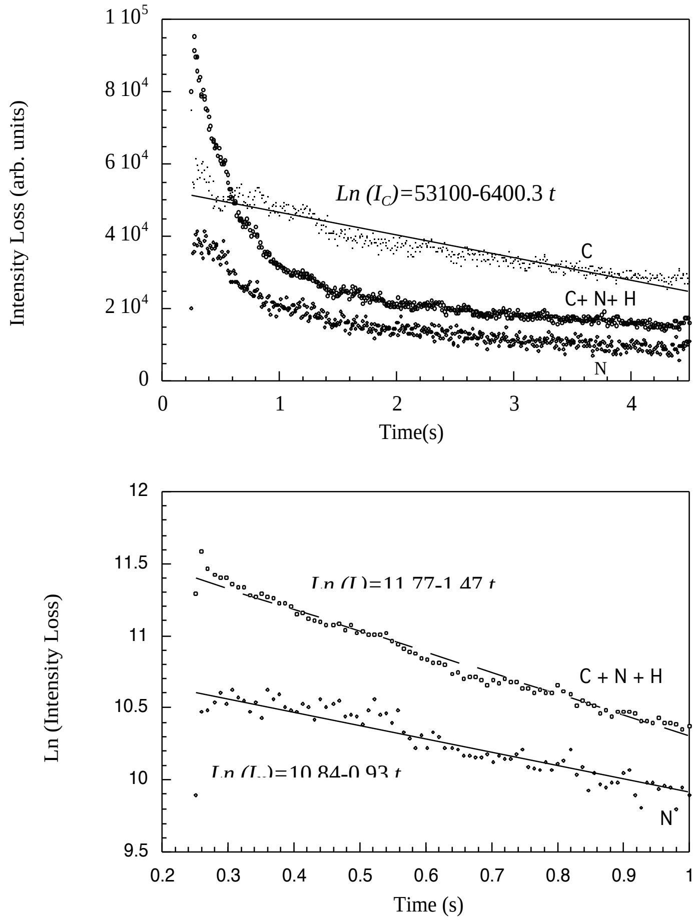

Figure 3.- a) Experimental variation of the C, N and total intensity. The N and total intensity follow an exponential law while the C intensity is linearly decreasing with time. (r is the confidence fitting parameter) b) Logarithmic variation of the nitrogen intensity, I_N, and total intensity, I_t.

Figure 2 shows normalised spectra corresponding to different stages in the melamine decomposition process. The original melamine spectrum is indicated as time=0. The spectra t_1, t_2, t_3 and t_4 were recorded after irradiating the melamine for 0.4, 2.7, 4.4 and 140 seconds, respectively. The spectra labelled melamine, t_1, t_2, and t_3 all present a strong π^* peak at the carbon edges. However, a strong decrease in the intensity of the π^* peak is noted in spectrum t_4. The shape of the C *K* and N *K* edges in the melamine and the t_1 spectra is characteristic of thick samples, since they exhibit an additional contribution at 310 and 420 eV respectively, an energy equal to the edge threshold plus the plasmon resonance energy. These additional features, due to multiple losses in thick samples, are not observed in spectra t_2 and t_3, which is an evidence for significantly thinner samples.

The details in the NES can be studied more closely. The *K* edges correspond to transitions from 1s states to unoccupied states above the Fermi level; the changes in the NES will thus reflect any change in the local bonding[27]. Therefore, it is interesting to compare the NES at the N *K* edge in the recorded spectra to corresponding data in CN molecular systems such as triazine[28] ($C_3H_3N_3$), pyridine[29] (C_5H_5N) and pyrrole[30] (C_4H_5N), (figure 4), which will also be used for testing the validity of our computational approach.

All these compounds are based on aromatic molecules in which the nitrogen atoms are present in sp^2 hybridisation, but where the N can still contribute differently to the molecular orbital structure. The fifth valence electron of the N atom can form a lone pair either with the remaining unhybridized $2p_z$ orbital, or with one of the sp^2 orbitals. The first case leads to a localized $2p_z$ lone pair and the three sp^2 hybrid orbitals bond to other atoms. This case is observed in the pyrrole molecule. If the fifth electron instead forms a lone pair with one of the sp^2 hybrid orbitals, the atom is left with two sp^2 hybrid orbitals and one unfilled $2p_z$, and can therefore form one π and two σ bonds as observed in the pyridine molecule. However, in the pyridine case, even though the N atom exhibits sp^2 hybridisation, it does not contribute any mobile electrons to the structure. Nitrogen is more electronegative than carbon and the nitrogens thus attract electrons from the rest of the molecule, leaving the C atoms electronically poor. The spectra of these molecules present a strong π* peak, which is found at 286.16 eV for *s*-triazine (286.1 eV), with the computed values in parenthesis. The π^* peak becomes broader in the case of pyrrole and pyridine and is found at 286.3 eV (286.4 eV) and at 284.88 eV (284.7 eV), respectively. The origin of the broadening in the π^* peak is the different chemical shift on the carbons induced by the presence of the nitrogen in the ring[20,31].

The situation is more complex for the nitrogen edge. The first peak at the N *K* edge at 398.8 eV (pyridine: 398.4 eV, triazine: 399.0 eV) displays similarities in shape and energy position for triazine and pyridine. This peak is associated with transitions from 1s core states to unoccupied molecular states of π* symmetry (π* peak). For pyrrole, this transition is shifted up in energy and is observed at 402.3 eV (402.4 eV); the sharp feature contains contributions both from the π* (dominating contribution) and some σ^* contribution at the same energy (at 0.5 eV higher energy in the TP calculation).

The agreement between the computed and experimental reference spectra is very good, both for the energy positions and relative intensities, but most importantly, for the overall appearance of the computed spectra.

After this general introduction to the spectral characteristics of relevant bonding situations, we now turn to a presentation of the experimental spectra of melamine at the different stages in the electron beam induced decomposition as shown in Fig. 3. Earlier *ab initio* calculations have shown that melamine is a nearly planar molecule where the amino-hydrogens are only slightly out of the triazine ring plane[32]. Even though melamine has three N atoms in the triazine ring and three N atoms in the amino groups, the nine C-N bonds are very similar with a distance similar to that of a single C-N bond[33].

Starting with the C *K* edge of the melamine spectrum we find a strong π* peak at 287.26 and a σ* peak at 296.8 eV. The value for the π* peak is higher than those observed for the reference CN-molecules, but the position and shape of the σ* peak is similar to that of triazine. The shift in the π* position relative to *e.g.* triazine is confirmed in the present theoretical calculations and is due to the presence of the additional electron-donating amino-groups at each carbon in the melamine molecule. The N *K* edge in the melamine spectrum shows a peak at 400.5 eV, which is the energy position typical of molecules such as ammonia (NH_3) and methylamine (CH_3NH_2)[34]. The σ* position at about 9 eV higher energy is consistent with the separation found from the carbon spectrum.

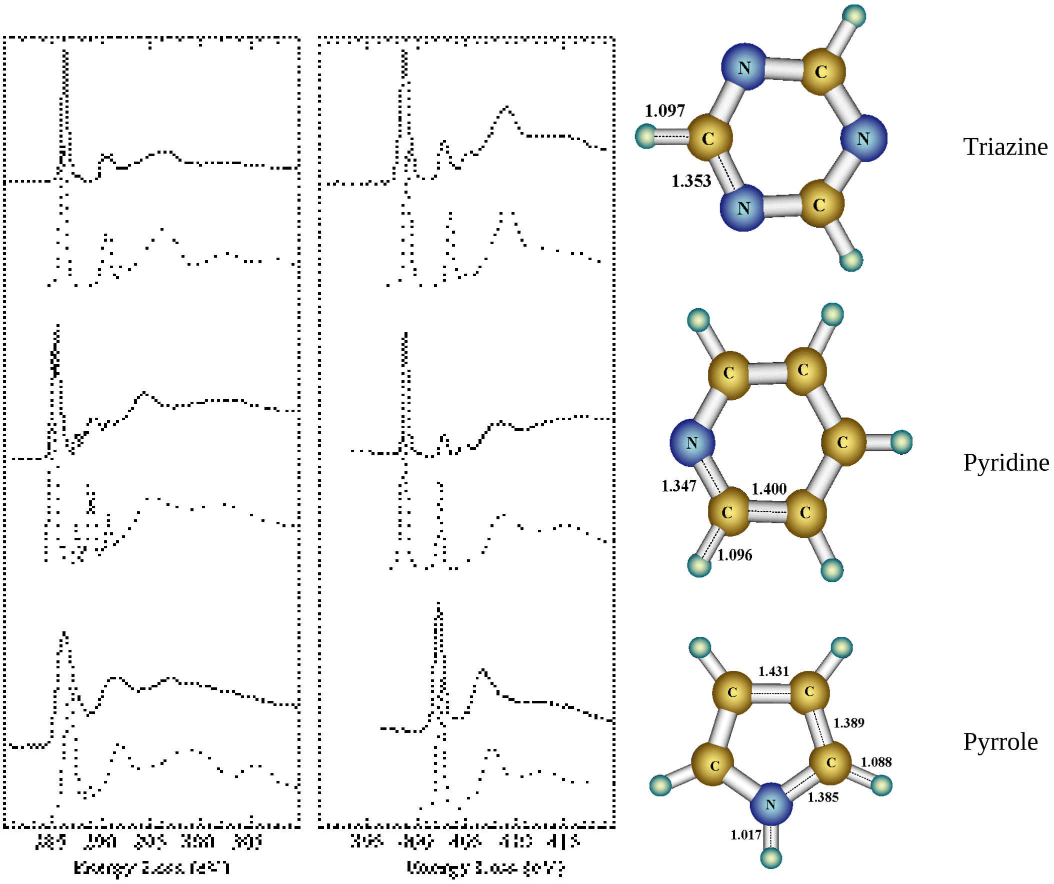

Figure 4.- Experimental (solid lines) and computed (dotted lines) C, N *K* edge spectra and structures for the molecules triazine, pyridine and pyrrole. The experimental data was obtained from the Hitchcock (http:/xray.uu.se/hypertext/corexdb.html) data-base. The bond distance are in Å.

In spectrum t_1, which corresponds to the highest intensity in the N K 401 peak, the C *K* edge presents the same structure as observed for melamine, but some differences are noticed in the N *K* edge. A reduction of the N/C ratio from 1.78 to 1.38 (a lower value than what would be expected for the melam or melem molecules) is observed and an additional sharp peak is observed at 401 eV. The absence of changes in the C *K* edge suggests that the Caromaticity structure of the molecule is not affected. The presence of a strong π^* peak at 401.1 eV has previously been reported for N_2 gas[35]1. The absence of changes in thickness and C *K* edge structure, together with the decrease of the N content, suggest a possible formation and elimination of N_2 during the first stage.

In spectrum t_2, the intensity of the π^* peak at the C *K* edge does not change drastically, a small decrease in the intensity and some changes in the σ shape are observed. The nitrogen content in the sample decreases from 1.38 to 0.70 N/C (t_2) and to 0.64 (t_3). Moreover, a strong loss of material is deduced from the vanishing of the multiple-loss shape, which is observable in the first spectra (melamine and t_1). Changes in the N *K* edge are more important with two new peaks observed at the N *K* pre-edge region (at 398.9 and 401.9 eV). During this stage of the process, comparing the t_2 and t_3 spectra we notice that the intensity of the peak at 401.9 eV decreases while the intensity of the 398.9 eV peak increases. These values correspond to those observed for the *s*-triazine molecule, but in the latter case the peaks are sharper than in the present experiment. This difference could be explained by the fact that the reference experiments were recorded at higher energy resolution in a synchrotron radiation ring. From the observations, we assume that the loss of nitrogen in the first stage of decomposition could be due to the loss of the amino groups, which does not influence the aromaticity of the molecule.

A 47% reduction of nitrogen content is observed in spectrum t_4, which was recorded after 140 seconds of irradiation. The π^* peak at the C *K* edge is weaker than in the t_1 and $t_{2,3}$ spectra. The nitrogen peak at the onset, on the other hand, is getting broader, exhibiting a shape which is quite common in CN thin films. It presents a shoulder-like feature, which most likely originates from contributions from various nitrogen-bonding configurations. The dependence of the positions of the different peaks on the different nitrogen atom bonding and surrounding atoms has been studied by Xin[37] who showed that both two- and three-coordinated nitrogen atoms display peaks in the 398-405 eV region.

In Figure 5, a scheme of the possible stages present in the decomposition process of melamine is displayed. The spectra from the different stages have been computed and compared to the experimental results, as described in the next section.

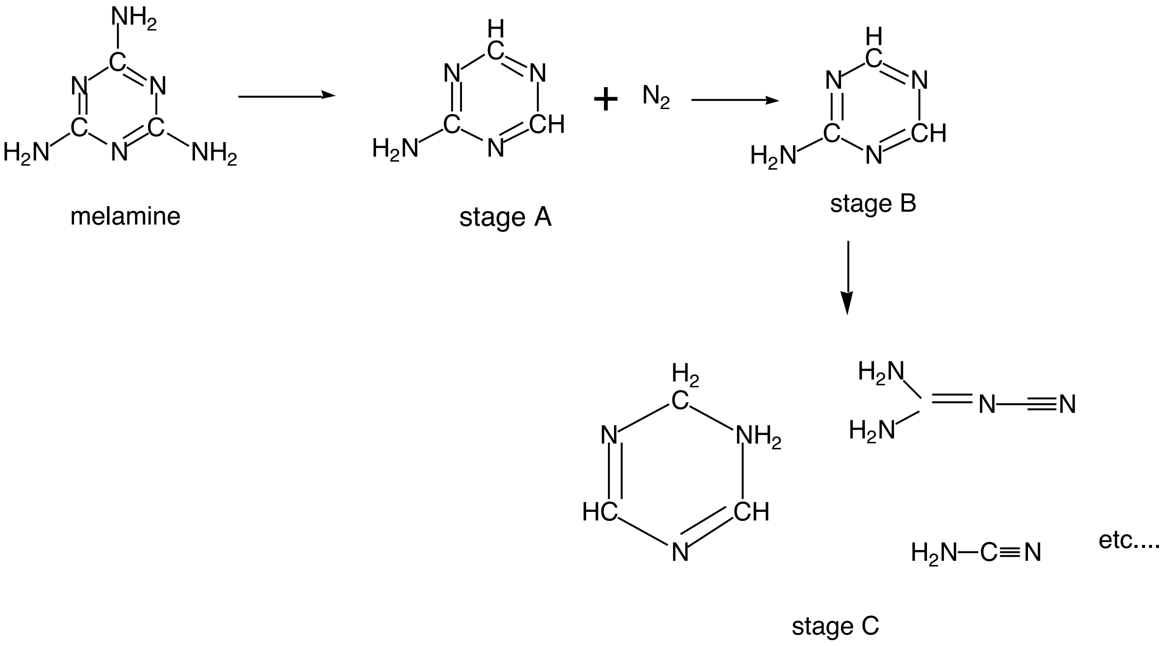

Figure 5.- Proposed mechanism for the first stages of the decomposition of melamine.

5. PROPOSED MECHANISMS AND COMPUTATIONAL RESULTS

The melamine and *s*-triazine have previously been shown to have different pathways of decomposition. The triazine molecule dissociates into three HCN fragments. The main molecular properties of the melamine are characterised by the interaction between π-electrons in the triazine ring and the lone-pair electrons in the amino groups[33]. Indeed, the melamine spectrum shows the aromaticity of the molecule (strong π* peak at the C *K* edge) and the symmetry of the bonds. The energy position of the N peak corresponds to the observed value in CN molecules with a single bond as for example in methyl-amino.

The melamine has mobile hydrogens, which can be shifted to the ring and enhance the decomposition process. (reference) This process has been previously studied and the formation of melam ($C_6H_9N_{11}$), melem ($C_6H_6N_{10}$) and CN fragments has been observed[24,25]. These molecules have not been observed by EELS analysis in the present study. The absence of melam and melem molecules can be explained by the high electron energy used during the present study. Ju *et al*[26] have shown that the higher the electron energy, the higher is the fraction of small fragments.

An individual study of the spectrum variations shows the different stages of the decomposition process as follows:

Starting with the initial melamine spectrum we find an excellent agreement between the computed and measured spectra for both the N and C *K* edges. The nitrogen spectrum is composed of contributions both from the ring atoms and from the amino groups, where the ring atoms give the main contribution to the π^* resonance at 400.1eV (computed), while the amino groups dominate the resonance at 404 eV. The relative intensities in these regions can thus be used to follow the removal of amino groups from the melamine. We have to keep in mind that the experiment was carried out in a melamine solid while the theoretical calculations have been performed on an isolated molecule, which could explain the differences observed in the σ part of the N K edge in the melamine spectrum.

At the first stages of the decomposition process, a decrease of nitrogen content (i. e with N:C from 1.78 to 1.38), combined with the appearance of a shoulder at the C *K* edge are observed, as seeing in spectrum t_1. It suggests that the eliminated N comes from the external amino groups of the melamine molecule, which do not affect the aromatic structure of the molecule, (figure 5, stage A). This is consistent with the computed spectrum, which obtains the spectrum of stage A, the carbon without the amino group is chemically shifted to 1.3 eV lower energy, whereas the two carbons with an amino group are unchanged in energy position compared to the melamine. This results in an intensity ratio of 1:2 of the shoulder to the main peak in the C K edge t_1 spectrum, which is also observed experimentally. This is consistent with an average initial loss of one amino group per melamine molecule. During the first 90 milliseconds of the process, an increase in intensity of the 401.03 eV peak in the N *K* edge is observed. Then the intensity starts decreasing until its disappearance after 1.2 seconds. The position of the N *K* edge in that state corresponds to the observed peak[35] for N_2 gas (401.1 eV), while the peak at 399.7 eV (computed) corresponds to the essentially unperturbed π^* of the ring; this now shows a higher intensity than the peak at 404 eV associated with the amino group, also a small contribution from stageA2 molecule, (their structure is displayed in inset figure 6a), could be present. Therefore, we can conclude that at the first stage of melamine decomposition, the formation (increase in the intensity) and elimination (decrease in intensity of the 401.1 eV peak) of N_2 gas is involved. The loss of nitrogen occurs mainly from the amino groups connected to the ring.

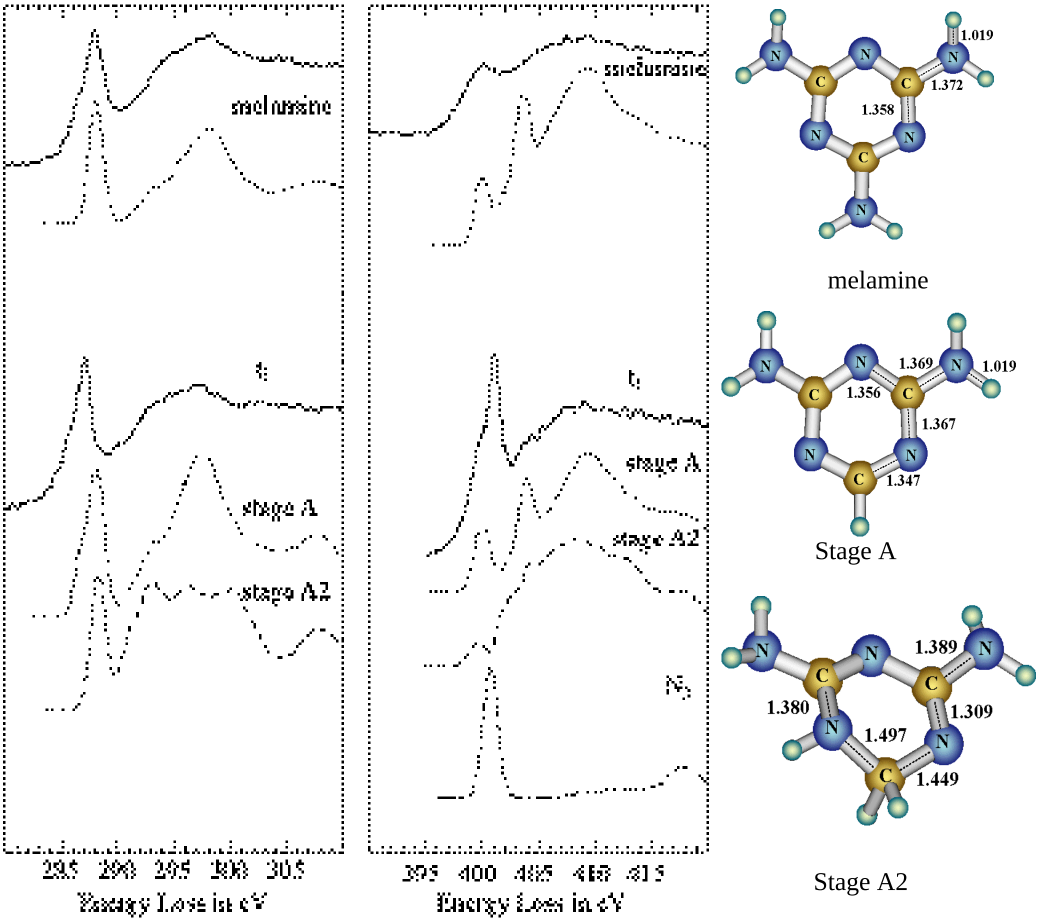

Figure 6a . - Experimental (solid line) and computed ELNES at the first decomposition state.The molecular structures are also displayed with the bond distance in Å.

As the amino groups are eliminated from the melamine molecule, there is no longer any interaction between the lone pairs in the amino groups and the π-electrons in the triazine ring and the C 1s π* peak is thus expected to split and shift in energy, as found for the spectrum of stage B. For the N K-edge a reduction of the intensity of the second (amino) peak is expected. The spectrum which corresponds to this stage, spectrum t_2, shows a reduction of material (vanishing of the multiple scattering) and two π* peaks at the N *K* edge at 401.9 and 398.9 eV. The position of such peaks is similar to those observed for the triazine molecule as well as for stage B and C.

We conclude that the spectrum t_2 corresponds to an intermediate in the melamine decomposition process, which contains different components such as triazine, stage B and stage C.

The last observed stage, spectrum t_3, shows a strong decrease in the intensity of the π^* peak at the C *K* edge, which suggests that the aromatic character of the ring is affected. The overall N/C ratio 0.47 is lower than the expected value for the triazine ring (N/C=1). The N *K* edge presents a feature, like the one observed when different N contributions are present. This stage suggests that a reduction of the carbon-nitrogen double bonds is taking place either through addition of hydrogen (computed stage C) or through bond cleavage (computed stage C2). The theoretical ELNES suggest that the spectrum t_3 is made of at least two components stage C2 and C. No further stages could be observed during the experiment, figure 6b.

For much longer (ca. 100s), an amorphous carbon deposit started to be present in the sample. From the pyrolysis experiment and the study by Ju *et al*[26], the formation of CN fragments is expected.

To find an explanation for the experimentally found result of a higher carbon than nitrogen amount, also the spectrum of CH_3CN with a nitrogen to carbon ratio of 1:2 was calculated. It

is also shown in the t_3 spectrum in fig. 6b, but it does not have any dominant peaks in common with the experimental spectrum, whereas it is very similar to the spectrum of stage C2. That is reasonable due to the similarity of these two molecules. We conclude from this that the experimentally found N/C ratios smaller than 1 are caused by local initial formation of the carbon deposit which can be observed macroscopically after 100s in experiment.

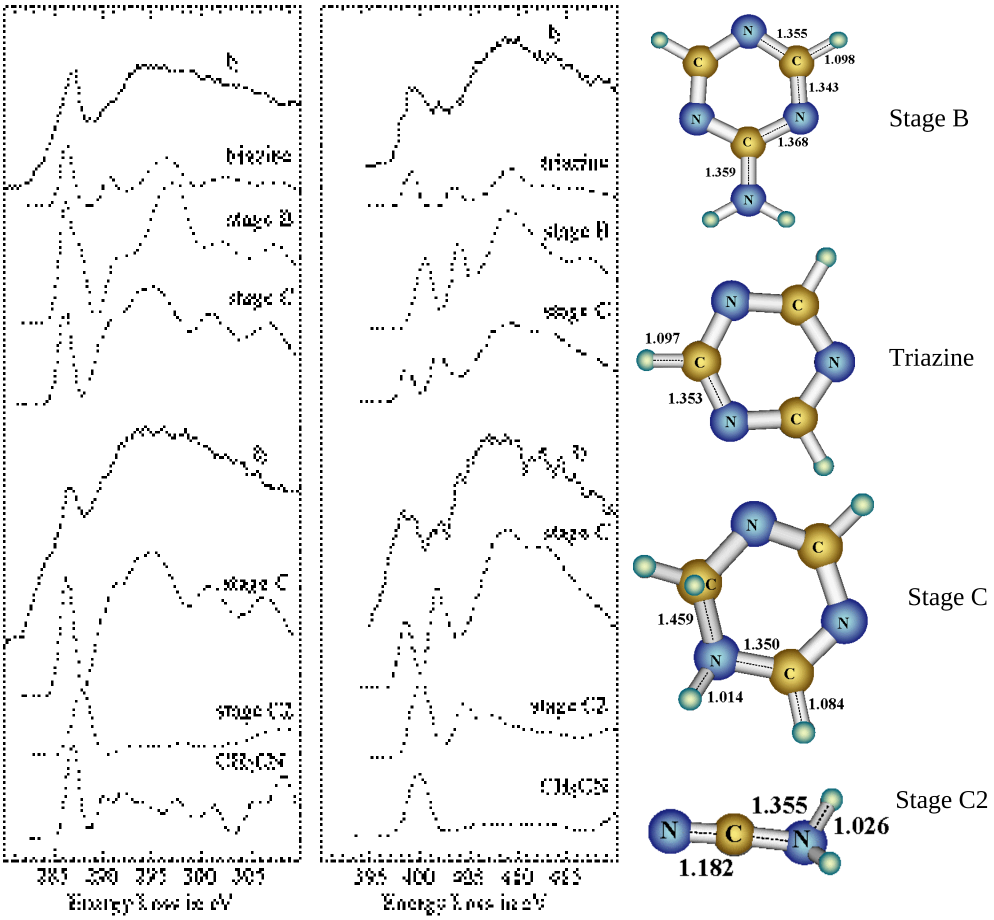

Figure 6b. - Experimental (solid line) and computed ELNES of the t_2 and t_3 decomposition state. The molecular structures are also displayed with the bond distance in Å.

6. CONCLUSIONS

The decomposition process of melamine exposed to a high-energy electron beam has been investigated by monitoring the changes in the Energy Loss Near Edge Structures (ELNES) using Time Resolved Electron Energy-Loss Spectroscopy (EELS). Calculations performed at the gradient-corrected DFT level using the deMon program were used in order to simulate the experimental ELNES observed at the different decomposition stages and to identify the different intermediate compounds produced during this degradation process. Results show a rather good agreement between simulated spectra resulting from a mixing of simulated ELNES on different CN molecules and experimental ELNES. From this comparison, we suggest that first the amino groups are eliminated as a release of N_2 gas. Then the degradation of the molecule occurs through a reduction of the carbon-nitrogen double bonds either by addition of hydrogen or by bond cleavage. If the irradiation is maintained over longer periods the formation of different CN fragments and polymerization products could then be possible.

7. ACKNOWLEDGEMENTS

K. Kordatos is thanked for useful discussions about the decomposition mechanism and M. Tence and W.K. Hsu for help with experiments. The financial support of the EU-TMR network *Synthesis, structure and properties of new carbon based hard materials* and the Swedish Foundation for Strategic Research is gratefully acknowledged.

8. REFERENCES

[1]A.Y. Liu and M.L. Cohen, "Prediction of new low compressibility solids," Science **245**, 841 - 842 (1989).

[2]S. Mendez Muhl, J.M., "A review of the preparation of carbon nitride films," Diamon Related Materials **8**, 1809-1830 (1999).

[3]H. Montigaud, B. Tanguy, G. Demazeau et al., "Solvothermal synthesis of the graphitic form of C3N4 as macroscopic sample," in *Nitrides and Oxynitrides* (2000), Vol. 325-3, pp. 31-36.

[4]D. W. He, F. X. Zhang, X. Y. Zhang et al., "Synthesis of carbon nitride crystals at high pressures and temperatures," Journal of Materials Research **13** (12), 3458-3462 (1998).

[5]L. Wan and R. F. Egerton, "Preparation and characterization of carbon nitride thin films," Thin Solid Films **279** (1-2), 34-42 (1996).

[6]N. Grobert, M. Terrones, S. Trasobares et al., "A novel route to aligned nanotubes and nanofibres using laser- patterned catalytic substrates," Applied Physics a-Materials Science & Processing **70** (2), 175-183 (2000).

[7]S. L. Sung, S. H. Tsai, C. H. Tseng et al., "Well-aligned carbon nitride nanotubes synthesized in anodic alumina by electron cyclotron resonance chemical vapor deposition," Applied Physics Letters **74** (2), 197-199 (1999).

[8]K. Suenaga, M. Yudasaka, C. Colliex et al., "Radially modulated nitrogen distribution in CNx nanotubular structures prepared by CVD using Ni phthalocyanine," Chemical Physics Letters **316** (5-6), 365-372 (2000).

[9]R. Sen, B. C. Satishkumar, A. Govindaraj et al., "B-C-N, C-N and B-N nanotubes produced by the pyrolysis of precursor molecules over Co catalysts," Chemical Physics Letters **287** (5-6), 671-676 (1998).

[10]H. L. J. Vandershall, Fire Flam **2**, 97 (1971).

[11]E. Kroke, M. Schwarz, V. Buschmann et al., "Nanotubes formed by detonation of C/N precursors," Advanced Materials **11** (2), 158-161 (1999).

[12]P. Ballonge and M. Tencé (Oral presentation).

[13]M. E. Casida, C. Daul, A. Goursot et al., deMon-KS StoBe version 1.0 ed. (deMon Software, 2001). (Carravetta,V., Duarte, H., Godbout, N.,Guan, J. Jamorski, C., Leboeuf, M., Malkin, V., Malkina, O., Nyberg, M., Pedocchi, L., Sim, F., Triguero, L., Vela, A.,(Contributing authors)).

[14]J.C. Slater, Adv. Quant. Chem? **6** (1) (1972).

[15]J.C. Slater and K.H. Johnson, Phys. Rev.B **5**, 844 (1972).

[16]H. Ågren, V. Carravetta, O. Vahtras et al., Theor. Chem. Acc **97** (14) (1997).

[17]L. Triguero, L. G. M. Pettersson, and H. Ågren, Phys. Rev.B **58**, 8097 (1999).

[18]L. Triguero, O Plashkevych, L. G. M. Pettersson et al., J. Electron Spectrosc. Relat. Phenom. **104**, 195 (1999).

[19]L.G.M. Pettersson, U. Wahlgren, and O. Gropen, Chem. Phys. **80**, 7 (1983).

[20]C. Kolczewski, R. Pütner, O. Plashkevych et al., J. Chemical Physics **in press** (2001).

[21]T. H. Dunning, J. Chem. Phys. **55**, 716 (1971).

[22]W. Kutzelnigg, U. Fleischer, and M. Schindler, *NMR-Basic Priniciples and Progress* (Springer Verlag, Heidelberg, 1990).

[23]R.D. Leapman, P. Rez, and D.F. Mayers, Journal Chemical Physiscs **72**, 1232 (1980).

[24]S. Ono, T. Funato, Y. Inoue et al., "Determination of melamine derivatives, melame, meleme, ammeline and ammelide by high-performance cation-exchange chromatography," Journal of Chromatography a **815** (2), 197-204 (1998).

[25]L. Camino G. Costa, "Thermal Behaviour of melamine," Journal of Thermal Analysis **34**, 423-429 (1988).

[26]S. Ju, Ch. Han, Ch. Wu et al., "The fragmentation of melamine: a study via electron impact ionization, laser desrption ionization and collision-induced dssociation, and density functional calculations of potential energy surface," J. Phys. Chem, B. **103**, 582-596 (1999).

[27]J. Stör, *NEXAFS Spectroscopy* (Springer-Verlag, Berlin Heidelberg, 1996).

[28]E. Apen, A. P. Hitchcock, and J. L. Gland, "Experimental Studies of the Core Excitation of Imidazole, 4,5- Dicyanoimidazole, and S-Triazine," Journal of Physical Chemistry **97** (26), 6859-6866 (1993).

[29]J. A. Horsley, J. Stohr, A. P. Hitchcock et al., "Resonances in the K-Shell Excitation-Spectra of Benzene and Pyridine - Gas-Phase, Solid, and Chemisorbed States," Journal of Chemical Physics **83** (12), 6099-6107 (1985).

[30]D. C. Newbury, I. Ishii, and A. P. Hitchcock, "Inner Shell Electron-Energy Loss Spectroscopy of Some Heterocyclic Molecules," Canadian Journal of Chemistry-Revue Canadienne De Chimie **64** (6), 1145-1155 (1986).

[31]C. Hannay, D. Duflot, J.P. Flament et al., J. Chem. Phys. **110**, 5600 (1999).

[32]Y. L. Wang, A. M. Mebel, C. J. Wu et al., "IR spectroscopy and theoretical vibrational calculation of the melamine molecule," Journal of the Chemical Society-Faraday Transactions **93** (19), 3445-3451 (1997).

[33]C. Sandorfy, *The Chemistry of the Carbon Nitrogen Double Bonds* (Interscience, 1966).

[34]G.R. Wyght and C.E; Brion, J. Electron Spectroscopy and Related (4), 25 (1974).

[35] R. McLaren, S. A. C. Clark, I. Ishii et al., "Absolute Oscillator-Strengths From K-Shell Electron-Energy-Loss Spectra of the Fluoroethenes and 1,3-Perfluorobutadiene," Physical Review a **36** (4), 1683-1701 (1987).

[36] S. Trasobares, O. Stéphan, C. Colliex et al., "Electron beam puncturing of carbon nanotube containers for release of stored N_2 gas," European Physical Journal B **22,** 117-122 (2001).

[37] H. Xin, W.P. Xu, X. Shi et al., "Formation of covalent solid CNx compounds by high dose nitrogen implantation into carbon thin films," Appl. Phys. Lett. **66** (24), 3290-3291 (1995).

PAPER V

Eur. Phys. J. B 22, 117–122 (2001)

THE EUROPEAN
PHYSICAL JOURNAL B
EDP Sciences

Electron beam puncturing of carbon nanotube containers for release of stored N_2 gas

S. Trasobares[1], O. Stéphan[1], C. Colliex[1,a], G. Hug[2], W.K. Hsu[3], H.W. Kroto[3], and D.R.M. Walton[3]

[1] Laboratoire de Physique des Solides[b], Université Paris Sud, bâtiment 510, 91405 Orsay, France
[2] ONERA - LEM, BP 72 - 29, avenue de la Division Leclerc, 92322 Chatillon Cedex, France
[3] School of Chemistry, Physics and Environmental Science, University of Sussex, Brighton BN1 9QJ, UK

Received 30 January 2001 and Received in final form 5 April 2001

Abstract. Carbon nanotubes containing nitrogen encapsulated in nanocontainers regularly distributed along the tube axis, have been produced by pyrolysing camphor in the presence of a mixture of nitrogen and ammonia gas. Spatially resolved electron energy-loss spectroscopy (EELS) analysis reveals that N_2 molecules are contained within the nanocapsules. The well-graphitized walls can be punctured by electron irradiation, thus partially releasing N_2. This process is accompanied by the formation of amorphous CN_x islands, as demonstrated by dynamic recording and analysis of time- resolved EELS sequences. Such local *in situ* electron beam nanomachining and nanoanalysis provide a method for producing under control new classes of nanodevices.

PACS. 79.20.Uv Impact phenomena (including electron spectra and sputtering) – 68.37.Lp Transmission electron microscopy (TEM) (including STEM, HRTEM, etc.) – 81.07.De Nanotubes

1 Introduction

Because they are hollow, carbon nanotubes [1] can be used as moulds for creating new nanostructures (*e.g.* metal nanowires, one dimensional crystals) [2–5] and as substrates for gas storage [6]. Recently, the successful incorporation of B and N into carbon nanotube walls has resulted in the modification of their electronic and mechanical properties [7,8]. However the identification of such complex B-C-N structures requires accurate nanometre-scale analysis which is available in high-resolution imaging and analytical electron microscopy. Such techniques can also be used to study the dynamic behaviour of small clusters within nanotubes induced by electron irradiation, *e.g.* the decomposition of silver nitrate [9] and the atomic rearrangement of tin oxide [10]. In this paper, the storage of N_2 in carbon nanotubes and its subsequent release by electron irradiation (exhibiting a gradual structural transformation due to C-N bond formation in the tube walls) have been studied, using EELS spectroscopy at subnanometer scale and with real-time recording at 10^{-2} s intervals.

2 Specimens and methods

Storage of N_2 in carbon nanotubes was achieved by the Fe-catalysed pyrolysis of camphor in the presence of a N_2/NH_3 flow. Two quartz boats, one containing camphor (200 mg, Allied Products, LTD, India) the other Fe powder (100 mg, Aldrich; particle size < 2 μm), were placed in a quartz tube (0.6 cm ID, length 60 cm) heated by two furnaces. The temperature of the second furnace (containing Fe-powder) was rapidly raised (50 °C/min) to 950 °C, whilst maintaining a flow of N_2/NH_3 (3:1 ratio, total flow 50 cm^3/min), and the temperature of the first furnace (containing camphor) was then gradually increased (10 °C/min) to 400 °C. Camphor (sublimation temp., ca. 200 °C) was thus sublimed from the first to the second furnace. The dark material, which formed in the second furnace, was allowed to cool to room temperature and subjected to electron microscopy analysis.

The carbon nanotubes were analysed by high-resolution transmission electron microscopy (HRTEM, TOPCON 002B) using a LaB_6 filament operating at 100 kV in order to minimise radiation damage. EELS analysis was performed using a VG 501 STEM, operating at 100 keV, equipped with a Gatan EELS spectrometer and an optical CCD camera as a parallel detector which provides an energy resolution of ca. 0.7 eV [11].

---

[a] also at Laboratoire Aimé Cotton, UPR 3321, Université Paris Sud, bâtiment 505, 91405 Orsay, France
e-mail: `colliex@lps.u-psud.fr`

[b] UMR 8502

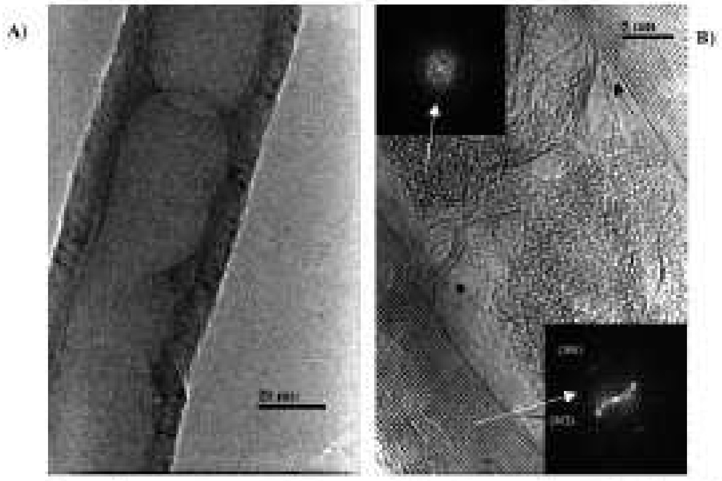

Fig. 1. A) TEM images of a carbon nanotube containing capsule-like structures along the tube axis. B) HRTEM image of well-graphitised tube walls and encapsulated amorphous material. Fourier analysis of amorphous carbon (top insert); Fourier analysis of graphitised tube walls (lower insert), revealing 0.21 nm and 0.34 nm *d*-spacings, corresponding to (100) and (002) lattice fringes. Localised transverse graphitic structures (2–3 layers) are also present (dark arrows).

This equipment is capable of monitoring in real time dynamic effects induced by electron irradiation in the nanostructures. A satisfactory signal-to-noise ratio on the characteristic signal of the involved elements *in situ* was thus obtained. Two different approaches for data acquisition were used during the present study: spatially resolved EELS (spectrum imaging) and time resolved EELS (chrono-spectroscopy) [12,13].

3 Results and discussion

3.1 Microstructure and chemical analysis

HRTEM reveals that the collected dark material contains mostly spiral carbon nanotubes. The tube lengths exceed $3\ \mu m$ and are highly uniform as regards their morphology, with external diameters ca. 50 nm. HRTEM also shows that the internal structures of the tubes consist of capsule-like adjacent compartments (25–30 nm in diameter; 50 nm in length) aligned with the tube axis (Fig. 1A). The nanotube walls are made of well-organised graphitic layers (Fig. 1B). Fourier analyses of the image of the tube walls shows two types of spacings: 0.21 nm and 0.34 nm, corresponding to (100) and (002) lattice fringes of graphite (lower inset, Fig. 1B). HRTEM also reveals the presence of small graphitic fragments, consisting of 2–3 layers (dark arrows, Fig. 1B). These fragments fence the compartments. Note that the compartments are partly filled with amorphous material (top inset, Fig. 1B).

Spatially resolved EELS, in the spectrum-imaging mode, has been used to map the elemental composition of the nanotubes. The sub-nanometre incident electron probe (0.5 nm) was scanned across the nanotube, as shown in Figure 2A, so that individual EELS spectra were acquired at regularly spaced locations with 1.6 nm steps. C and N intensity profiles, extracted from the individual spectra (using the normal background subtraction method [14]), are displayed in Figure 2B. The C profile indicates that the tube walls consist only of carbon (position A, Fig. 2A; spectrum A, Fig. 2C). A small N absorption edge begins to emerge when the probe approaches the inner layers of the tube (position B, Fig. 2A; spectrum B, Fig. 2C). The intensity of the N absorption edge significantly increases at position C (Fig. 2A; spectrum C, Fig. 2C). Figures 2B and 2C clearly indicate that N is not a constituent of the tube walls.

Line scans were also carried out in order to study the Electron Energy-Loss Near Edge Fine Structures (ELNES) of the C K-edge and N K-edge (Fig. 2C). The observed C K-ELNES are similar to that of graphite, consisting of a strong peak at 285.5 eV, associated with transitions from the 1s core to π^* unoccupied states, and a characteristic σ^* broad band with four well- defined features from 291 eV up to ca. 310 eV [15]. Local anisotropy effect is observed in materials, which have oriented π and σ bonds, as it is the case of graphite. The π band, close to the Fermi level, results from the interaction between orbitals of p_z symmetry and the σ band, at lower energy, results from interaction between orbitals of p_{x-y} symmetry. The high anisotropy is due to the fact that p_z orbitals are perpendicular to the graphite planes and p_{x-y} orbitals are lying within the planes. When EELS analysis is performed, because in our scattering geometry, the mean momentum transfer is perpendicular to the beam, the local anisotropy effects can be observed while scanning

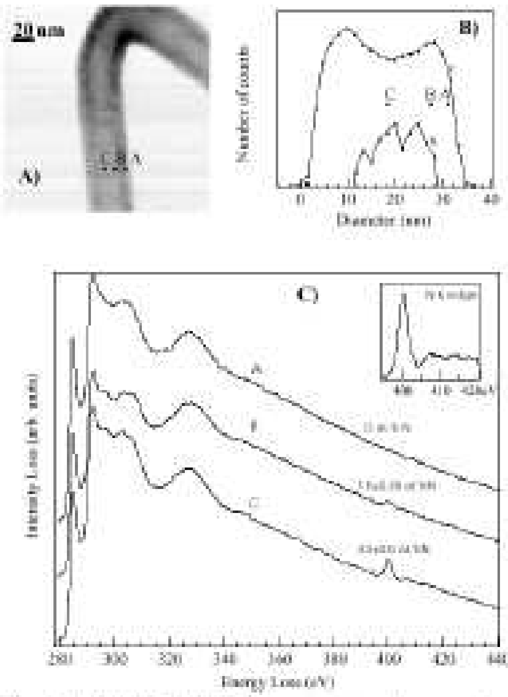

Fig. 2. A) Bright Field STEM image of a carbon nanotube. B) EELS chemical spatial profiles across the nanotube (positions A, B and C, Fig. 2A), extracted from the individual spectrum after background subtraction; insert shows the N-K ELNES corresponding to N_2. C) Normalised spectra recorded when the beam is focused on the position A). The C and N K-edges are similar to those observed in pure graphite and N_2 gas respectively.

the probe. The lattice orientation with respect to the incident beam varies gradually; it results in changes in the intensity ratio π^*/σ^*, which is higher for the edge position than for the central position. The N K-edge shows a strong peak (inset Fig. 2C) which is similar in shape and energy (401.1 eV) to that observed for gaseous N_2 [16], and is completely different from that of the nitrogen K-edge ELNES observed for solids, e.g. amorphous CN_x [17]. The EELS analysis clearly indicates that N_2 gas is trapped within the nanocapsules during nanotube growth. This result differs from a previous report where N was found to be incorporated into the hexagonal carbon network when melamine was pyrolised in Ar atmosphere, thus forming localised CN_x domains in the tube walls [18]. A more complete study of the catalytic pyrolysis of melamine [19] shows that N is not incorporated in the nanotubes when N_2 gas is used while on the other hand, the presence of trapped gas has been demonstrated when the pyrolysis is carried out in a N_2/NH_3 atmosphere. It is noteworthy that N_2 is not trapped within tubes when the pyrolysis experiment is carried out in a N_2 flow. It suggests that NH_3 may be decomposed during the tube-wall fabrication process, e.g. $2NH_3 + 2C \rightarrow C_2H_6 + N_2$, particularly at the inner layers. Accordingly, gaseous N_2 molecules are trapped within the tubes as demonstrated by the EELS local analysis and the C_2H_6 molecules would not be incorporated into the hexagonal carbon network, but encapsulated as amorphous materials (Fig. 1B).

3.2 Beam-induced dynamical effects

The electron microscope has also been operated in the chrono-spectroscopy mode, [12] in order to assess the stability of the nanotube structure under the electron beam. We have found that the beam is able to puncture the tube walls, thus partly releasing N_2 gas, and this process is accompanied by a gradual change in the tube wall structure. C-N bond formation appears to take place during the release of N_2 gas via the broken walls or disintegrated graphitic domains.

The above description reflects the structural and chemical changes, which occur in tube walls during irradiation as recorded in real time. A 0.5 nm diameter probe is targeted at a selected area of a tube containing N_2, e.g. at the centre of the nanocapsule, and a series of time-dependent spectra is then recorded: a selection among 150 spectra, recorded at 600 millisecond intervals, are shown in Figure 3A. (The electron dose is proportional to the recording time; beam dose = time × 10^9 e^-/nm^2 s.) After irradiation for 50 s, corresponding to an electron dose of 5×10^{10} e^-/nm^2, the nanotube gets punctured, as observed from the high angle annular dark field (HAADF) image (central dot, insert, Fig. 3A). In the HAADF image, the vacuum signal is seen in dark and the corresponding HAADF profiles (Fig. 3B) are calibrated, assuming zero intensity in vacuum. From the HAADF profiles extracted from the respective images before and after puncturing ($HAADF_{before}$ and $HAADF_{after}$), a total reduction of 50% in mass occurred, suggesting that the hole has been drilled through only one side of the tube walls, either upper or lower (Fig. 3B). Four spectra, corresponding to different radiation times, are displayed in Figure 4A. Large characteristic signals for C and N are evident in spectra a, b and d, while a very weak N signal is present in spectrum c.

Time-dependent intensity profiles, extracted from the individual spectra after background subtraction [14], are shown in Figure 4B for both C and N. The carbon thickness profile (calculated by integrating the intensity over the whole spectrum) decreases regularly during the first 50 s and then fluctuates around a stable value. These fluctuations may be due to uncontrolled minor changes in beam position during the subsequent 150 s. By contrast, the N signal increases by a factor of ca. 4 over the first 40–50 s; it then drops sharply, almost vanishing before increasing again until it reaches a constant average value (t > 100 s). The same behaviour has been observed for several nanocapsules along one tube and for several tubes. It is of quite general reproducibility.

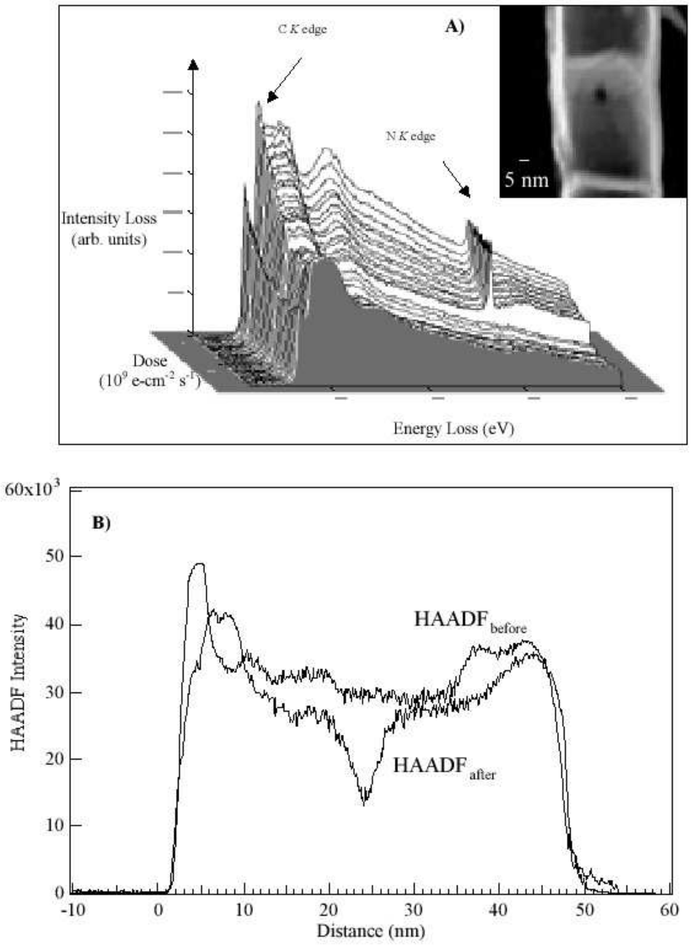

Fig. 3. A) Time sequence EELS spectra recorded at 600 milliseconds intervals. As the radiation time is prolonged, the intensity of the C signal decreases. For N, an increase in signal intensity is observed before it drops sharply. Insert shows an HAADF image of the nanotube being punctured (dark hole, ca. 4 nm in diameter) by the electron beam. B) HAADF intensity profiles before and after puncturing. A drop ca. 50% of thickness at the puncture position is clearly seen, suggesting that only one side of the tube walls (top or bottom) has been drilled.

The changes in the C and N K-edge fine structures (Fig. 4B) provide probes for monitoring the modifications in bonding and environment around both C and N atoms. As mentioned above, the C and N K-edge profiles, before beam irradiation, are similar to those observed in pure graphite and N_2 gas respectively. Spectra recorded during the first stage of irradiation (*i.e.* before drilling) show a gradual change in the C K-edge fine structures (decay and broadening of π^*, vanishing of the σ^* structures) corresponding to the destruction of the graphitic structure and formation of amorphous material, whilst the N K-line keeps its characteristic N_2 shape and intensity. Subsequently the N_2 peak decays abruptly to be replaced by a new fine structure, corresponding to solid CN_x. To further confirm the existence of two successive profiles for the N-K fine structures, corresponding to different phases, the whole set of spectra acquired during a time sequence have been processed using a multivariate statistical analysis (MSA) method [20]. This approach can classify and identify the different characteristic fine structures, which appear in a set of spectra. Only two components have come out of the present analysis. Figure 4C shows these two reference edge shapes which can be attributed respectively to N in a gas phase and N in a solid phase (N-bulk) similar to that observed in CN materials. Figure 4D displays the corresponding time dependence of the existence of these two reference profiles; N appears only as a gas during the first 40 seconds of the investigation and in

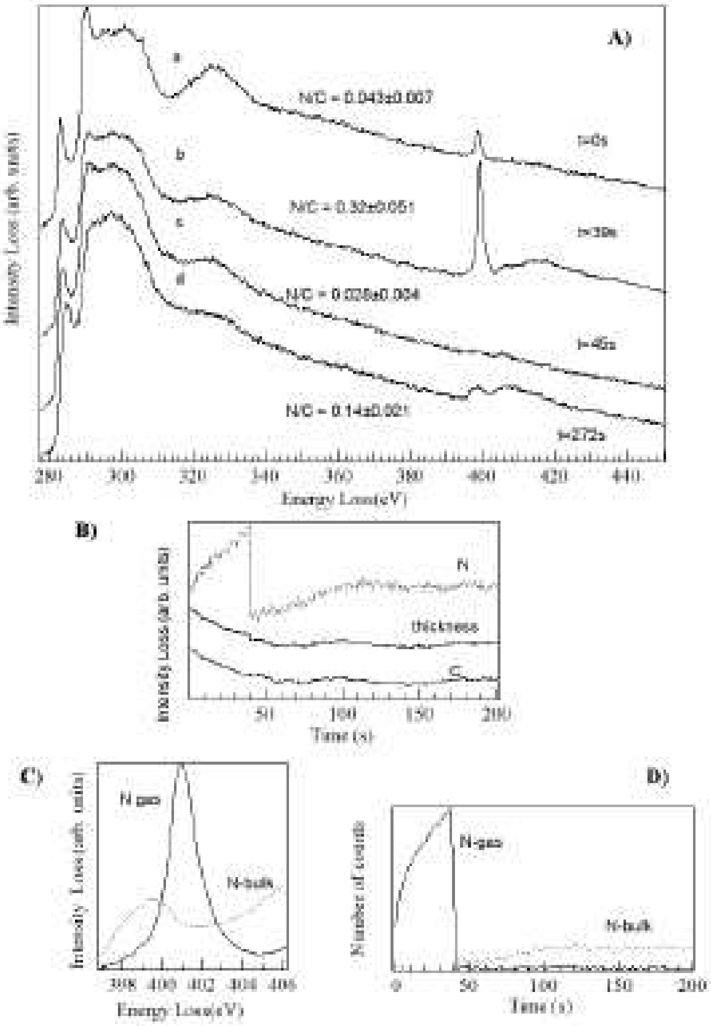

Fig. 4. A) Normalised spectra recorded at different times on the same position during the acquisition of a chronospectroscopy sequence. B) Time dependent profiles of the C and N evolution, and the thickness signal during irradiation. C) Fine structures for the two types of N configurations (N_2 and CN_x) deduced from a multivariate statistical analysis of the spectral sequence. D) Time dependent profiles for the two MSA components; N in N_2 phase (before puncture, i.e. the intensity drops at 42 s), and N in CN_x solid state (after puncture).

a solid environment afterwards. The content of N in the solid state increases until it reaches a constant value of 12 ± 1.6 at.%.

The strong increase in the N signal detected over the first stage of irradiation (Fig. 4B) is likely due to the fact that the N_2 molecules are weakly physisorbed in the porous structures inside the individual nanocapsules, and are attracted towards the electron probe by Coulombic forces, thus increasing the number of N atoms measured by the beam. This behaviour is in fact quite similar to the well-known contamination process involving the diffusion to the position of the primary beam of physisorbed carbonaceous materials under the strong incident flux of the primary electron probe. In the present situation, the Coulombic attraction may be due to positively charged N_2 molecules, the ionisation being a consequence of an Auger process after primary excitation; such a process has been clearly identified in studies of insulating materials [21]. Consequently, the gas pressure locally increases. When the tube walls are thin and the pressure is sufficiently high, puncturing occurs. The gas is released from the nanocapsules, resulting in the observed abrupt decrease in the N_2 profile (Fig. 4B). Based on a quantitative analysis of the individual spectra in the EELS sequence, we estimate that the number of N_2 molecules/nm^3 just prior to drilling is ca. 11/nm^3, *i.e.* four times that in the initial state. This value corresponds to an increase in the N_2 pressure from ca. 80 to 300 atm at the apex of the electron probe.

The more moderated but still noticeable increase in the N-peak intensity after gas release from the nanocapsule ($t > 50$ s, spectrum b, Fig. 4A) is due to the residual N_2, which has not been released by the puncturing and is still situated in the nanocapsule near to the electron beam. EELS spectra, recorded at different locations within the same nanocapsule but at a distance from the puncture, reveal the presence of $< 2\%$ of N. However, the observed small amount of N makes quantitative analysis of gaseous N difficult. These remaining N atoms could diffuse towards the electron beam and be incorporated into the highly defective C matrix near to the probe. The incorporation process is supported by detection of the N K-edge fine structure, corresponding to CN_x solid material during the final stages of irradiation (spectra c and d, Fig. 4A). The incorporation of N increases when the C K-ELNES evolves towards amorphous carbon. This result is in agreement with general observations on disorganised CN_x materials: the more amorphous-like C-K edge profile, the highest N content is observed. The incorporation process involves ca. 20 nm domains, as does the formation of amorphous material.

4 Conclusions

Carbon nanotubes containing-N_2 have been formed by pyrolysing camphor in the presence of N_2/NH_3. The high-energy electron nanoprobe embodied in an electron microscope has been used as a local nanoanalysis tool to demonstrate the existence of nanocontainers arranged in series, which store the N_2 gas. It has furthermore been used to generate localized damage to the nanostructure, to follow the release of trapped gaseous N_2, and to monitor the associated structural changes in the *in situ* bonding configuration. This feasibility experiment suggests a variety of new applications. It has been shown theoretically that small domains of CN in graphitic materials should behave as metallic islands with local properties varying with size [22]. Consequently, nanotubes made of a periodic distribution of CN monodomains alternating with N_2 gas nanocontainers, such as those produced in this work, constitute potential candidates for fuel- cell batteries and nanosized electron devices.

We thank M. Sharon for the camphor samples, and M. Tencé (LPS, Orsay) for designing and running of new equipment and software essential for the success of this experiment. We also acknowledge financial support provided by the EU-TMR network, the EPSRC and the Royal Society of Great Britain.

References

1. S. Iijima, Nature **354**, 56 (1991).
2. P.M. Ajayan, S. Iijima, Nature **361**, 333 (1993).
3. C. Guerret-Piecourt, Y. Lebouar, A. Loiseau, *et al.*, Nature **372**, 761 (1994).
4. W.K. Hsu, S. Trasobares, H. Terrones, *et al.*, Chem. Mat. **11**, 1747 (1999).
5. R.R. Meyer, J. Sloan, R.E. Dunin-Borkowski, *et al.*, Science **289**, 1324 (2000).
6. G.E. Gadd, M. Blackford, S. Moricca, *et al.*, Science **277**, 933 (1997).
7. O. Stéphan, P.M. Ajayan, C. Colliex, *et al.*, Science **266**, 1683 (1994).
8. N. Grobert, M. Terrones, S. Trasobares, *et al.*, Appl. Phys. A **70**, 175 (2000).
9. D. Ugarte, A. Chatelain, W.A. de Heer, Science **274**, 1897 (1996).
10. J. Sloan, J. Cook, J.R. Heesom, *et al.*, J. Crystal Growth **173**, 81 (1997).
11. P. Ballongue, M. Tencé, private communication (2000).
12. C. Colliex, M. Tencé, E. Lefevre, *et al.*, Mikrochimica Acta **114**, 71 (1994).
13. C. Jeanguillaume, C. Colliex, Ultramicroscopy **28**, 252 (1989).
14. R.F. Egerton, *Electron Energy-Loss Spectroscopy in the Electron Microscope* (Plenum Press, New York, 1996), p. 245.
15. O. Stéphan, P.M. Ajayan, C. Colliex, *et al.*, Phys. Rev. B **53**, 13824 (1996).
16. R. McLaren, S.A.C. Clark, I. Ishii, *et al.*, Phys. Rev. A **36**, 1683 (1987).
17. K. Suenaga, M. Yudasaka, C. Colliex, *et al.*, Chem. Phys. Lett. **316**, 365 (2000).
18. M. Terrones, P. Redlich, N. Grobert, *et al.*, Adv. Mater. **11**, 655 (1999).
19. S. Trasobares, unpublished.
20. N. Bonnet, N. Brun, C. Colliex, Ultramicroscopy **77**, 97 (1999).
21. J. Cazaux, Ultramicroscopy **60**, 411 (1995).
22. X. Blase, Comput. Mater. Sc. **17**, 107 (2000).

PAPER VI

SPATIALLY RESOLVED EELS ON CARBON-BASED NANOSTRUCTURES

C. Colliex [1], M. Kociak, O. Stephan, K. Suenaga [2]**, S. Trasobares**

Laboratoire de Physique des Solides, Bldg 510, Université Paris-Sud, 91405 Orsay (France)

[1] *also at Laboratoire Aimé Cotton, Bldg 505, Université Paris-Sud, 91405 Orsay (France)*

[2] *presently at Japan Science and Technology Corporation, ICORP "Nanotubulite" project, Meijo University, Nagoya 468-8502 (Japan)*

Proceedings of NATO school

"Nanostructured carbon for advanced applications", Erice, Juin 2000.

1 INTRODUCTION

An electron energy-loss spectroscopy (EELS) experiment measures the energy distribution of a monochromatic electron beam, which has been scattered by a target. It therefore corresponds to a transfer of energy E from the primary beam of energy E_0 into the probed sample. Such an inelastic event reflects the dynamic response of the specimen. Depending on the nature of the target (gas, surface, thin film) and on the primary energy (from a few eV up to the MeV range), the investigated excitation spectrum covers a wide energy range from the meV to the keV (i.e. from the IR to the X-ray photon domain).

In the present contribution, our scope is restricted to EELS measurements performed within the context of a transmission electron microscope, where one can take benefit of all the possibilities of the instrument to select a given area of the object, to visualize it and to characterise its structure by imaging and diffraction before investigating its local electronic properties by EELS. Many reviews have already been devoted to this subject (Colliex [1,3,4], Egerton [2], as well as in the books edited by Disko and al. [5] and by Reimer [6], which should be read for further introduction to the technique and its applications). In this specific case, the recorded inelastic data, corresponding to the inelastic scattering of typically 100-300 keV incident electrons by thin foils or nano-objects, deal with the excitation spectra of the different electron populations in the target. If the used geometry offers a good angular resolution, the study of the dispersion curves E(**q**) is accessible, where **q** is the momentum transfer in the collision. On the other hand, if the incident beam is focused into a probe of small size on the specimen, the momentum distribution is averaged over the illumination and collection angles, but one can pick out the information from a reduced area of the specimen, which can be as small as a fraction of nanometer.

Carbon-made materials have been the field of major discoveries over the past fifteen years, with the identification of new phases, beyond the well-known diamond, graphite and amorphous structures. These novel morphologies include building blocks in the nanometer size range, such as the fullerene molecules (C_{60}, C_{70}, C_{84}...) identified by Kroto et al. [7], the carbon onions discovered by Ugarte [8] and the carbon nanotubes first reported by Iijima [9].

These discoveries have stimulated a huge effort to understand the atomic arrangements and bonds involved in these nano-objects, to master new routes for improving the production of selected species, to measure their mechanical and electronic properties or to identify fields of application. In this task, electron microscopy techniques have played a major role. More specifically, the purpose of the present chapter is to illustrate how far spatially resolved EELS studies performed in the electron microscope on single isolated objects have been fruitful. This is true not only for pure carbon nanostructures but also when they have been doped with other elements, and in particular with nitrogen.

As an example, in an EELS spectrum recorded on a carbonaceous material (see fig. 1), one identifies two major contributions : (i) in the 10 to 30 eV range, the dominant contribution is concentrated in plasmon lines (BP, SP) which reflect the collective nature of the dielectric response of the 2s and 2p hybridized valence electrons to the impinging electron

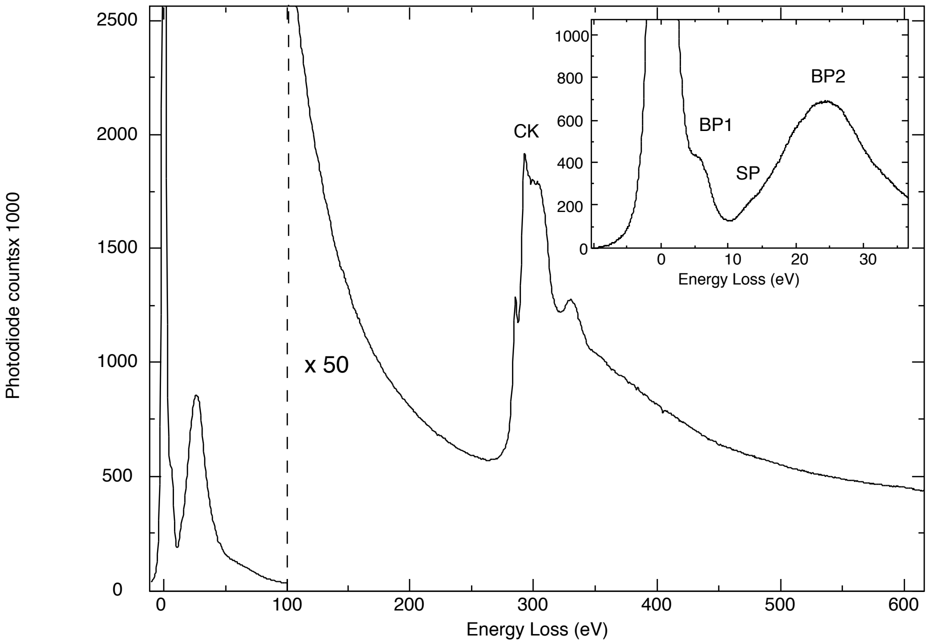

Figure 1 : Characteristic EELS spectrum recorded on an isolated multi-walled carbon nanotube (MWCNT), emphasising the collective plasmon peaks (BP an SP) and the atomic 1s core-loss excitation with its fine structures.

probe; (ii) on the contrary, the core 1s electrons on the carbon atoms are excited mostly individually from their low-lying energy level up to vacant electron states above the Fermi level. These excitations give rise to a characteristic K–edge marked by a sharp threshold at an energy of the order of 285-290 eV, superposed on a smoothly decreasing background. This edge is very well adapted to EELS investigations. Its detection reveals the presence of carbon atoms within the area illuminated by the primary electron probe. Its intensity can be used to determine the involved number of C atoms, if one knows the value of the atomic scattering cross section. Furthermore the analysis of the fine structures observed above the edge is a map of the distribution of unoccupied electron states involved in the bonding of the excited atom with its neighbours. However, this transition must satisfy the dipolar selection rules valid for the small angle scattering conditions, generally used in such experiments, i.e. s-type electrons are promoted to p-type states for the present case (we would also observe dominant p to d transitions when the excited electron is on a 2p or 3p state).

Table I summarises the different types of information contained in an EELS spectrum :

The first three columns point out where the required information has to be searched for and the last column gives a few hints on how to process the recorded spectra to have access to a refined information. It is clear that depending on the elements present in the investigated specimen area, the level of analysis to be performed may be quite different.

Let us point out the EELS features, which are relevant to the study of carbon-based material :

(i) the carbon K-edge is the ideal signal for EELS analysis : it lies at about 300 eV, which is the perfect energy range for EELS spectroscopy; it offers strong excitation cross-sections, so that good signal-to-noise ratios are obtained even from small numbers of atoms. Consequently, the fine structures, which can substantially vary as a function of the environment and molecular bond of the excited atom, can be recorded with best available energy resolution (see the book by Stöhr[10] which displays many spectra of carbon K-edges in various molecules).The main differences between the graphite and diamond C-K edges are due to the difference in hybridisation : sp^2 (with a strong pre-edge π^* feature, a few eV below the major contribution to σ^* band) or sp^3 (in which case the tetrahedral bonded atoms involveonly σ bonds and no π^* pre-peak is then detected). This difference has been used to quantify the sp^2/sp^3 ratio in DLC compounds[11].

(ii) the low energy-loss domain (between a few eV and about 30 eV) is dominated by the presence of collective excitations at about 6 and 25 eV which correspond to the bulk plasmons of two different families of electrons and are generally designated as π (BP1) and σ(BP2) plasmons. This is an oversimplified view. Of course, the first π-type plasmon does not exist in diamond specimens. Furthermore, the situation is made more complex for graphite as

Table I Summary of the different types of information contained in an EELS spectrum:

Energy-loss domain	**Relevant feature of interest**	**Accessible type of information**	**Required processing technique**
Whole spectrum (0→keV) and zero-loss peak	Ratios of intensity I_T and I_O	Local thickness, determination of total inelastic cross-section	Measurement of intensities (avoid saturation effects)
Low-loss region (2 → 30 eV)	Bulk plasmon peak position (BP)	Average electron density	Measurement of the energy of plasmon resonances
Low-loss region (2 → 25 eV)	Weak features, generally below the BP peak position	Interband transitions, joint density of states	Deconvolution techniques, Kramers-Kronig analysis, use of dielectric functions
Low-loss region (2 → 20 eV)	Weak features at glancing incidence on surfaces and interfaces : surface plasmons (SP)	Dielectric interface and surface properties	Identification and localization of the modes, impact parameter dependence, dielectric constant modelling
Core-loss region (50 → 2000 eV and more)	Presence and weight of core-loss edges	Qualitative and quantitative elemental analysis	Detection and measure-ment of edge intensity (background subtraction, derivative spectra analysis, MLS fitting)
Core-loss region (50 → 2000 eV)	Distribution of fine structures over the first 50 eV above core-edge threshold	Unoccupied density of states (involving bonding type, charge transfer, site symmetry, bond length)	Analysis of core NES (comparison with reference spectra, modelling with band calculations)
Core-loss region (200 → 2000 e)	Distribution of oscillations over 50 – 300 eV range above threshold	Radial distribution function	Analysis of core-EXELFS data (similar to EXAFS analysis)
Core-loss region (400 → 1500 e)	Characteristics of white-line features (sharp narrow peaks on selected 2p or 3d edges)	Density of local d- or f-type holes (measurement of local magnetic moment)	Comparison with multiplet calculation (influence of core-hole, of crystal-field..)

anisotropy effects occur : collective excitations have to be assigned not to specific families of electrons, but to specific families of allowed band-to-band transitions. When recording EELS spectra from nanostructures with noticeable fractions of surface atoms, the collective excitation modes localized on surfaces (SP) are also clearly visible, as it will be further demonstrated for carbon nanotubes.

2 INSTRUMENTATION, DATA ACQUISITION, PROCESSING AND INTERPRETATION

In the environment of an electron microscope, EELS spectroscopy is performed by inserting a spectrometer (generally of the homogeneous magnetic prism type), either at the end of the column or within the column between the objective and the projection lenses. Instead of discussing here the respective advantages and limitations of each solution, we want to focus on how to relate, in such a machine, the spatial and the spectral information.

The EELS spectrum is recorded from a given specimen area, either defined by an aperture in the conventional CTEM or by the size and position of the probe in the Scanning TEM. It can therefore be designated as a distribution I_{xy} (E) for E varying by energy increments E_i over the different elements of the detector. Nowadays with parallel detectors (PDA or CCD), this energy step can vary typically from 5 meV up to 5 eV, depending on the magnification of the spectrum on the detection plane. In order to investigate the spatial dependence of the EELS spectrum, the simplest way consists in scanning the probe over the area of interest and in acquiring a family of $N_1 \times N_2$ spectra, corresponding to the $N_1 \times N_2$ pixels successively addressed in this process. This mode has been proposed by Jeanguillaume and Colliex [12], as the "image-spectrum" mode. Its operation and output have extensively been described in recent publications [13,14].

An alternative approach is to filter, with an energy selection slit, the energy of electrons used to make an image on a 2D detector. In this case, one records at once a distribution $I_E(x,y)$ over the whole N × N image. This approach, generally known as ESI (energy selective imaging) or EFTEM (energy filtered TEM), is very efficient for providing the information contained in a limited number of energy channels (E_i) – as many as the number of successively recorded energy filtered images – over large numbers (N^2) of pixels.

In the present work, we have privileged the acquisition of complete EELS spectra with best energy resolution over 1024 channels, for a limited number of pixels, i.e. from typically a few 10^2 up to a few 10^4. This has been made possible by implementing the image-spectrum recording mode, as a routine technique on a dedicated STEM – see refs. (4), (13), (14) for a more complete description of the basic components of the machine -. It offers the simultaneous capability of visualising the object topography through the annular detectors (small angle for diffraction contrast, large angle for "Z" or mass-thickness contrast) and of recording the sequence of EELS spectra. Practically, in best conditions, we can record spectra with 0.3 eV energy resolution on the zero-loss peak, 0.6 eV energy resolution on a core-loss edge, from a 0.5 nm probe diameter and within a time of a few ms for plasmon losses up to a few 100 ms for core-loss edges (using a new optically coupled detector developed and realised by P. Ballongue and M. Tencé at Orsay).

Consequently, one can easily imagine how fruitful this approach can be for characterising isolated nanostructures, which one can selectively chose, using the efficient zooming capability of the scanning microscope. As an example, fig. 2 shows two sets of spectra acquired while scanning the primary 100 keV electron probe across a single carbon nanotube, the diameter and number of walls of which can be accurately determined by the normal imaging techniques. Both sequences of spectra are typically made of 50-100 individual spectra, acquired with a 0.5 nm probe and 0.3 nm step increments. Total acquisition times are of the order of 1 s for the low energy-loss domain (between 5 and 30 eV) and 10 s for the carbon K-edge (between 270 and 330 eV). Energy dispersion has been optimised in each case as a function of the total energy-loss domain explored. The low loss spectra clearly exhibit the π and σ- type bulk plasmons which are of highest weight close to the centre of the tube, but also demonstrate some noticeable changes and shifts when the probe is close to the external surfaces of the tube. Furthermore signals between 10 and 15 eV become dominant when the incident electrons travel in vacuum at a given impact parameter (which can be up to 10 nm) away from the outer tube. The interest of such measurements, which we have called Near Field EELS [15], will be more extensively discussed in a next paragraph.

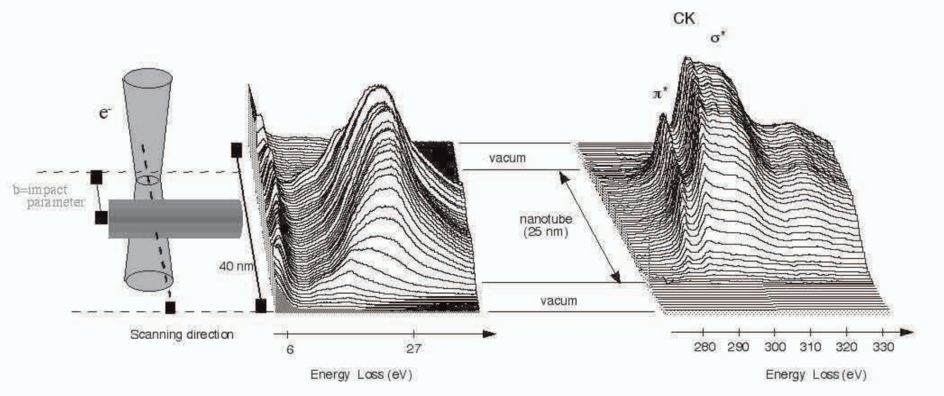

Figure 2.- Spectrum-line (i.e. sequence of spectra recorded while scanning the primary electron probe across an isolated carbon nanotube) exhibiting the spatially dependent behaviour of the two major types of excitation : plasmons between 10 and 30 eV and 1s core-losses between 280 and 330 eV.

As for the carbon C-K core edge, its appearance is obviously restricted within the carbon nanotube. It systematically displays two components corresponding to the π* and σ* unoccupied electron states. However, a closer inspection of the weight and shape of these two peaks reveals changes when the probe moves from the centre to the outer parts of the tube. These changes are due to anisotropy effects : in the centre, the incident electrons travel perpendicular to the graphene layers (i.e., parallel to the $\vec{c}$ axis) and therefore most collected inelastic electrons correspond to a $\vec{q}$ momentum transfer perpendicular to the c axis. On the contrary, near the edge of the tube, the electrons travel parallel to the graphene layers, i.e. perpendicular to the $\vec{c}$-axis and therefore the dominant scattering processes involve as well $\vec{q}$ momentum transfers parallel to the $\vec{c}$-axis (i.e. towards the outer of the tube) as transfers perpendicular to the axis (along the tube axis direction). This situation has been fully described by Stephan [16].

The acquisition of sequences of EELS spectra, rather than of individual spectra, has enormously changed the impact of the method, and consequently has required the development of adapted processing routines. Some of them are simple extensions of the techniques previously developed for processing individual spectra and can be straightforwardly used for providing elemental maps – see Tencé et al. [17] –. Others consider the sequence of spectra as a multidimensional data set and statistical approaches (MSA for instance) have been implemented to search for the hierarchical importance of stable and variable components – i.e. for identifying the specific near edge features appearing at the apex of an interface [18] –. Generally speaking, the trend is now to search for the gradients of spectral fine structures as a function of probe position, before trying to interpret all the fine structures.

For this final task, several routes have become available. The first one is to compare the recorded spectra with reference ones previously acquired on standards – this is the "fingerprint" approach –. Along this direction, the development of an EELS and XAS library of core-edge fine structures constitutes a fruitful support [19]. As already mentioned, spectra recorded on different types of molecules containing C atoms is very useful to assist us in the identification of bonds involved in molecular solids and compounds. A more elaborate approach is to simulate the EELS spectra from atomistic structure models using theoretical descriptions. Two classes of methods have emerged, the first ones use *ab initio* density of states calculations, the others rely on a real space description in terms of multiple scattering of the outgoing wave within clusters of increased dimensions. Both have been tested with more or less success on structures implying carbon atoms.

3 CARBON NANOTUBES

Carbon nanotubes constitute nano-objects perfectly suited for EELS investigations in a STEM. As a matter of fact, there is no special EM specimen preparation procedure required. The nanotubes are dispersed in a solvent and a drop of this mixture is deposited on a holey carbon thin foil. They stick to the surface of the supporting film due to the strong surface tension forces. Many of them can be seen self-supported across holes or protruding over vacuum. There is consequently no underlying support contributing to the spectra. Furthermore, their natural size, in the nanometer scale transversally and in the micrometer scale longitudinally, are quite favourable : they can be considered as thin objects and the weight of multiple scattering is very weak. They are generally studied with their axis lying within the specimen grid plane, i.e. perpendicular to the direction of the primary beam. High resolution EM images, recorded in this geometry, have been used by Iijima [9] to identify about 10 years ago, the atomic structure of multi-walled carbon nanotubes.

EELS spectroscopy can be used for several purposes : (i) for elemental analysis of composite nanotubes ; (ii) for probing the electron states in individual carbon nanostructures of different geometries ; (iii) for investigating the collective dielectric response (bulk and surface plasmons) in different types of nanotubes : multi-walled (MWCNT), single-walled (SWCNT) or ropes of SWCNT.

3.1 Elemental analysis of composite nanotubes.

In this mode, one records sequences of EELS spectra while scanning the probe across selected nanotubes. Then the different core-loss peaks are identified and their weights in each spectrum are scaled with the corresponding atomic cross sections, so that one can provide maps of the atomic composition of each element present in the tube. This technique has been used successfully to analyse Mn filled nanotubes [20] or to reveal the role of the impurity sulphur atoms, contained in the graphite electrodes of the arc-discharge, as a key wetting agent in the metal filling process of the nanotube core hole [21]. More recently, hybrid

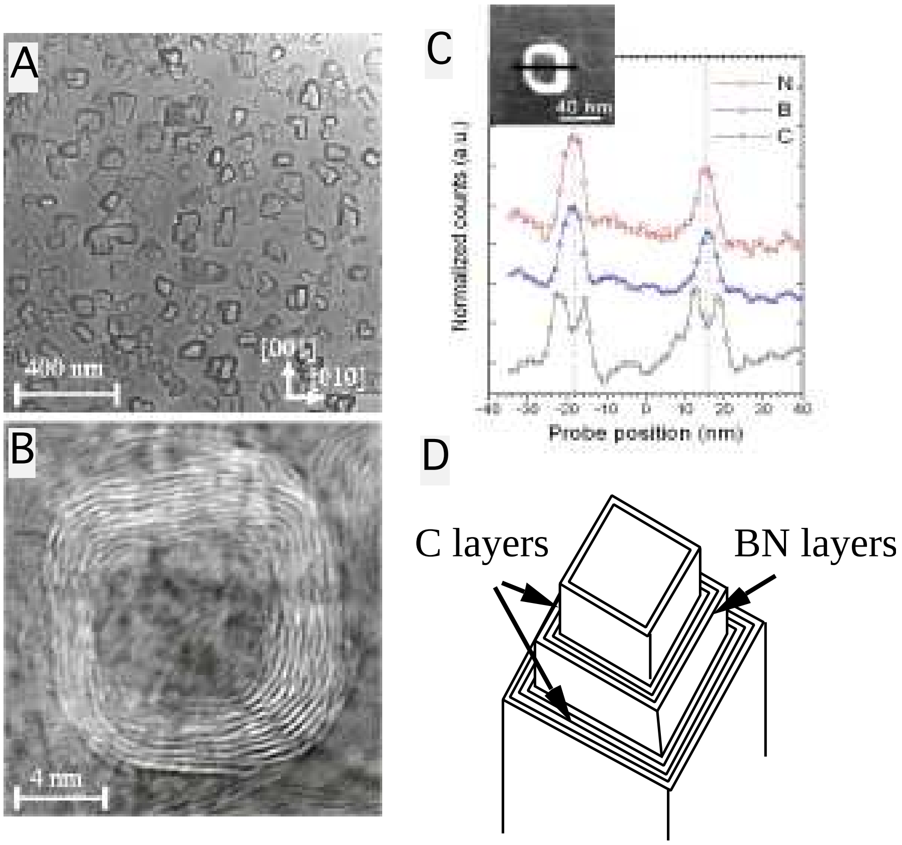

Figure 3.- EELS elemental analysis of nanoboxes grown by reactive dc magnetron sputtering from a B_4C target in mixed N_2/Ar discharges on self-patterned NaCl substrates : (A) and (B) plane-view TEM micrographs ; (C) EELS elemental profiles of B, C and N signals ; (D) schematic representation of the nanostucture morphology and composition (courtesy of M. Johansson et al. [24])

nanotubes made of boron, carbon and nitrogen have been shown to exhibit coaxial morphologies. The perfect correlation between the B and N peaks and their obvious anticorrelation with the C peak are signatures of a complete phase separation within the layers, of the three elements into a pure boron nitride phase and a pure carbon one [22].

This demixion has been proved to be quite general, independent of the morphology of the nano-object [23]. In figure 3 we present another example of such a phase separation between C and BN layers, encountered in nanoboxes, grown with a quite different technique : reactive sputtering of a B_4C target in mixed argon and nitrogen discharges, the final compound being grown on self-patterned NaCl substrates [24].

The characteristic morphology of these nano-features, seen end-on, with walls perpendicular to the substrate surface and exhibiting rather sharp (rectangular) corners, is obviously induced by the NaCl (001) surface substrate. It has been shown to reconstruct into square or rectangular-shaped morphology under pre-exposure to a low energy electron beam. It constitutes another demonstration of a three-shell structure in the walls of the BN/C nanoboxes : each wall is made of a C layer on the inside and the outside and a BN one in the middle. The average thickness of each layer varies from one to five nm. The 90° curvature is partially preserved during the growth process by the existence of 4-atom BN units in the building inner frame. The use of spatially resolved EELS has also lead to the discovery of coaxial structures, either involving a thin coverage of vanadium oxide over the surface of a carbon nanotube behaving as a template [25], or combining silicon-based nanowires with C : BN : sheaths of a few nm thick [26].

3.2 Unoccupied density of states in carbon nanostructures as a function of stacking and curvature.

As already demonstrated, the pixel per pixel exploration of the carbon K-edge fine structure across an isolated nanotube offers the possibility of monitoring changes induced by the variation of the local orientation of the layers with respect to the direction of the incident electron (see fig. 2). For a thick MWCNT, each spectrum averages over the trajectory of the electron, the information delivered by graphene layers of varying tilt and curvature and it is not easy to push further the analysis. Over the past few years, different graphitic carbon "nanotubulites", exhibiting original morphologies, have been synthesised : multi-walled carbon nanotubes in cross section, aggregates of nanohorns [27], aggregates of various sized fullerenes, double walled carbon nanotubes, free standing single graphene layers. In these architectures, the graphene layers may be coupled or decoupled, and they show increasing curvature from planar graphite ($R = \infty$) to the smallest nanotube ($R \cong 0.3$ nm). Our technique has been used to monitor the changes in the position, shape and intensity of the unoccupied π^* and σ^*-type bands, when positioning the incident electron probe on each of these specific configurations [28]. Fig. 4 displays a selection of these spectra, as a function of R. One notices, as R decreases, a reduction and slight broadening of the π^* peak, a clear decay of the first peak (b) at the onset of the σ^* band, a merging and a shift towards lower energies of the different higher energy features of the σ^* band (i.e. peaks labelled c, d and e in fig. 4). In a previous paper [29] dealing with spectra recorded on a MWCNT and on an isolated SWCNT, the two extreme cases in the present series, i.e. corresponding to spectra (I) and (V), had been compared. A LMTO-ASA calculation of the p- component in the unoccupied density of states had been successful in explaining the relative stability of the π^* feature as long as the corrugation of the graphene sheets does not exceed 8°, and the general shift of the gravity centre of the σ^* band towards lower energies. However, it had failed to explain the decay of the first peak (b) of the σ^* band. More recently, the experimental data shown in fig. 4 have been reconsidered within the frame of *ab initio* electronic structure calculations, incorporating the simulation of EELS spectra [28]. This revisited theoretical description has emphasised the correlation between the systematic variations of the EELS data and the curvature of the graphene sheet on one hand, and the limited effect of the inter-layer interaction on the electronic structures of unoccupied states on the other hand.

This study demonstrates that spatially resolved EELS approaches provide useful information complementary to Scanning Tunneling Spectroscopy measurements, for the exploration of electron structures in single isolated nanostructures [30]. While the latter ones are best suited to explore with atomic spatial resolution electron states on both sides of the Fermi level, the former ones investigate states over extended energy windows, at a nearly equivalent level of spatial resolution.

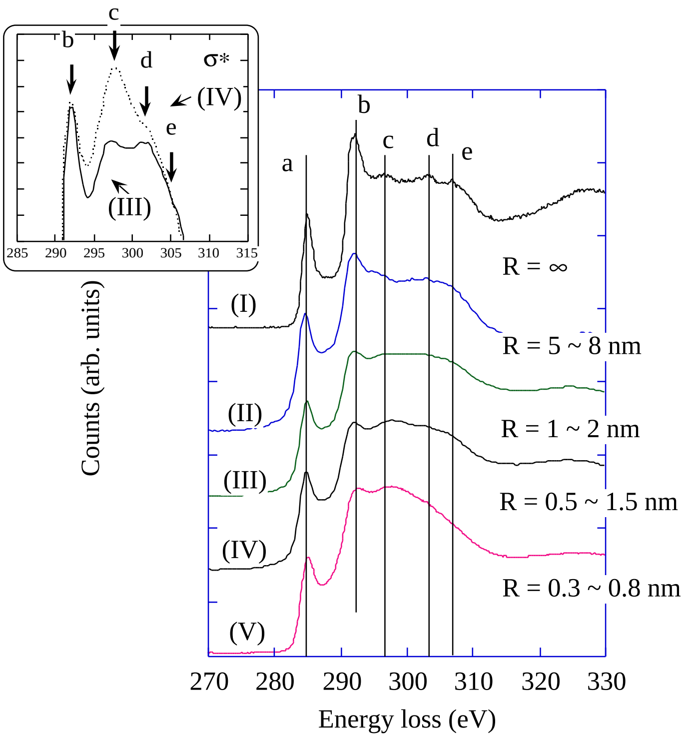

Figure 4.- Set of C-K edge fine structures recorded on isolated graphene layers of different radius of curvatures. The inset is an enlarged view of the fine changes observed at the threshold of the σ* band when the radius of curvature typically decreases from above to below one nanometer.

3.3 Plasmons in isolated CNT.

As shown in fig. 2, single isolated carbon nanotubes can be selected in a STEM ADF image and their valence electron excitation spectrum explored, while scanning the incident electron beam from intersecting trajectories to non-intersecting, or "aloof", trajectories. This EELS technique, as demonstrated in [15, 31], offers some unique advantages with respect to the equivalent photon beam technique. It can unambiguously discriminate bulk excitation modes, which only appear when the electron beam travels through the tube, from surface modes which can also be excited from the outside. Fig. 5a introduces a classical interpretation : the Coulomb field created by the propagating incident electron polarises the nanotube, which therefore radiates an induced electromagnetic field. The work created by the interaction of this induced field acting back on the propagating electron at velocity $\vec{v}$, is responsible for the energy loss measured at an impact parameter as high as 10 nm or more from the outer surface of the tube. This near-field EELS spectroscopy covers a broad spectral range extending far into the VUV domain. The varying impact parameter can be used as an extra parameter to test descriptions of the interaction between a swift electron and a medium of given polarisability, shape and size. It generally gives rise to quasi-exponential decays of the different surfaces loss peaks in vacuum, with characteristic decay lengths varying as $E^{-1/2}$. These peculiar properties of the technique had been pointed out about a decade ago by Howie et al. [32], Ugarte et al. [33], for a set of different geometries : planar external surfaces, truncated surfaces, concentric spheres.

We have applied this technique to different cylindrical or spherical nano-objects, varying in composition (carbon or boron nitride), in inside and outside diameters and in number of walls. The major response of a weakly bound population of electrons is collective an appears as a bulk plasmon corresponding to a longitudinal electron density wave. In the case of a nanoparticle made of wrapped layers, the situation is made more complex by anisotropy effects and boundary conditions, which impose the existence of extra modes of electron oscillations localised on the inner and outer surfaces,

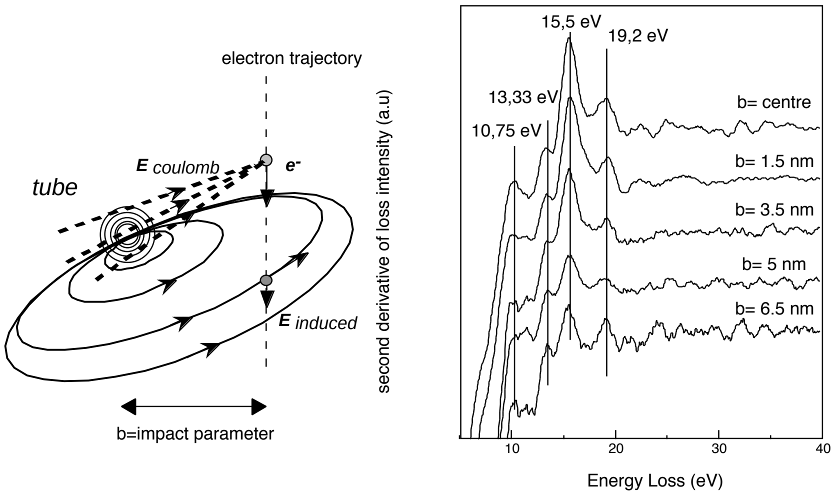

Figure 5.-Left : Schematic representation of the electromagnetic coupling between an incident electron of high velocity and a polarisable nanoparticle ; right : set of EELS spectra (in the second derivative mode) recorded at different impact parameters with respect to the centre of an isolated 2-wall carbon nanotube.

i.e. the surface plasmon modes. These modes can best be detected from outside. For tubes or onions made of a reasonable number of walls, Kociak et al. [34] have shown that a classical continuum dielectric model could positively account for the observed surface plasmon excitations in highly anisotropic curved and hollow nanostructures. This geometry, as already noticed, adds a specific complexity : the spatial variation necessarily encompasses a change in tilting angle, i.e. a variable relative contribution of $\vec{q}\perp\vec{c}$ (in plane) and $\vec{q}/\!/\ \vec{c}$ (out of plane) momentum transfers. Furthermore, the excited modes in a spherical geometry are labelled following a $\ell = 1 \dots \infty$ multipolar quantum number, while in a cylindrical geometry the index is $m = 1 \dots \infty$, the azimuthal quantum number.

In a compound where different families of interband transitions can be identified, it has been shown that for each family of allowed interband transitions, there exists a plasmon mode for the bulk as well as for the surface. Consequently :

(i) the 6 eV peak (BP 1) in fig. 1 corresponds as a matter of fact to a BP and to a SP associated with the π-π* transitions for the in-plane dielectric function of graphite ($\varepsilon_{\perp}$) ;

(ii) the 27 eV peak (BP 2) and 17-18 eV peak (SP) correspond to the σ-σ* transitions for the in-plane dielectric function of graphite ($\varepsilon_{\perp}$) ;

(iii) the weaker 23 eV and 14 eV peaks, revealed in the second derivative mode, correspond to both σ-π* and π-σ* transitions for the out-of-plane dielectric function of graphite ($\varepsilon_{//}$).

Furthermore, slight shifts in energy position detected when varying the impact parameter, are interpreted in terms of change of the most excited ℓ quantum number value, from $\ell = 1$ (dipolar) far from the surface where the field is quasi uniform, towards $\ell = \infty$ (multipolar) as b is reduced close to zero.

What happens when the size of the nanotube becomes smaller and smaller, i.e. when the number of walls is reduced to one ? The recorded spectra exhibit noticeable differences. Fig. 5b displays spectra recorded on a 2-wall carbon nanotube in the energy range dealing with σ-type features. No bulk plasmon can then be detected. Each of the in-plane and out-of-plane σ-type surface plasmons seems to be split into two modes The lower mode of the σ in-plane SP at about 15.5 eV and the higher mode of the σ out-of-plane SP, at about 13.3 eV, seem to give rise to an enhancement of the former one and a lowering of the latter one. This is not a meaningless remark when one knows that for an isolated single-wall CNT, one observes only one peak at 15 eV. Within the frame of the dielectric description above, if still applicable, it is reasonable to admit that there is no longer any argument to distinguish between symmetric and antisymmetric modes because both inner and outer surfaces coincide for one single atomic layer. However it is more reasonable at this stage to consider that the limit of validity of the dielectric model has been reached, and that an alternative route, considering the SWCNT as a quantum object, has to be explored to account for the existence of a single well defined mode.

4 EELS ON CN_X NANOSTRUCTURES.

It is now well established that for carbon nanotubes, electrical as well as mechanical properties depend on structural atomic arrangements responsible for size, diameter and chirality, and also on atomic defects. If hetero-atomic NT would be built, these properties should also be dependent on the chemistry. In particular, the introduction of nitrogen atoms into the architecture of carbon-based nanotubes might :

(i) modify electron transport properties by n-type doping ;

(ii) take benefit of the high strength predicted for CN bonds, in C_3N_4 structure for instance.

Consequently, several attempts have been made to grow CN_X nanotubes. Our preliminary experience relies on the systematic investigation of magnetron sputtering techniques used by the Linköping University group to grow thin foils of CN_X materials. Using complementary characterisation tools (among which the EELS studies performed in Orsay), this group has demonstrated the existence of a fullerene-type structure obtained for a given set of deposition parameters (gas nature and pressure, substrate temperature in the range 300-400°C) -see (35). This structure displaying interesting mechanical behaviour, i.e. strengthening effects associated with a very high elasticity, has been shown to consist of a nanocomposite embedding of cross-linked fullerene-like or nanotubular structures with curved and buckled basal planes, in a generally amorphous material. Similar results with respect to the nanostructure, as well as to the mechanical behaviour, had been reported for fullerene-like carbon nanocomposites [36].

In the following, different ways of producing CN_X nanotubes are compared in terms of chemical composition and bonding mechanisms involved to incorporate N atoms in tubular architectures. It will be shown that the preferential growth of carbon graphitic layers is in conflict with the insertion of N atoms, so that composite morphologies are generally preferred. These observations have stimulated further studies, as well theoretical as experimental, to improve our understanding of CN_X nano-structures growth. We will conclude with the study of dynamic behaviours encountered within this very rich family of objects.

4.1 Characterisation of different types of CN_X nanotubes

Three different routes, one unexpectedly discovered and the two others aiming at this specific goal, have been used to produce nanotubular objects containing both carbon and nitrogen. The first one is the PVD magnetron sputtering already described [37], the second one is the CVD deposition of nickel phtalocyanin [38], the third one is the pyrolisis of an organic precursor molecule melamine ($C_3N_6H_9$) in the presence of Ni catalyst [39]. In all cases, tubular structures have been observed. In the first one, tubes were short, homogeneous in composition with a maximum value of x up to 0.3 – 0.4, and a poorly organised crystallinity of the walls (buckled and interlinked). This structure has been obtained, without the assistance of catalytic particles and at low temperatures of the support (i.e. between 300 and 400°C). The two other techniques have produced long nanotubes of a few micrometer length with different morphologies, the first one with a herring bone organisation of graphitic layers around an amorphous core. The final one grown by pyrolisis exhibits a very characteristic cellular morphology (see fig. 6), with shuffled double lateral walls and a rather regular distribution of transversal walls. EELS line profiles across these two types of nanotubular morphologies reveal rather strong inhomogeneities in nitrogen content. For CVD deposed specimens, the nitrogen content is very low within the well-organised walls, is maximum (up to 15 at %) in the amorphous core, but is still of 5 to 8 % on the surface.

It has been proposed that this nitrogen content could correspond to two types of bonding, the most abundant one in the centre of the tube within a rather randomly distributed carbon backbone, the second one of less abundance being fixed on the dangling bonds of the carbon atoms at the rim of graphene sheets along the outer surface. In the specimen grown by pyrolisis from molecular melamine precursor, the composition is again inhomogeneous with more nitrogen inserted into the poorly organised carbon structures in the centre up to 10-15 at %, while the rate of nitrogen in the outer walls remains limited below 5 at %.

All these observations lead to the following conclusions (see also table II) :

(i) nitrogen atoms are poorly incorporated in well organised graphitic stackings ;

(ii) the more nitrogen in a structure, the more disorganised and defective it is ;

(iii) nitrogen atoms can be accomodated along edges or surfaces, if they are not too many and if the temperature is not too high.

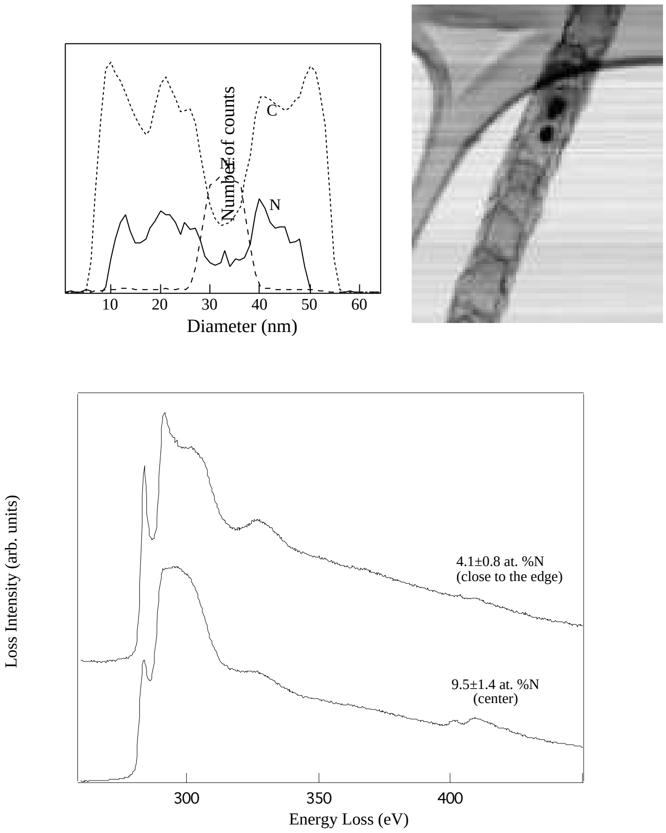

Figure 6.- Carbon nanotubes grown by pyrolisis from a N-rich organic precursor (melamine) in the presence of catalytic Ni nanoparticle (one is visible as a dark spot in the STEM bright field micrograph). The variation of the EELS specific C, N and Ni signals, deduced from the K and L_{23} edges, is shown in the top left figure. Finally two spectra exhibiting the weight and shape of the C and N K edges are displayed at the bottom.

Consequently, several approaches, as well theoretical as experimental, have been investigated in order to understand the mechanisms of insertion and bonding of nitrogen atoms into a carbon matrix.

Table II.- Comparison of the properties of CN_X nanotubes grown by different methods

	Magnetron sputtered from a carbon electrode in a nitrogen atmosphere	**CVD deposition of Ni phtalocyanin**	**Pyrolisis of a molecular organic precursor (melamine)**
Source of the specimen	Univ. Linköping (Sweden)	NEC, Tsukuba (Japan)	Univ. Sussex (U.K.)
Growth temperature	350°C	700-800°C	650 – 950°C
Use of catalyst	no	Yes : Ni	Yes : Ni, Fe
Structure	Tubular or leek-like	Tubular	Tubular with wrapped walls and compartments
Layers morphology	Heavily buckled	Buckled, herring-bone type	Very buckled
Nitrogen content	Homogeneous	Inhomogeneous	Inhomogeneous
N/C atomic ratio	Up to 15-30 at %	5 at % most in graphitic layers; ≅ 15 at % in amorphous regions	2 – 5 % in the envelope ; 10 – 15 % in the centre
Speculated growth history	Simultaneous	Layer by layer	Layer by layer

4.2 Nitrogen bonding in a carbon matrix

The insertion and bonding of nitrogen atoms into graphite-type carbon distorts and breaks its structural order, so that the regular stacking of graphene layers is changed into an amorphous or fullerene-type material, with buckled and cross-linked units.

In order to understand this effect, *ab initio* calculations (using the DFT total energy scheme with soft pseudo-potential, plane wave basis, and GGA calculated exchange energies) have been carried out, for different graphite derived model structures, when one over four atoms of carbon is nitrogen-substituted [40]. The basic idea is that a nitrogen atom prefers a site with a pyramidal short-range environment. When introduced into a perfect graphene layer, it is responsible for distorsions and instabilities so that their nearest neighbouring carbon atoms have also to adjust by adopting out-of-plane configurations. This is the starting point of induced corrugations and consequent cross-linking between nearest-neighbour graphene layers. These calculations have first shown that the stabilisation energies for different modes of dimerised or polymerised structures are not much higher than those for flat N-substituted graphite. Consequently, entropy effects may become important and a wide variety of local structures encountered. Furthermore, the calculation of energy barriers between them leads to relatively small values. Consequently at room temperature, C_3N compounds may transform dynamically from one structure to another over a limited period of time ($\lesssim 1$ s). Such a fluidity for an open structure could explain the absence of clearly identifiable fine structures, because the accompanying calculations of density of states have led to a set of different features, which could superpose and give rise to the generally featureless C edges, generally encountered in amorphous carbon phases.

The detailed observation of the N-K fine structures has revealed a very stable broad σ^* peak of triangular shape, but a diversity of π^* lines with many cases of splitting. It suggests that the nitrogen atoms can be involved in different types of bonding. In order to verify this assumption, the structural and chemical properties of CN_x thin films have been monitored during in-situ annealing experiments in a TEM column [41]. EELS measurements performed at temperatures up to 1000°C have shown that a high proportion of the initial nitrogen atomic content (between 65 an 80 %) is released during annealing at 1000°C. Furthermore a splitting of the N-K π^* line appears when these films are heated at temperatures above approximately 700°C. This behaviour has been explained by the formation of molecular nitrogen, in agreement with a process of nitrogen release during graphitisation confirmed by HREM images, while the remaining nitrogen might be bound in pyridine-like structures which would limit the growth of the graphitic layers.

4.3 Dynamics of beam-induced reactions in carbon-nitrogen systems

The high detection efficiency of the newly installed CCD-based parallel EELS detector has offered new possibilities for monitoring transient phenomena under the influence of the primary electron beam. As a matter of fact, fluxes of the order of a few 10^9 electrons/nm^2.s are available in a focused STEM probe, and spectra can be recorded at a rate approaching 10^2 Hz, which means that the early stages of beam induced specimen transformation can be investigated. The technique of acquiring spectral sequences, for a fixed probe, is easily derived from the spectrum-imaging mode, by maintaining the current in the scanning coils at a stable value. It was introduced, nearly a decade ago as the "chronospectroscopy" mode [42], but its use has remained limited until the recent technological improvements.

The previous static studies have demonstrated the difficulty of introducing nitrogen atoms into a graphitic network, the varsity of the obtained structures and the possibility of coexistence between different types of bonding. Furthermore theoretical calculations have suggested the "fluidity" of the grown structures exhibiting a rather high proportion of open space.

Over the past few years, the Sussex group has explored new routes for synthesising CN_x nanotubes, relying on the pyrolisis of organic molecules in the presence of iron and nickel catalysts [43]. Two possibilities have been considered : (i) the use of a nitrogen-rich precursor molecule, such as melamine – $C_3H_9N_6$ – with an initial N/C ratio of 2, in the presence of argon-carrier gas ; (ii) the use of a nitrogen-deprived molecule, such as camphor – $C_{10}H_{16}O$ – in the presence of a nitrogen-rich carrier gas. In both cases, CN_x nanotubes have been successfully grown, as already discussed in paragraph 4.1 for the melamine precursor – see fig. 6 and table II – and as shown in fig. 7 and discussed later for the camphor precursor.

In order to understand why the final concentration of nitrogen in the CN_x nanotubes grown from a precursor with a ratio x = [N]/[C] = 2, is only of the order of 0.1 – 0.2 maximum, we have used the incident electron beam in the STEM to mimic the decomposition process of melamine molecules, which have been found to be very sensitive to radiation damage [44]. EELS fine structures have been recorded at different stages of the electron beam induced transformation of an initial specimen made of melamine powder. The rates of mass loss and of specific element (C and N) loss have been measured, together with the recording of both C and N-K edge fine structures at different stages of the evolution of the specimen. The preferential release of nitrogen has been confirmed. In the sequence of involved events, different processes have been identified, involving first the desorption of the external amino groups, then the rearrangement of the aromatic rings and finally the breaking into CN_X fragments.

When the tubes have been grown from a precursor without nitrogen and the nitrogen fed in the gas phase during the pyrolisis in reactor, new tubular configurations have been found [45]. The tubes are generally spiralling, they are long (a few µm) and have a rather uniform external diameter of the order of 50 nm. Similarly to those grown from the melamine precursor, they exhibit a compartment morphology with regularly spaced cavities of the order of 30-80 nm along the tube axis (see fig. 7). Spatially resolved EELS analysis across the tubes has shown that the rather well organised graphitic external walls contain very little nitrogen while a concentration of a few atomic % can be found within the inner cavities filled with poorly organised material. More interesting is the fine structure on the nitrogen K-edge which is typical of the N_2 phase, while the C-K edge corresponds to graphite. Furthermore, over the first 40 seconds in the time-resolved mode, the nitrogen signal regularly increases (up to 25-30 at %), until it suddenly vanishes. This behaviour suggests that in this type of nanotube the different cells constitute independent capsules filled with nitrogen gas. This gaseous content can be released under the impact of the electron beam, which punctures the walls of the tube.

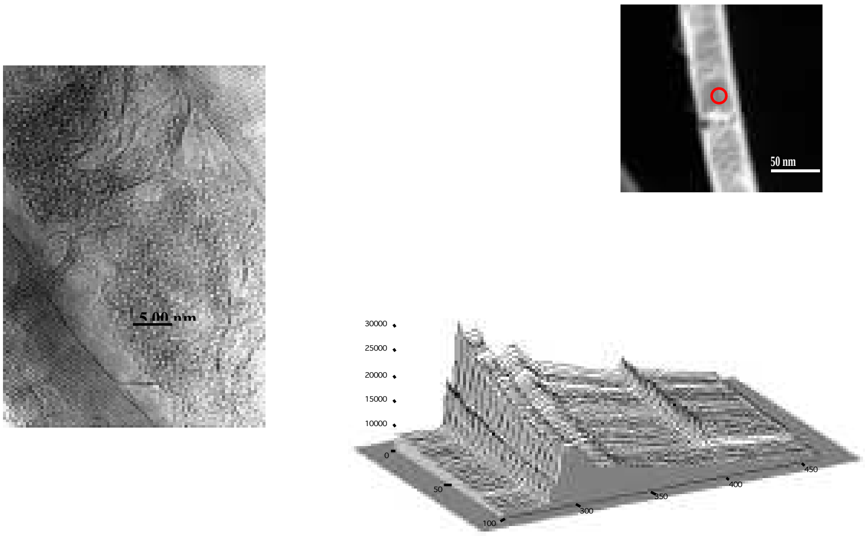

Figure 7.- HREM image of a CN_x nanotube grown by pyrolisis of camphor molecules under a flow of N_2/NH_3 gas, with well organised graphitic walls and disorganised material inside. Assemblies of a few graphite layers seem to constitute e frame of the transverse compartment walls. ADF STEM image showing the point of EELS analysis at the apex of one capsule. Time sequence of EELS spectra demonstrating the release of N_2 molecules and the change of fine structures in the carbon K-edge.

These two examples demonstrate how the electron beam can be used simultaneously to modify the carbonaceous specimen and to monitor the associated chemical and electronic changes.

5 CONCLUSION

This review paper has demonstrated a few unique capabilities offered by spatially resolved EELS techniques, to explore local chemical and electronic properties in carbon-based nanostructures. The spatial resolution is far better than for any other spectroscopic tool, except that offered by scanning tunnelling spectroscopy, which however can only investigate surface electron states over a limited energy range. The energy resolution, in the sub-eV scale, is quite adapted to perform a systematic analysis over an extended energy range covering a broad spectral domain. It lies however substantially below the energy resolution offered by modern synchrotron facilities. Consequently, it is clear that this first generation of new results should stimulate further work for designing and building a next generation STEM, aiming at typical values of 0.2 nm and 0.2 eV in terms of spatial and energy resolution. Several solutions have been already successfully tested : the spherical aberration corrector by Krivanek et al [46], the monochromator with different designs calculated and presently under test [47,48]. In parallel, all components have to be improved, in particular in terms of electrical and mechanical stability. Finally, great care has to be devoted to the detection strategy with an ultimate efficiency aiming at counting any electron scattered by the specimen, whatever may be the momentum and energy transferred in the collision event.

The second major message which has been delivered, in particular through the latter examples, is the potentiality of transforming the electron microscope from a passive into an active machine. In other terms, the general conception of the instrument is quite well suited to the selection, observation and characterisation of unique isolated nano-objects, during in-situ experiments : irradiation with the primary electron beam or with an external photon beam, heating over different temperature ranges as already demonstrated in the present paper. It can also involve controlled strain during in-situ deformation. Such a preliminary experiment has recently been achieved, to relate the local changes in electron states measured by EELS, with the in-situ applied deformation of a single carbon nanotube [49]. All these considerations should convince us that all conditions are now gathered for the future STEM microscopes to be run as nano-laboratories.

6 ACKNOWLEDGEMENTS

This work has been performed with the support of CNRS (France), of an international cooperation project ICORP between CNRS (France) and JST (Japan) – the Nanotubulite project – under the direction of S. Iijima and C. Colliex, of an European Training and Mobility of Researchers program on Carbon-based hard materials, coordinated by S. Csillag (Stockholm). Special thanks are due to all our colleagues who have been involved over the past five years, in the production and characterisation of new carbon-based films, nanostructures and nanotubes, in particular P. Bernier et al. (Montpellier), H. Pascard et al. (Palaiseau), L. Hultman et al. (Linköping), V. Serin et al. (Toulouse), H. Kroto et al. (Brighton). The permanent support of M. Tencé (LPS, Orsay) for the design, realisation and running of new pieces of equipment and software has been essential for the success of many experiments reported in the present review. Finally, one of us (CC) is kindly indebted to the organisers of the School for having offered him the opportunity of preparing and presenting this text.

7 REFERENCES

1 Colliex, C. (1984) Electron energy-loss spectroscopy in the electron microscope, in *Advances in Optical and Electron Microscopy*, eds. R. Barer and V.E. Cosslett, Academic Press, London, Vol. 9, pp. 65-177

2- Egerton, R. (1996) *Electron Energy-Loss Spectroscopy in the Electron Microscope*, 2nd edition, Plenum Press, New York

3- Colliex, C. (1992) Electron energy-loss spectroscopy on solids, in *International Tables of Crystallography*, Kluwer Press, Vol. C, pp. 338-359

4.- Colliex, C. (1995) Investigation of local electronic properties in solids by transmission electron energy-loss spectroscopy, in *Core Level Spectroscopies for Magnetic Phenomena*, Eds. P.S. Bagus, G. Pacchioni and F. Parmigiani, NATO ASI Series B : Physics, Vol. 345, pp. 213-233

5.- Disko, M.M., Ahn, C.C. and Fultz, B. (1992*) Transmission Electron Energy-Loss Spectrometry in Materials Science*, TMS Warrendale, Pa 15086

6.- Reimer, L. (1995) *Energy-Filtering Transmission Electron Microscopy*, Springer Series in Optical Sciences, vol. 71, Springer Verlag, Berlin, Heidelberg, New York

7.- Kroto, H.W., Heath, J.R., O'Brien, S.C., Curl, R.F. and Smalley, R.E. (1985*)* C_{60} buckminsterfullerene*, Nature* **318**, 162-164

8.- Ugarte, D. (1992) Curling and closure of graphitic networks under electron-beam irradiation, *Nature* **359**, 707-709

9.- Iijima, S. (1991) Helical microtubules of graphitic carbon, *Nature* **354**, 56-58

10.- Stöhr, J. (1996) *NEXAFS Spectroscopy*, 2nd edition, Springer Series in Surface Sciences, vol. 25, Springer Verlag, Berlin, Heidelberg, New York

11.- Bruley, J.et al. (1995) Quantitative near-edge structure analysis of diamond-like carbon in the electron microscope using a 2-window method, *J. Microscopy* **180**, 22-32

12.- Jeanguillaume, C. and Colliex, C. (1989) Spectrum-image : the next step in EELS digital acquisition and processing, *Ultramicroscopy* **28**, 252-257

13.- Bouchet, D. et al. (1998) Mapping the chemistry and electron states in nanostructures with a subnanometer probe of high energy electrons, *in "The Electron", Proc. International Centennial Symposium on the Electron, Cambridge,* Eds. A. Kirkland and P.D. Brown, The Institute of Materials, pp. 247-257

14.- Colliex, C. et al. (1999) Electron energy-loss spectroscopy (EELS) on nano-dimensional structures, *J. Electron Microscopy* **48** (Suppl.) 995-1003

15.- Cohen, H., Maniv, T., Tenne, R., Rosenfeld-Hacohen, Y., Stephan, O. and Colliex, C. (1998) Near-field electron energy-loss spectroscopy of nanoparticles, *Phys. Rev. Lett.* **80**, 782-785

16.- Stephan, O. (1996) *Etude de la chimie locale et de la structure électronique de nanotubes de crabone purs ou composites par spectroscopie de pertes d'énergie d'électrons*, Thèse de doctorat, Université de Paris-Sud

17.- Tencé, M., Quartuccio, M. and Colliex, C. (1995) PEELS compositional profiling and mapping at nanometer spatial resolution, *Ultramicroscopy* **58**, 42-54

18.- Bonnet, N., Brun, N. and Colliex, C. (1999) Extracting information from sequences of spatially resolved EELS spectra using multivariate statistical analysis, *Ultramicroscopy* **77**, 97-112

19.- Serin, V. and Sikora, T (2000), see EELS library at www.cemes.fr/eelsdb/

20.- Ajayan, P.M. et al. (1994) Growth of manganese filled carbon nanofibers in the vapor phase, *Phys. Rev. Lett.* **72**, 1722-1725

21.- Demoncy, N., Stéphan, O., Brun, N., Colliex, C., Loiseau, A. and Pascard, H. (1998) Filling carbon nanotubes with metal by the arc-discharge method : the key role of sulphur, *Eur. Phys. J. B* **4**, 147-157

22.- Suenaga, K., Colliex, C., Demoncy, N., Loiseau, A., Pascard, H. and Willaime, F. (1997) Synthesis of nanoparticles and nanotubes with well-separated layers of boron nitride and carbon, *Science* **278**, 653-655

23.- Suenaga, K., Willaime, F., Loiseau, A. and Colliex, C. (1999) Organisation of carbon and boron nitride layers in mixed nanoparticles and nanotubes synthesised by arc-discharge, *Applied Physics A* **68**, 301-308

24.- Johansson, M.P., Suenaga, K., Hellgren, N., Colliex, C., Sundgren, J.E. and Hultman, L. (2000) Template synthesised BN:C nanoboxes, *Appl. Phys. Lett.* **76**, 825-827

25.- Ajayan, P.M., Stéphan, O., Redlich, Ph. and Colliex, C. (1995) Carbon nanotubes as removable templates for metal oxide nanocomposites and nanostructures, *Nature* **375**, 564-567

26.- Zhang, Y., Suenaga, K., Colliex, C. and Iijima, S. (1998) Coaxial nanocable : silicon carbide and silicon oxide sheathed with boron nitride and carbon, *Science* **281**, 973-975

27.- Iijima, S. et al. (1999) Nano-aggregates of single-walled graphitic carbon nano-horns, *Chem. Phys. Lett.* **309**, 165-170

28.- Suenaga, K., Sandré, E., Colliex, C., Pickard, C.J., Kataura, H. and Iijima, S. (2001) EELS investigation of electron states in isolated carbon nanostructures, Phys. Rev.B, 6316, (16), 5408.

29.- Stephan, O., Ajayan, P.M., Colliex, C., Cyrot-Lackmann, F. and Sandré, E. (1996) Curvature induced bonding changes in carbon nanotubes, *Phys. Rev. B* **53**, 13824-13829

30.- Wildöer, J., Venema, L.C., Rinzler, A.G., Smalley, R.E. and Dekker, C. (1998) Electronic structure of atomically resolved carbon nanotubes, *Nature* **391**, 59-62.

31.- Williams, P., Lévy-Clément, C., Brun, N. and Colliex, C. (2000) Near-field electron energy-loss spectroscopy in porous silicon, *J. Porous Materials* **7**, 159-163

32.- Howie, A. and Milne R.H., (1985) Excitations at interfaces and small particles, *Ultramicroscopy* **18**, 427-434

33.- Ugarte, D., Colliex, C. and Trebbia, P. (1992) Surface and interface plasmon modes on small semiconducting spheres, *Phys. Rev. B* **45**, 4332 - 4343

34.-Kociak, M., Henrard, L., Stéphan, O., Suenaga, K. and Colliex, C. (2000) Plasmons in layered nanospheres and nanotubes investigated by spatially resolved EELS, *Phys. Rev. B* **61**, 13936-13944

35.- Hellgren, N., Johansson, M.P., Broitman, E., Hultman, L. and Sundgren, P.E. (1999) Role of nitrogen in the formation of hard an elastic CNx thin films by reactive magnetron sputtering, Phys. Rev. B **59**, 5162 -5169

36.- Amaratunga, G.A.J., Chhowalla, M., Kiely, C.J., Alexandrou, I., Aharonov, R. and Devenish, R.M. (1996) Hard elastic carbon thin films from linking of carbon nanoparticles, *Nature* **383**, 321-323

37.- Suenaga, K. et al. (1999) Carbon nitride nanotubulite : densely-packed and well aligned tubular nanostructures*, Chem. Phys. Lett.* **300**, 695-700

38.- Suenaga, K., Yudasaka, M., Colliex, C. and Iijima, S. (2000) Radially modulated nitrogen distribution in CN_x nanotubular structures prepared by CVD using Ni phtalocyanin, *Chem. Phys. Lett.* **316**, 365-372

39.- Terrones, M., Hsu, W.K., Kroto, H.W. and Walton D.R.M. (1999) Nanotubes : a revolution in materials science and electronics, in *Topics in Current Chemistry,* vol. **199**, Springer Verlag Berlin Heidelberg, pp. 190-233

40.- Sandré, E., Pickard, C.J. and Colliex, C. (2000) What are the possible structures for CN_x compounds ? The example of C_3N, *Chem. Phys. Lett.* **325**, 53-60

41.- Grillo, S., Hellgren, N., Serin, V., Broitman, E., Colliex, C. and Hultman, L. (2001) Monitoring the structural and chemical properties of CN_x thin films during in-situ annealing in a TEM, *Eur. Phys. J. : Applied Physics*, **13**, (2), 105.

42.- Tencé, M. et al. (1989) Electron irradiation effects : a time-energy representation, *Inst. Phys. Conf. Series* **98**, 311-314

43.- Terrones, M. et al. (1999) Carbon nitride nanocomposites : formation of aligned nanofibers, *Advanced Materials* **11**, 655-659

44.- S. Trasobares[1], R. Räty[1], N. Borglund[4], A, Bassan[4], C. Kolczewski[4], L.G.M. Pettersson[4], G. Hug[2], C. Colliex[1,3,] S. Csillag[4]. (2001) A route to study the carbon-nitrogen bond in CN_x thin films : EELS chrono-spectroscopy of the molecular melamine precursor, submitted.

45.- Trasobares, S. Stéphan, S. Colliex, C. Hug, G. Hsu, W.K., Kroto, H.W., Wlaton, D.R.M.. (2001) Electron beam puncturing of carbon nanotubes containers for release of stored N_2 gas. **22,** 117. *Eur. Phys. J* B.

46.- Krivanek, O.L., Delby, N. and Lupini, A.R. (1999) Toward sub-angström electron beams, *Ultramicroscopy* **78**, 1-11

47.- Terauchi, M., Tanaka, M., Tsuno, K. and Ishida, M. (1998) Development of a high energy resolution electron energy-loss spectroscopy microscope, *J. Microscopy* **194**, 203-209

48.- Mook, H.M. and Kruit, P., (1999) *Ultramicroscopy* **78**, 43-51

49.- Suenaga, K., Colliex, C. and Iijima, S. (2001) In-situ electron energy-loss spectroscopy on carbon nanotubes during deformation, (2001) *Appl. Phys. Lett.,* **78**, 1, 70.

8.-ACRONYMES

AFM	Atomic Force Microscopy
BF	Bright Field
CCD	Charge-Couple Devices
CTEM	Conventional-TEM
CVD	Chemical Vapour Deposition
DC	Direct current
EDX	Energy Dispersion X-ray
EELS	Electron Energy Loss Spectroscopy
ELNES	Electron Loss Near Edge Structure
ERDA	Elastic Recoil Detection Analysis
EXAFS	Extended Fine Structures
fcc	face centred cubic
g-C_3N_4	graphitic C_3N_4
HADF	High Annular Dark Field
HAADF	High Angle Annular Dark Field
HFCVD	Hot Filament Chemical Vapour Deposition
HRTEM	High Resolution Transmission Electron Microscope
IBAD	Ion Beam Assisted Deposition
IR	Infra Red
I-V	current Intensity-applied voltage
MO	Molecular Orbitals
MSA	Multivariate Statistical Analysis

MWNT's	Multi-Walled Nanotubes
NMR	Nuclear Magnetic Resonance
NNLS	Non Negative Least Square fitting
PDA	Photo Diode Array
PECVD	Plasma Enhanced Chemical Vapour Deposition
PVD	Physical Vapour Deposition
rf	radio frequency
SEM	Scanning Electron Microscopy
STEM	Scanning Transmission Electron Microscope
STM	Scanning Tunneling Microscopy
SWNT's	Single-Walled Nanotubes
TED	Transmission Electron Diffraction
TEM	Transmission Electron Microscopy
TMR	Training Mobility Research
XPS	X-ray Photoelectron Spectroscopy
STM	Scanning Tunneling Microscopy
SAADF	Small Angle Annular Dark Field
0, 1, 2, D	0, 1, 2 Dimensional